University of Wollongong

Research Online

University of Wollongong Thesis Collection 1954-2016

University of Wollongong Thesis Collections

2003

Radiation hardness study of high purity silicon and the development of a radiation damage monitoring system for silicon devices in mixed radiation fields

Mark Reinhard
University of Wollongong
Follow this and additional works at: https://ro.uow.edu.au/theses

University of Wollongong

Copyright Warning

You may print or download ONE copy of this document for the purpose of your own research or study. The University does not authorise you to copy, communicate or otherwise make available electronically to any other person any copyright material contained on this site.

You are reminded of the following: This work is copyright. Apart from any use permitted under the Copyright Act 1968, no part of this work may be reproduced by any process, nor may any other exclusive right be exercised, without the permission of the author. Copyright owners are entitled to take legal action against persons who infringe their copyright. A reproduction of material that is protected by copyright may be a copyright infringement. A court may impose penalties and award damages in relation to offences and infringements relating to copyright material. Higher penalties may apply, and higher damages may be awarded, for offences and infringements involving the conversion of material into digital or electronic form.

Unless otherwise indicated, the views expressed in this thesis are those of the author and do not necessarily represent the views of the University of Wollongong.

Recommended Citation

Reinhard, Mark, Radiation hardness study of high purity silicon and the development of a radiation damage monitoring system for silicon devices in mixed radiation fields, Ph.D. thesis, Department of Engineering Physics, University of Wollongong, 2003. http://ro.uow.edu.au/theses/155

Research Online is the open access institutional repository for the University of Wollongong. For further information contact the UOW Library: research-pubs@uow.edu.au

RADIATION HARDNESS STUDY OF HIGH PURITY SILICON AND THE DEVELOPMENT OF A RADIATION DAMAGE MONITORING SYSTEM FOR SILICON DEVICES IN MIXED RADIATION FIELDS

A thesis submitted in fulfilment of the

requirements for the award of the degree

Doctor of Philosophy

from

UNIVERSITY OF WOLLONGONG

by

Mark Reinhard, BSc.(Hons)

Centre of Medical Radiation Physics (CMRP)

Department of Engineering Physics

2003

ABSTRACT

This thesis describes an experimental study into the radiation hardness of high purity silicon. This material is principally used in the manufacture of silicon based microstrip detectors and other similar devices.

Radiation detector test structures which had been fabricated on the base of different types of silicon were exposed to ~ 1 MeV neutrons. This was done to determine the role of different impurities in the formation of radiation induced crystallographic defects within the silicon lattice. Oxygenated silicon, nitrogenised silicon and silicon containing the standard residual impurities was investigated. The effect of the deep level states associated with the defects on the detector electrical properties was also studied.

At the relatively high neutron fluence employed, up to 7.5×10^{13} $n\cdot cm^{-2}$, the conventional capacitance based Deep Level Transient Spectroscopy (DLTS) technique is not applicable. In order to detect and measure the properties of the defects a new technique was used known as Optical Deep Level Transient Conductance Spectroscopy (ODLTCS). Spectral features identified in the ODLTCS spectra were attributed to known radiation induced defects in silicon through the comparison of the measured energy levels of the associated deep level states and the measured introduction rates with data contained in the literature.

Using ODLTCS the kinetics of the growth and contraction of particular defect concentrations in each of the irradiated detector types was measured as a function of room temperature annealing. Correlation in the evolution of the radiation induced C_i-O_i defect and the short term annealing of the effective impurity concentration (N_{eff}) was observed. Based on this finding a microscopic explanation for the improved radiation hardness of oxygenated silicon is described. Other possible mechanisms of defect engineering were also investigated.

No deep level defect identified from the ODLTCS spectra could be attributed to the long term reverse anneal of N_{eff}. This suggested that the responsible defect had an energy state

outside the ODLTCS detection limit of less than |0.16 eV| as measured from either the conduction or valence band edge.

Significant reduction in the production rate of the V-O defect was observed in nitrogenised silicon. Evidence supporting possible metastability of the V-O defect was also obtained.

Another important aspect of this research was the development of technologies for use in the on-line monitoring of radiation damage to silicon devices in mixed radiation fields. It is shown that a PIN Dosimeter diode which has been calibrated in an epithermal neutron beam in terms of $\Phi_{eq,1MeV,Si}$ can be used to measure $\Phi_{eq,1MeV,Si}$ in a fast neutron field. This finding supports the use of a PIN Dosimeter Diode for measuring $\Phi_{eq,1MeV,Si}$ in neutrons fields with any arbitrary energy spectra.

The response of the PIN Dosimeter Diode in a high energy electron field in terms of $\Phi_{eq,1MeV,Si}$ is studied. Based on experimental findings it is reasoned that a PIN Dosimeter Diode can provide a universal means of measuring dose associated with Non Ionising Energy Loss (NIEL) in silicon when exposed to any mixed radiation field in terms of $\Phi_{eq,1MeV,Si}$.

Sensors for measuring dose due to Ionising Energy Loss (IEL) in SiO_2 when exposed to mixed radiation fields were also investigated. It is shown that an IEL sensor based on a photodetector is not suitable in a radiation environment containing NIEL type radiations. An alternative sensor in the form of a MOSFET is found to be suitably radiation hard against dose associated with NIEL and able to measure IEL over a wide range of response.

Based on the MOSFET and PIN Dosimeter Diode results a Radiation Damage Monitoring System is designed for the measurement of damage to electronic devices in mixed radiation fields. The system was implemented in the *Belle* experiment at the KEK *B*-Factory in Japan, and within the lepton collider at SLAC in the USA.

ACKNOWLEDGEMENTS

I would like to begin by thanking my supervisors Prof. Anatoly Rosenfeld of the Centre of Medical Radiation Physics at the University of Wollongong and Dr Dimitri Alexiev from the Radiation Technology and Standards Group at ANSTO. Both gentleman gave generously with both scientific support and encouragement throughout the full term of my candidature.

Professor Rosenfeld has established at the University of Wollongong the Centre for Medical Radiation Physics of which he is the Director. Professor Rosenfeld's international recognition and extensive body of knowledge in the development of semiconductor detectors and dosimeters for clinical applications in radiation protection, radiation oncology and nuclear medicine as well as high energy physics applications, has contributed significantly to the successful completion of this thesis.

I would also like to thank the following people. Prof. John Boldeman for providing the opportunity to gain a licence to operate the ANSTO 3 MV Van de Graaff accelerator and for many useful discussions in nuclear physics. Dr David Cohen, Alec Croal, Dr Nick Dytlewski, John Fallon and other team members of ANSTO's Ion Beam Applications and Accelerator Operations Groups for scientific and technical support in utilization of the 3 MV Van de Graaff accelerator. Martin Carolan for performing the PIN Dosimeter Diode calibrations at Petten, in addition to many useful scientific discussions. To past and present members of the Centre of Medical Radiation Physics. Peter Inhat for construction of the readout circuitry for the RDMS. Dr Michael Lerch for scientific discussions. Dr Jamisen of the Microanalytical Research Centre of Melbourne University for the IBICC measurements. Alan Williams, Megan Williams, Li Mo, Dr Ian Donelly and Dr Kevin Varvell of the former ANSTO Physics High Energy Physics Group for many invaluable discussions and support. Alan Willliams provided extensive assistance in a wide variety of technical matters. Dr Scott Butcher of Macquarie University for scientific discussions on semiconductor device characterisation and behaviour. SPA Detector Pty. Ltd. of the Ukrain for the generous supply of detector test structures. Dr Francois Lemeilleur for the supply of novel detector materials on behalf of the ROSE collaboration. Dr

Bhaskar Mukherjee for many scientific discussions. Dr Henk van de Gaast for scientific discussions on radioactivity measurement. Dr Robin Walsh and Dr Refaat El Hajje for many useful discussions on nuclear physics. Geoff Watt, Dino Ius, Mark Hurry, Graham Carter, Bob Phillips and Keith Butterfield for technical advice on various matters 'electronic'.

The financial support of the Department of Physics at the University of Wollongong and the Australian Institute of Nuclear Science and Engineering (AINSE) for research grants to use the facilities at ANSTO, is gratefully acknowledged.

But most importantly to my family and friends I owe my greatest thanks for their support and patience. In particular I thank my partner Lisa.

TABLE OF CONTENTS

LIST OF TABLES / LIST OF FIGURES

Tables

Figures

Introduction

The search for new particles such as heavy leptons and the Higgs boson, predicted in extensions to the Standard Model, as well as studies of the top quark and searches for supersymmentry, are part of the broad experimental program to be carried out in the next generation of colliders. The success of these experiments will in part depend on the performance of the inner detectors used for vertex reconstruction. In the current generation of colliders, segmented silicon detectors of pixel and microstrip designs are used for this task. Multiple layers of such detectors are placed surrounding the collider beam pipe. The path of charged particles which are produced in a collision event are tracked by the individual detector layers as they emerge from the beam pipe. The decay vertex is then determined by extrapolating the paths back to the point of origin. Such detectors can provide the necessary spatial resolution for this task. They also exhibit fast response times, which coupled with modern signal processing electronics, allows the detectors to handle the high count rates and high event multiplicity associated with these colliders. In many cases the performance criteria for such detectors in the next generation of colliders will exceed the capabilities of present technology. One particular area of concern is the radiation hardess of the detector systems.

In the ATLAS experiment, to be built to operate at the Large Hadron Collider (LHC), the intensity of the radiation field is expected to be three orders of magnitude greater than that of existing proton-proton colliders [1,2]. The radiation field will be most intense at the inner most regions of the experiment closest to the collider beam pipe. Placement of the inner most detector layers relative to the particle beam pipe will be a crucial balance of performance and survivability. As the distance between the inner most detector layers and the beam pipe is reduced, the accuracy in which the decay vertex can be measured is improved. The higher

radiation levels at these points will however lead to a more rapid accumulation of radiation damage. The consequence of this could be premature failure of the detector system.

The main mechanisms of radiation damage will be via the deposition of ionizing and non-ionizing energy. The dose associated with ionizing energy loss (IEL) is responsible for the build up of charge within the CMOS devices of the detector front end electronics. The dose associated with non-ionizing energy loss (NIEL) is responsible for atom displacements within the silicon bulk of the detectors.

The damage to the silicon bulk has been foreseen as the limiting factor in detector operation at ATLAS. The atomic displacements cause disruption to the regular crystal periodicity which induces localised energy states within the silicon bandgap. Such states, which are commonly referred to as deep levels, will alter the electrical properties of the detector in a number of ways. They lead to an increase in the rate of carrier generation causing an increase in the detector reverse current. They increase the rate of carrier recombination, and act as sites for temporary carrier trapping, which both lead to a reduction in the charge collection efficiency. All of these effects reduce the detector signal to noise ratio.

The deep levels are also capable of electrically compensating the shallow level impurity states. If in sufficient concentration, this will change the material resistivity. Such changes are to the detriment of detector performance. It is the resistivity which controls the operating voltage of the detector. The operating voltage must be equal to or greater than the voltage required to fully deplete the detector substrate. This ensures that the detector can collect all of the signal produced following passage of a charged particle. At a lessor voltage incomplete charge collection would occur and the signal to noise ratio may be too low to detect the incident particle. The dependence of the full depletion voltage, V_{FD}, on the bulk resistivity is given by:

$$V_{FD} = \frac{a}{r}$$

where: a = constant dependent in part on the substrate thickness,

r = substrate resistivity.

Experimentally it has been shown that under 1 MeV neutron irradiation the resistivity of high purity *n*-type silicon will at first increase with the neutron fluence. A maximum is reached at a neutron fluence of about 10^{12} cm^{-2} [see for example Ref. 3]. At this point the material conductivity changes from *n*-type to *p*-type. With further irradiation the resistivity decreases until saturation at a neutron fluence of around 10^{15} cm^{-2}. This has been explained as being the result of the creation of deep level acceptor states and the removal of shallow level donor states [3].

The inversion in conduction type from *n*- to *p*-type does not prevent the detectors from functioning. This is because such detectors have a p^+nn^+ type structure which after type inversion becomes p^+pn^+. At the point of inversion the *p*-*n* junction reverts to the rear side of the detector. Full depletion can still be achieved, albeit from the opposite side of the detector. The reduction in resistivity with further irradiation does however cause an increase in V_{FD} to levels which become unsustainable. The application of higher voltages causes excessively high reverse currents and in some cases breakdown of the detector junction. With present detector technology the maximum fluence of 1 MeV neutrons to which the detector can be exposed before possible failure is about 10^{14} cm^{-2} to 10^{15} cm^{-2}. In ATLAS this fluence will be reached in the vicinity of the microstrip detectors during the ten years of operation.

The behaviour of the silicon resistivity under neutron irradiation is further complicated by the effects of room temperature annealing. At the completion of irradiation the resistivity of type inverted silicon will at first increase with short term annealing of the damage. This is beneficial and results in a reduction in the full depletion voltage. Following this short term anneal is a long term reverse anneal of the damage. During this phase the resistivity decreases to

a value that is less than that found prior to the initial short term annealing stage. This further degrades the situation.

Similar effects have been observed in silicon detectors irradiated by other particles which deposit NIEL such as protons [4] and pions [5].

To address this issue the Experimental High Energy Physics community has commissioned extensive radiation hardness testing programs. Two different approaches are being pursued. In the first approach the radiation hardness of existing microstrip detector technologies is being investigated. The purpose here is to accurately determine the operating characteristics of the detectors in an ATLAS type radiation field so that reliable projections of the detector performance throughout the duration of the ATLAS experiment can be made. Detectors can then be properly situated within the ATLAS environment at points which will satisfy the necessary balance in performance and survivability. The success of this approach is in part dependent on the accuracy in which the radiation field can be predicted in advance of collider commissioning. It is also somewhat dependent on there not being any unexpected increases in the radiation field due to beam steering accidents.

In the second approach the development of radiation hardened detector technologies is being investigated. This would allow enhanced longevity of operation of such detectors in ATLAS and a reduced vulnerability to unexpected increases in the radiation field.

This thesis is concerned with both approaches to radiation damage studies of silicon detectors. An overview of the contribution made is given in the following section.

Thesis Overview

The development of radiation hard silicon requires a better understanding of the defects responsible for the detrimental changes to resistivity as well as the mechanism of defect accumulation under irradiation and during the subsequent reordering effects of room temperature annealing. A particular problem in this field is the limited experimental means of characterising deep level defects in highly irradiated detector grade silicon. The powerful Deep Level Transient Spectroscopy (DLTS) technique is not capable of measuring defects in silicon irradiated by an equivalent 1 MeV neutron fluence in excess of 10^{11} cm^{-2}. This fluence is an order of magnitude less than the equivalent 1 MeV neutron fluence expected within the inner regions of the ATLAS detector in a single month of operation. Here a new approach for the observation of deep level defects in highly irradiated silicon is investigated. The technique is called Optical Deep Level Transient Conductance Spectrometry (ODLTCS). The technique is used to observe deep level defects in silicon detector test structures which have been exposed to a fast neutron fluence of 10^{13} cm^{-2}.

A possible means by which silicon detectors might be radiation hardened against NIEL is through material engineering of the silicon substrate impurity content. The presence or absence of particular impurities is known to significantly affect the formation of deep level defects in radiation damaged silicon. For example, in silicon grown by the Czochalski (CZ) technique, the generation rate of mid band states under neutron irradiation was observed to be less than in neutron irradiated silicon grown by the Float Zone (FZ) technique [6,7]. The main difference between these two types of silicon is the greater oxygen content in the CZ silicon. It was reasoned that the presence of oxygen, which was known to form the stable V-O defect, was acting as a sink for vacancies [8]. Associated with the V-O defect is an electrical state at E_c - 0.18 eV. This state is relatively benign in terms of the effect on the electrical properties of the

material. As consequence of the increased production of benign V-O defects is the suppression in the production of other defects which are associated with mid band states and therefore more detrimental to the electrical properties of the material. One such example is the divacancy defect.

The behaviour of other impurities in silicon is also of interest. Nitrogen is known to modify the behaviour of defects in silicon at the microscopic level. Solute trapping of nitrogen during silicon crystal growth has been used to increase the physical strength of low oxygen content wafers. Nitrogen has also been reported to be more effective than oxygen for pinning dislocations and suppressing slip and warp during silicon wafer processing [9,10]. Swirls and other lattice defects were found to be reduced in nitrogenised silicon [11]. The effect of nitrogen on the formation of radiation induced crystallographic dislocations both during the irradiation period and during the subsequent reordering process is not known.

These findings, relating to both oxygen and nitrogen, were obtained for silicon with a high impurity content and a low resistivity. Identical behaviour in high resistivity silicon is presently under urgent study by the ROSE collaboration in CERN. Both oxygenated and nitrogenised high purity silicon has been produced by Polovodice in Prague and processed into detector test structures. These have been supplied by the ROSE collaboration to various laboratories including the Centre of Medical Radiation Physics at the University of Wollongong for study.

Here the detectors were studied using the ODLTCS technique. The aim was to observe the evolution of neutron induced defects with room temperature annealing. The results were used to determine a mechanism by which detector grade silicon could be radiation hardened against damage caused by NIEL.

Another major impediment in radiation hardness studies is the difficulty in comparing neutron damage results obtained at facilities with different neutron spectra. This is on account of the energy dependence of displacement damage by neutrons in silicon. One means of comparing irradiating conditions is to use the equivalent 1 MeV neutron fluence in silicon methodology. Here a wide neutron energy fluence is quoted in terms of the fluence of monoenergetic 1 MeV

neutrons which would cause an equivalent deposition of non ionizing energy as would the actual wide energy neutron spectrum in silicon. This single parameter is defined as:

$$\Phi_{eq,1MeV,Si} = \frac{\int_0^{\infty} \Phi(E) F_{D,Si}(E) dE}{F_{D,1MeV,Si}} \qquad (1)$$

where: $\Phi(E)$ = incident neutron energy spectrum,

$F_{D,Si}(E)$ = neutron displacement damage function for silicon as a function of energy (damage KERMA), and

$F_{D,1MeV,Si}$ = displacement damage reference value for silicon at 1 MeV (damage KERMA at 1 MeV).

A determination of $\Phi_{eq,1MeV,Si}$ requires knowledge of Φ(E). In all but the simplest neutron fields measurement of Φ(E) is complicated and time consuming. A dosimeter which is capable of responding directly in terms $\Phi_{eq,1MeV,Si}$ in any neutron field would provide a useful alternative. Such a reference dosimeter would also be useful for characterising the neutron fields of other facilities involved in electronic device radiation hardness testing programs. Such a dosimeter in the form of a PIN Dosimeter Diode manufactured from high purity silicon is studied. In particular it is shown that the dosimeter can accurately measure $\Phi_{eq,1MeV,Si}$ in a neutron field with an energy spectrum much different to the energy spectrum of the neutron field used for calibration of the device.

While most concern regarding radiation damage in silicon detectors relates to future hadron collider experiments, damage to detector systems in lepton collider experiments can also be anticipated. The radiation fields in lepton collider experiments are characterised by a mixed field of energetic electrons and soft *x*-ray synchrotron radiation. In terms of NIEL in silicon it is

well known that 1 MeV electrons are considerably less damaging than say 1 MeV neutrons. The damaging efficacy of GeV energy electrons is however not so well known. It was recently shown that in terms of the change to the reverse current of a silicon microstrip detector that 500 MeV electrons were similarly damaging to 1 MeV neutrons and high energy protons [12]. This result was obtained during a beam steering accident at the OPAL experiment of the LEP in CERN. Electrons with such energies will impinge on the silicon detectors of the *Belle* experiment at the KEK *B*-factory in Japan. In this particular experiment an operational limitation to the silicon detectors on account of NIEL from the electrons is not anticipated for the fluence predicted. This conclusion was reached for normal operating conditions and does not account for the possibility of beam steering accidents.

Due to uncertainty in the radiation field at *Belle* a radiation monitoring system was proposed by the *Belle* collaboration to measure the radiation levels within the silicon vertex detector on-line. The proposed system was based on a photodetector sensor with the capacity to measure the integrated ionising dose and ionising dose rate. The system did not have the capacity to measure non-ionising energy loss in silicon. And further, it is shown here that the photodetector sensor is itself not radiation hardened against NIEL damage. Exposure of the sensor to 20 MeV electrons results in accumulated NIEL damage that will cause the sensor to continuously underestimate the IEL dose.

An alternative radiation damage monitoring system is proposed which is capable of measuring both IEL in silicon dioxide and NIEL in silicon. Two independent sensors are used. The IEL sensor is based on a special type of MOSFET known as a RADFET. This device more accurately responds to IEL damage in silicon dioxide than a photodetector based on silicon. This is important since the IEL causes radiation damage to the CMOS electronics of the detector front end electronics and not the silicon bulk of the detectors. The device is also radiation hard against damage associated with NIEL (unlike the photodetector sensor). The second sensor for measuring the NIEL in silicon is a PIN Dosimeter Diode. It is shown that this device can respond to NIEL damage in silicon caused by high energy electrons in terms of the equivalent 1

MeV neutron fluence. This is important as it will allow a direct means of comparing radiation hardness results caused by high energy electrons with the extensive database of radiation hardness results on silicon devices known in terms of the equivalent 1 MeV neutron fluence in silicon. The response of the PIN Dosimeter Diode is not sensitive to the accumulation of IEL. It is further postulated that the system based on MOSFET and PIN Dosimeter Diode sensors is capable of monitoring radiation damage to silicon devices in any mixed radiation field.

Both sensors are incorporated into a prototype radiation damage monitoring system for silicon devices which is universal in different mixed radiation fields. A developed system has been installed within the *Belle* experiment at the KEK *B*-Factory as well as within the lepton collider at SLAC in the United States.

Chapter 1

Silicon based Microstrip Detectors: Applications in Experimental High Energy Physics

This chapter provides an overview of the use and operation of high purity silicon based microstrip detectors in experimental High Energy Physics (HEP).

1.1 Experimental High Energy Physics

The purpose of experimental HEP is to gain further understanding of the fundamental nature of matter and energy. From the 1930's physicists used the naturally occurring cosmic ray background as a tool for their investigations. Today the tools are large particle accelerators and complex detector systems developed by teams of 100's of scientists and technicians. The accelerators take particles, such as electrons or protons, and accelerate them to speeds near that of the speed of light. The energetic particles are then made to collide with either fixed targets or other accelerated beams of particles travelling in the opposite direction. Measurement of the radiation emerging from a collision is then used to study the structure and nature of matter.

Two contemporary HEP experiments are of pertinent interest to the work undertaken in this thesis. The first is ATLAS, which is to be built at the LHC in CERN. And the second is *Belle,* which has already been built at the KEK *B*-Factory in Japan. A general summary of these experiments, and the radiation fields they are exposed to is now described.

1.1.1 The Large Hadron Collider (LHC)

The LHC is presently under construction within the existing 27 km circumference tunnel of the Large Electron Positron (LEP) collider at CERN. When commissioned, the LHC will be capable of bringing counter rotating beams of protons with energies of 7.7 TeV into head-on

collisions. The final centre-of-mass energy of about 15 TeV will be the largest energy probed by a particle collider. The maximum design luminosity will be ~ 10^{34} $cm^{-2} \cdot s^{-1}$. This will be achieved using proton beams made up of separate bunches of ~ 2800 protons which will cross within the collider experiments every 25 ns.

The phenomena produced by the LHC will be observed in two general purpose experiments called ATLAS (a toroidal large acceptance spectrometer) and CMS (compact muon solenoid), as well as a detector for high energy collisions of heavy ions called ALICE and a detector for *B* meson physics called LHC-*B*. Australian laboratories will participate in the ATLAS experiment as part of the Australian High Energy Physics collaboration.

1.1.2 ATLAS

ATLAS is designed to exploit the full discovery potential of the LHC. The major experimental goals, as outlined in [1], will be to investigate the origin of mass at the electroweak scale, to search for a variety of particles including the Higgs particle, W' and Z' like objects and supersymmetric particles, as well to investigate compositeness of the fundamental fermions, CP violation in *B*-decays and the properties of the top quark.

The general layout of the ATLAS detector is shown in Figure 1.1. The detector is configured with inner and outer superconducting magnets. The solenoid of the inner magnet, which encircles an inner detector cavity, will have a diameter of 2.4 m and a length of 5.5 m. It will produce a magnetic field with a strength of 2 T. The outer magnet is to be a superconducting air-core toroid magnet system consisting of a 26 m long barrel with eight coils located at various radial distances from the centre axis in addition to two end-cap toroids.

An inner detector is to be contained within a cylindrical cavity of length 6.80 m and radius 1.15 m. It will consist of a combination of silicon pixel and microstrip detectors as well as continuous straw-tube tracking detectors. The purpose of the inner detector will be to perform pattern recognition, momentum vertex measurements and electron identification. External to the

inner detector are to be highly granular Liquid Argon (LAr) electromagnetic sampling calorimeters of various designs. The calorimetry is to be surrounded by a muon spectrometer.

The overall size of the ATLAS detector, based on initial design plans, is 22 m in diameter, and 42 m in length. The total weight of the structure will be approximately 7000 tons.

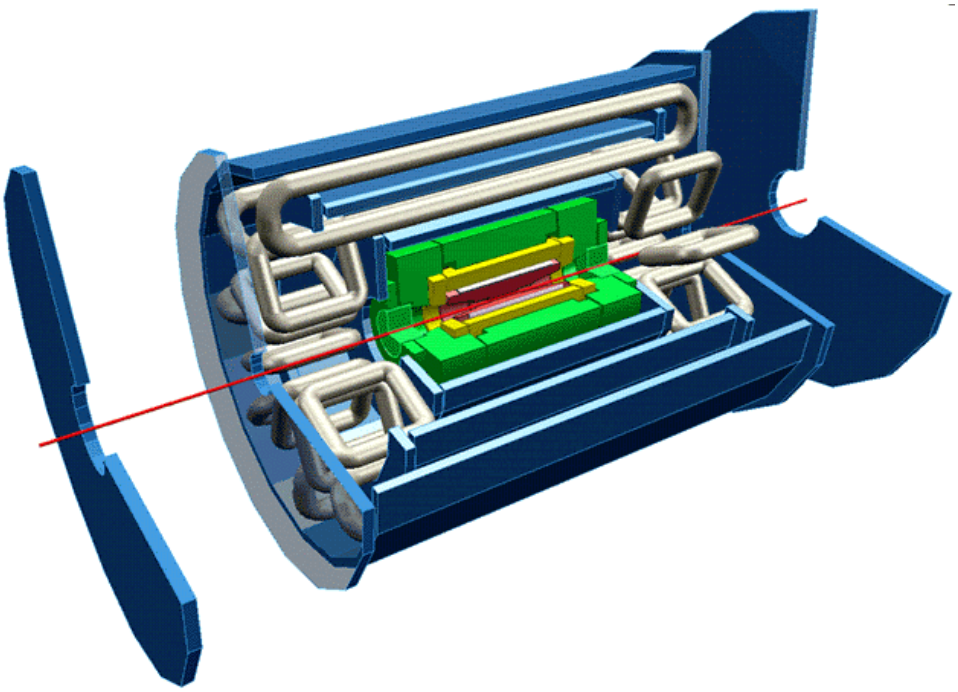

Figure 1.1: Layout of the ATLAS detector. The SCT is located within the inner most regions of the detector. More details can be obtained from the ATLAS web site http://pdg.lbl.gov/atlas/etours_exper/etours_exper08.html

1.1.2.1 The ATLAS Semiconductor Tracking Detector (SCT)

Part of the inner detector is the Semiconductor Tracking Detector (SCT). It will consist of approximately 2.3 m^2 of silicon pixel detectors and 63 m^2 of silicon microstrip detectors. The

pixel detectors will be located closest to the beam pipe. They will be arranged in two barrel layers which will wrap around the beam pipe. Additional pixel detectors in the form of eight disks (or wheels) will be positioned at both ends of the barrel layers orientated normal to the beam pipe. The pixel detectors will provide two measurement points for each charged particle track within a pseudo rapidity[1] of $|h| \leq 2.5$.

The microstrip detectors will be located outside the pixel layers in an arrangement consisting of four barrel layers and a series of disk layers. The position of these layers relative to the beam pipe will very much depend upon the results of radiation damage studies. It is anticipated that a total of 11 424 microstrip detectors will be used. All detectors will be single sided. The barrel layers will be built using identical modules. Each will consist of two pairs of detectors mounted back to back. One pair will be mounted with readout strips aligned along the *z*-axis (the *z*-axis is parallel with the particle beam line), and the other pair at an angle of 40 mrad to the *z*-axis. Each individual detector substrate will contain 768 strips of length 62 mm laid with a pitch of 80 μm. The silicon substrate will be 63.6×64 mm^2 in area and will have a thickness of 300 μm. The detectors will be capable of measuring the position incidence of a charged particle with a spatial resolution of ≤ 20 μm.

More extensive details on the SCT detectors the reader is referred to the ATLAS SCT technical design report (TDR) [1].

1.1.2.2 The Radiation Environment within the ATLAS SCT

The radiation environment within the ATLAS SCT is made up of contributions from a variety of different sources. The main source will be radiation produced as a direct result of a collision between protons in the counter rotating beams. Other radiation will be produced as a result of beam-gas interactions as well as interactions of lost beam particles with the accelerator

[1] Pseudo rapidity, h, is given by $h = \ln\left[\tan\frac{q_{cm}}{2}\right]$, where q_{cm} is the polar angle measured from the beam line *z*-axis.

beam pipe walls. Almost all of this radiation will pass through the SCT. Some of this radiation, upon being absorbed within the distant calorimeters, will result in the production of tertiary radiation in the form of electrons, photons and neutrons. A component of this radiation will be redirected back through the SCT.

Detailed calculations of the anticipated particle fluence and dose rates within the SCT have been published within the ATLAS Technical proposal [1]. The important results are summarised in point form below:

- A high fluence of albedo neutrons will be present throughout the inner detector. The fluence is expected to be quite uniform (to a first order approximation) at all points within the SCT and will make a significant contribution to the total NIE damaging fluence. At the outer most SCT layers, due to the fall off in the fluence of other particles, the neutron fluence will dominate.

- A charged hadron fluence consisting of protons, antiprotons, pions and kaons is the dominate damaging radiation within the inner most SCT detector layers. The fluence varies approximately as r^{-2}, where r is the distance measured from beam line in a direction orthogonal to the beam line axis.

- The photon dose is not expected to be significant in terms of damage to the SCT detectors. The dose rate will however strongly affect the detector occupancy. The photon dose is also of some concern to the operating performance of the CMOS electronics located adjacent to microstrip and pixel detectors.

The total particle fluence within the barrel region of the SCT, in terms of an equivalent 1 MeV neutron fluence, has been estimated to be 2.7×10^{13} $cm^{-2}\cdot yr^{-1}$ [1]. A similar fluence is predicted within the forward SCT modules.

A more detailed study of the SCT radiation field has been performed by Gorfine [2]. A breakdown in the contribution of individual radiation types to the total damage fluence was determined. Using Gorfine's data a plot was produced showing the contribution of different radiations to the total yearly ATLAS particle background as a function of *r* (see Figure 1.2). The data confirms the results listed above and emphasises the important role that charged particles will play in the damage fluence at the innermost radii. The data shows that the most significant component is the pion fluence. At the larger radii the neutron component still dominates.

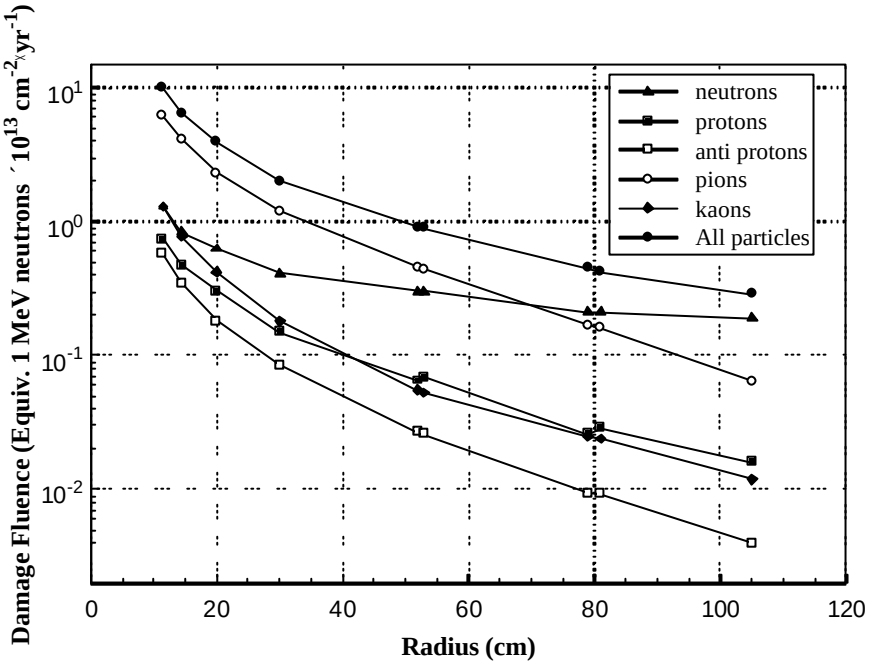

Figure 1.2: Fluence for various particles in a year of operation of ATLAS plotted as a function of radius. All data taken from Ref. [2].

1.1.3 The *Belle* Experiment at the KEK *B*-Factory

The KEK *B*-Factory is a high luminosity asymmetric e^+e^- collider built at KEK, Japan. For the *Belle* series of experiments, which are directed towards the study of CP violation in bottom

quark decays, the collider will accelerate positrons to an energy of 3.5 GeV with a beam current of 2.6 A, and electrons to an energy of 8 GeV with a beam current of 1.1 A [13]. The energies have been tuned to produce the Y(4S) resonance which dominantly decays to a pair of B^o and B^o bar particles. B^o mesons, composed of a heavy b-quark and a light quark, are unstable particles which decay shortly after production.

A primary goal of the *Belle* experiment is to observe time-dependent CP asymmetries in the decays of B mesons. Doing so requires the measurement of the difference in *z*-vertex positions for B meson pairs with a precision of approximately 100 μm.

The high electron and positron beam currents of the KEK *B*-Factory are necessitated by the need to acquire a data sample of order 10^8 meson decays for successful verification of the *Belle* experimental goals [13].

1.1.3.1 The *Belle* Silicon Vertex Detector (SVD)

Measurement at *Belle* of a B^o meson decay vertex will be done by tracking the charged particles produced in the decay using the Silicon Vertex Detector (SVD). A technical description of the SVD is available from the *Belle* collaboration [341]. It consists of three silicon layers in a barrel-only design and covers a solid angle $23° < \theta < 139°$ where θ is the angle from the beam line axis. The barrel layers are located at radii 30, 45.5 and 60.5 mm. Each layer is constructed from independent ladders. Each ladder comprises double sided silicon strip detectors (DSSD) reinforced by boron-nitride support ribs.

Each DSSD is manufactured from of 300 μm thick substrate of high resistivity *n*-type silicon. All substrates are rectangular in shape with an overall size of 57.5×33.5 mm^2.

In all DSSDs the strips are formed on both sides. *p*-strips are formed on the junction side and run parallel to the long side of the detector. This will permit measurement of the *r*-f coordinates of the incident charged particles. The *n*-strips are orthogonal to the *p*-strips permitting measurement of the *z* coordinate. All of the strips are individually biased via

integrated polysilicon bias resistors. The strips and the Al contacts are separated on both sides by thin insulating (SiO_2 and Si_3N_4) layers that form integrated AC-coupling capacitors for signal readout. A double metal layer (DML) structure is used for readout of the *n*-strips.

The ability of the SVD to resolve the vertex of a *B* meson decay improves with the inverse of the distance between the decay vertex and the first super layer. It is important that this distance is minimised to achieve the highest level of performance. At the closest point, the first layer will be ~ 2 mm away from the beam pipe outer wall [14].

1.1.3.2 The Radiation Field within the *Belle* SVD

The high particle energy and high beam currents of the KEK *B*-Factory and the close proximity of the *Belle* SVD to the beam pipe will expose the detector components (both DSSDs and CMOS electronics) to radiation levels much in excess of those produced in previous lepton e^+e^- collider experiments.

There are three main sources of radiation within the *Belle* SVD:

- Quadruple magnets near the longitudinal ends of the detector structure will generate synchrotron radiation in the energy range of 5 – 15 keV.
- Residual gas molecules within the beam pipe will scatter many of the leptons which upon striking the beam pipe wall will produce secondary showers of particles and photons.
- Radiation produced as a direct result of a e^+e^- collision.

An enhanced intensity of radiation will exist at small angles from the beam axis. This will render the closely positioned SVD detector modules vulnerable to damage.

To understand how the silicon microstrip detectors will perform in this radiation field, as well as within the ATLAS experiment, it is necessary to first consider some of the basic properties of silicon as well as the basic function of a silicon based microstrip detector.

1.2 Silicon Based Detectors

Silicon based detectors have and continue to be used widely in both science and industry for the detection of ionising radiation. Details on their operation and areas of application can be found in various texts (see for example [15-17]).

The development of position sensitive detectors for experimental HEP began in around 1980. The impetus for this development was the discovery of the J/Ψ meson and the associated quantum number called 'charm'. Charmed particles are produced in high energy hadronic interactions. They are unstable and have a lifetime of approximately 10^{-13} to 10^{-12} seconds. The study of these short lived particles required detectors which were capable of detecting charged particles with spatial resolutions of order 10 μm. The capability to handle high particle densities and high event rates was also required of the detector systems.

It was found that by segmenting the face of a surface barrier detector into many separate detecting elements, and by reading the signal from each element separately, that the spatial resolution of an incident charged particle could be dramatically improved. The necessary segmentation of the detector substrate on a micron scale was achieved by applying the planar process which had been developed for the microelectronics industry [18,19]. The planar process is a set of techniques performed on the upper surface of semiconductor substrates for the formation of miniature sized device structures. These techniques include oxide passivation, photo engraving and ion implantation. The various techniques are described extensively in various texts see for example Ref. [20].

The necessary advances in detector signal processing, in order to handle the associated increase in channel numbers, was provided by the availability of highly integrated low noise analogue electronics. The integrated circuitry could be mounted directly adjacent to the finely segmented detector structures.

The fabrication of microstrip detectors has been done using other semiconductor materials such as GaAs. Despite the superior properties of some III-V and II-VI semiconductors in the area of carrier mobilities, silicon still remains the premier material for HEP applications. This is a consequence of the unique physical properties of silicon and its native oxide (SiO_2); and to a lessor extent the superiority of silicon technology over that of other semiconductor technologies.

Some of these factors are now discussed.

1.2.1 Properties of Silicon

Silicon is a group 4 element with atomic number 14. Some of the basic physical properties of silicon in the solid state are listed in Table 1.1. This data has been collated from Kittel [21] and the EMIS data review series [22]. Unless otherwise stated the values pertain to measurement conditions of 300 K and 1 atm.

Table 1.1: Physical properties of silicon in the solid state.

Atomic Number	14
Group	IV
Atomic Weight	28.0855 amu
Atomic Density	5×10^{22} cm^{-3}
Density	2.3290 $g{\cdot}cm^{-3}$
Electron Configuration	1s2. 2s2. 2p6. 3s2. 3p2
Crystal Structure	Diamond cubic lattice
Space Group	Fd-3m
Bonding	Directional covalent
Lattice Parameter (298 K)	5.4310626±0.0000008 Angstrom
Nearest Neighbour Distance	2.35 Angstrom
Bulk Modulus	9.784×10^{10} Pa
Thermal Conductivity	1.56 $W{\cdot}cm^{-1}{\cdot}K^{-1}$

Fourteen electrons surround the silicon nucleus. The 1*s*, 2*s* and 2*p* states are completely filled. The remaining four electrons partially fill the 3*s* and 3*p* states. Upon crystallisation these states intermix to form four sp^3 hybrid orbitals which are filled by the four unpaired electrons of an atom and an unpaired electron from each of four nearest neighbour atoms. In doing so four equally spaced directional covalent bonds are formed. The resulting structure, characterised by the tetrahedral bonding arrangement, is the diamond cubic lattice. The unit cell of this structure with a lattice constant a = 0.5431 nm is shown in Figure 1.3. There are eight atoms in the unit cell located at the points (0,0,0), (0,½,½), (½,0,½), (½,½,0), (¼,¼,¼), (¾,¼,¼), (¾,¾,¼) and (¾,¼,¾).

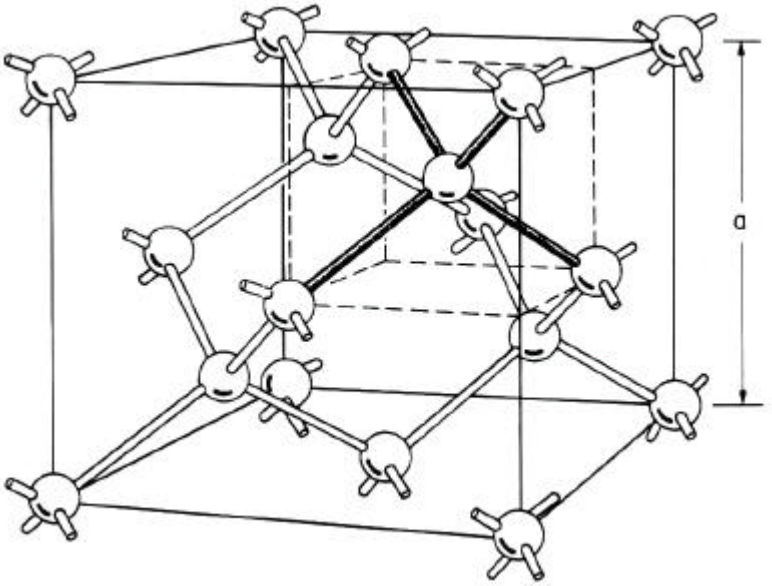

Figure 1.3: Unit cell of silicon with a lattice constant of a = 0.54310626 nm (diamond lattice). The tetrahedral bonding arrangement is highlighted for the atom located within the dotted cube. Figure reproduced from Sze [20].

Crystalline silicon is stable and physically robust. The various descriptors of mechanical properties such as the elastic constants, the bulk modulus, Young's modulus, the modulus of compression, the shear modulus and poisson's ratio all elucidate a material which is stiff, hard,

rigid and highly resistant to deformation. The values of these physical descriptors can be found in references [23] and [24]. The diamond cubic lattice is however quite open in comparison to other crystal configurations; the maximum proportion of the available volume which may be filled by hard spheres is only 0.34 [21]. Interstitial atoms can be accommodated in the interatomic voids located along the body diagonals (as shown in Figure 1.4). This fact explains the relatively high solubility and high diffusivity of many impurity atoms in silicon.

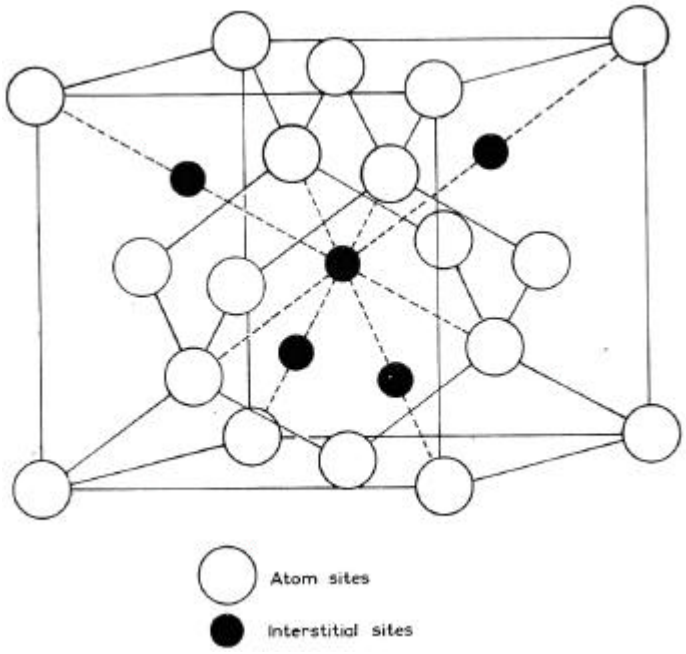

Figure 1.4: Unit cell of the diamond structure showing the interatomic voids located along the body diagonal. Figure reproduced from [25].

The important electrical properties of semiconductor silicon are listed in Table 1.2. Unless otherwise stated the data was taken from [20] and pertain to measurements conditions of 300 K and 1 atm.

The electrical properties are a consequence of the formation of sp^3 hybrid bonding and antibonding bands. The bonding band, otherwise known as the valence band, contains four quantum states per atom and is completely filled at 0 K. The antibonding band, otherwise

known as the conduction band, contains four quantum states per atom all of which are unoccupied. The two bands are separated by an energy gap within which no energy states exist.

Table 1.2: Electrical properties of semiconductor silicon.

Dielectric Constant	11.9
Bandgap Type	Indirect
Bandgap (300 K)	1.125 eV [2]
Bandgap (0 K)	1.170 eV [2]
Intrinsic Carrier Density (RT)	1.45×10^{10} cm^{-3}
Intrinsic Resistivity (RT)	~ 230 kΩ·cm
Mean energy for e-h production	3.62 eV
Electron Mobility (300 K)	1450 cm^2·V^{-1}·s^{-1}
Hole Mobility (300 K)	450 cm^2·V^{-1}·s^{-1}
Carrier Saturation Velocity (300 K)	10^7 cm·s^{-1}
Breakdown Field (abrupt junc., high ρ)	3×10^5 V·cm^{-1}

The band structure of silicon is complex. Schematic representations exist in various texts for example see Ref. [26]. In crystal momentum space the minimum of the conduction band is displaced from the valence band zone centre. Direct band to band transitions are unlikely and indirect band to band transitions are the norm. At 300 K and 1 atm the minimum width of the bandgap is 1.125 eV. The intrinsic carrier concentration at 300 K is 1.45×10^{10} cm^{-3}. This is well below that which typifies semiconducting behaviour. Silicon is thus an extrinsic semiconductor usually doped with group III and group V elements. The acceptor dopants are most commonly B, Al, or Ga, and the donor dopants, Sb, P or As. Concentrations can be varied from residual impurity concentrations of as low as ~ 10^{11} cm^{-3} up to maximum concentrations of order 10^{19} – 10^{20} cm^{-3}. At the maximum concentrations not all impurities will be ionised at room temperature. The corresponding resistivity can vary from ~ 10^{-3} Ω·cm to tens of kΩ·cm.

The mobility of electrons and holes at room temperature in high purity silicon is 1450 and 450 $cm^2 \cdot V^{-1} \cdot s^{-1}$ respectively [20]. The higher mobility of electrons is due to their smaller effective mass relative to that of the holes. The mobility of the electrons is however quite low in comparison to the mobility of electrons in other semiconductor materials (for example, in GaAs, μ_n = 8500 $cm^2 \cdot V^{-1} \cdot s^{-1}$).

The dominant scattering mechanisms in silicon are lattice scattering and ionised impurity scattering. The effect on mobility of both mechanisms is temperature dependent. For lattice scattering the mobility is approximately proportional to $T^{-3/2}$ and is thus the dominant mechanism at high temperatures. For ionised impurity scattering the effect on mobility is approximately proportional to $T^{3/2}$ and is thus the dominant mechanism at low temperatures. Ionised impurity scattering is also directly proportional to the impurity concentration. For impurity concentrations below about 10^{14} cm^{-3} the effect is negligible and the mobility of both carriers reaches the maximum value limited only by lattice scattering.

For low electric fields, less than approximately 10^3 $V \cdot cm^{-1}$, the drift velocity of electrons and holes in silicon increases linearly with both the electric field strength and the carrier mobility. For an electric field above 10^3 $V \cdot cm^{-1}$ the dependence is sub-linear as the mobility becomes electric field dependent due to the effects of intravalley acoustic deformation potential scattering and intravalley phonon scattering [27]. At room temperature, saturation of the carrier drift velocity occurs at an electric field strength of 7×10^3 $V \cdot cm^{-1}$ for electrons and 2×10^4 $V \cdot cm^{-1}$ for holes. The drift velocity for both electrons and holes at saturation is ~ 10^7 $cm \cdot s^{-1}$ [17]. These electric field strengths are well below the dielectric breakdown field of 3×10^5 $V \cdot cm^{-1}$.

The mean energy required to liberate an electron-hole (*e-h*) pair in silicon by either minimum ionising particles (mips) or photons of energy >> 3.6 eV at room temperature is 3.62 eV. The fano factor, a measure of the fluctuations in the number of carriers produced by ionising radiation, is ~ 0.11. The *e-h* pair liberation energy is independent of the energy of the

radiation and varies only slowly with temperature [28]. The average energy loss per unit length, $\frac{dE}{dx}$, for minimum ionising particles (mip), is 3.2 MeV·cm^{-1}.

1.2.1.1 High Purity 'Detector Grade' Silicon

For radiation detector applications *n*-type silicon with a high resistivity and a low defect concentration is required. *n*-type is preferred on account of the higher mobility of electrons compared to that of holes. The high resistivity is required to permit the full depletion of wide substrates at a relatively modest voltage. For energy resolving detectors a depletable thickness of ~ 1 mm is required. The corresponding resistivity is 20 kΩ·cm or higher. For energy sampling detectors, commonly referred to as $\frac{dE}{dx}$ detectors, a depletable thicknesses of order 300 µm is required. The corresponding resistivity is of the order of 2-5 kΩ·cm. A low defect concentration is necessitated in both applications to give a long minority carrier lifetime. This minimises the generation current which in a detector structure gives rise to noise.

The process used for the production of electronic grade silicon is not adequate for the production of detector grade silicon. Additional processing steps are required to reduce the impurity concentration and to more closely match the donor and acceptor concentration in order to obtain a high resistivity. Due to the effect of electrical compensation between shallow level donor and acceptor states, the effective impurity concentration (N_{eff}) which controls resistivity is given by $|N_D - N_A|$, where N_D is the donor concentration and N_A is the acceptor concentration. For high resistivity material the acceptor dopant is B and the donor dopant is P. These impurities are present in residual amounts at the minimal concentrations required. The ionisation energy of P and that of B in silicon is 0.045 eV and 0.044 eV respectively [29]. Both electrical states are completely ionised at room temperature. To achieve the necessary reductions in impurity content only the Float zone (FZ) method can be used. The Czochalski (CZ) method always results in silicon with a high impurity content. This is due to the contact of

the silicon with the quartz crucible and the subsequent diffusion of crucible born contaminants into the silicon melt. The FZ method is crucible free. In this method a region of molten material between the interface of the polycrystalline rod and the interface of the solidified single crystal rod is moved upwards. The use of a RF coil to provide heat eliminates the contact of the liquefied silicon with contaminant containing surfaces. Impurities are gettered from the starting silicon by performing repeated FZ refining steps. The lower solubility in the solid phase than in the liquid phase of most impurities in silicon permits their removal from the solid. Notable exceptions are oxygen and boron. Following this process the electrically active impurities which remain in the highest concentrations are boron and phosphorus. Typical concentrations are of order 10^{12} cm^{-3}. To obtain a high resistivity *n*-type material an *n*-type silicon rod with a low boron concentration is selected. A carefully calculated number of FZ refinement steps are then performed in order to reduce the phosphorus concentration to a level just above that of the boron concentration.

A major problem encountered with the FZ growth technique for high resistivity silicon production is a lack of spatial uniformity of the resistivity throughout the single crystal ingot. Thermal asymmetry during the growth stage causes radial variations in the temperature profile of the ingot. This has a considerable effect on the phosphorus concentration due to the relatively low segregation coefficient of phosphorus in comparison to the higher segregation coefficient of boron (the segregation coefficient of P and B is 0.35 and 0.8 respectively). The temperature striations associated with the thermal asymmetry produce similar striations in the phosphorus concentration. In electronic grade silicon this effect is alleviated by the use of neutron transmutation doping (NTD). This process involves the introduction of a homogeneous phosphorus concentration via the transmutation of the uniformly located silicon isotope ^{30}Si to ^{31}P following neutron capture and subsequent beta decay, ($^{30}Si(n,\gamma)^{31}Si \rightarrow {}^{31}P + {}^{-}b$). Production of high purity detector grade silicon with a high degree of uniform spatial resistivity using NTD has been shown to be feasible [30, 31], albeit for small 1 cm^3 volumes.

Further information regarding the production and characteristics of detector grade silicon is available [32,33].

1.2.1.2 Silicon Dioxide, SiO_2

In order to fabricate functional electronic devices from semiconductor material using the planar process (including radiation detectors), it is necessary to have a compatible material for electrical insulation. In the case of silicon the native oxide, SiO_2, is such a material.

With a band gap of 9 eV, SiO_2 provides high quality electrical insulation. In addition, SiO_2 provides good passivation of the silicon surface by effectively reducing the concentration of electronic states which arise at the surface of clean crystalline silicon by up to five orders of magnitude [34]. SiO_2 can be used for selective masking during either diffusion or ion implantation associated with device processing. It provides surface protection from contamination, and can be used for impurity gettering.

SiO_2 can support high electric fields. Experimental observations have shown that electric field breakdown does not occur until electric strengths exceed 10 to 30 $MV \cdot cm^{-1}$ [35].

Amorphous layers of SiO_2 are grown on silicon substrates at high temperatures in a nitrogen or argon ambient containing a small concentration of O_2 and H_2O vapour. The procedure is extremely controllable and results in stable and highly reproducible $Si\text{-}SiO_2$ interface characteristics.

The $Si\text{-}SiO_2$ system forms the basis for many devices classes including metal-insulator-semiconductor (MIS) structures such as MIS field-effect-transistors (MISFET) and charged-coupled-devices (CCD). It is the basis for metal-oxide-semiconductor (MOS) type structures including complementary-MOS (CMOS) used extensively in the production of low power consuming integrated circuitry. It is also the basis of semiconductor-on-insulator (SoI) technology. SoI type devices are becoming increasingly important as this technology permits

high device density and a built in immunity to the latchup effect found in CMOS devices as well as providing a reduction in parasitic capacitance which affects device speeds.

SiO_2 is essential in segmented silicon detector technology. The electrical insulation properties are used for detector element isolation and allow guard rails to be formed. Guard rails permit a dramatic reduction in detector leakage currents. The surface protectant properties permit long term stability of the operating characteristics by providing a defence against impurity contamination. The use of the oxide as a mask against impurity diffusion and ion implantation permits accurate micron sized features to be fabricated on the detector surface.

The presence of silicon dioxide in silicon detectors and the associated front end electronics does introduce some sensitivity to the effects of radiation. Ionising energy loss within the oxide causes a build up of charge within these insulating layers. This effect is discussed in Chapter 2.

Other silicon insulator technologies that are important for silicon devices include silicon nitride (Si_3N_4) and silicon oxynitride ($SiN_{(x)}O_{(y)}$). Silicon oxynitride shows a better ability to reduce impurity diffusion and a better electric field breakdown behaviour than SiO_2. Further, it has a higher dielectric constant, and is associated with a lower interface trap density than SiO_2. Little is known regarding the radiation hardness of this material or Si_3N_4.

1.2.2 Microstrip Detectors

The structure of a typical silicon microstrip detector is shown in Figure 1.5. The detector bulk is usually manufactured from an *n*-type silicon substrate with a resistivity of 2-5 kΩ·cm and a thickness of about 300 μm. Equally spaced p^+ strips are formed on the front surface of the substrate by implantation of boron to produce abrupt p^+-*n* junctions with the detector bulk. The typical width of a strip is 10 μm. The strip pitch may vary from 20 to 200 μm depending upon the desired application. The p^+-*n* junction strips are electrically isolated from one another by a region of SiO_2. On the rear side of the substrate a thin n^+ region is formed through either implantation or diffusion of either phosphorus or arsenic. The role of this region is threefold; 1)

Permits operation of the detector in the over depleted mode ensuring a maximum detector sensitive volume; 2) Guards against the detrimental effects of electric field punch through; 3) Improves the quality of the ohmic contact.

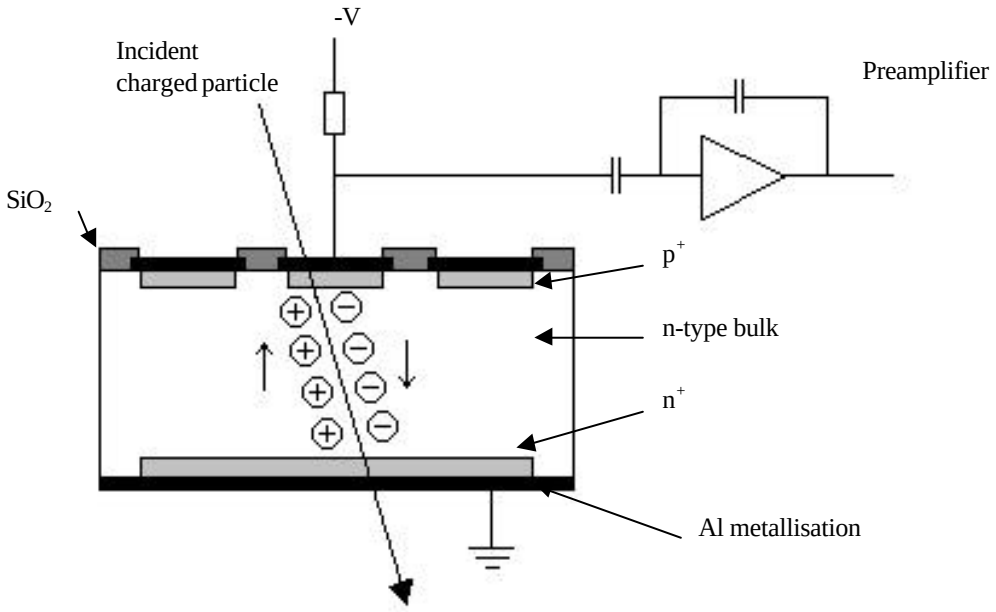

Figure 1.5: A simple schematic of a microstrip detector.

The p^+-n junctions are reverse biased with a sufficient voltage to fully deplete the detector bulk of free carriers. A minimum ionising particle (mip) which traverses the silicon bulk will produce an ionised track of e-h pairs. These charge carriers are free to move under the influence of the electric field. Electrons will move towards the n^+ contact and holes will move towards the p^+ strips. The moving charge induces a current to flow in the external circuit which constitutes a measurable signal.

Generally the signal will be induced on a number of strips located in the vicinity of the ionised track. The position of incidence is obtained by determining the centre of gravity of these signals. The resolution that can be achieved is mostly dependent upon the strip pitch. A smaller strip pitch (i.e. more strips per unit width), will produce a detector with a better spatial resolution. Spatial resolutions of order 2.8 μm have been achieved for a strip pitch of 20 μm

[36]. This is close to the theoretical limit imposed by the range of delta rays and the effect of charge cloud diffusion.

A large number of strips requires a large number of electronic readout channels. This is undesirable because of the considerable physical size of the electronics to be accommodated close to the detector as well as the need to remove the high heat load of the operating circuitry. The number of readout channels can be reduced by using capacitive charge division [37]. Here only a fraction of the strips are readout. The charge induced on intermediate strips is capacitively coupled to the nearby readout strips via the inter-strip capacitance. A correct electric field profile below the non-readout strips is achieved by maintaining the electrical potential of these strips at a value equal to the potential of the readout strips. Highly resistive strip interconnects are formed by sputtering sub millimetre wide regions of amorphous silicon between the detector strips. Only a moderate reduction in the spatial resolution results from this approach. For example, a detector with a strip pitch of 20 μm gave a spatial resolution for incident mips of 4.5 μm when every third strip was readout [36]. Readout of every 6^{th} strip in the same detector gave a spatial resolution of 7.9 μm.

In order to reduce scattering in the inner detector, which impacts upon momentum resolution, it is necessary to minimise the quantity of material which makes up the inner detector. The number of silicon layers and the thickness of each layer should therefore be minimised. The necessary substrate thickness is in part determined by the required input charge for the preamplifier. No internal amplification exists within a microstrip detector. The input charge is that generated purely by the energy lost by the incident ionising radiation within the detector bulk. A mip traversing 300 μm of silicon will produce approximately 23 000 electron-hole pairs which corresponds to an average charge of 4 fC [38] (variations in this value exist due to the random nature of atomic interactions). This is usually adequate considering the availability of low noise electronics with an equivalent input charge noise of < 0.4 fC. Signal to noise ratios of 20:1 are routinely achieved. A ratio of approximately 10:1 is adequate to

maintain a tolerable noise/hit frequency. If the noise levels can be reduced further then so too can the detector thickness.

Two additional limitations to the detector substrate thickness also need to be considered. The first involves signal losses to the ground plane of the detector. Signal losses are only avoided when the capacitance between adjacent readout strips is greater than the capacitance between the strips and the detector back plane. The capacitance between the strips and the back plane at full depletion decrease linearly with increase in overall detector thickness. Secondly, a sufficient thickness for a self supporting structure is an important engineering consideration. A substrate thickness of at least 280 um is required to satisfy all of these considerations.

1.2.2.1 Advanced Features of Microstrip Detectors

Silicon microstrip detector technology is constantly advancing with new or modified structures permitting improvements in the detector performance and range of applications. Some of the recent and important modifications to the basic structure of silicon microstrip detectors are double sided strip detectors, capacitively coupling and guard rails.

Double Sided Strip Detectors (DSSD)

In the standard configuration of strip detectors with p^+ strips on the front side and an n^+ region on the rear side only one coordinate of position can be readout. An additional coordinate can be obtained if the rear side n^+ contact is also segmented into individual strips positioned orthogonally to the front side p^+ strips. This is advantageous because it effectively reduces the quantity of silicon detector layers required to locate the path of a charged particle.

For such a detector to function correctly it is necessary to electrically isolate the n^+ strips from one another so that the detector signal is not shared from strip to strip and the spatial information lost. This is done by separating the n^+ strips with SiO_2. The SiO_2 layer will however contain $^+$ve charge and thus electrons will accumulate below the Si-SiO_2 interface within the *n*-

type silicon bulk. This charge will act as a low resistance conduction path effectively removing the strip isolation. Methods to circumvent this effect involve the addition of "*p*-stop" implants between the n^+ strips [40,41].

A second problem which must be overcome is how to make electrical contact with both sets of orthogonal readout strips. It is undesirable to mount sets of readout electronics at two different locations on the same detector substrate. A solution to this problem involving a double–metal layer has been developed, see for example [42]. Such detectors are being used at the *Belle* experiment at KEK.

Capacitance Coupled Strip Detectors

a.c. coupling between the detector readout strips and the signal processing electronics is most commonly used as opposed to direct coupling. This is done to shield the electronics from the d.c. component of the detector leakage current. A large valued coupling capacitor is required. This is difficult to fabricate using existing microelectronics processing technologies. Instead the capacitance coupling can be implemented into the detector structure [43]. This is achieved by inserting an insulating layer of SiO_2 between the strip implants and the Al metallisation. In doing so the biasing resistors must also be accommodated. These can be formed on the detector substrate using polysilicon layers.

Guard Rings

When positive charge becomes trapped within the SiO_2 on the outer detector substrate surface inversion layers may form within the silicon bulk. This charge accumulation can lead to an extension of the depletion region towards the detector edge. If the depletion region reaches the region surrounding the charge a low resistance conduction path is created. The result is a dramatic increase in the leakage current. To eliminate this problem various guard ring structures may be used. Such structures act to reduce the applied voltage over a short distance from the

junction region to the extremities of the silicon substrate in a well controlled manner. One such structure is the "overlapping gate" [44]. This structure consists of multiple p^+ implanted concentric rings which surround diode structures. Adjacent implants are connected via a layer of SiO_2 and Al metallisation is used to complete each ring. The resulting structure is a series of *p*-channel MOSFETs. A carefully controlled bias is then applied to each of the rings so as not to exceed the threshold voltage of the MOSFETs. Under this condition current is prevented from flowing from ring to ring and hence the p^+ rings are electrically isolated from the ground plane.

1.3 Conclusion

The electrical properties of high purity silicon, the existence of a compatible insulator as well as the adoption of processing techniques from microelectronics, have lead to the successful implementation of silicon microstrip detectors in various HEP experiments. No other detector medium including other semiconductor types have yet shown the overall performance characteristics of silicon based microstrip detectors.

The success of ATLAS is crucially dependent upon the performance of the SCT and in particular the microstrip detectors. The detectors must be able to withstand the extreme radiation environment for the 10 year duration of the experiment. In the following chapter the current understanding of radiation effects in silicon microstrip detectors is described along with a brief history of radiation damage studies in crystalline silicon.

Chapter 2

Radiation Effects in Silicon and Silicon Microstrip Detectors

2.1 Introduction

The success of ATLAS is critically dependent upon the radiation hardness of the silicon microstrip detectors. For this reason over recent years a major effort has been directed to study firstly the radiation hardness of currently available detector technologies in an ATLAS type radiation field. And secondly, to develop improved radiation hard detector technologies. This chapter gives an overview of the work carried out so far. A focus is given on the effect radiation has on silicon detectors at both a macroscopic level by describing the device performance characteristics, as well as at an atomic structural level by describing the nature of radiation induced defect complexes.

Many of the contemporary reviews of radiation damage in silicon detectors have neglected to discuss contributions made to the field of radiation effects during the period from 1948 to around 1965. This was an essential period, the results from which are providing insights into how the radiation hardness of detector materials can be improved today. For this reason a brief review of this period is given as an initial starting point for the chapter.

2.2 Radiation Effects in Semiconductors (1948 – 1965)

Investigations into radiation effects in semiconductor materials began in the late 1940's shortly after the first demonstration of a sustained nuclear reaction. About this time Wignor predicted that fast neutrons would be capable of producing structural changes (atomic displacements) in crystalline materials. The first experimental studies were carried out on

neutron irradiated single crystals of germanium revealing an acute sensitivity of the electrical properties to radiation.

In 1948 Davies et al. [45] showed that as a function of neutron fluence the resistivity of *n*-type germanium increased and reached a maximum. At this point the material type converted from *n*-type to *p*-type. With further irradiation the resistivity decreased as the material became more *p*-type. For *p*-type germanium the resistivity was found to steadily decrease as a function of neutron fluence. In this case no type inversion was observed. The rate of resistivity change in both material types was not affected if the irradiating neutron beam from a reactor source was filtered through a cadmium plate. Heat treatment at 400°C was found to almost completely restore the resistivity to the original unirradiated value. Additionally, the conductance of irradiated materials stored at room temperature was found to decrease in an asymptotic manner with time.

The cadmium result indicted that impurities produced by thermal neutron induced transmutations were not responsible for the observed alteration in the resistivity. Rather, the changes were correctly explained as being due to the creation of radiation induced lattice damage and the associated production of new acceptor states within the germanium bandgap. The high temperature anneal restored the lattice to its pre irradiation state via the diffusion of the displaced atoms back to their regular crystallographic sites. A model was proposed which postulated the radiation induced generation of germanium vacancy and interstitial pairs. According to the model proposed by J Lark Horowitz, each of these defects was responsible for the generation of two levels within the bandgap [46]. The change in resistivity after irradiation was explained as a result of room temperature assisted annealing of the lattice damage.

Similar results were reported in other studies of germanium under irradiation by deuterons [47], reactor neutrons [48], [49], alpha particles [50] and fast neutrons [51]. Further confirmation that lattice defects were responsible for the observed change in the electrical properties was obtained by Crawford who demonstrated that the production of neutron transmuted impurities in neutron irradiated germanium was negligible [49].

Semiconductor silicon was also studied. Under irradiation the resistivity of silicon behaved in a different way than in germanium. As a function of neutron fluence the resistivity of both *n*-type and *p*-type silicon was found to increase [48]. Type inversion was not observed. High temperature annealing restored the pre irradiation resistivity.

The correlation of radiation damage with a reduction in the minority carrier lifetime was reported [52]. This parameter was found to be hundreds of times more sensitive to radiation than the material resistivity [53]. The changes in minority carrier lifetime in electron irradiated silicon was used to estimate the energy required to displace a single silicon atom. A value of 27.6 eV [53] was measured which compared favourable to a theoretically calculated value of 25 eV [54].

While work continued into the measurement of radiation induced changes to the electrical properties, studies commenced into the detection and identification of the electrical states and microscopic nature of the introduced defects. Electrical states were measured deep within the bandgap of silicon using infrared absorption techniques [55-57], Hall effect measurements [58-60], and by minority carrier lifetime measurements as a function of sample temperature [61,62]. Electron spin resonance (ESR) was also used to investigate the structure of the radiation induced defects [63].

Defect production in silicon containing different initial starting impurities was studied. In 1956 an important finding related to the identification of a defect involving oxygen impurities [64,65]. Named the “A-centre”, after a prominent infrared absorption signature [50], this defect was revealed to consist of a paired vacancy and oxygen complex, V-O. This result demonstrated the importance of the impurity concentration as a predictor of radiation damage. Differing initial impurity concentrations were also found to affect the rate of room temperature annealing [66].

A second radiation induced defect in silicon involving an impurity atom was identified in 1959 [65]. Known as the “E-centre”, this defect was identified using ESR to be associated with the pairing of a vacancy and a phosphorus atom, V-P [65].

Studies were performed into the dependence of defect production rates on the sample temperature during irradiation. Higher defect concentrations were found in room temperature irradiated silicon as opposed to 77 K irradiations [67]. This indicated that 2nd order processes were involved in the creation of stable defects. Also, the defect introduction rates in silicon varied considerably between materials irradiated by electrons and neutrons [68]. The variation was different for particular defect types [68]. Energetic photons were also shown to be capable of displacing atoms in solids [69].

The presence of defect clusters in neutron irradiated silicon, previously predicted by Vard [70], was inferred from ultrasound measurements [71]. Cluster sizes were estimated to be of the order of 100 to 2700 Angstroms in diameter. Theoretical predictions had indicated that clusters would contain approximately 10^5 to 10^6 atoms with a spherical radius of 150 to 200 Angstroms [72]. Diffusion theory predicted that many of the vacancies and interstitials produced in a primary process were annihilated shortly after production [72].

By the end of the 1950's most of the important radiation induced displacement damage effects in silicon had been observed and described at least in a qualitatively way. The A-centre and E-centre had been identified and the associated energy level measured. Sufficient experimental evidence was thus available to surpass the early damage model proposed by J. Lark Horowitz.

Another radiation induced defect in silicon was described in 1961 by Corbett and Watkins [73]. The defect, detected in infrared studies as the Si-J or Si-C centre [74], was identified as a divacancy complex, V-V. Initially it was thought to be a primary defect although it was later shown (1969) that the major fraction of the defect concentration was produced through a 2nd order process [75]. Production studies using electron irradiation at energies from 0.7 MeV to 1.5 MeV showed that a threshold for creation existed for the primary production path [76].

Further investigations were carried out into the A-centre using infrared absorption [77-81]. Low temperature studies (~ 4 K) confirmed that the defect was not produced in a primary process but rather, following the diffusion of liberated vacancies throughout the crystal until the

subsequent capture at the site of an interstitial oxygen atom [82]. Studies of the bonding nature revealed that the normal Si-Si bond was interrupted to form a non-linear Si-O-Si bond with the oxygen atom located at the vacancy site [77].

The production rate of the A-centre was found to be 10 times greater than the production rate of the divacancy. Importantly it was noted that in silicon containing a high oxygen content that the introduction rate of mid band centres was inhibited [83,84]. This result demonstrated that the oxygen atoms acted as a sink for vacancies. Thus it was reasoned that high purity material with low oxygen content would be more sensitive to radiation effects [75].

Thermal annealing studies were performed with the aim of determining the temperature at which defects could be eliminated [85]. Most significantly it was found that distinct annealing stages existed in 1 MeV electron irradiated silicon, while no such distinct stages were present in neutron irradiated silicon [86]. This was considered consistent with the annealing of defect clusters which are present in both neutron irradiated silicon [86,87] and in high energy electron irradiated silicon (E_e > 15 MeV) [88]. For 1 MeV electron irradiated silicon defect complexes are not produced on account of the lower energy imparted to the primary silicon displacement by the incident 1 MeV electron.

In around 1965 the published literature indicates a shift had commenced in the radiation effects community into two different directions. In the first, which used similar methodologies to the previous work, effort concentrated on studying silicon material containing different impurities at different concentrations. Most of this work has little relevance to modern high purity detector materials and as such will not be described here. The second direction was more technologically driven as researchers investigated the radiation hardness of particular device structures such as diodes and transistors [89]. The ever increasing importance and reliance on semiconductor devices as well as the uniqueness of each device in terms of its radiation hardness meant that comprehensive testing was required. Such a program of radiation hardness testing has been carried out for silicon microstrip detectors in recent years.

2.3 Radiation Effects in Silicon Microstrip Detectors

It can seen from the above review that the effects of type inversion, minority carrier lifetime reduction, room temperature annealing, defect clustering, the defect formation process and the identification of the most prominent defects in silicon had already been done prior to the implementation of the first microstrip detectors in HEP experiments. It was thus anticipated well in advance that such detectors would be vulnerable to performance degradation in high radiation fields. The magnitude of the effects could not adequately be predicted. One reason for this uncertainty was the fact that the silicon studied previously was of low resistivity and generally low in quality in comparison to that used in modern detector applications. Additionally, the uniqueness of microstrip detector structure and differences in device processing steps would also have contributed. For this reason the experimental HEP community commissioned extensive radiation damage programs in the form of various collaborations such as RD8 and RD2.

The main findings up until around the start of this thesis are now described.

2.3.1 Reverse Current

In 1984 Kraner predicted that the most detrimental effect to silicon detectors operating in high radiation fields would be an increase in the reverse current [90]. An increase in the reverse current constitutes a reduction in the S/N ratio by means of an increase in N.

Experimental studies found that the reverse current increased in silicon detectors irradiated by 24 GeV·c^{-1} protons [91], 9 to 21 MeV protons [92], 12 GeV protons [4], 800 GeV protons [93], mixed radiation with a significant fast neutron component [94], mixed hadrons [95], reactor neutrons [96], GeV muons [97] and high energy antiprotons [98]. The increase was found to be proportional to the irradiating particle fluence for protons up to a fluence of 10^{14} cm^{-2} [99], 1 MeV neutrons up to a fluence of 5×10^{13} cm^{-2} [3], mixed energy neutrons up to a

fluence of 10^{15} cm^{-2} [100], 14 MeV neutrons within a fluence range of 10^{9} to 10^{12} cm^{-2} [59] and 25 MeV protons in a fluence range of 10^{9} to 2×10^{12} cm^{-2} [101].

The cause of the reverse current increase was assumed to be due to the creation of deep level defects which acted as centres for carrier generation. Considerable experimental evidence exists in support of this assumption. The radiation induced reverse current is proportional to the square of the detector reverse voltage (the depletion depth is proportional to the square of the reverse voltage) [101,102]. The reverse current increase scales in proportion to the device area [103]. The reverse current increase is independent of surface structural variations including SiO_2 thickness, the presence of buried n^+ layers and implanted p^+ strip width [4]. Measurement of the temperature dependence of the increased reverse current was found to be consistent with the Boltzmann relationship [4,96]. (The theory of generation-recombination current associated with deep level defects is described in the elementary paper by Shockley, Hall and Read [104]).

The dependence of the reverse current increase on material type has also been investigated. Simultaneous exposure of both *n*-type and *p*-type silicon to fast neutrons showed that a detector manufactured on the base of *p*-type silicon was associated with a 30 % greater reverse current increase than in *n*-type silicon exposed to the same dose [3]. This result was contradicted by a similar study which showed that a detector with an *n*-type bulk was associated with a 30-50 % greater increase of the reverse current than for a detector with a *p*-type bulk [4]. A more recent study showed the reverse current increase for detectors based on *n*-type and *p*-type diodes was rather similar at least up to a neutron 1.85×10^{13} cm^{-2} [105]. In another study no dependence was found on silicon resistivity over a range of 1.5-5 kΩ·cm [106]. The reverse current damage constant was the same for resistivities from ~ 10 Ω·cm up to 5 kΩ·cm, but at higher resistivities it was found to increase [107]. In another study it was found to be independent for resistivities from 1 kΩ·cm to 80 kΩ·cm [108].

Experiments on the bias dependence of the detector reverse current increase showed no difference between detectors irradiated with or without application of an operating bias [99,103]. Another study involving two detectors, one biased and one not biased on the same

substrate, showed a greater increase of the reverse current for the biased detector [109]. The additional reverse current in the biased detector was attributed to the contribution of surface current due to the presence of energy states located at the Si-SiO_2 interface [109].

An early investigation into the effects of exposure of ion implanted detectors to mixed radiation fields demonstrated a dependence of the reverse current increase on the time scale of the irradiation [94]. This result is now understood to be associated with a reduction of the radiation induced reverse current due to annealing of the damage at room temperature [110]. Reduction of the radiation induced reverse current with room temperature annealing is known to be significant. Following 800 MeV proton irradiation the radiation induced reverse current annealed by 50 % over a period of 50 days [99]. A 20-30 % reduction was observed over a 2 month period following exposure to neutrons with a peak energy of 1 MeV [100]. The decrease was observed to be exponential with time during a 50 day period following exposure of a silicon detector to reactor neutrons [96]. A decrease of 25 % in 12 days and not more than 30-40 % in 5 months was observed following exposure of a silicon detector to 1 MeV neutrons [105]. No further reductions of reverse current with room temperature annealing were observed beyond a period of 150 days following high energy proton irradiation [111]. A long term study of silicon detectors irradiated by 24 $GeV{\cdot}c^{-1}$ protons showed no evidence of reverse annealing of the reverse current (as is exhibited for the effective impurity concentration), over a temperature interval of -20°C to 0°C [112].

Based on the proportionality between the reverse current increase per unit volume and the irradiating particle fluence, the reverse current damage constant, α, can be defined by:

$$\frac{\Delta I}{vol} = a\Phi \qquad (2.1)$$

where: vol = the detector depleted volume,

ΔI = the change in the reverse current following irradiation,

Φ = the irradiating particle fluence.

α has been calculated for various experimental conditions. In Table 2.1 a collection of experimental determinations of α has been compiled based on recently published work. A graphical representation of this data is shown in Figure 2.1. Considerable variations in α from experiment to experiment are apparent. The variations are mainly a product of the differing experimental conditions such as irradiating particle types and energy, the time the measurement was performed after irradiation, and the temperature of the device during measurement. An average value of $\alpha_{av} = 3.2\times10^{-17}$ A·cm^{-1} can be obtained for silicon detectors made from high resistivity *n*-type silicon using only the measurements performed at 20° (or normalised to 20°C) and measured well after the effects of room temperature annealing have receded.

The room temperature annealing of the leakage current has been parameterised by various groups [99,109] using the function:

$$\frac{\Delta I(t)}{\Delta I(t_o)} = \sum_{i=1}^{5} A_i \exp\left[-\frac{t}{t_i}\right] \qquad (2.2)$$

valid for t > 1 hr. Or by the function [103]:

Table 2.1: Reverse current damage constant determinations for various experimental conditions.

Year	Ref.	Irradiating Conditions	a ($A \times cm^{-1}$)	Error ($A \times cm^{-1}$) $\times 10^{-17}$	Temp (°C)	Time	Silicon Bulk	Device Form
1987	[95]	hadron, 200GeV	1.30E-17	0.4	20	-	n-type Si, 3 kΩ·cm	p^+nn^+, strip detector, pitch 20, 280 um
1988	[4]	p, Synchrotron (KEK), 12 GeV	3.00E-17	-	25	45 hrs.	n- and p-type Si, high resistivity	pn, 30×30 mm^2, strip pitch 0.5 mm, varying surface structure
1989	[96]	n, reactor spectrum	6.60E-17	-	20	3 wks	n-type Si, 4 kΩ·cm	PIN photodiode, 1 cm^2, 200 um (Hamamatsu)
1990	[97]	pions , 300 GeV Pi beam	4.50E-17	3.5	-	3 wks	n-type Si, high resistivity	pn surface barrier, diffused and ion implanted, varies sizes
1990	[99]	pions, 800 MeV	4.20E-17	0.29	20	-	n-type Si, high resistivity	p^+nn^+, photodiodes (#S1723 Hamamatsu
1991	[100]	n, spallation source, peak 1MeV	3.00E-17	-	20	4 days	n-type Si, 3-5 kΩ·cm	test structures (SI, Oslo)
1991	[113]	n, 252Cf, over 100 days	4.80E-17	0.90	20	-	n-type, 4-6 kΩ·cm	p^+nn^+ ion implant., 5×5mm^2 & 10mm^2, 400 um
1992	[103]	n, spallation source, norm 1 Me	5.30E-17	0.59	20	-	FZ n-type Si, 3-5 kΩ·cm	p^+nn^+ diffused, varied sizes
1992	[106]	n, spallation source, peak 1MeV	2.00E-17	-	-	10 days	n-type Si, ~ 5 kΩ·cm (Wacker)	p^+nn^+, 280 um
1992	[114]	n, spallation source, peak 1MeV	2.68E-17	0.66	20	1 wk	FZ n-type Si <111>, 3-6 kΩ·cm	p^+nn^+, 0.5×0.5 cm^2, 400um
1992	[114]	n, spallation source, peak 1MeV	1.74E-17	-	20	6 months	FZ n-type Si <111>, 3-6 kΩ·cm	p^+nn^+, 0.5×0.5 cm^2, 400um
1992	[114]	n, spallation source, peak 1MeV	3.80E-18	-	0	6 months	FZ n-type Si <111>, 3-6 kΩ·cm	p^+nn^+, 0.5×0.5 cm^2, 400 µm

Table 2.1: Reverse current damage constant determinations for various experimental conditions. CONT...

Year	Ref.	Irradiating Conditions	a (A/cm^{-1})	Error (A/cm^{-1}) ´ 10^{-17}	Temp (°C)	Time	Silicon Bulk	Device Form
1992	[3]	n, ~ 1 MeV	3.10E-17	0.20	20	short	n-type Si, 12.2 kΩ·cm	p^+nn^+, 1 cm^2, 317 µm (Micron)
1992	[102]	n, spallation source, peak 1MeV	3.60E-17	0.20	20	1 hr	n-type Si, 2.6-12.9 kΩ·cm	p^+nn^+, ion implantation, varies sizes
1993	[116]	n, ~ 1 MeV	6.70E-17	0.40	20	corr A [1)]	n-type Si, high resistivity	p^+nn^+, 1 cm^2, 300 µm
1993	[116]	p, 24 GeV/c, CERN PSAIF	7.90E-17	0.40	20	corr A [1)]	n-type Si, high resistivity	p^+nn^+, 1 cm^2, 300 µm
1993	[117]	n, Be(d,n)B E=6.2MeV, eq 1 MeV	8.00E-17	-	-	corr A [1)]	n-type, 6 kΩ·cm,	surface barrier, 0.2-2 cm^2, 400 µm
1993	[111]	p, 650 MeV	3.00E-17	0.29	20	short	n-type Si, 4 and 12 kΩ·cm	p^+nn^+, 1 cm^2, 200 µm (Hamamatsu), and 300um (Micron)
1993	[111]	p, 650 MeV	6.00E-18	0.10	20	long	n-type Si, 4 and 12 kΩ·cm	p^+nn^+, 1 cm^2, 200 µm (Hamamatsu), and 300um (Micron)
1993	[18]	fast neutrons, 3-12 MeV	6.29E-17	0.69	-	1 week	n-type Si, 1.3 kΩ·cm	p^+nn^+, 0.25 cm^2, 300 µm (JINR L)
1993	[118]	fast neutrons, 3-12 MeV	3.50E-17	0.40	-	6 months	n-type Si, 1.3 kΩ·cm	p^+nn^+, 0.25 cm^2, 300 µm (JINR L)
1993	[119]	n, varies facilities	8.80E-17	-	20	-	n-type Si, 6-9 kΩ·cm	p^+nn^+, segmented ion implanted detectors taken from UA2
1994	[105]	n, av. ~ 1 Mev, CERN/PSAIF	3.10E-17	0.20	20	2 hours	n-type Si, high resistivity	p^+nn^+, ion implanted, varies size
1994	[105]	p, 24 GeV/c, CERN/PS	4.90E-17	0.20	20	2 hours	n-type Si, high resistivity	p^+nn^+, ion implanted, varies size
1994	[112]	p, 24 GeV/c	4.90E-17	0.10	20	long	n-type Si, ~ 9 kΩ·cm	p^+nn^+, ion implanted, 1 cm^2, ~ 300 µm

Table 2.1: Reverse current damage constant determinations for various experimental conditions. CONT...

Year	**Ref.**	**Irradiating Conditions**	a **(A/cm^{-1})**	**Error (A/cm^{-1}) ´ 10^{-17}**	**Temp (°C)**	**Time**	**Silicon Bulk**	**Device Form**
1994	[112]	p, 24 GeV/c	1.80E-17	0.10	10	long	n-type Si, ~ 9 kΩ·cm	p^+nn^+, ion implanted, 1 cm^2, ~ 300 µm
1994	[112]	p, 24 GeV/c	1.17E-17	0.03	0	long	n-type Si, ~ 9 kΩ·cm	p^+nn^+, ion implanted, 1 cm^2, ~ 300 µm
1994	[112]	p, 24 GeV/c	3.70E-18	0.01	-20	long	n-type Si, ~ 9 kΩ·cm	p^+nn^+, ion implanted, 1 cm^2, ~ 300 µm
1994	[120]	p, 500 MeV SATURNE cyclotron	3.60E-17	-	-	short	n-type Si, high resistivity	p^+nn^+, strip detector, 50 µm pit (SI)
1994	[120]	p, 500 MeV SATURNE cyclotron	2.00E-17	-	-	30 days	n-type Si, high resistivity	p^+n, strip detector, 50 µm pitch
1995	[127]	p, 24 GeV/c proton synchrotron	5.40E-17	0.5	20	short	n-and p-type Si, 1.5-80 kΩ·cm	p^+n, ion implanted, 1 cm^2, 100-300 µm
1995	[127]	p, 24 GeV/c, proton synchrotron	2.50E-17	-	20	long	n-and p-type Si, 1.5-80 kΩ·cm	p^+n, ion implanted, 1 cm^2, 100-300 µm
1995	[121]	n, reactor spectrum, eq 1 MeV	8.90E-17	1	-	short	FZ n-type Si <111>, 2-7 kΩ·cm	p^+n, 2×2 cm^2 and 0.5×0.5 cm^2 (SGS-Thompson), 400 µm

1) Corrected for room temperature annealing.

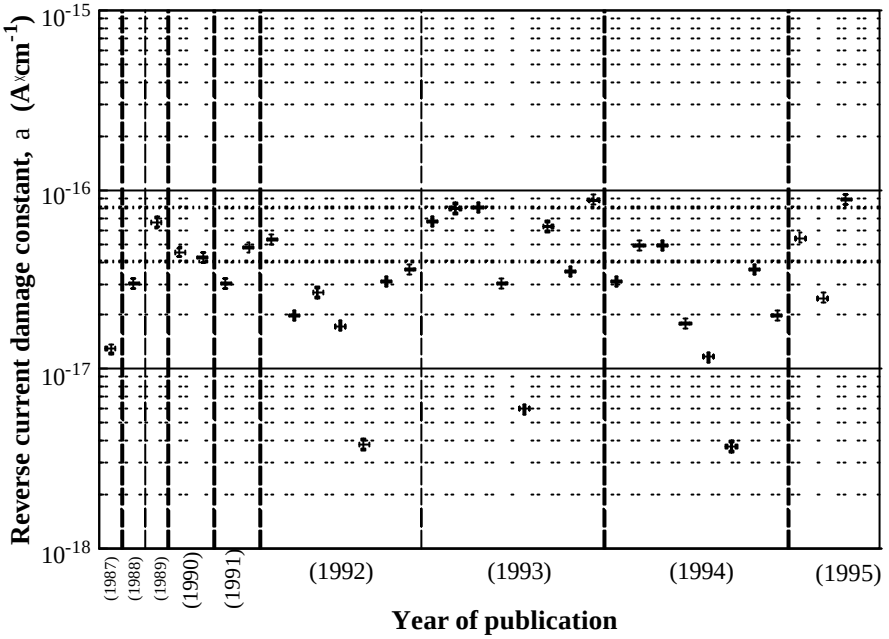

Figure 2.1: Reverse current damage constant for detectors irradiated under various conditions. Data taken from [4,95-97,99,100,102,103,105,106,111,112-121,127].

$$\frac{\Delta I(t)}{\Delta I(t_o)} = \sum_j \frac{A_j}{t} t_j \left(1 - e^{-\frac{1}{t_j}}\right) \qquad (2.3)$$

Alternatively, the reverse current damage constant has been modelled using the function [122]:

$$a_n = 10^a t^k \times 10^{-17} \qquad (2.4)$$

where: $a = 1.17 \pm 0.01$

$k = (11.45 \pm 0.86) \times 10^{-1}$

A clear assignment of the defect responsible for the reverse current increase has not been achieved. The inconclusive results regarding material type dependence do not eliminate the possibility that the responsible defect is associated with a re-configuration of the shallow level impurities of phosphorus or boron into defect complexes. Both are present in similar concentrations in *n*- and *p*-type high resistivity silicon. This possibility is supported by a result which found that the annealing of the reverse current was similar for 300 to 700 Ω·cm silicon as well as for high resistivity silicon [122].

Other defects have been proposed as being responsible. Annealing studies showed that the reverse current decreased with the annealing of the E-centre at 150°C [98]. Elsewhere it was reported that the room temperature annealing of the reverse current corresponded with the elimination of the C_i defect which has a high carrier capture cross section [123]. The divacancy was not considered to be a major source of the reverse current [110]. For a neutron fluence of ~ 10^{13} cm^{-2} the A-centre, E-centre and divacancy (V-V) concentrations have been observed to saturate while conversely the leakage current continues to increase [124]. This suggests that not one of these defects alone or even all of them combined is solely responsible.

Other mechanisms which are not associated with deep level defects may also be important. A study of the radiation induced reverse current increase in a large statistical survey of silicon microstrip detectors showed that while the majority of detectors behaved according to the average reverse current damage constant, a small but significant percentage of ~ 3.5 % had a much higher increase than that predicted by the average reverse current damage constant would predict [125]. Only one third of these strips had abnormally high pre irradiation reverse currents. This result has not been well explained.

To prevent the reverse current increases from affecting detector operation it has been suggested that the shot noise associated with reverse current could be reduced by using fast shaping times [126]. The shot noise associated with the reverse current, I_R, is given by:

$$s_{shot}(RMS \quad electrons) = \sqrt{\frac{I_R \cdot t_s \cdot A}{q}} \qquad (2.5)$$

where: q = the electron charge,

t_s = amplifier shaping time,

A = a constant which is dependent upon the type of shaping employed by the preamplifer and filter circuitry.

At the time of writing, measurements are being performed to ascertain if sufficient signal can be collected using fast shaping times for detectors irradiated to the equivalent 1 MeV neutron fluence expected during the 10 year operating lifetime of the ATLAS experiment. This solution however does not reduce the detrimental effects of resistive heating and the possibility of thermal runaway. Since the reverse current is known to obey the Boltzmann relationship, it has also been suggested that the reverse current could be reduced by operating the detector at a lower temperature. Significant reductions have been observed for detectors irradiated by hadrons and stored at 0ºC [111,112,128]. It was shown that cooling to about 0ºC enabled a reduction of the reverse current, thereby allowing operation at high voltages following irradiation by 1 MeV neutrons at a fluence of ~ 3×10^{13} cm^{-2} [129]. Operating at reduced temperature was found to reduce the reverse current by approximately a factor of two for every 7°C reduction in temperature [130]. The observed reduction was found to be slightly less than that predicted by the Boltzmann factor [111,112,119,128]. Where this apparent anomaly was observed it was suggested that low temperature storage reduced the amount of room

temperature annealing of the defects responsible for the reverse current. Subsequent warm up of detectors irradiated at - 20°C to room temperature restored the room temperature annealed reverse current [119].

High temperature annealing studies have shown that the radiation induced reverse current can be further reduced. After annealing at 250°C, the reverse current of silicon detectors exposed to 200 GeV muons was reduced to 15 % of that immediately after irradiation [97]. Due to engineering considerations, high temperature annealing will not be possible for detectors operating in an ATLAS type scenario.

2.3.2 Charge Collection Efficiency

For unirradiated silicon microstrip detectors operated under full depletion, the charge collection efficiency (CCE) is approximately 100 %. A degradation of CCE under irradiation may be anticipated based on the ability of radiation induced defects to act as charge trapping centres.

In early studies of the charge collection efficiency of irradiated silicon detectors no reductions in CCE were observed [91]. Ion implanted silicon detectors were irradiated with 24 $GeV \cdot c^{-1}$ protons up to a maximum fluence of 8.3×10^{13} cm^{-2} but showed no pulse height degradation in response to incident minimum ionising particles [91]. Response of a silicon detector to ^{106}Ru beta particles following exposure to "noninteracting relativistic particles" at a fluence of 6.8×10^{13} cm^{-2} showed a small reduction of collected charge [94]. In this case the reduction was attributed to a smaller depleted volume associated with changes to the effective impurity concentration.

In a more recent study an 8 % loss in the pulse height of a silicon detector in response to penetrating beta rays was observed. The detector had been exposed to 800 GeV protons at a fluence of 1.5×10^{14} cm^{-2} [93]. This was interpreted as a result of trapping of electrons at the SiO_2 surface due to ionisation induced charge build up within the SiO_2 layer.

Reductions to CCE which are attributable to carrier trapping at deep level defects have been reported. A pulse height reduction, which was attributed to recombination of charge at radiation induced deep levels, was observed in silicon detectors irradiated by 12 GeV protons to a fluence of 1.7×10^{14} cm^{-2} [4]. In this case pulse height reduction of order 10 % was observed in response to beta particles from ^{90}Sr. Similar reductions in response to beta particles from ^{106}Ru and gamma rays from ^{241}Am were observed in PIN photodiodes [96]. These results were attributed to recombination centres in the detector bulk following exposure to reactor neutrons with a fast neutron component at a fluence of 8×10^{12} cm^{-2}.

Observation of the current pulses produced within a silicon detector in response to ^{106}Ru beta particles with energies greater than 2 MeV (selected by an external trigger), and α particles from ^{241}Am, showed that following irradiation by ~ 1 MeV neutrons to a fluence of 1.12×10^{14} cm^{-2} that the current pulse had a smaller amplitude and a longer pulse length [115]. This result was significant as it demonstrated a definite charge collection deficit and an increase in charge collection time following neutron irradiation.

The use of a preamplifier with a short shaping time restricts the total charge collected and measured as the final signal. A study of a neutron irradiated silicon detector with a fast amplifier showed that the reverse current could be suppressed without affecting the charge collection efficiency following irradiation with neutrons to a fluence of 2.7×10^{13} cm^{-2} (normalised to 1 MeV) [129]. Using prototype ATLAS electronics consisting of low noise preamplifiers with peaking times of 20 ns, a charge collection deficit of 6 % in response to ^{90}Sr beta particles was measured following irradiation by neutrons to a fluence of 2.7×10^{13} cm^{-2} [128]. For a neutron fluence of 1.25×10^{14} cm^{-2} a deficit of 10 % was observed in CCE due to incident alpha particles using an amplifier with a shaping time of 20 ns [111]. Similar degradation of CCE was observed for detectors irradiated by 24 $GeV{\cdot}c^{-1}$ protons and 1 MeV neutrons [112,116].

No defects have been identified as being responsible for the charge collection reduction. Although electron traps have been identified as being more effective than hole traps at reducing the collectable charge [115].

Some disagreement exists between the dependence of the charge collection deficit with the irradiating particle fluence. In one study involving neutrons, a logarithmic dependence with fluence was reported [131]. While in another study, a linear dependence with neutron fluence was observed [115].

The CCE has been parameterised by a linear increase with irradiating particle fluence according to:

$$\frac{Q_o - Q_{irr}}{Q_o} = g\Phi \qquad (2.6)$$

where: γ = $(0.024 \pm 0.004)\times10^{-13}$ cm^{-2} [135],

Q_o = collected charge prior to irradiation,

Q_{irr} = collected charge after irradiation.

No room temperature annealing of the charge collection deficit has been observed for periods of at least 8 months following 24 $GeV{\cdot}c^{-1}$ proton irradiation and 1 MeV neutron irradiation [116,128].

Both FZ grown silicon and MCZ grown silicon suffered the same charge collection losses after neutron irradiated to a fluence of 9.9×10^{13} cm^{-2} [132].

2.3.3 Carrier Mobility

The carrier mobility in silicon may also be affected by the introduction of radiation induced defects as a result of the impurity scattering effect. A reduction in carrier mobility will cause a reduction in the collected signal.

Results on the effect of radiation on carrier mobility have been reported. Following irradiation by 1 MeV neutrons to a fluence of $10^{13}\,cm^{-2}$, the carrier mobility was determined by theoretical fitting of the observed current pulses. A reduction of 4.9 % for electrons and 1.6 % for holes was determined [132]. However, in another study involving neutron irradiation of a fluence of ~ $1\times10^{14}\,cm^{-2}$, no changes to the mobility were observed above the experimental error of 5 % [133]. Theoretical studies predict that impurity scattering by radiation induced defects is not expected until a neutron fluence of order $10^{15}\,cm^{-2}$ [134].

2.3.4 Effective Impurity Concentration

For complete charge collection it is also important that the depletion depth should correspond to the physical width of the detector. The voltage required for full depletion, V_{FD}, is given by:

$$V_{FD} = \frac{q w^2 N_{eff}}{2 e_o e_{Si}} \qquad (2.7)$$

where: e_{Si} = the dielectric constant of silicon,

w = physical width of the detector,

N_{eff} = effective impurity concentration.

Operation of the detector at a voltage less than V_{FD} will not permit all charge to be collected via a carrier drift transport process. Operation at a bias voltage greater than V_{FD}, in the so called over depleted mode is preferred on account of the increase of the electric field strength within the depleted volume. The electric field as a function of depth, x, is given by:

$$E(x) = -\frac{qN_{eff}w}{e_o e_{Si}}\left[1-\frac{x}{w}\right] \qquad (2.8)$$

where: x = the depletion width.

Improved performance is expected based on the increased carrier drift velocity and the reduced charge collection time. The carrier drift velocity dependence on the electric field for electrons is given by:

$$u_n = -m_n E \qquad (2.9)$$

where: m_n = the mobility of electrons.

This enhancement is particularly important where the signal integration time is short.

The maximum voltage available to reverse bias a detector is limited in HEP experiments on account of power consumption considerations and power supply design factors. The possibility of premature junction breakdown is also reduced with a lower applied bias voltage. From Equation 2.7 it is apparent that N_{eff} should be as low as possible to minimise the necessary voltage for full depletion.

In the presence of deep level defects N_{eff} is given by:

$$N_{eff} = \left| N_A - N_D + n_{T,A} - n_{T,D} \right| \qquad (2.10)$$

where: N_A and N_D = the shallow level acceptor and donor concentrations,

$n_{T,A}$ and $n_{T,D}$ = the deep level acceptor and donor trap concentrations.

The inclusion of radiation induced deep level defects will lead to alterations in N_{eff}.

A change in the depletion depth of a medium resistivity silicon based *p*-*n* junction device under neutron irradiation was reported in 1964 [94]. Exposure of silicon based radiation detectors to 24 GeV·c^{-1} protons showed that the bias required to fully deplete the detector increased linearly with proton fluence up to 8×10^{13} cm^{-2} [91]. It is now known that under neutron irradiation, the effective impurity concentration of high resistivity *n*-type silicon will at first decrease, reach a minimum at which point the material type changes from *n*-type to *p*-type and with further irradiation N_{eff} will increase. An experimental measure of this behaviour is shown in Figure 2.2.

This change in conductivity type, commonly known as “type inversion” has been observed in silicon detectors under neutron irradiation [103,106,115,121,133,135-137], under high energy proton irradiation [92,93,110,69,126,140], under muon irradiation [119], and under mixed hadron irradiation [95]. In Figure 2.3 the conversion fluence for these various irradiating particles in shown. For this set of experimental data the conversion occurs on average at an equivalent 1 MeV neutron fluence of 10^{13} cm^{-2}.

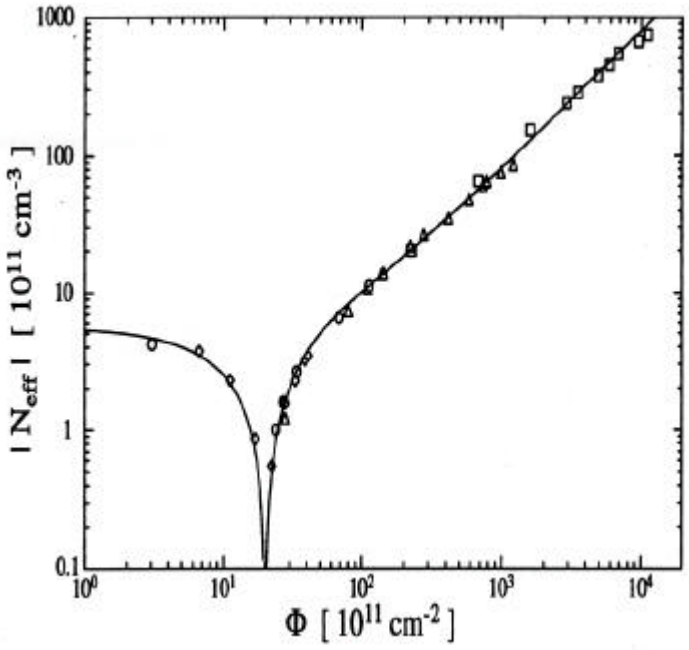

Figure 2.2: The effective impurity concentration (which controls resistivity) as a function of 1 MeV neutron fluence. Figure reproduced from [128].

After type inversion the detector continues to function without a change to the polarity of the reverse bias. This is on account of the p^+-n-n^+ structure. Following type inversion the structure becomes p^+-p-n^+. The junction is transferred from the front side to the rear side. This has been confirmed by studies of charge collection in inverted detectors using alpha particles incident on the rear side contact [see for example Ref. 3]. Based on a change in the sign in Hall effect measurements, type inversion was confirmed in substrates of silicon with no diode structure [100]. Although evidence for the transfer of the junction have been seen, some alpha particle induced events with high amplitude (hence not diffusion related), are still detected with alpha particles incident on the front side of an inverted detector operated at low voltages [63]. This suggests the presence of local junctions possibly due to regions of n-type silicon which remain in the inverted material.

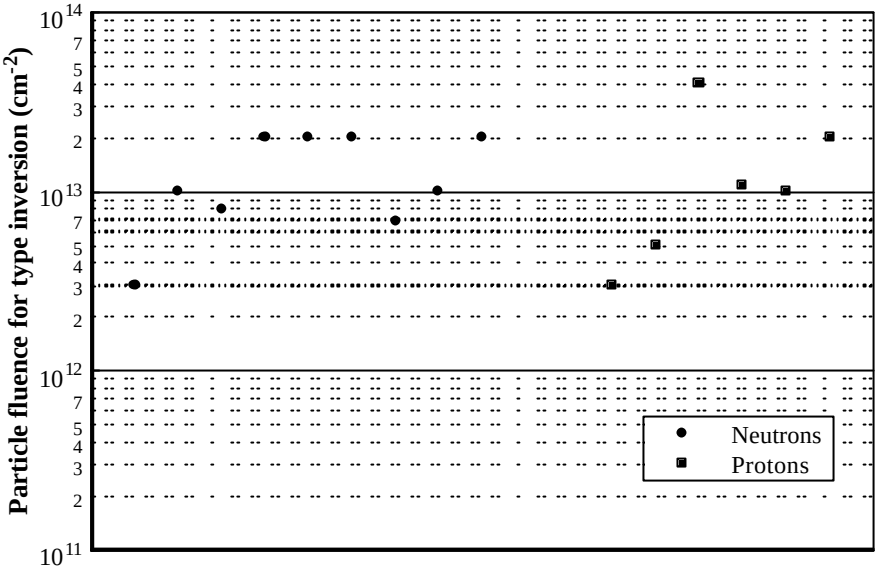

Figure 2.3: Particle fluence at which type inversion was observed for neutron irradiated and proton irradiated silicon detectors. Data taken from [3,92,103,106, 109-111,120,121,133,135,137-139].

The change of the N_{eff} has been parameterised using the following function [see Ref. 102 and references contained within]:

$$N_{eff} = N_o \exp(-c\Phi) + b\Phi \qquad (2.11)$$

The first term in Equation 2.11 accounts for the removal of the initial shallow level impurities. The second term accounts for the creation of new acceptor like states.

Studies of *n*-type and *p*-type detectors have shown that N_{eff} behaves similarly for a neutron fluence greater than 10^{13} cm^{-2} indicating that the accepter creation occurs at the same rate for both material types [119].

The fluence at which type inversion occurs was found to be lower in a detector irradiated at lower temperature [112,139]. This was explained by a reduction in the production rate of acceptor centres at reduced temperature [119,130].

For high resistivity diodes there is a lower impurity concentration to be compensated and the type inversion occurs at a lower fluence [102]. The inversion fluence can be parameterised according to:

$$\Phi_{inv} = (18 \pm 0.6) N_{eff,0} \qquad (2.12)$$

Based on this result it was reasoned that it would be possible to radiation harden the detectors against alteration to N_{eff} by using low to medium resistivity (300 to 2000 Ω·cm) *n*-type silicon as opposed to high resistivity silicon [132].

Other attempts to radiation harden the bulk through selective impurity inclusion have also been made. Silicon with an inclusion of ~ 0.1% germanium was studied under neutron irradiation [127]. In terms of the inversion fluence no difference was observed when compared to regular high resistivity silicon. Silicon with similar N_{eff} values but higher boron concentrations were found to invert at lower neutron fluences [127].

The parameterisation of N_{eff} in Equation 2.11 does not explain the long term behaviour of N_{eff}. At the completion of irradiation and storage of a detector at room temperature, N_{eff} continues to change. In the short term a decrease in N_{eff} occurs. This is followed by a sustained long term increase in N_{eff}. The trend is shown in Figure 2.4. In terms of the detector operating

voltage, the initial decrease in N_{eff} is a positive annealing effect. It has been observed to occur over a period of 3 weeks [115], 10 days [112], 15 days [141], 5 days [111], 10 days [142] and 20 days [110].

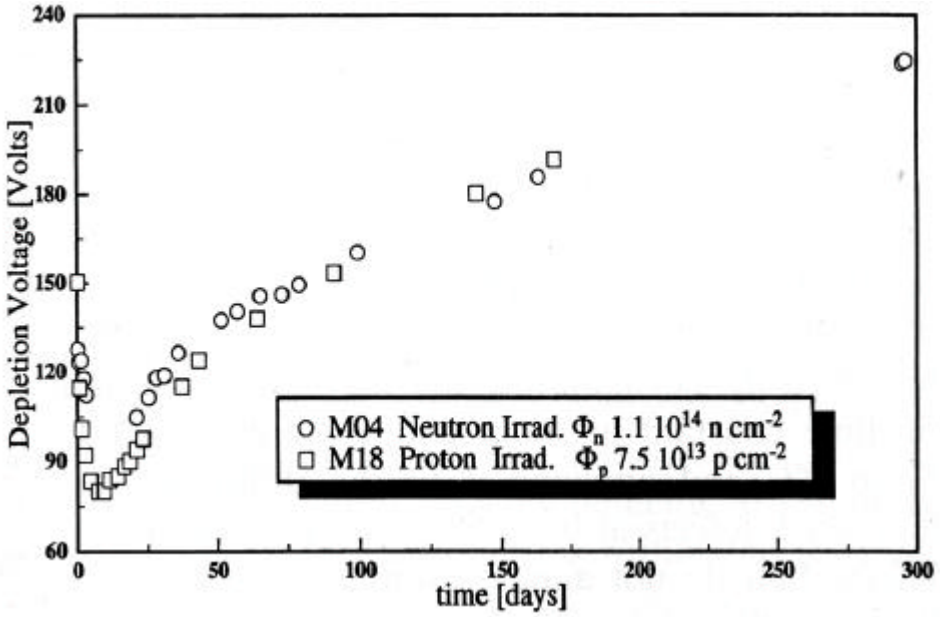

Figure 2.4: Evolution of the depletion voltage as a function of time after irradiation (The full depletion voltage is directly proportional to N_{eff}). Figure reproduced from [128].

The subsequent long term increase of N_{eff} is detrimental and is often referred to as reverse annealing. Observation of this stage has shown that reverse annealing is still occurring at least 250 days after irradiation [142]. Elevated temperature studies have demonstrated that saturation occurs after an equivalent period of 10 years at room temperature [127].

It has been shown that detectors kept at low temperature after irradiation do not exhibit the long term reverse annealing effect [111,112,130,138,143,144]. If the detector is restored to room temperature the reverse annealing begins with the same time constants as for devices that were not previously cooled [139].

The reverse annealing effect does not appear to have any dependence on the starting resistivity of the silicon for the initial starting range of N_{eff} from 0.45×10^{12} to 2.46×10^{12} cm^{-3} [141]. This suggests that the reverse annealing effect is not related to intrinsic radiation induced defects or impurities with concentrations greater than ~ 5×10^{12} cm^{-3}. This result is contradicted by the finding that the reverse annealing was less in silicon with a resistivity of ~ 1.5 kΩ·cm [127].

Detectors fabricated using different thermal oxidation processes giving higher concentrations of carbon and oxygen have been studied. No difference in the reverse annealing of N_{eff} was seen for oxygen and carbon concentrations varied between 10^{16} to 10^{17} cm^{-3} [146].

Full depletion voltages can effectively be reduced by reducing the substrate thickness. For substrates of thickness 250 μm, V_{FD} was reduced by 30 % over that in 300 μm substrates without significantly degrading the signal to noise ratio [139]. Engineering considerations may prevent reductions of the substrate thickness below 300 μm for the ATLAS experiment.

2.3.5 Surface Damage

The trapping of charge within the dielectric layers of SiO_2 and Si_3N_4 used on the surface of silicon detectors as a result of ionising energy loss can cause long term effects on detector operation. Detector parameters such as the interstrip capacitance and the interstrip isolation can be affected. Generation of excessive surface currents and the possibility of premature breakdown is also possible.

The interstrip capacitance is a critical parameter in terms of the overall input capacitance to the preamplifier and its influence on noise. An increase can be expected based on the build up of

trapped positive charge in the oxide which causes an increase in the charge density of the accumulation layer at the Si-oxide interface [144]. Increases of between 10 % and 20 % have been observed in microstrip detectors following exposure to ionising radiation [143]. A maximum increase of ~ 30 % was observed for *p*-type strips with a saturation occurring at an ionising dose of 500 krad [147]. Further details of this effect in different silicon detector technologies are available [147-150].

The accumulation of free electrons in the silicon side of the Si-oxide interface will also cause a reduction in the electrical isolation between the n^+ electrodes of double sided strip detectors. Decreases have been seen under a moderate proton fluence [95] and under neutron irradiation [103]. In both cases the reductions were considered tolerable. For high luminosity ATLAS type fields, the reductions are anticipated to be tolerable even after many years of operation [143].

Ionising energy loss will also impact on the operation of the CMOS electronics. Here a build up of charge within the oxide layer and the associated electron accumulation layer in the semiconductor material will cause a shift in the threshold voltage of the transistor. While radiation hard technologies are available from industry, considerable effort is being made to produce radiation hard detector electronics with low power consumption and low noise characteristics specifically for ATLAS applications [see the review in Ref. 147].

2.3.6 Pion Induced Damage

In radiation damage studies performed up until the mid 1990's, very little consideration of the effects of pions had been made. The calculated projections of the radiation levels in the ATLAS inner detector have showed that pions will make a significant contribution to the hadron fluence [151,152]. Indeed within the barrel region, up to a radius of ~ 40 cm from the beam line axis, pions, within an energy of 0.1 to 1 GeV, are anticipated to represent the major

contribution to the total particle fluence. For this reason an accurate prediction of the full extent of damage could not be made.

Additionally, the early calculations of the NIEL of pions in silicon at high energies were simply based on extrapolations from the damage data at lower energies and did not in any way deal with the actual physical situation. The early calculations showed that pions were similarly damaging to 1 MeV neutrons [153]. More recent calculations indicate that the NIEL will be enhanced around a pion energy of ~ 200 MeV due to the existence of the Δ resonance[2] [154]. The degree of this enhancement is uncertain with the most recent calculations anticipating that pions with a momentum of 250 MeV·c^{-1}, (K.E.=149 MeV), are up to 1.6 times more damaging than 1 MeV neutrons [155]. Considerable attention has now been focused on determining the true extent of pion induced damage in silicon detectors.

Studies have been performed using high flux pion beams with energies within the range of 60 to 600 MeV. Pions can be produced using a high current proton beam made incident upon a graphite target. They are transferred by a beam line containing a magnet-spectrometer in order to selectively enhance the pion flux from other particles according to the charge to momentum ratio. Residual background proton and antiprotons are removed through absorption in filter plates, see for example [156].

Experimental results reveal that the pion induced radiation effects are similar in terms of type as well as magnitude to that of 1 MeV neutron induced radiation effects. Evolution of the effective impurity concentration has been observed with type inversion occurring at pion fluences ranging from (4-6)×10^{12} cm^{-2} [157-161]. Evolution of the effective impurity concentration as a function of room temperature annealing was found in all but one of these studies to correspond closely with 1 MeV neutron irradiated silicon detectors. In one study, observation of the saturating full depletion voltage showed that 350 MeV·c^{-1} π^+ particles were 20 % more damaging than 1 MeV neutrons [160]. It can be said that in terms of changes to the

[2] The delta resonance, 1232 MeV in mass with a width of ~100 MeV, is associated with pion absorption and dominates π-nucleon scattering between 100 and 300 MeV in pion energy.

effective impurity concentration, pions, within the energy range investigated, are at least as damaging as 1 MeV neutrons.

The reverse current damage constant, α, as measured immediately after irradiation was found to be similar to that associated with 1 MeV neutrons, $\alpha_\pi = (8.8\pm0.2)\times10^{-17}$ A·cm^{-1} [160] and $\alpha_\pi = (10.1\pm0.2)\times10^{-17}$ A·cm^{-1} after scaling by the associated NIEL factor of k = 0.93 [161], and slightly higher at $\alpha_\pi = 12.2\times10^{-17}$ A·cm^{-1} [159]. The long term 'stable' value of the reverse current damage constant, α_∞, was again found to be similar to that of 1 MeV neutrons, $\alpha_{\infty,\pi} = 3.04\times10^{-17}$ A·cm^{-1} after scaling by the associated NIEL factor of k = 0.93 [161], higher at, $\alpha_{\infty,\pi} = 3.5\times10^{-17}$ A·cm^{-1} [160] and $\alpha_{\infty\pi} = (4.0\pm1.0)\times10^{-17}$ A·cm^{-1} [158], and in another case was found to be lower at, $\alpha_{\infty\pi} = (2.2\pm0.2)\times10^{-17}$ A·cm^{-1} [157]. Apart from this last value, the reverse current increase generally appears to be on average fractionally larger than the corresponding values associated with 1 MeV neutron irradiated silicon detectors. Although in the higher valued cases, no indication was given that scaling using the NIEL factor was employed. Close observation of the reverse current as a function of room temperature annealing for both pion and neutron irradiated silicon detectors have showed the same time dependence. This indicates that the damage due to both particle types is based on the same type and mixture of defects [159]. In terms of the reverse current damage constant, only weak evidence has been found to support the prediction of enhanced damage associated with the pion energy region about the delta resonance [160,161].

The reduction of the charge collection efficiency (CCE) was found to be the same as that associated with 1 MeV neutron irradiation [161,162]. After 10^{14} π^+cm^{-2}, a CCE of 88% was found with good agreement for both 24 GeV·c^{-1} protons and 1 MeV neutron irradiation [160]. It was pointed out that optimum CCE can be achieved by over biasing the pion irradiated detectors [162,161].

The similarity of damage between pions and 1 MeV neutrons with the appropriate scaling based on NIEL factors, would seem to indicate that the well established results for 1 MeV

neutron irradiated silicon can be used for predictions of the pion induced damage of silicon detectors. Regardless of this possibility, experimental studies have been performed using high flux pion beams to extensively map out the pion induced changes of the detector leakage current [157,159-161,163,164] as well as the evolution of the full depletion voltage [157-161,163-165] as a function of irradiation and room temperature annealing over the lifetime of various HEP experiments.

While the exact value of NIEL as a function of energy about the resonance is not precisely known, the experimental evidence obtained to date indicates that the levels of damage associated with pion irradiation in silicon detectors can well be anticipated based on experimental studies and the pion fluence predictions for the various HEP experiments.

2.4 Radiation Induced Defect Complexes in Silicon

As previously mentioned, a deep level defect may act as a site for carrier trapping, as a site for carrier recombination, as a site for carrier generation, or as an electrical compensating centre. The effect which dominates will depend on properties of the defect such as the energy level and cross sections for capture of carriers, as well as the concentration of the defect and other factors such as the temperature and doping conditions of the substrate. Identification of defects present in irradiated silicon and the properties of these defects is thus an important aspect in determining the radiation hardness of a particular material or device. Such information can also assist in the development of strategies to improve radiation hardness either through changes to the device design or though defect engineering of the materials used.

As discussed at the beginning of this chapter considerable progress into the identification of radiation induced defects in silicon was made during the early work in the 1960's by Corbett and Watkins. Sensitive techniques such as electron paramagnetic resonance (EPR) and electron-nuclear double resonance (ENDOR) were used. The associated energy states were identified using infrared absorption, photoluminescence and measurement of the material conductivity and

minority carrier lifetime as a function of temperature. Later the technique of deep level transient spectroscopy was used. Although this work was done for low resistivity silicon with high impurity content, the fundamental properties of the defects found in both high resistivity and low impurity content silicon should be similar. The effect of individual defects on the macroscopic properties of a detector will depend on other factors.

Under irradiation the primary produced defects in silicon are silicon interstitials and silicon lattice vacancy sites. Isolated interstitials and vacancies are not stable defects. Many will annihilate shortly after production according to the reaction:

$$I + V \rightarrow \text{ - (recombination)}$$

where: I = silicon interstitial,

V = silicon lattice vacancy.

Vacancies and interstitials which don't immediately recombine can diffuse through the material. The silicon interstitial is mobile at temperatures greater than ~ 4 K. The vacancy site is mobile at temperatures greater than ~ 100 K [166]. Stable defects are produced when these mobile species are captured by another defect, which may be an impurity atom, forming a stable defect complex.

The type of defects produced can be divided into two types, those produced with a silicon interstitial association and those produced with a vacancy association. Vacancy related defects will be discussed first.

2.4.1 Vacancy Related Defects

A number of vacancy related defects have been observed. The most relevant of these to detector grade silicon is the divacancy V-V, the A-centre V-O and the E-centre V-P.

The divacancy may be produced as either a primary defect or through a secondary process according to the reaction;

$$V + V \rightarrow (V\text{-}V)$$

A detailed description of the divacancy was given by Watkins and Corbett [73] using EPR. They attributed four possible charge states to the defect of magnitude +1, 0, -1 or –2. Depending upon the charge state, the defect may behave as either an acceptor or donor state. The positive charge states correspond to donor like states and are located in the lower half of the bandgap. The negative charge states correspond to acceptor like states and are located in the upper half of the bandgap. The energy levels and carrier capture cross sections for the divacancy defect are summarised in Table 2.2.

The A-centre was first described by Watkins and Corbett [64,65]. It was shown that this defect was formed by the capture of a vacancy by a static oxygen atom located at an interstitial site according to the reaction:

$$V + O \rightarrow (V\text{-}O)$$

Table 2.2: Characteristics of radiation induced defects in silicon. Data taken from [167, and references contained within].

Defect	Charge State	Energy Level (eV)	Carrier capture cross section (cm^2)	
Divacancy	-2		-	-
	-1	$E_c - 0.23$	$\sigma_n = 2\times10^{-16}$	-
	0	$E_c - 0.41$	$\sigma_n = 4\times10^{-15}$	$\sigma_p = 2\times10^{-16}$
	+1	$E_v + 0.25$	-	-
A-Centre	-1		-	$\sigma_p \sim 10^{-14}$
	0	$E_c - 0.18$	$\sigma_n \sim 10^{-15}$	-
E-Centre	-1		-	$\sigma_p \sim 10^{-13}$
	0	$E_c - 0.44$	$\sigma_n > 10^{-16}$	-
C_i	0		-	$\sigma_p \sim 7\times 10^{-18}$
	+1	$E_v + 0.27$	?	-
C_i - O_i	0		-	-
	+1	$E_v + 0.38$	-	-
C_i - P_i (IA)	-1		-	-
	0	E_c - 0.38	-	-
C_i - P_i (IB)	-1		-	-
	0	E_c - 0.07	-	-
C_i - P_i (IIA)	-1		-	-
	0	E_c - 0.26	-	-
C_i - P_i (IIB)	0		-	-
	+1	E_c - 0.32	-	-
C_i - P_i (III)	0		-	-
	+1	E_c - 0.23	-	-
$C_i - C_s$ (A)	-1		-	-
	0	E_c - 0.17	-	-
$C_i - C_s$ (B)	-1		-	-
	0	E_c - 0.11	-	-

The A-centre is associated with an electron trap which is located in the upper half of the bandgap. The energy level and carrier capture cross section for this defect is listed in Table 2.2.

It is important to note that the production of the A-centre begins to saturate at the relatively modest neutron fluence of 5×10^{12} cm^{-2}. This can be explained as a result of the exhaustion of impurities and not due to a limitation of vacancies [168]. An additional study of FZ silicon with a low oxygen concentration and MCZ silicon with a high oxygen concentration showed a smaller concentration of A-centres in the FZ material [169]. This indicates no vacancy limited formation.

The E-centre was described by Watkins and Corbett [65] from results of EPR and ENDOR experiments. The defect consists of a vacancy trapped at a substitutional site of a phosphorus atom. The defect is produced via the reaction:

$$V + P \rightarrow V\text{-}P$$

The E centre has an acceptor like energy level located in the upper half of the bandgap. The energy level and carrier capture cross section are listed in Table 2.2.

In detector grade silicon the concentration of P is much less than that within low resistivity silicon and may exceed the oxygen concentration. Experimentally the rate of E-centre formation has been found to decrease with increasing oxygen concentration [170,171]. This indicates that oxygen is an effective site for the trapping of vacancies and its presence may reduce the formation of E-centres.

2.4.2 Silicon Interstitial Related Defects

The silicon interstitial is a highly unstable species due to its natural affinity for the silicon lattice. It is highly effective at ejecting substitutional located impurity atoms into interstitial

sites. In particular, the interstitial silicon atom can eject a substitutionally located carbon atom which are present in relatively high concentrations (compared to other impurities) in detector grade silicon. The reaction proceeds according to:

$$I + C_s \rightarrow C_i$$

At temperature T > 300 K interstitial carbon atoms are highly mobile, with a diffusion rate considerably larger than that of substitutional carbon atoms [339]. The isolated C_i defect is associated with two energy states within the silicon forbidden band [172-174]. The species is eventually captured by other impurity atoms to form stable complexes. The most likely reactions are associated with interstitial oxygen, substitutional phosphorus and substitutional carbon;

$$C_i + O_i \rightarrow C_i - O_i$$

$$C_i + P_s \rightarrow C_i - P_s$$

$$C_i + C_s \rightarrow C_i - C_s$$

The energy levels of these defects are listed in Table 2.2.

The C_i - O_i defect is most important in silicon containing a high oxygen concentration or in high resistivity silicon where the concentration of P is low [175].

The C_i - P_s defect was identified using DLTS [176]. The defect is thought to exist in five different configurations. The configurational state at any one time is assumed to be dependent on the sample temperature and biasing conditions of the device.

The C_i - C_s defect is most prominent in silicon which contains a high carbon concentration but low oxygen concentration [175]. The defect has been observed to exhibit bi-stability [177-179]. This bi-stability is thought to be associated with a molecular bond switching mechanism between two different configurations [179].

2.5 Conclusions

This review demonstrates that considerable knowledge has been gained in the area of radiation effects in silicon over the preceding 50 years. In terms of the survivability of silicon based detectors at ATLAS the most important radiation effect is the evolution of the effective impurity concentration, N_{eff}. At this stage further experimental detail is required into the extent that N_{eff} will evolve as a function of time in an ATLAS type radiation field.

In order to radiation harden detectors against detrimental changes in N_{eff} further experimentation is required. The key to this research would seem to be through a closer look at the role that impurities play in the formation of stable radiation induced defects and the associated deep level defects.

The initial stages of the experimental program of this thesis were carried out with the aim of better understanding radiation effects in detector grade silicon and to seek strategies to improve the radiation hardness of this material.

Chapter 3

Experimental Study of Neutron Damaged Silicon Detectors

3.1 Introduction

In this chapter an ab initio study into the effects of 1 MeV neutron irradiation on silicon detectors is described. The aim of this study was twofold. The first aim was to develop good experimental procedures and technical competency in the characterisation of silicon radiation detectors before and after irradiation. The second aim was to identify the key research directions to be followed in the subsequent studies.

Brief descriptions of the standard techniques employed in this experimental study are described here. In the later sections of the chapter a new technique for the characterisation of deep level defects in silicon is examined and described. The technique known as Optical Deep Level Transient Conductance Spectroscopy offers a new means by which defects in highly irradiated silicon detectors can be observed.

3.2 Detector Test Structures

Silicon microstrip detectors presently being used or planned for use in HEP experiments were not available for this study. Rather, small sized detector test structures purposely manufactured for experimental investigation were obtained. Such devices provide a means of investigating the effects of radiation on the properties of the silicon bulk in addition to the effects on detector performance. A quality assurance approach with real sized microstrip detectors is being performed elsewhere, such as within the CERN Detector R&D Collaboration RD8.

The devices used were supplied by 'SPO Detector' Ltd., from the Ukraine [180]. A schematic of one such device is shown in Figure 3.1. The device was processed from high purity *n*-type silicon with a resistivity of ~ 1.5 kΩ·cm and a thickness of 360 μm. The substrate area is 12 mm × 4 mm. On this substrate three separate planer p^+-n-n^+ detectors have been fabricated. The area of each detector is 3 mm × 3 mm. The front side p^+ region was produced by ion implantation of boron, and the back side n^+ region was produced by phosphorus implantation. The implanted regions were metallised with a thin layer of aluminium. A small bonding pad is located at one corner of the front side metallisation. This allowed electrical contact to be made without causing damage to the detector junction area or creating a physical obstruction to the sensitive volume of the detector. The separation between adjacent detectors is 1 mm. This is considerably larger than the substrate thickness. For this reason capacitive coupling between two detectors should be minimal and each detector will behave as an isolated parallel plate capacitor.

Two identical devices were used which were identified as device 'U4' and device 'U5'. The individual detector elements on each device were labelled 'a, b and c'. So for example the middle detector of device U4 was labelled U4b.

To facilitate electrical characterisation the devices were mounted in purpose made holders as shown in Figure 3.2. Each holder consisted of a brass plate bent at one end through 90° to form an 'L' shape. A thin sheet of indium foil was secured to an abraded region of the holder base. The device was then placed rear side down on this surface. A hole drilled on the vertical section of the holder accepted a cylindrical teflon sleeve. At the centre of the sleeve was an electrical feed through wire electrically insulated from the brass base. The wire was bent at an angle of 90° down towards the base plate to make contact with the detector bond pad. A small gold leaf was placed between the bond pad and wire to improve electrical contact. The device was physically held in place by a light downward force from this wire.

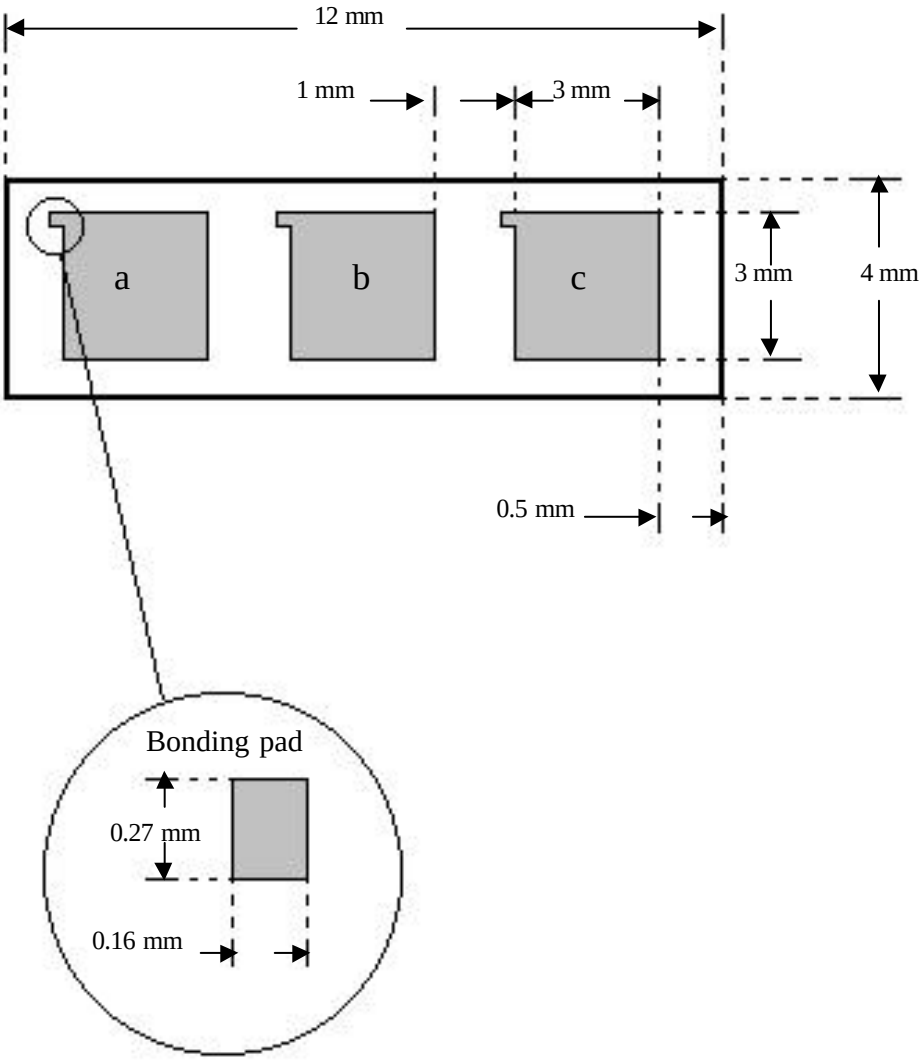

Figure 3.1: Layout of a detector test structures. Dimensions were measured using a microscope and calibrated scale. The three detector structures are labelled ‘a, b and c’. Devices were supplied by ‘SPO Detector’ Ltd., Ukraine [180].

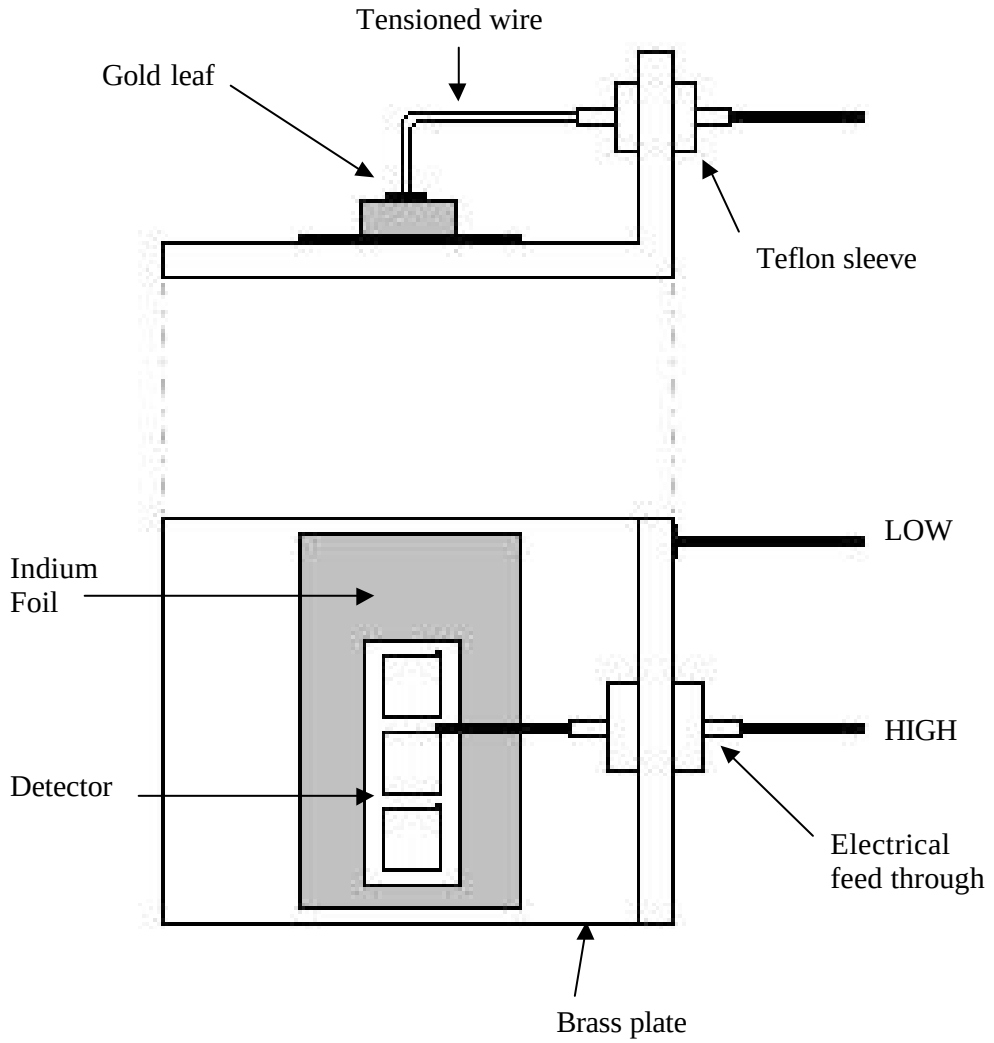

Figure 3.2: Device holder mount for the electrical characterisation.

3.3 Characterisation of the Unirradiated Detectors

The pre irradiated electrical properties of the bulk substrate and p^+-n junction, as well as the detector performance, were elucidated using semiconductor device characterisation techniques and detector testing procedures. Some basic description of the techniques is given in addition to the actual experimental results obtained.

3.3.1 Capacitance Voltage Measurements (*C-V*)

The effective impurity concentration which controls the substrate resistivity can be determined from a measure of the detector capacitance as a function of reverse voltage (*C-V* measurement).

3.3.1.1 The Principle of the *C-V* Measurement

Under the collective assumptions of the depletion approximation the relationship between the device capacitance, reverse voltage and effective impurity concentration, N_{eff}, for an abrupt junction is given by Equation 3.1 (taken from Ref. [20]):

$$C = \frac{e_o e_{si}}{x_d} = \sqrt{\frac{q e_o e_{si} N_{eff}}{2(V_{bi} - V_R)}} \qquad (3.1)$$

where:
- e_{si} = dielectric constant of silicon,
- e_o = permittivity of free space,
- q = charge of an electron,
- x_d = width of the depletion region,
- V_{bi} = junction built in potential,
- V_R = externally applied reverse voltage,
- C = junction capacitance (per unit area).

For an abrupt junction a plot of C^{-2} versus V_R gives a straight line with a slope inversely proportional to N_{eff}. V_{bi} can be determined from the *y*-axis intercept.

The impurity concentration can also be determined as a function of depletion depth using:

$$\frac{dC^{-2}}{dV_R} = \frac{2}{qe_o e_{si} N_{eff}(x_d)} \qquad (3.2)$$

Measurement of the capacitance is most commonly performed using a capacitance bridge. This type of instrument provides a test signal to the sample in the form of a sinusoidal waveform with an amplitude of typically 50 mV and a frequency of typically 1 MHz. This a.c. signal is superimposed on a d.c. voltage offset which permits the detector junction to be reverse biased. The bridge measurement circuitry detects the induced current and by means of a phase detector the conductance and capacitance contributions associated with the detector complex impedance are separated. The steady state reverse current associated with the junction reverse bias is filtered from the signal.

The capacitance measured in this way is a differential capacitance corresponding to the response of the depletion region edge to a change of ΔV_{test} in the reverse bias. The capacitance is given by:

$$C = \frac{dQ_d}{dV_{test}} \qquad (3.3)$$

where: Q_d = the charge due to the uncompensated majority carrier centres, or net space charge contained within the depletion region.

It can be shown that the measured differential capacitance is equivalent to the capacitance expression given in Equation 3.1 (see for example Blood and Orton, Ref. [181]). It is valid for an arbitrary distribution of impurities throughout the depletion region.

3.3.1.2 *C-V* Measurement of the Detector Test Structures

For this series of measurements the detectors were kept at room temperature and under vacuum (< 10 mPa). Light was excluded from the measurement chamber. A BOONTON capacitance bridge Model 7200 was used with a sinusoidal waveform of amplitude, V_{test} = 45 mV and frequency, ω_{test} = 1 MHz.

In Figure 3.3 a plot of the *C-V* data for the detectors of device U4 is shown. The capacitance has been corrected for the parasitic capacitance contribution of both the holder and measurement leads. The same characteristic curve was obtained for all three detectors. At the maximum reverse voltage full depletion was not observed as indicted by the failure of the curve to reach a stable minimum capacitance. The reverse bias was limited to - 40 V due to a software bug in the instrument interface program (the problem was rectified for all future measurements). Similar results were obtained for the detectors of device U5.

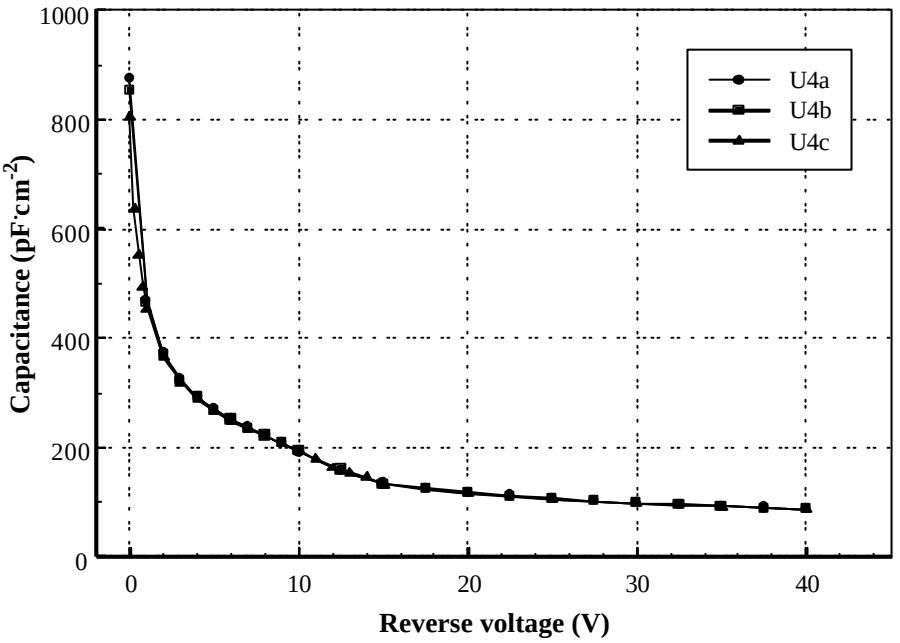

Figure 3.3: Capacitance as a function of reverse voltage for detectors U4a, b and c.

Close observation of Figure 3.3 reveals an unusual shape in the *C-V* curve in the region between 2 V and 15 V. The cause of this anomaly was not immediately apparent. It is more clearly identified as a kink in a plot of C^{-2} versus V_R, as shown in Figure 3.4. The effect is voltage dependent. This indicates it is not associated with a parasitic capacitance like that attributable to measurement leads as these effects are voltage independent. An identical curve was found using a LEADER LCR-740 LCR Bridge indicating that the effect was associated with the device under test and not simply an instrumental anomaly.

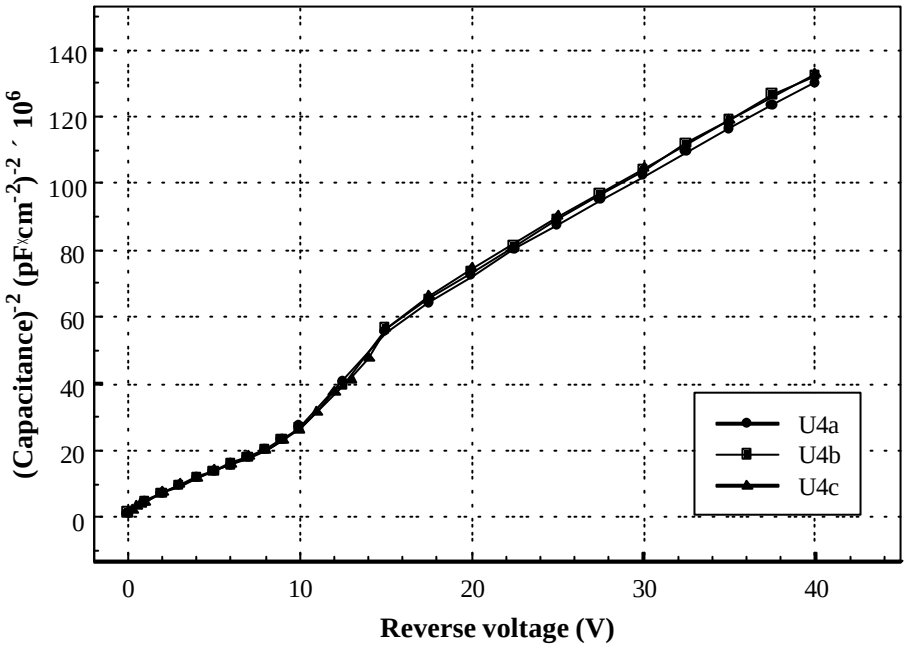

Figure 3.4: Inverse capacitance squared versus reverse voltage for detectors U4a, b and c. The kink in the curve at low voltages is clearly visible.

Well known device effects which can cause departure from the depletion approximation for the *C-V* relation defined by Equation 3.1 include series resistance effects and peripheral capacitance effects. The series resistance effect is associated with the resistance of both the

undepleted detector bulk and the electrical contacts. The equivalent circuit of the device under test, as assumed by the capacitance meter circuitry, consists of a capacitor in parallel with a resistor. In the case of a detector the capacitance is the depletion capacitance and the parallel resistance is that associated with the junction. The resistive contribution of the undepleted detector bulk and contact resistances are ignored. Both of these components will act in series with the junction equivalent circuit.

The peripheral capacitance effect is associated with the capacitance contribution of the depletion region edge which is not included in the parallel plate capacitance result. Neither of these effects are consistent with the observed data.

To identify the cause a plot of the theoretical junction capacitance given by Equation 3.1 was produced. A value of V_{bi} = 0.74 V and $N_{eff} = 3.5\times10^{12}\,\mathrm{cm}^{-3}$ were used. The value of N_{eff} was estimated from the region of the C^{-2} versus V_R curve far removed from the kink. The value of V_{bi} is typical of such a device. A comparison of the calculated curve with the experimental *C-V* data is shown in Figure 3.5. Close correlation is found for the region $V_R > 15$ V. The calculated curve was then subtracted from the experimental curve to more clearly identify the shape of the additional capacitance as a function of voltage. The residual curve is plotted in Figure 3.6.

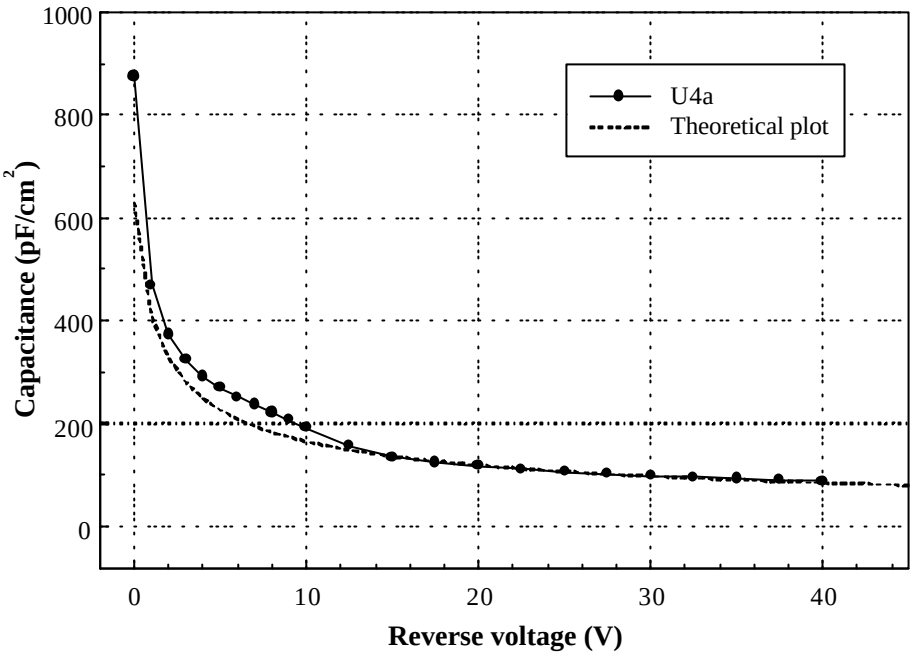

Figure 3.5: Comparison of experimental *C-V* curve for detector U4a with a theoretical plot from Equation 3.1 using V_{bi} = 0.74 V and N_{eff} = 3.5×10^{12} cm^{-3}.

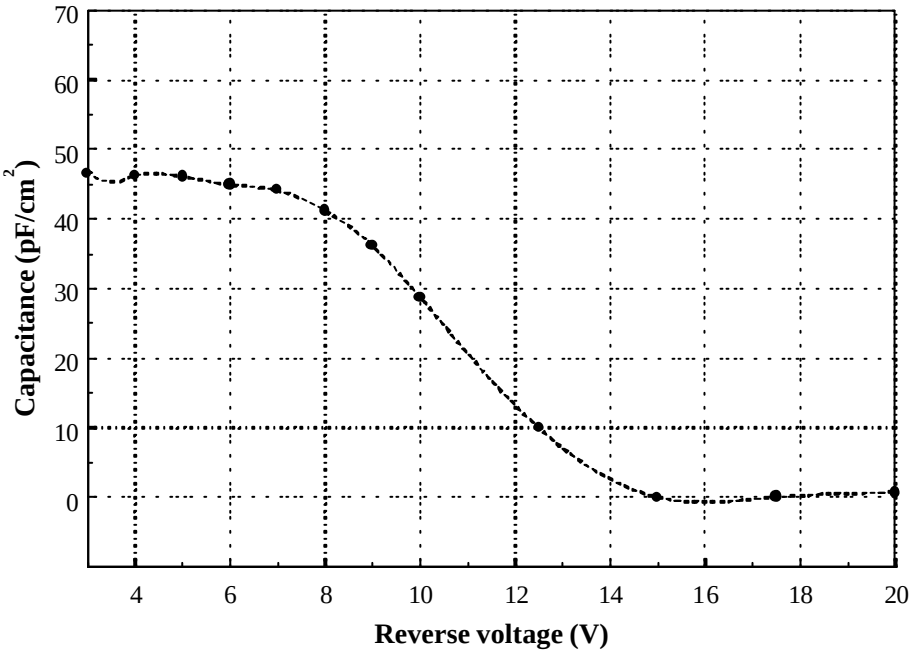

Figure 3.6: Residual capacitance between experimental curve and theoretical curve.

3.3.1.3 MOS Capacitor Effect on Detector C-V

Upon preparation of this residual capacitance curve it was immediately apparent that the shape was the same as that of the high frequency capacitance-voltage curve of a MOS device. For a comparison see Figure 27 (a), p. 194 of Ref. [20]. A MOS device consists of a layered structure of metal-oxide-semiconductor. The semiconductor substrate can be either *n*- or *p*-type. If *n*-type, and the metal is biased with a negative potential, the phenomena of inversion can occur. Here the concentration of holes, which are the minority carriers in the *n*-type semiconductor, will exceed the concentration of the electrons. An 'inversion layer' is formed in the semiconductor close to the interface with the insulator region. With increasing voltage the capacitance of the device will decrease as an electron depletion region is formed. Once strong inversion has occurred the depletion region expansion is halted and a minimum capacitance is reached. The strong inversion condition is imposed by the substrate impurity concentration and is characterised by the MOS threshold voltage. If the metal is biased with a positive voltage then an enhanced electron concentration is produced within the *n*-type semiconductor region. This is called the accumulation case. In this situation the capacitance stays relatively constant with increasing voltage. For a *p*-type substrate inversion will occur on application of a positive bias to the metal, while accumulation will occur for a negative bias.

The existence of a MOS structure on the surface of these detectors could occur under two different scenarios. It could either be associated with an excessive interfacial layer between the p^+ region and the Al metallisation, or due to with some overlap of the Al metallisation with the SiO_2 layer used to passivate the surface of the detector. The first scenario can be eliminated immediately. The inversion layer formed on application of a negative potential and is thus associated with an *n*-type semiconductor substrate. For the second scenario the small bonding pad was considered the most likely location of the MOS structure.

It was important to correctly determine the contribution of the MOS capacitance as it will have a non negligible affect on the slope of the detector C^{-2} versus V_R curve and hence the measured effective impurity concentration.

The equation which describes the MOS capacitance is:

$$C = \frac{C_o}{\sqrt{1 + \frac{2e_o^2 e_{ox}^2 V}{qN_{eff} e_o e_{si} d^2}}} \qquad (3.4)$$

where: C_o = the oxide capacitance, given by $e_{ox} \cdot d^{-1}$,

d = the oxide thickness,

e_{ox} = the dielectric constant of the oxide.

The area of the bonding pad was measured to be 4.32×10^{-4} cm^2. The dielectric constant of silicon dioxide is 3.9. The capacitance taken from Figure 3.6 at a voltage of 0 V and corrected for the detector area is 4.14 pF. Using Equation 3.4 the thickness of the oxide is 0.36 μm.

The MOS capacitance in the strong inversion region is given by:

$$C_{\min} = \frac{e_o e_{ox}}{d + \left(\frac{e_{ox}}{e_s}\right) w_M} \qquad (3.5)$$

where: w_m = the maximum depletion layer width of the MOS device.

The magnitude of w_m is dependent upon the impurity concentration of the semiconductor bulk. For high resistivity silicon $w_m \sim 10$ μm [20]. The minimum capacitance, C_{min}, is 940 pF·cm^{-2}. This gives a total capacitance contribution of 0.40 pF when the area of the bonding pad is considered (4.3×10^{-4} cm^2). For these particular detectors a capacitance of 0.40 pF corresponds to approximately 15 % of the detector capacitance in the fully depleted condition. For the

accurate determination of the detector bulk effective impurity concentration it is important that this parasitic capacitance be subtracted from the measured detector capacitance.

3.3.1.4 Peripheral Capacitance Correction Factor for Square p-n Junctions

For an accurate determination of N_{eff} from *C-V* data it is also necessary to correct for the peripheral capacitance. Under the depletion approximation it is assumed that when a p^+-*n* junction is reverse biased, the depletion region extends into the *n*-type bulk with a cross section equal to that of the junction area i.e. on the basis of plane parallel geometry. Lateral expansion of the depletion region around the peripheral of the junction is ignored.

In devices where the junction area is large in comparison to the depletion depth, which is the case for devices based on low resistivity silicon, this effect can largely be ignored. For high resistivity substrates, such as in the detector structures studied here, the effect is significant and requires correction.

Goodman [182] approximated the capacitance due to the lateral expansion effect in circular junctions as:

$$C_p = \frac{\varepsilon_o \varepsilon_{si} pp}{2} \qquad (3.6)$$

where: p = perimeter of the contact.

An improved approximation was provided by Copeland [183]. The peripheral capacitance was represented by:

$$C_p = \varepsilon_o \varepsilon_{si} \pi r b \qquad (3.7)$$

where: r = the radius of the circular contact,

b = a constant.

b was found to be equal to 1.5. By comparison, the equivalent value of b for the Goodman model is π.

The Copeland correction was applied to the measured C-V data. Figure 3.7 shows the uncorrected data along with the corrected data in a C^{-2} versus V plot. Significant improvement to the linearity can be observed. Comparison of the corrected data to a straight line revealed that linearity was still not observed. It appears that an additional component of capacitance must be subtracted.

The validity of using the Copeland peripheral capacitance correction was questioned. It was initially derived for circular junction areas and does not give account for square junction areas. It was hypothesised that the additional capacitance is associated with the lateral expansion of the depletion region from the corners of the square junction. The Copeland correction was not formulated to account for this contribution.

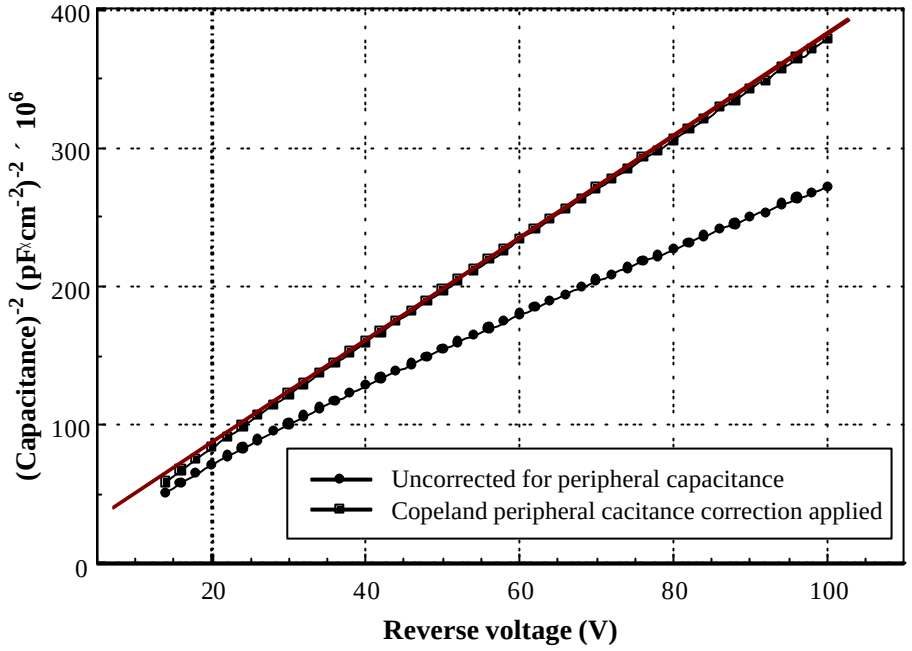

Figure 3.7: C^{-2} versus V_R for data uncorrected for peripheral capacitance and data corrected for peripheral capacitance using the Copeland expression.

A direct experimental observation of the lateral expansion of the depletion region about the corner of the junction was done using the technique of Ion Beam Induced Charge Collection (IBICC). In this technique a narrow beam of heavy ions is made incident on the surface of the detector structure. The beam is then scanned across the device with sub micron accuracy. The *e-h* pairs generated within the silicon as a result of the ion's energy loss are collected under the action of the applied electric field. A charge sensitive preamplifier and pulse height processing system allows the detector charge collection characteristics to be studied. The additional data regarding the spatial incidence of the ion beam allows a map of the relative charge collection efficiency across the scanned region to be constructed.

For this experiment the IBICC technique was used to profile the electric field around the edge and corner of a detector in order to directly observe the lateral expansion effect. The IBICC measurements were performed using the Nuclear Microprobe system of the Microanalytical Research Centre within the School of Physics at the University of Melbourne. This facility has been able to achieve a beam spot size of 0.05 μm for 2.4 MeV He^+ ions [184].

The U4 and U5 devices were not used. It was considered that the heavy ion beam could cause radiation damage to the detector bulk and jeopardise the integrity of the detectors for the subsequent radiation hardness study. An alternative detector with a square junction was obtained. A schematic of the detector used is shown in Figure 3.8. The detector had standard p^+nn^+ structure with an implant area of 5×5 mm^2. The junction was surrounded by a guard ring structure. The guard ring and detector junction edge were separated by a distance of 100 μm. A layer of SiO_2 had been grown over the interlaying region.

The IBICC measurements were performed using 2.8 MeV He^+ ions at approximately 1500 ions per second. Typical spot size was 0.1 μm. The LET for this ion in silicon is approximately 1 MeV·cm^2·mg^{-1}. Penetration depth is about 10 μm. Two types of scans were performed. In the first a line scan was made from a point outside the detector substrate to a point approximately 0.3 mm inside the detector window region. The step between each measurement was 0.5 μm. Scans were done with the detector reverse biased at voltages of 0, -2, -5, -10, -50, -100 and -120 V. The full depletion voltage for this detector was -170 V. Soft breakdown at a reverse voltage of approximately -140 V prevented measurements at full depletion. In the second scan a square region of area 1000 μm × 1000 μm located about a detector corner region was made. In this case the detector was biased with a reverse voltage of -120 V. For both measurements the guard ring was left floating. The results of the line scan are shown in Figure 3.9.

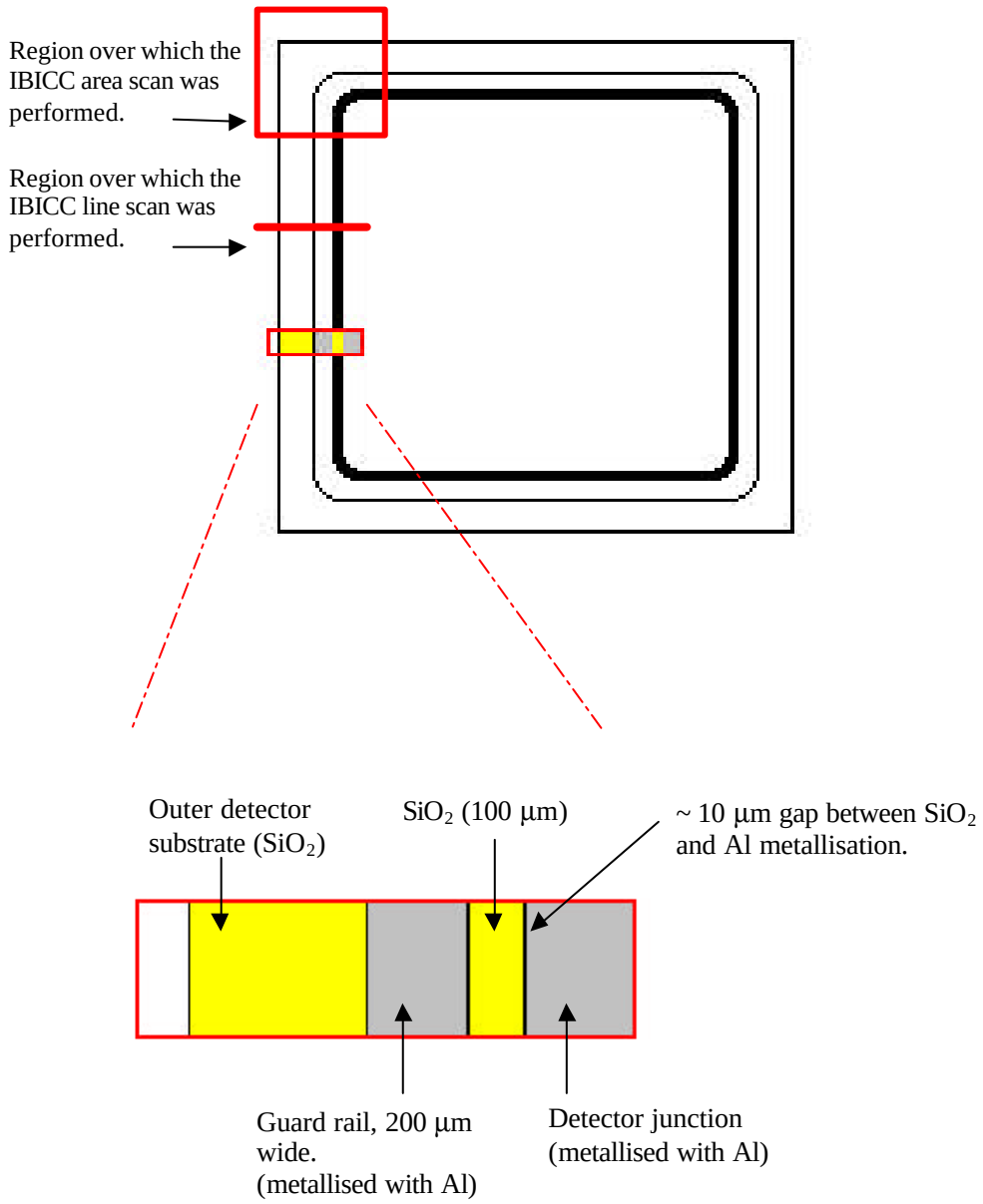

Figure 3.8: Layout of the detector used in the IBICC measurements. Note the narrow gap (~ 10 µm) between the detector Al metallisation and SiO_2 layer. The regions over which the IBICC area scan and line scan were performed are shown.

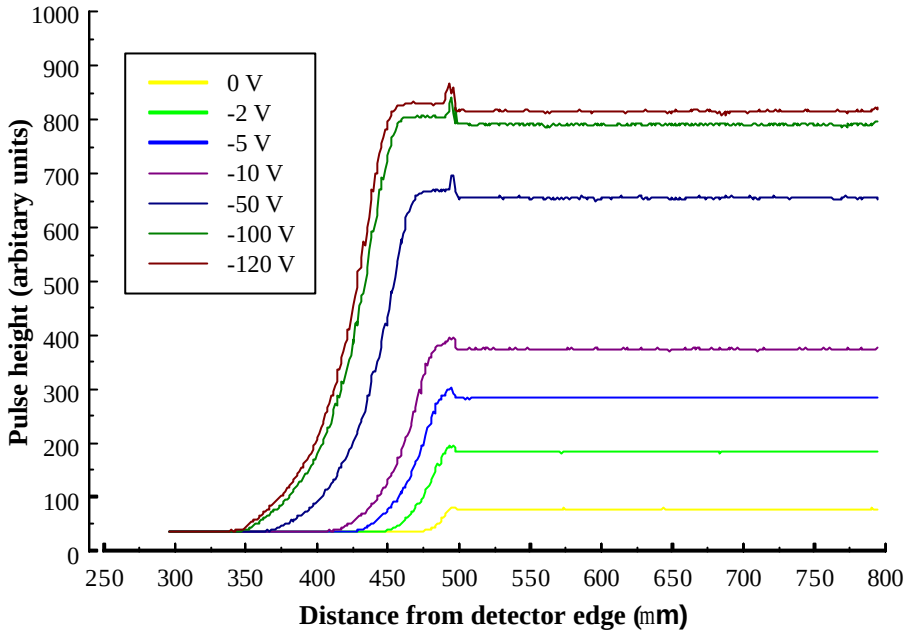

Figure 3.9: Horizontal line scans performed using 2.8 MeV He^+ ions.

For the region greater than 500 μm a plateau in the pulse height can be seen at all voltages. As the voltage is increased the plateau height increases. This corresponds to the expansion of the depletion region into the substrate bulk and the corresponding increase of carrier drift through the device. A net movement of charge through the device induces charge to flow in the external circuit. The pulse height of the signal produced will be proportional to the distance through which the charge carriers move in the device. i.e. charge collection efficiency increases towards 100% as the applied voltage approaches that required for full depletion. To the left of the plateau region a small peak can be seen at all voltages. The width of the peak is approximately 10 μm. In terms of the detector structure this region corresponds to the gap

between the detector window Al metallisation and the region of SiO_2. The lack of an interfacial layer in this region permits all of the He^+ ion energy to be deposited within the silicon bulk. Therefore more charge is available for collection and a higher pulse height is observed. This result is also the first indication of the effect of lateral expansion of the depletion region beyond the edge of the detector window (the edge of which is bounded by the Al metallisation). To the right of this peak, and at low voltages, the pulse height degrades as the beam approaches the edge of the device substrate. This result is almost certainly the effect of charge diffusion from the region of zero electric field into the depletion region where the electrical field exists and is able to act on the charge and produce the observed signal. At higher voltages, for example at -120 V, in the region to the right of the narrow peak exists a second plateau of approximate width 40 μm. This region corresponds to the area over which the SiO_2 layer has been deposited. The excellent charge collection in this region, as demonstrated by the large signal pulse height, indicates that the transport process in this region must be one of drift under the influence of an electric field. Extension of the electric field into this region can only be explained as a result of lateral expansion. The slightly higher pulse height in this region as opposed to the pulse height for beams incident on the detector junction region indicates that less energy is lost in the SiO_2 layer than within the Al metallisation and inactive p^+ region. The effect of lateral expansion can be seen to increase with increasing bias.

The results of the area scan are shown in Figure 3.10. The relative charge collection efficiency as a function of position can be compared to the line scan result. The narrow band of highest pulse height, shown in grey, is located around the perimeter of the detector window. This corresponds to the 10 μm wide peak seen in the line scan measurements. The lateral expansion of the depletion region about the corner of the detector can also be seen. The additional capacitance due to this region must therefore be acknowledged in the calculation of the correct peripheral capacitance correction for square junction areas. The literature does not advise on the exact form of such a correction.

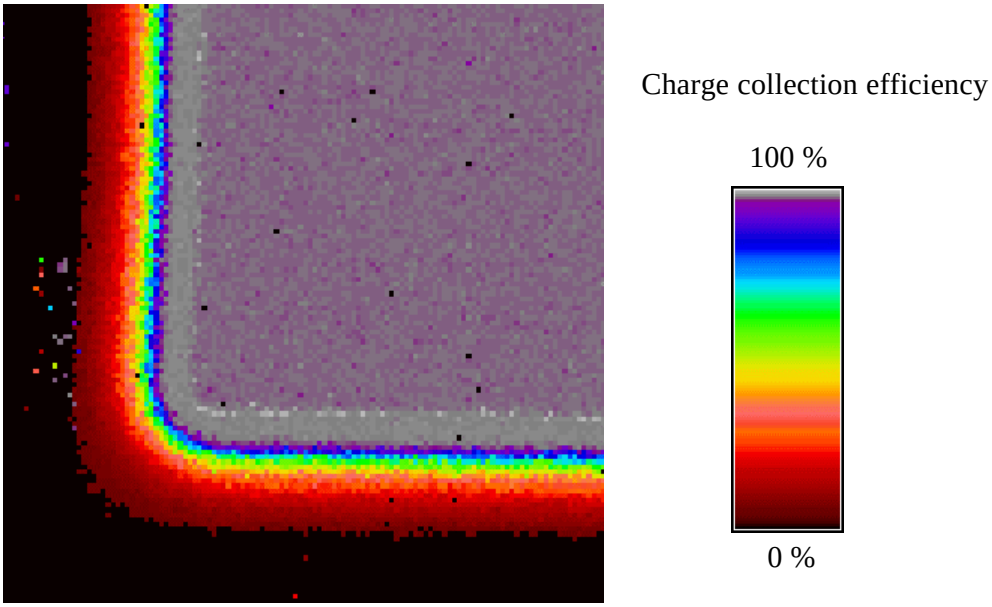

Figure 3.10: IBICC area scan (1000 × 1000 μm) centred over a corner region of the detector using 2.8 MeV He^{+} ions.

To account for this effect the following procedure was undertaken. It was assumed in a first approximation that the magnitude of the peripheral capacitance for the square contact was proportional to the perimeter of the contact:

$$C_p = e_o e_{Si} pk \qquad (3.8)$$

The proportionality factor, *k*, was introduced.

The magnitude of *k* was found by numerical solution. *C-V* data was taken from a series of detectors with square geometry and areas of 1 cm^2, 0.25 cm^2 and 0.09 cm^2. Three detectors of each size were used. A correction for the MOS capacitor effect was only required for the detectors with area 0.09 cm^2. The other detectors did not have a bonding pad. The size of the peripheral capacitance was found by applying a small correction, C_p, to the measured capacitance, C_m, of the form:

$$C = C_m - C_p \qquad (3.9)$$

where: C_p = is the small capacitance correction associated with the peripheral capacitance .

Since a linear relationship should exist between C^{-2} and V_R, the first derivative of C^{-2} with respect to V_R should be equal to a constant. To determine the size of C_p the first derivative of C^{-2} with respect to V_R was plotted as a function of V_R. The value of C_p was then optimised to give a slope to this curve of 0. This corresponds to a constant value for the first derivative as a function of V_R. An alternate means of determining C_p was to determine the 2nd derivative of C^{-2} with respect to V_R and optimising C_p so that the 2nd derivative was equal to zero.

Both methods were employed yielding the same results for each detector. The results are summarised in Table 3.1. The optimal peripheral capacitance was then used to determine *k* from Equation 3.8. The equivalent value of *b* from the Copeland equation was also determined.

The average value of *k* was found to be 0.876. The equivalent value of *b* was 1.98. The result was consistent for the detectors with perimeters from 12 mm to 40 mm. By comparison, the value of *b* for the circular geometry junction was 1.50 [183]. For all future *C-V* measurements this new peripheral capacitance correction formula was applied.

Table 3.1: Peripheral capacitance correction results.

Detector Area (cm^2)	Peripheral capacitance (pF)	*k*	*b*
1.00	3.72	0.883	1.99
1.00	3.72	0.883	1.99
1.00	3.71	0.880	1.99
0.25	1.85	0.878	1.98
0.25	1.87	0.887	2.00
0.25	1.83	0.868	1.96
0.09	1.10	0.870	1.96
0.09	1.11	0.878	1.98
0.09	1.09	0.862	1.95

3.3.2 Current Voltage Measurements (*I-V*)

Current-Voltage measurements (*I-V*) can provide useful information regarding properties of the junction as well as the material bulk.

3.3.2.1 The Principle of the *I-V* Measurement

The theoretical current of a *p-n* junction is given by the ideal diode equation written as (from Ref. [20]):

$$J = J_p(x_n) + J_n(-x_p) = J_s\left[\exp\left(\frac{qV}{kT}\right) - 1\right] \qquad (3.10)$$

where: T = temperature,

k = Boltzmann constant,

J_n, J_p = current density due to electrons and holes within the *p* and *n* regions of the junction respectively,

x_n, x_p = distance measured from the junction centre into the *n*-type region and *p*-type region respectively.

And J_s is given by:

$$J_s = \frac{qD_p p_{no}}{L_p} + \frac{qD_n n_{po}}{L_n} \qquad (3.11)$$

where: $D_{n,p}$ = diffusion constant of electrons and holes,

p_{no} = equilibrium concentration of holes in the *n*-side of the junction,

n_{po} = equilibrium concentration of electrons in the *p*-side of the junction,

$L_{p,n}$ = diffusion length of electrons and holes in the region in which they are minority carriers.

For reverse voltages greater than ~ $3kT \cdot q^{-1}$ (= 0.078 V @ 300K), the current density approaches a constant value given by J_s, which is equal to the sum of the diffusion currents only.

Equation 3.10 is derived under the condition of low level injection so that the minority carrier densities are small compared to the majority carrier densities. Under forward bias this will no longer be the case as the concentration of minority carrier densities significantly exceeds the equilibrium values. The phenomena of recombination current must be considered. The current density associated with recombination effects is given by (from Ref. [20]):

$$J_{rec} \cong \frac{qw}{2} s_o n_{th} N_t n_i e^{qV/2kT} \qquad (3.12)$$

where: N_t = concentration of recombination centres,

V_{th} = thermal velocity of carriers,

s_o = capture cross section.

For conditions where $p_{no} >> n_{po}$ and $V \geq 3kTq^{-1}$ the total forward current is given by:

$$J_F = q\sqrt{\frac{D_p}{t_p}}\frac{n_i}{N_D}e^{qV/kT} + \frac{qwn_i}{2t_r}e^{qV/2kT} \qquad (3.13)$$

where: t_r = the effective recombination lifetime given by $(s_o n_{th} N_t)^{-1}$.

The forward current can be represented empirically by:

$$J_F \sim \exp\left(\frac{qV}{hkT}\right) \qquad (3.14)$$

The factor h is the ideality factor. In the absence of recombination current h equals 1.

3.3.2.2 *I-V* Measurement of the Detector Test Structures

The reverse *I-V* characteristics of the U4 and U5 detectors were measured using an analog Keithley 602 solid state electrometer. The detector was placed in series with two 1 MΩ resistors. A reverse voltage was applied using a Fluke 415B High Voltage Power Supply.

J_s can be estimated from Equation 3.11 by substituting $L_{n,p}=(D_{n,p}\cdot t_{n,p})^{-1}$ and using the typical values of $p_{no} = 5.3\times10^{7}$ cm^{-3}, $n_{po} = 100$ cm^{-3}, $D_p = 11.7$ cm$^2\cdot$s^{-1}, $D_n = 37.5$ cm$^2\cdot$s^{-1}, $t_p = 10^{-3}$ s, $t_n = 10^{-6}$, $N_A = 1\times10^{19}$ cm^{-3} and $N_D = 4\times10^{12}$ cm^{-3} to give a total diffusion current of 9×10^{-10} A$\cdot$cm^{-2}. For the detector area of 0.09 cm^2 this current density corresponds to a current of 8.1×10^{-11} A. The actual measured reverse current for the U4 detectors is shown in Figure 3.11. The reverse current observed experimentally is approximately three orders of magnitude greater than the calculated value.

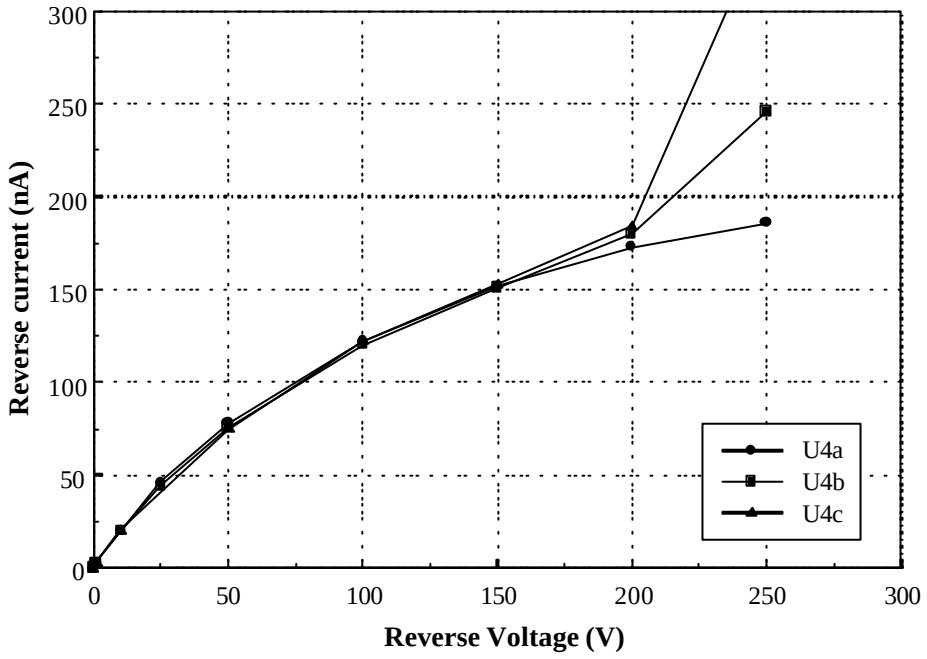

Figure 3.11: Reverse current versus reverse voltage for detectors U4a, b and c.

The ideal diode equation does not account for minority carrier effects. These include carrier recombination (as discussed previously), and carrier generation. Under reverse bias the concentration of carriers within the depletion region is very low and the carriers produced are immediately swept out by the electric field. Under these conditions recombination can be

considered to be negligible. The additional current is most likely associated with the generation of carriers within the large volume of the depletion region. This can be a result of intrinsic effects but is greatly enhanced by the presence of deep level defects located at mid band positions. The current density due to generation within the depletion region is usually parameterised by:

$$J_G = \frac{q n_i x_d}{t_g} \qquad (3.15)$$

where: t_g = the generation lifetime.

The density of electrons within the p^+ region, p_{no}, is very small in comparison to the density of holes within the *n-type* region notated by n_{po}. The first term of Equation 3.11 can thus be neglected. The total reverse current density is now given by:

$$J_R \cong q\sqrt{\frac{D_p}{t_p}}\frac{n_i^2}{N_D} + \frac{q n_i x_d}{t_g} \qquad (3.16)$$

As the depletion region increases the first term becomes insignificant. The second term associated with generation current will increase in proportion to the depletion region depth x_d. The depletion depth is in turn proportional to the square root of the reverse voltage. The increase of the reverse current of detector U4b was plotted as a function of the $V_R^{1/2}$. The graph is shown in Figure 3.12. Proportionality was observed in all detectors confirming that the source of the additional current is associated with carrier generation within the depletion region.

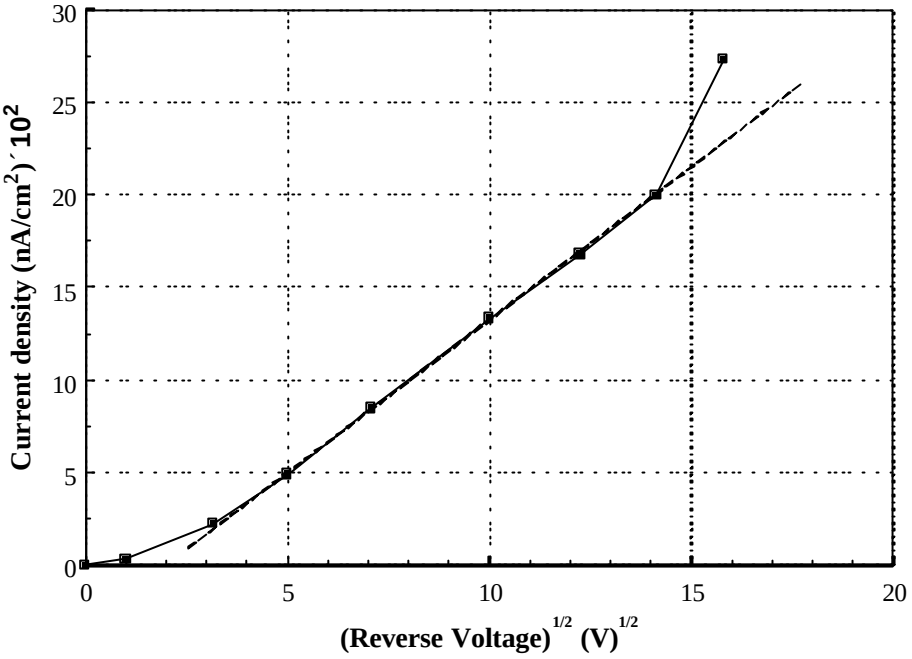

Figure 3.12: Reverse current density as a function of the square root of the reverse voltage for detector U4b.

Equation 3.15 is derived under the condition that the value of the generation lifetime is the same within all regions of the depletion region. The average slope in the curve of Figure 3.12 was measured giving a value 9.07×10^{-5} A·cm^{-3}. The generation lifetime, t_g, was calculated to be 2.6×10^{-5} s. Alternatively, this can be written as the generation rate which is equal to the inverse of the generation lifetime, and is equal to 3.8×10^{4} s^{-1}. This is considerably higher than expected based on the thermal generation rate of intrinsic carriers indicating the presence of deep level defects within the forbidden gap.

Measurement of the forward current was done using a Keithley 237 Voltage Current Source measurement unit. The voltage range investigated was 0 V to 0.6 V for all detectors apart from detector U4b in which case the maximum voltage was extended to 0.95 V. The

forward current versus voltage curves are shown in Figure 3.13 for the detectors of substrates U4. Identical curves were obtained for the detectors of substrate U5.

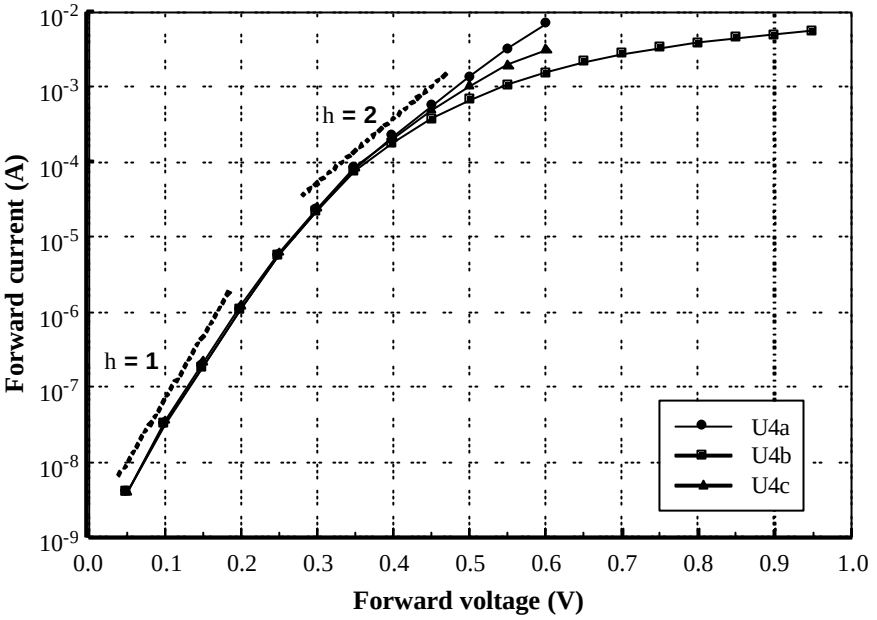

Figure 3.13: Forward current measured as a function of forward voltage for detectors U4a, b and c.

Shown in Figure 3.13 are two lines drawn with the slope associated with an h value of 1 and 2. It can be seen at low forward voltages (0 V to 0.3 V), which corresponds to low level injection, that the data fits quite well to a line of slope $h = 1$. This indicates that the current density is dominated by diffusion current. At low current levels usually recombination current will dominate. The lack of recombination dominated current indicates the low concentration of defect centres. This is a good indicator of a high quality junction.

At higher forward voltages (around 0.3 to 0.5 V) the data begins to deviate from this trend approaching a case of $h = 2$. This would seem to indicate that recombination current is

beginning to dominate. This is however unlikely since diffusion current would normally dominate in this region. Another possible explanation is that of a series resistance effect. If a considerable series resistance is present a voltage drop across this region will occur. For these detectors such a resistance can be expected as a result of the high resistivity of the undepleted detector bulk. The resistance is given by $R = \rho w A^{-1}$ which is equal to 1100 Ω·cm × 0.0360 cm / 0.09 cm^2 = 440 Ω. The voltage drop for a forward current of 1×10^{-3} A is 0.44 V. It should be expected that this is the major source of the observed deviation and $\eta > 1$.

3.3.3 Deep Level Transient Spectroscopy (DLTS)

It was important to identify and characterise defects present in the detector test structure substrate prior to the planned neutron irradiation in order to avoid any confusion with the inevitable radiation induced defects. Defects may be present in the unirradiated material as a result of the inclusion of foreign atomic impurities during the silicon crystal growth stage, or introduced later in the subsequent detector fabrication.

Deep level defects in semiconductor materials and devices can be detected and characterised using Deep Level Transient Spectroscopy (DLTS).

3.3.3.1 The Principle of the DLTS Technique

DLTS was introduced by Lang in 1974 [185]. The principle of the technique depends on two phenomena. Firstly, the variation of the capacitance of a *p-n* junction[3] due to the changing space charge density within the depletion region and secondly, the capture and emission of charge carriers by deep level defects. In a DLTS measurement a depleted region of a *p-n* junction is briefly collapsed by reducing the reverse bias. Any deep level defects present are then able to capture the introduced free carriers and become filled. The reverse bias is then

[3] The DLTS technique can also be used on semiconductor materials with other diode structures such as Schottky junctions.

reapplied and the remaining free carriers removed from the depletion region. Then, in a thermally stimulated process, the carriers trapped at the site of a defect are re-emitted and sweep out of the depletion region under the action of the electric field. This results in a transitory change in the space charge density which is observed as a change in the junction capacitance.

Under certain conditions this capacitance transient will be exponential with time. The rate is dependent upon the activation energy of the defect state. As each defect possesses a unique activation energy the emission rate of each defect will be different. The rate is also dependent upon the sample temperature. At lower temperatures the thermal emission rate of any particular defect will be less than the rate for the same defect at higher temperatures. This is due to the increased availability of thermal energy within the lattice at higher temperature. The transient capacitance signal is processed in such a way that a selected emission rate will produce a maximum signal output. By scanning the sample temperature the emission rate of a particular defect will pass through the selected rate window. A plot of this signal as a function of the sample temperature generates a spectrum of defects present within the sample.

This rate window can be constructed by various means. One such method is the "Correlation Method" [186]. Here an exponential waveform is produced, the decay rate of which may be externally selected. This waveform and the test sample capacitance transient are multiplied together and the resulting signal integrated to give a d.c. voltage output. The output signal is a maximum when the two decay rates are equal. The correlation method provides a high sensitivity. Other methods used for rate window construction include Boxcar integration and the lock in amplifier technique.

A more thorough explanation of DLTS can be found in either of the two Refs. [185,187].

3.3.3.2 DLTS Measurement of the Detector Test Structures

A DLTS measurement was performed on only one detector on each substrate. It was assumed that each detector, having experienced the same processing steps in addition to being produced from the same initial silicon, would contain the same defects.

The experimental conditions were as follows; A reverse bias of 16 V was applied which corresponded to a depletion depth of ~ 75 μm. A repetitive pulse of amplitude 15.5 V was used to collapse the depletion depth to a distance of ~ 13 μm. The width of the pulse was 500 μs which was sufficiently wide to fill any conceivable trap with carriers. The measurement was performed over a temperature range of 320 K to 20 K. Correlator rate windows of 5.24, 10.20 and 24.95 ms were used.

The DLTS spectra obtained revealed the presence of two small amplitude peaks centred at temperature's of 165 K and 270 K. These peaks were labelled peak A (165 K) and peak B (270 K). The peak temperature and weighting function time constant parameters are tabulated in Table 3.2.

Table 3.2: DLTS peak parameters for detector U4c.

Time constant, τ_c (msec)	Peak A : Temperature (K) error: ± 0.5 K	Peak B : Temperature (K) error: ± 0.5 K
3.30	173.0	284.0
10.20	165.0	270.0
24.95	157.5	262.5

An arrhenius plot of this data is shown in Figure 3.14. The slope was measured and the defect energy calculated. The trap capture cross section was also calculated from the *y*-axis intercept. The results are tabulated in Table 3.3.

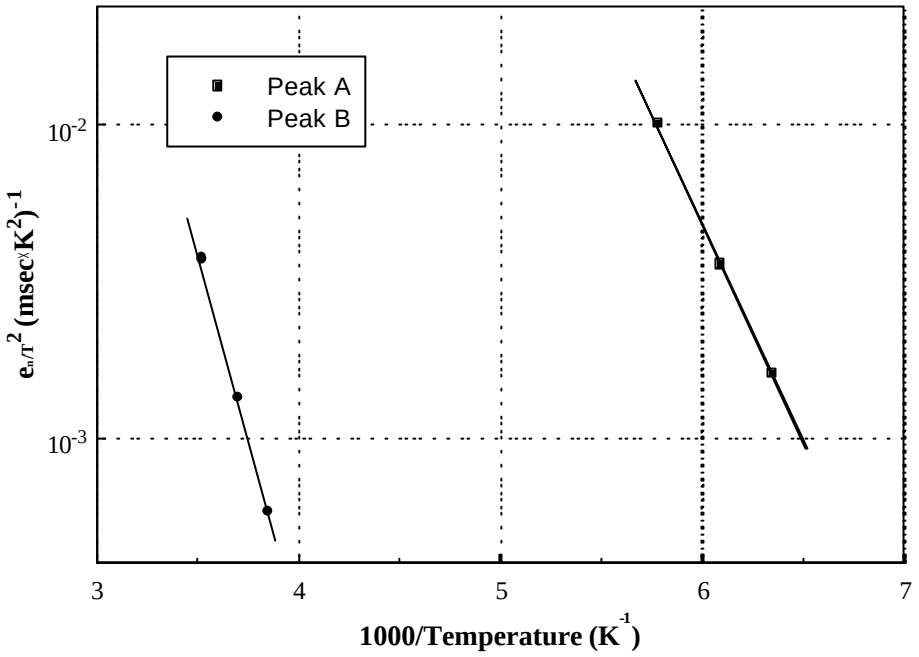

Figure 3.14: An Arrhenius plot for Peak A and Peak B of detector U4c.

Table 3.3: Trap parameters for detector U4c.

Peak	Defect energy, E_t (measured from the conduction band edge) (eV)	Trap capture cross section, σ (cm^2)
A	0.28 ± 0.02	5.1×10^{-18}
B	0.54 ± 0.04	1.0×10^{-16}

The parameters of the defect associated with Peak A do not correspond to any listed in the silicon defect catalogues [188,189]. The defect has similar parameters to a defect reported by Schulz, [190] in high resistivity silicon based devices with significant oxide formations. (It was not observed by Schulz in the spectra of non-passivated samples). The parameters reported were $E_t = E_c$ - 0.26 eV and $s = 1.5\times10^{-17}$ cm^2. This defect has also been observed by Verbitskaya et al. [191]. The parameters reported by Verbitskaya were, $E_t = E_c$ - 0.27 eV and $s = 1\times10^{-17}$ cm^2. The defect was found to occur only after heat treatment at temperatures above 1000°C used during the oxidation process.

The parameters of the defect associated with Peak B are similar to those of a defect also observed by Schulz [190]. The parameters reported were $E_t = E_c$ - 0.53 eV and $s = 3.5\times10^{-15}$ cm^2. The defect was observed in samples containing a gold electrode. The data for an acceptor level due to the presence of Au is $E_t = E_c$ - 0.54 eV and $s = 2.18\times10^{-15}$ cm^2 [192]. The diffusion of gold into the bulk requires temperatures of up to 600 to 700°C [193]. These temperatures could be reached during various device fabrication processes.

The signal strength of both of these peaks was weak and a reliable measurement of the defect concentrations could not be obtained. The small signal strength is an indicator of a low concentration. The presence of the defects in test structures is noted but not considered to be of any real significance.

3.3.4 Alpha Particle Spectrometry

Alpha particle spectrometry was used to determine the energy resolution of the detectors and to provide a baseline for observing any degradation of the charge collection efficiency post neutron irradiation.

For these measurements the devices were mounted within a specially designed cryostat. A spectroscopic grade Am-241 source with a thin exit window for alpha particles was placed at a distance of 1.5 cm above the detector junction under study. The depth of penetration of 5.5 MeV

alpha particles in silicon is approximately 20 μm. Reverse biased detectors were coupled to a Canberra Model 2003 charge sensitive pre amplifier via a 0.01 μF capacitor. The main amplifier was a Canberra spectroscopy amplifier Model 413. Guassian pulse shaping was used with a time constant of 1 μs. The output pulse was analysed by a Nucleus MCA computer card. Measurement was performed under vacuum conditions (~ 10^{-5} Pa) and at room temperature (24 - 26 °C).

The MCA spectra showed the presence of the main Am-241 alpha peak at an energy of 5.486 MeV. The FWHM of this peak was not worse than 32.3 keV. The best detector had a FWHM of 24.1 keV. The less intense 5.443 MeV alpha particle was also just resolved in all detectors. The relative intensity of these two peaks of 85 % for the 5.486 MeV peak and 15 % for the 5.443 MeV peak correlated with the known emission ratio of theses two alpha particles in the decay of Am-241.

3.4 Neutron Irradiation

3.4.1 Description of the Neutron Irradiation Facility

Neutron irradiations were performed at a monoenergetic fast neutron facility located at the Lucas Heights Research Laboratories of ANSTO in Sydney, Australia.

The facility consists of a positive ion accelerator, a series of beam lines and a number of experimental stations. One of these stations was equipped with a neutron production target. The accelerator is a 3 MV horizontal Van de Graaff (type KN-3000) which is capable of accelerating singly charged positive ions up to energies of 3 MeV. The machine is installed in a heavily shielded cell adjacent to the experimental area. Control is facilitated from a dedicated room also adjacent to the experimental area. The accelerated ion beams leave the accelerator and through a series of analysers and switching magnets can be deflected into the appropriate beam line to terminate at the required experimental target. The experimental area in which the target is located is bounded by heavily shielding concrete blocks which rise to a height of 6 m as

measured from the floor. Access to this area during beam on periods is not possible due to an interlocking mechanism between the entry gates and the beam control.

The target used for this work was a thin lithium metal target. The neutrons are produced by bombarding the target with energetic protons according to the reaction:

$$p + Li^7 \rightarrow Be^7 + n \qquad (3.17)$$

The reaction has a Q value of -1.646 MeV. The corresponding threshold is 1.8811 MeV (for protons measured in the laboratory frame of reference [194]). For protons of energy 2.7 MeV, neutrons with energies of 0.995 MeV are produced in the forward direction. At other angles the neutron energy is less as a result of the anisotropy of the reaction. The neutron yield is also anisotropic. A second reaction channel with a threshold of 2.378 MeV also exists and is associated with the $Li^7(p,n)Be^{7*}$ reaction. The contribution of this second reaction to the total neutron yield is in most cases negligible.

The lithium targets are produced regularly for each major experiment. The preparation involves the evaporation of a thin film of high purity lithium metal onto the inner surface of a copper flange. This is done in a conventional tungsten filament low vacuum metal evaporator. The target is then transferred and attached to a dedicated accelerator beam line under a continuously purged atmosphere of argon. This is to prevent oxidation of the lithium metal. Target thickness can be estimated from the quantity of lithium metal evaporated and the solid angle that the copper flange presents to the filament. A more accurate measurement of target thickness can be made when the target is in use on the beam line. This involves the measurement of the neutron yield as a function of proton energy. In the laboratory frame of reference the neutron yield in the forward direction is sharply peaked about the reaction threshold. By measuring the neutron yield from the reaction threshold and up until the proton energy at which the neutron yield first starts to decrease, the target thickness can be obtained in terms of the proton energy lost in the target. For targets produced here typical thicknesses of

100 - 250 keV could be obtained in one evaporation step. Thicker targets can be produced by multiple evaporation steps.

In the neutron irradiations undertaken in this work proton energies of between 2.6 and 2.7 MeV with typical beam currents of 24.0 μA were used. Due to this relatively high target current cooling was required in order to reduce the loss of target caused by excessive heating. This involved the application of a fine water spray directed towards the target in addition to continuous rotation of the target cap to reduce any localised heating.

The closest scattering surface from the point of neutron production is the floor at a distance of 1.4 m. To reduce the flux of backscattered neutrons the floor has been covered with 12 cm thick paraffin blocks. The next closest scattering surface is more than 3 metres away from the neutron producing target.

The neutron flux could be monitored during irradiation using a calibrated neutron long counter which was placed several metres from the neutron source. Such a detector is characterised by an almost uniform detection efficiency for neutrons of energies about 1 MeV. The beam current on the target could also be measured using a Faraday cup and the accumulated charge determined using a current to frequency converter and a counter/timer unit. This allows measurement of the neutron flux as a function of target current and not as a function of time. This removes the effect of beam current fluctuation on measurement of the neutron yield.

3.4.2 Neutron Irradiation of the Detector Test Structures

A neutron energy of 1 MeV was desired requiring a proton energy of 2.7 MeV. Due to machine instability at 2.7 MV the voltage was reduced to a more stable operating voltage of 2.6 MV. The corresponding 2.6 MeV protons produce neutrons of energy 0.891 MeV in the forward direction [194]. The target thickness in terms of proton energy loss was measured to be 200 keV. This proton energy loss in the target results in a range of neutron energies from the maximum of 0.8898 MeV to a minimum of 0.679 MeV. The minimum neutron energy corresponds to the minimum proton energy of 2.4 MeV.

The neutron flux was monitored by the neutron long counter which was positioned at a distance of 3.038 m from the target in the zero degree beam line direction. The measured neutron fluence was estimated to be accurate to 20 %.

The detectors were mounted at a distance of 18.9 mm from the target. They were positioned orthogonally to the beam line axis in order to achieve a variation in neutron fluence across the two substrates. The irradiation was performed over a period of two days in two separate 10 hr sequences. A contour map of the neutron fluence across the two substrates is shown in Figure 3.15.

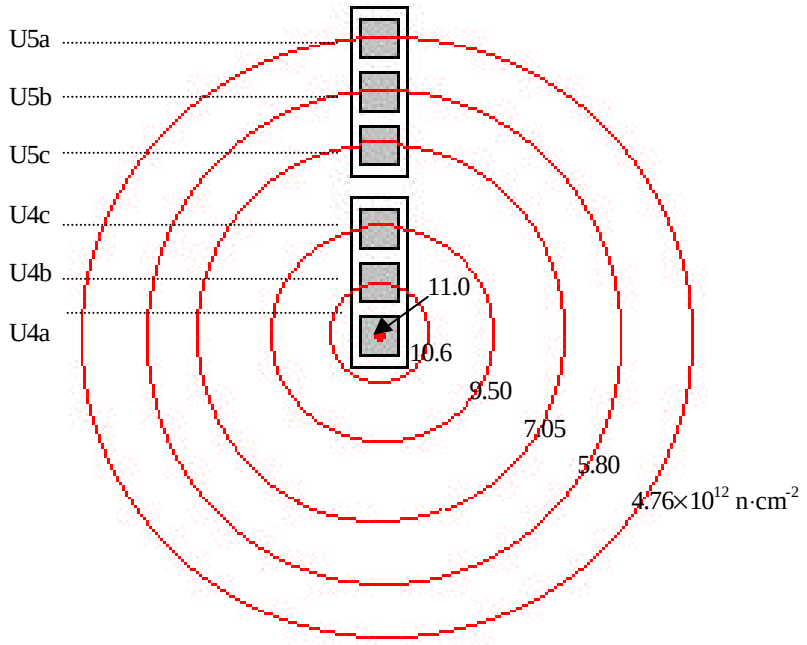

Figure 3.15: Neutron fluence contour map. Detector U4a was exposed to the highest neutron fluence.

3.5 Post Irradiation Measurements

Following irradiation the device package was checked for radioactivity which may have been induced through neutron activation. None was observed. Residual activity can occur in neutron irradiation of microelectronic devices where gold is used in the fabrication of electrical contacts.

The devices were removed from the irradiation facility and transported to the semiconductor laboratory for post irradiation characterisation.

3.5.1 Effective Impurity Concentration (from *C-V* Measurements)

The change to the effective impurity concentration was measured using the capacitance voltage technique. Measurement was performed over a voltage range of 0 V to - 100 V. A plot of the capacitance per unit area versus the reverse voltage is shown in Figure 3.16 for all detectors. The plotted data was not corrected for the MOS capacitor effect associated with the bonding pad which can be seen in the 0 - 15 V region.

It can be seen that the curve becomes ‘flattened’ for detectors irradiated with a higher neutron fluence. The curve shape no longer appears to follow the *C-V* relationship described by Equation 3.1. This is most likely the result of radiation induced deep level defects present in concentrations comparable to the shallow level impurity concentration.

To correctly understand this result the effect of deep level defects on the capacitance was considered from a theoretical point of view. This was done by considering the effect of a mid band acceptor state in the form of a radiation induced defect present within the high resitivity *n*-type bulk of a p^+-*n* junction device. In this analysis the acceptor impurity was assumed to have two charge states, -1 if occupied by an electron, and 0 if unoccupied. The band structure of the reverse biased junction is shown in Figure 3.17. No features are detailed in the p^+ region. In the *n*-type region the electrical states of shallow level donor impurities, with energy E_D and concentration N_D, are shown close to the conduction band edge. Similarly, the electrical states of

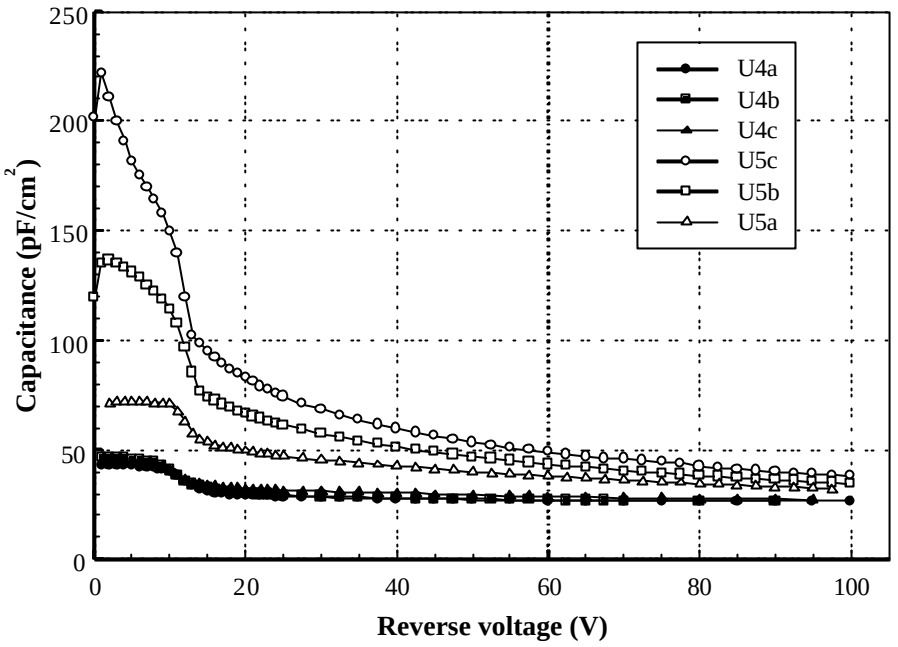

Figure 3.16: *C-V* curves for the detectors U4a, b and c and U5a, b and c following neutron irradiation.

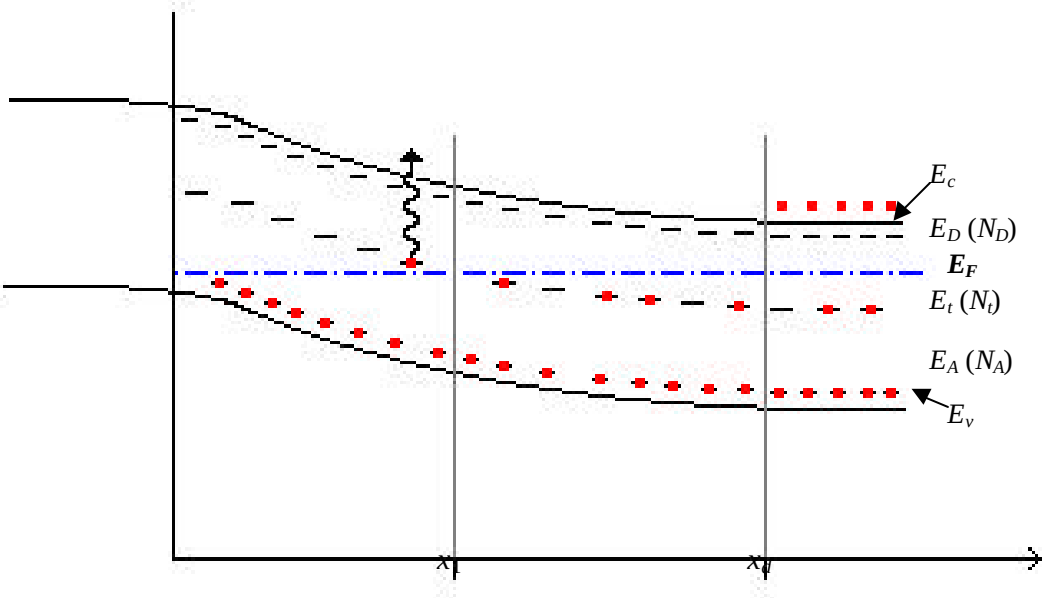

Figure 3.17: Energy band diagram of a p^+-n junction with a deep level defect at an energy E_t and concentration N_t. The ionised shallow donors, shown as a dash at energy E_D are positively charged.

shallow level acceptor impurities, with energy E_A and concentration N_A, are shown close to the valence band edge. A deep level defect is shown with energy E_t located at mid band positions through the material. To simplify the text, from here on this deep level defect will be referred to as a 'trap'. The concentration of the trap is N_t. The Fermi level (E_F) is shown. The depletion region edge, x_d, is shown at the point where the bands become flat.

To understand the measured capacitance in this model the space charge within the depletion region needs to be considered. For distances less than x_d the shallow level donor impurities are ionised and contribute a space charge density of $+qN_D$. In the same region, the shallow level acceptor impurities are occupied by an electron and contribute a charge density of $-qN_A$. The net charge density due to the shallow level impurities is therefore $qN_D - qN_A$. The contribution of the trap to the space charge in this region will depend on its charge state. Due to band bending the trap energy level will cross the Fermi level at some distance x_1. Assuming steady state conditions, traps located at distances less than x_1 will be unoccupied by an electron and will have a charge state of zero. These traps will make no contribution to the space charge density. Those traps located at distances greater than x_1 but less than x_d will be occupied by an electron and be in a charge state of -1. They will make a contribution of $-qN_t$ to the space charge density.

The total space charge density within the depletion region is summarised by:

$x < x_1$ Charge density = $q(N_D - N_A)$

$x_1 < x < x_d$ Charge density = $q(N_D - N_A - N_t)$

If the reverse voltage is increased by a small increment ΔV then further band bending will occur and the depletion region will extend by Δx_d. The space charge about the depletion region edge due to shallow level impurities will increase by $q(N_D - N_A)\Delta x_d$. A contribution from traps located about x_d will also contribute a charge of $qN_t\Delta x_d$ (a response from the trap is not required

as its charge state is not altered under this situation). The band bending will also cause the Fermi level to decrease about x_1. This will cause some filled traps to be raised above E_F. These traps will seek to emit the electron under thermal stimulation. The rate of emission will be e_n. Hence, after a long period compared to e_n^{-1}, there will be a decrease in the space charge of magnitude $qN_t\Delta x_1$ as the trap charge state changes from -1 to 0.

Now, if the reverse voltage is decreased by the initial increment ΔV, the space charge density due to the shallow level impurities will almost immediately resume the situation prior to the application of ΔV. The traps about x_1 will move below the Fermi level again. They will seek to trap an electron in order to become occupied. Under the conditions imposed by the depletion approximation no free electrons can exist within the depletion region. In a real situation however electrons are able to diffuse into the depletion region to a distance characterised by the debye length, L_D. These electrons are available to be captured by the trap at a rate equal to the capture rate, c_n. It can be shown that for $E_t \approx E_F$, as is the case about x_1 that $c_n \approx e_n$ [181]. So that the response of the trap to either an increase or decrease of the reverse voltage is dependent upon the emission rate of the trap and its value relative to the rate of change of ΔV. If the frequency of the capacitance meter test signal is ω_{test}, then when $e_n >> \omega_{test}$ the trap can respond to the signal and make a contribution to the change in space charge. If $e_n << \omega_{test}$ then the trap is not capable of responding to the signal and will not make a contribution to the changing space charge. Hence for situations where the concentration of traps is comparable or greater than the net concentration of shallow level impurities, the capacitance measurement will be frequency dependent. In the high frequency limit the trap cannot contribute to the measured capacitance.

While the contribution of these traps cannot be detected in a high frequency capacitance measurement it is important to realise that in the steady state they will still contribute space charge and as such will affect the net effective impurity concentration and hence the full depletion voltage of the detectors.

In the experimental results of Figure 3.16 it can be seen that the capacitance at low voltages decreases for detectors irradiated with a higher neutron fluence. At higher voltages the effect is

less evident as the capacitance of all detectors approaches a minimum capacitance. This minimum in capacitance is given by the geometrical capacitance:

$$C = \frac{e_o e_{Si} A}{w_d} \qquad (3.18)$$

where: w_d = the detector thickness.

For these detectors the geometrical capacitance can be calculated to be 28.7 pF·cm^{-2}. All experimental curves can be seen to be approaching this value.

The small change of C as a function of V gives a C^{-2} versus V curve with a substantially reduced slope. Calculation of the effective impurity concentration from the slope will give an erroneous result. N_{eff} can however still be obtained from a C versus V curve. For detector U4b the C-V curve is shown in Figure 3.18. The slope can be seen to change at a reverse voltage of approximately 60 V. The transition to an almost flat type region is indicative of the full depletion capacitance having been reached. Construction lines were extrapolated from both regions and the point of interception obtained. This occurred at a voltage of 60 V. Using Equation 3.1 the effective impurity concentration can be calculated from the full deletion voltage to give 5.9×10^{11} cm^{-3}.

Verification of this result can be obtained by an independent measurement of the full depletion voltage. This was done by measuring the charge collection characteristics of the detector to ionisation produced just within the non junction side of the detector. Collection of charge from this region can only occur when the depletion region extends throughout the detector volume. Alpha particles from ^{241}Am were used to deposit energy at the rear side of the detector. The detector holder was modified to include a small hole in the brass base to permit the alpha particles to reach the rear of the detector. The range of the Am-241 alpha particles in

silicon is only 20 μm. Type inversion of the detector bulk was not anticipated on account of the modest neutron fluence. The junction should still exist at the front of the detector. The response of the detector as a function of reverse voltage is shown in Figure 3.19. The full depletion voltage was estimated from the point of intersection between a line extrapolated from the undepleted region and a line extrapolated from the fully depleted region of the charge collection curve. A full depletion voltage of 68 V was determined. The corresponding value of N_{eff} is 6.7×10^{11} cm^{-3}. This is in good agreement with the value calculated from the *C-V* measurement.

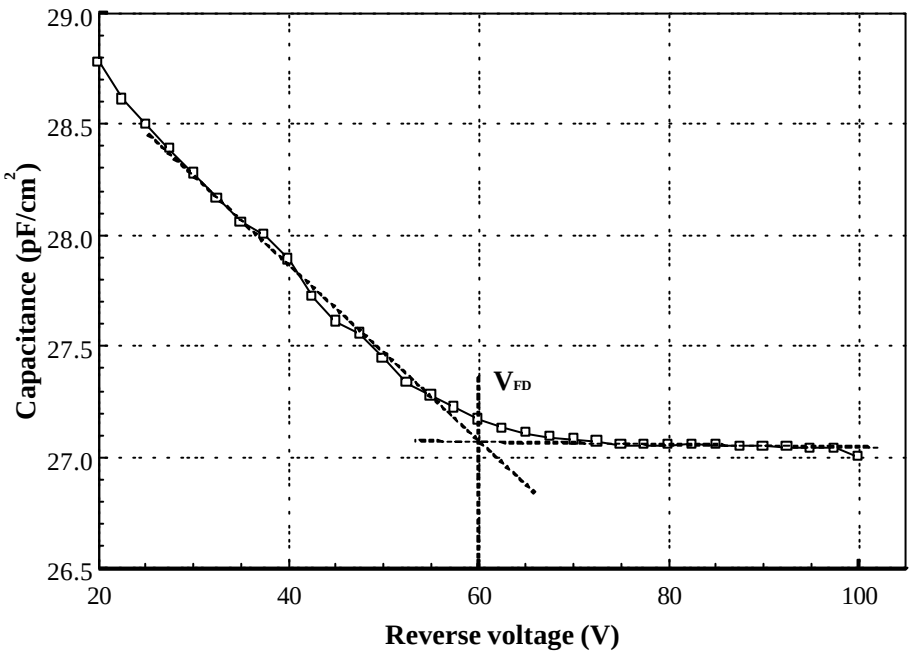

Figure 3.18: Full depletion depth (and hence the effective impurity concentration) can still be obtained from the *C-V* curve of a neutron irradiated detector.

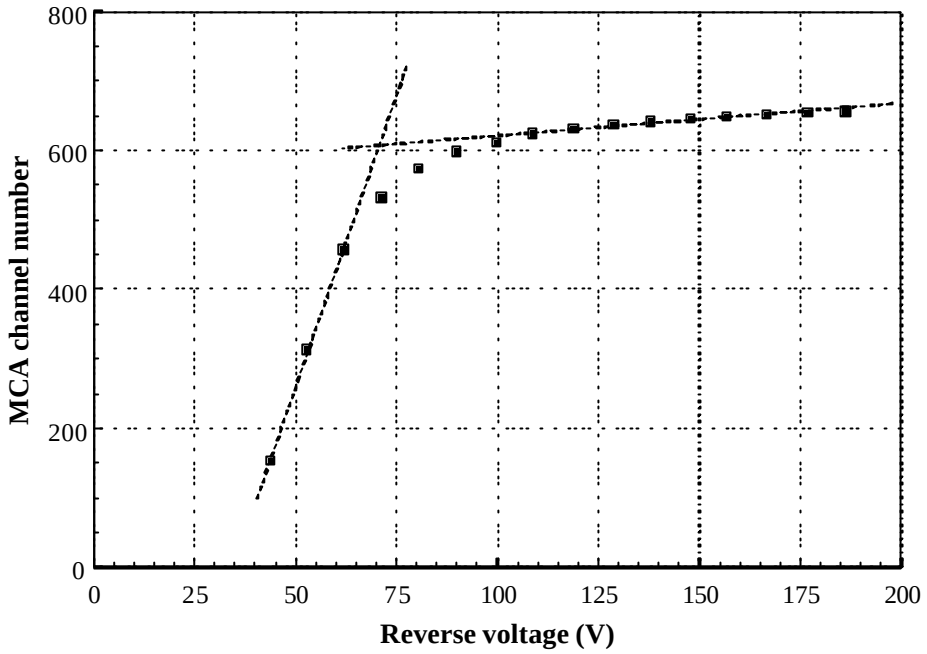

Figure 3.19: Detector response to 5.5 MeV alpha particles incident on the rear contact. Full depletion estimated at a reverse voltage of 68 V.

3.5.2 Detector Reverse Current (from *I-V* Measurements)

Current voltage measurements were performed the day following irradiation. Measurements were performed using a Keithley 237 High Voltage Source Measure unit. The measured reverse current was normalised to a temperature of 20°C using:

$$I(293.2) = I(T)\left[\frac{293.2}{T}\right]^2 \exp\left[-\frac{E}{2k}\left(\frac{T-293.2}{T\times 293.2}\right)\right] \qquad (3.19)$$

where: T = temperature at which the measurement was performed (K),

E = the width of the Si bandgap (an improved fit with experimental data is found using E = 1.2 eV [195]).

The measured reverse current was used to determine the reverse current damage constant, α, (defined by the parameterisation given in Equation 2.1 of Chapter 2). The reverse current at full depletion was used. The full depletion voltage was obtained from the change in slope of *C-V* curves and confirmed from charge collection studies of rear incident Am-241 alpha particles. The detector volume in all cases was 0.00324 cm^{-3}. A summary of the results is tabulated in Table 3.4. It was observed that the value of α was greater in the detectors exposed to a higher neutron fluence. The exception was U5b where a lower value was observed in comparison to detector U5c. The neutron fluence was determined from the response of the calibrated long counter. A pictorial representation of the results is shown by the square data points in Figure 3.20.

Table 3.4: Reverse current damage constant, α.

Detector	ΔI (μA)	Neutron Fluence, $(cm^{-2}) \times 10^{12}$	α $(A \cdot cm^{-1}) \times 10^{-17}$
U4a	2.82	11.0	7.91
U4b	2.71	10.6	7.89
U4c	2.28	9.50	7.41
U5a	1.35	7.05	5.91
U5b	9.70	5.80	5.16
U5c	9.00	4.76	5.84

For these calculations no consideration was given to the neutron fluence energy spectrum. Such a consideration should be made on account of the neutron energy dependence of the silicon damage KERMA. Using the data published in ASTM [16] a plot was made of the silicon damage KERMA as a function of neutron energy over the region of interest (see Figure 3.21). Using the Li^7 reaction kinematics, the minimum and maximum neutron energy were calculated

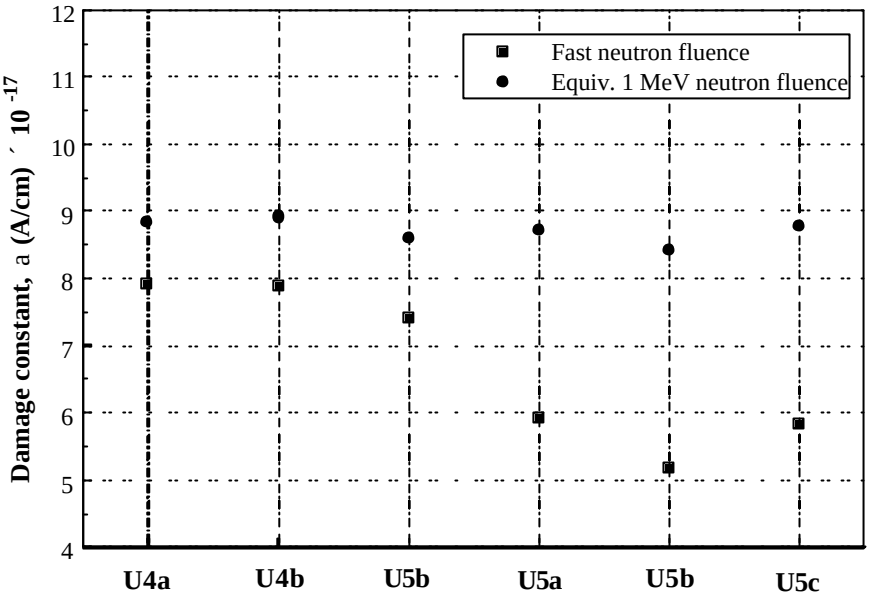

Figure 3.20: Reverse current damage constant determined using the measured fast neutron fluence and for the equivalent 1 MeV neutron fluence.

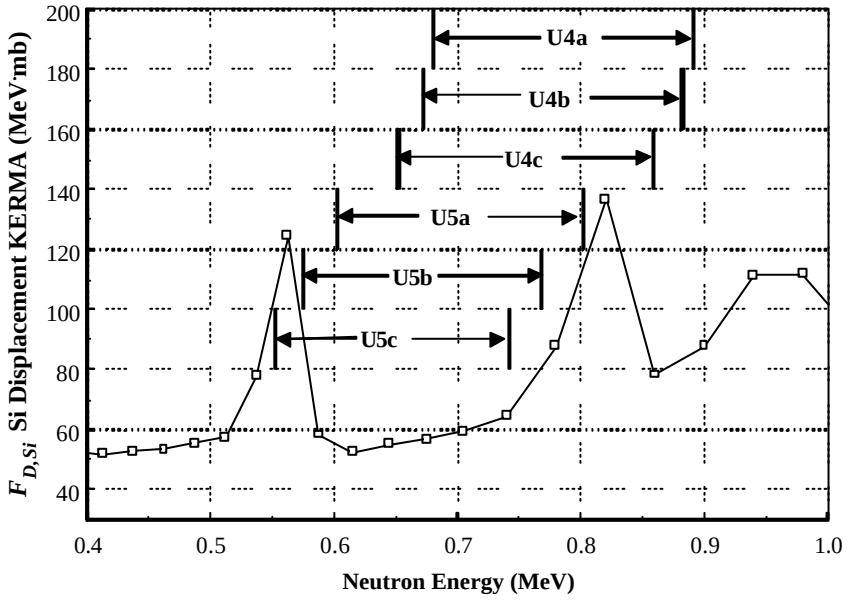

Figure 3.21: Silicon damage (or displacement) KERMA plotted as a function of energy. Data taken from [16]. The neutron energy range experienced by each detector is shown.

for each angle at which a detector was positioned relative to the beam line axis. The range of neutron energies experienced by each detector is also shown in Figure 3.21. The corresponding damage KERMA can be seen to decrease for the detectors from U4a to U5b. Due to the presence of a narrow resonant feature at a neutron energy of ~ 0.55 MeV, the U5c detector was exposed to a harder radiation field (in terms of silicon damage KERMA), than detector U5b. The equivalent 1 MeV neutron fluence to which each detector was exposed was determined by normalising the average silicon damage KERMA value for each neutron energy range, to the silicon damage KERMA for 1 MeV neutrons (95 MeV·mb). The correction factor along with the corrected reverse current damage constant are tabulated in Table 3.5.

Table 3.5: Corrected calculation of the reverse current damage constant from the equivalent 1 MeV neutron fluence.

Detector	Angle	Maximum neutron energy (keV)	Minimum neutron energy (keV)	Average Damage KERMA (MeV·mb)	Correction factor (95 MeV·mb / Av. D. KERMA)	α (corr) ($A \cdot cm^{-1}$) $\times 10^{-17}$
U4a	0°	891	680	85.17	1.12	8.83
U4b	11.3°	882	672	84.1	1.13	8.91
U4c	21.7°	859	652	81.87	1.16	8.60
U5a	36.8°	802	603	64.29	1.48	8.73
U5b	43.4°	768	575	58.29	1.63	8.41
U5c	48.8°	742	552	63.17	1.50	8.78

The reverse current damage constant corrected for the equivalent 1 MeV neutron fluence is shown by the circular data points in Figure 3.20. It can be seen that the considerable deviations seen previously have been removed. For the corrected data an average value for α of 8.71×10^{-17} $A \cdot cm^{-1}$ was obtained. This value is consistent with published data where measurement of the reverse current was performed immediately after irradiation (see Chapter 2).

3.5.3 Degradation of Detector Energy Resolution (from Alpha Particle Spectrometry)

Alpha particle spectrometry was performed using the same experimental conditions used prior to irradiation. Results showed that in the fully depleted mode of operation no alteration in the charge collection efficiency had occurred. The experimental uncertainty in this determination was estimated to be better than 5 %.

A significant reduction occurred in the detector resolution of the 5.486 MeV alpha peak. In detector U4a, the most heavily irradiated detector, the FWHM for the 5.486 MeV peak increased from 28.1 keV before irradiation to 40.3 keV. Smaller increases were observed in the less irradiated detectors. In all detectors it was no longer possible to clearly resolve the 5.443 MeV peak.

3.5.4 Radiation Induced Deep Level Defects

While DLTS has been used widely for the characterisation of radiation induced deep level defects in low resistivity ($r < 100\ \Omega$·cm) or electronic grade silicon, its use in irradiated detector grade silicon has been limited. Studies have generally been limited to detectors irradiated by a low neutron fluence (~ 10^9 cm^{-2}) [197-204]. For detectors irradiated by a high neutron fluence the technique fails. This is on account of the requirement for successful application of DLTS that the deep level defect concentration is much less than the shallow level background concentration. This is usually summarised by the requirement, $N_t < 0.1 \times N_{dop}$. Here N_{dop} is the effective impurity concentration due to shallow level impurities only. According to Fretwurst et al. [202], the neutron fluence (at 1 MeV), must be below ~ 1×10^{12} cm^{-2} in order for DLTS to be suitable for high purity silicon detectors .

In the experimental study performed here even the least irradiated detector (U5a) was exposed to an equivalent 1 MeV neutron fluence of 3.16×10^{12} cm^{-2}. DLTS measurements were performed in any case in order to observe how the neutron irradiation affected the spectrums.

Measurements were performed using various time constants (3.30, 10.20, 24.95, and 47.20 ms), a steady state reverse bias voltage of - 10 V and a pulse of 9.5 V with a width of 500 μsec. The measurements were performed over a temperature range of 50 to 310 K. The spectra collected showed no evidence of a physically valid peak and are not reproduced here.

3.5.4.1 Failure of DLTS in Highly Irradiated Silicon

To understand why DLTS is not applicable to highly irradiated silicon begin by considering the depletion capacitance of a *p*-*n* junction device given by:

$$C = A\left(\frac{\varepsilon_o \varepsilon_{Si} q}{2}\right)^{\frac{1}{2}}\left(\frac{N_{SCR}}{V_{bi} - V_R}\right)^{\frac{1}{2}} \qquad (3.20)$$

where: N_{SCR} = is the space charge density given by:

$$N_{SCR} = N_d - N_a - n_T(t) \qquad (3.21)$$

where: $n_T(t)$ = is the concentration of deep level defects occupied by electrons.

To simplify the analysis let N_{dop} be the effective doping density due to the shallow level impurities only, i.e.:

$$N_{SCR} = N_{dop} - n_T(t) \qquad (3.22)$$

so that:

$$C = A\left(\frac{e_o e_{Si} q}{2}\right)^{\frac{1}{2}}\left(\frac{N_{dop} - n_T(t)}{V_{bi} - V_R}\right)^{\frac{1}{2}} \qquad (3.23)$$

Equation 3.23 can be re-written as:

$$C = A\left(\frac{e_o e_{Si} q N_{dop}}{2(V_{bi} - V_R)}\right)^{\frac{1}{2}}\left(1 - \frac{n_T(t)}{N_{dop}}\right)^{\frac{1}{2}}$$

$$= C(\infty)\left(1 - \frac{n_T(t)}{N_{dop}}\right)^{\frac{1}{2}} \qquad (3.24)$$

where: $C(\infty)$ = the capacitance at time t = ∞, or steady state capacitance.

In most cases the assumption can be made that $N_{dop} >> n_T(t)$, hence a first order expansion of Equation 3.24 yields:

$$C(t) = C_o\left(1 - \frac{n_T(t)}{2N_{dop}}\right) \qquad (3.25)$$

so that:

$$\frac{\Delta C(t)}{C(\infty)} = \frac{C(t) - C(\infty)}{C(\infty)} = -\frac{n_T(t)}{2N_{dop}} \qquad (3.26)$$

The change in occupancy of a deep level defect due to a thermally stimulated process is given by:

$$n_T(t) = n_T(0)\exp[-e_n \cdot t] \qquad (3.27)$$

Substituting Equation 3.27 into Equation 3.26 gives:

$$\Delta C(t) = \frac{C(\infty) n_T(0)}{2 N_{dop}} \exp[-e_n \cdot t] \qquad (3.28)$$

which shows the usual result that the capacitance transient is exponential.

For highly compensated or high resistivity material the defect concentration, N_T, may be similar in magnitude or in some cases greater than the shallow level doping density, N_{dop}. In this case a first order expansion of Equation 3.24 is not valid. Experimentally the capacitance transient will not be exponential and the routine DLTS signal processing will not produce the correct result. This restriction of $N_t << N_{dop}$ is the reason for the limitation of conventional DLTS analysis to high purity silicon irradiated to a neutron fluence of less than 10^{11} cm^2 [202]. About this fluence the concentration of mid band centres becomes comparable to the shallow level impurity concentration.

Some attempts have been made to analyse non-exponential capacitance transients [205-207]. These examples have involved sophisticated analysis which is not always compatible with standard DLTS instrumentation. No such analysis has been applied to highly neutron irradiated detector grade silicon.

3.5.4.2 Alternative Deep Level Defect Characterisation Techniques

Other techniques based on semiconductor transients have been designed to deal with or are suitable for characterising deep level defects in high resistivity or highly compensated materials.

A close derivative to the conventional DLTS is Constant Capacitance DLTS (CC-DLTS). In this approach the capacitance of a junction device is kept constant as filled defect states are allowed to de-excite. This is done by varying the reverse voltage applied to the junction during the transient phase using feedback circuitry [208-210].

The voltage transient is given without approximation by:

$$V - V_{bi} = -\frac{q\varepsilon_o\varepsilon_{Si}A}{2C^2}\left(N_{dop} - n_T(0)\exp\left[-\frac{t}{t_e}\right]\right) \qquad (3.29)$$

This expression is valid for any value of n_T because the space charge region is held constant throughout the experiment. The technique requires the use of feed back circuitry which leads to a substantial decrease in the defect detection sensitivity as compared to conventional DLTS. It has not been applied to the case of highly irradiated silicon detectors.

Thermally Stimulated Current (TSC) or Thermally Stimulated Conductivity has been used to study defects in detector grade silicon irradiated with an equivalent 1 MeV neutron fluence of up to 10^{12} cm^{-2} [211-215]. In TSC the device is cooled under reverse bias to a low temperature at which point the traps are filled by reducing the reverse voltage to zero. A reverse bias is then applied and a heating cycle initiated. Upon heating, the trapped carriers are released under thermal stimulation and the conductivity of the device monitored by way of the induced current in an external circuit. The spectra obtained is usually complex and may involve a considerable number of unresolved peaks due to the contribution of many closely spaced defect states. The sensitivity of the technique is dependent upon the background conductivity of the device. At high temperatures (above ~ 250 K), where the device conductivity is high, the technique fails. For this reason TSC is not suitable for defects with energy states located about the centre of the bandgap which have the slowest emission rates. It is these defects which are of most concern in radiation hardness studies of silicon microstrip detectors.

The weakness of TSC at high temperatures can be overcome by combining the measurement with a repetitive rate window approach as in DLTS. Such techniques have a variety of names including Optical Transient Current Spectroscopy (OTCS), Photo Induced Current Transient Spectroscopy (PICTS) or (PICS), Current DLTS (I-DLTS) or Laser DLTS (L-DLTS). All techniques are similar and involve the repetitive filling of energy levels states at

a particular temperature using photon induced carrier generation by sample illumination with a laser light source. When the light source is turned off the thermal emission of the carriers occurs producing a current transient. This transient is then analysed using the rate window approach. The technique has successfully been applied to silicon detectors irradiated with fast neutrons to a fluence of up to 1.7×10^{15} cm^{-2} [217-218].

In general, these technique are constrained by the complexity encountered in the analysis stage. The current transient equation contains a temperature dependent term which is not easily quantified. This aspect is discussed extensively by Blood and Orton [181].

Additional techniques are clearly required. One such technique may be ODLTCS.

3.6 Optical Deep Level Transient Conductance Spectroscopy (ODLTCS)

The technique, known as Optical Deep Level Transient Conductance Spectroscopy (ODLTCS), was original developed for use with semi insulating or well compensated materials which didn't require the use of ohmic contacts. The processing of ohmic contacts and the associated high temperature treatment produces defect annealing and other unwanted material alterations. The initial paper describing this technique and its application in characterising defects in CdTe was published in 1992 by Alexiev et al. [219]. Such materials cannot be characterised by conventional DLTS.

The principle of the technique is based on a conductance transient as opposed to a capacitance transient in the regular DLTS measurement. In the original format the technique did not use samples with a diode structure but rather a contactless configuration whereby the sample behaved as a lossy dielectric. The sample was placed across the tank circuit of a 40 MHz marginal oscillator. Changes in the sample conductance were observed as a change in the amplitude of the oscillating signal.

A more complete description of the technique and its applicability to highly irradiated detector grade silicon where a diode structure is present will be given. The technique will be used to successfully characterise radiation induced defects in the neutron irradiated detectors.

3.6.1 The Principle of ODLTCS

The basic principle of ODLTCS involves the periodic filling of deep level defects with carriers generated in the test material through illumination with a pulsed light source. As the defect states subsequently re-emit the carriers in a thermally stimulated process they become available for conduction. The resulting change of the conductance is processed using a rate window in the same way as it is done in capacitance based DLTS. By scanning the sample temperature a spectrum of defects is generated in the usual way.

Measurement of the conductance transient is done by placing the sample across the tank circuit of a 40 MHz marginal oscillator. At this frequency the sample capacitance and other parasitic capacitances become negligible and the conductive component of the sample impedance dominates. The technique has already been applied to CdTe [219], semi-insulating GaAs [220,221] and semiconducting GaAs [222]. In these applications the samples had no electrical contacts and behaved as a lossy dielectric. CdTe is a highly compensated semiconductor which exhibits some semi insulating behaviour. This is not unlike highly irradiated detector grade silicon where the shallow level impurities are highly compensated by mid band electrical states. At very high neutron fluence the fermi level in silicon becomes pinned around the centre of the bandgap. It is reasoned here that ODLTCS would also be suitable for highly irradiated detector grade silicon.

The ODLTCS technique was previously applied to high resistivity silicon [340]. While the work of Butcher et al. was brief in its examination of defects in silicon, it provides a good experimental basis for a full examination of the ODLTCS technique as it applies to detector grade highly neutron irradiated silicon.

3.6.1.1 Photoconductive Transients

To better understand the operation of the marginal oscillator detector used for measuring photoconductive transients, consider a brief review of the electronic processes governing the optically stimulated carrier trapping and emission.

The emission rate, e, of a carrier trapped on a centre with activation energy depth, E_T, is given by the relation:

$$e = \tau^{-1} = \frac{s\,\mathrm{v}N}{g}\exp\left[-\frac{E_T}{kT}\right] \qquad (3.30)$$

where: τ = the trap decay time constant,

σ = the capture cross section of the trap for carriers,

N = the density of states in the band at temperature T,

v = the average thermal velocity of carriers at temperature T,

g = the degeneracy of the trap.

Equation 3.30 can be rewritten as:

$$\ln[t] = c + \frac{E_T}{kT} \qquad (3.31)$$

where: c = a constant.

From equation 3.31 (with suitable corrections for the temperature squared variation of $\varkappa N$), experimentally measured values of E_T can be obtained. Furthermore, if n_T is the number of trapped carriers, the rate of change of trapped carriers with time will be given by:

$$\frac{dn_T}{dt} = -n_T \cdot e \qquad (3.32)$$

The solution of Equation 3.32 is:

$$n_T = n_{To} \exp(-e \cdot t) \qquad (3.33)$$

where: n_{To} = the number of initially trapped carriers following a pulse of light.

If the carriers recombine in a characteristic time τ_R, which is short compared to the period of emission, the time dependent variation in concentration of excess free carriers Δn will be given as:

$$\Delta n = -\frac{\mathrm{d}n_\mathrm{T}}{\mathrm{dt}} t_\mathrm{R} \qquad (3.34)$$

and by substitution of Equation 3.33 into Equation 3.34 gives:

$$\Delta n = n_{To} e t_R \exp(-e \cdot t) \qquad (3.35)$$

Thus, the photo-induced trap-emitting conductance of the sample will decay exponentially in time with a period e^{-1} for the condition stated. Using a Miller type exponential correlator [186],

it is possible to measure directly the trap emission rate from the sample transient conductance at any temperature. Use of the Miller correlator for detection of a transient signal of the form given by Equation 3.35, because of the presence of the emission factor, e, requires re-calculation of the correlator response function given earlier by Miller et al. [186]. The recalculated response function is given by Alexiev, Butcher and Tansley [223].

A further consideration for the silicon detectors is the presence of a rectifying junction. In the case where ohmic contacts are present (as for PICTS) the material can be viewed as being in a neutral thermodynamic state with the Fermi-level being approximately constant throughout. The electron-hole pairs injected from the light source interact with empty electron trapping states above the Fermi-level and hole trapping states below the Fermi-level so that the same defects are observed throughout the region. When a barrier is present there will be a depletion region near the barrier, even at zero bias. This is due to the built in bias of the *p*-*n* junction. In the presence of this depletion region there will be some band bending near the barrier which may allow the observation of trapping levels which would not otherwise be seen if ohmic contacts were in use. This may be viewed as a further advantage of ODLTCS since the band bending in the depletion region will allow defect levels to be detected which are not scanned by the change of Fermi-level with temperature in the neutral region.

3.6.1.2 Description of the Marginal Oscillator Circuit

The following description of the marginal oscillator circuit has been reproduced here with kind permission of Alexiev et al. [219].

In essence, the marginal oscillator converts small changes in the tank or tuned circuit resistance into a change in amplitude of the oscillation. This may be brought about by enveloping the sample with the tank coil, as in nuclear magnetic resonance (NMR) spectroscopy, or by placing a shunt conductance, in the form of a parallel plate cell containing gaseous ions, across the resonant circuit, as in ion cyclotron resonance (ICR) measurements.

The effect of a lossy conductance in a photoconductor may be similarly detected by placing the device in shunt with the oscillator tank coil. Here, the detector was placed across the parallel resonant circuit of the simple, positive feedback oscillator circuit. The circuit employed was a modified Franklin oscillator design described by Idione and Brandenberger [224]. The circuit is shown in Figure 3.22.

Inductor L_1 and variable capacitor C_1 are the essential components of the parallel resonant oscillator tank circuit (resonant frequency ~ 40 MHz). Inductor L_2 and capacitor C_2 limit the passage of lower frequencies (e.g., microphonic signals) directly through the first stage field-effect transistor (FET), F_1, of the oscillator. Demodulation of the radiofrequency signal occurs at the drain of F_1 by a process similar to plate detection. The signal is then passed via the radiofrequency filter capacitor C_3 through a coupling capacitor C_4 to a buffer amplifier. The circuit shown in Figure 3.22 is a modification of the original designed to increase the pass band of the coupling components, C_4 and R_3, at low frequencies so as to accommodate demodulated photoconducting decay signals with periods up to ~ 100 ms.

The demodulated signals from the buffer amplifier are processed by the Miller exponential correlator-integrator unit, the output signal from which is fed a data logger along with the test sample temperature.

3.6.2 Experimental Apparatus Design and Construction

The marginal oscillator and envelope detector circuit was constructed on a PCB with a single sided metallised copper plate. The circuit layout was designed so as to house the radio frequency sensitive components in a small copper case. This case acted as a Faraday cage excluding external electromagnetic signals from being coupled into the amplifier stage. A stable low ripple power supply was used for the FETs, F_1 and F_2. The completed circuit board is shown in Figure 3.23.

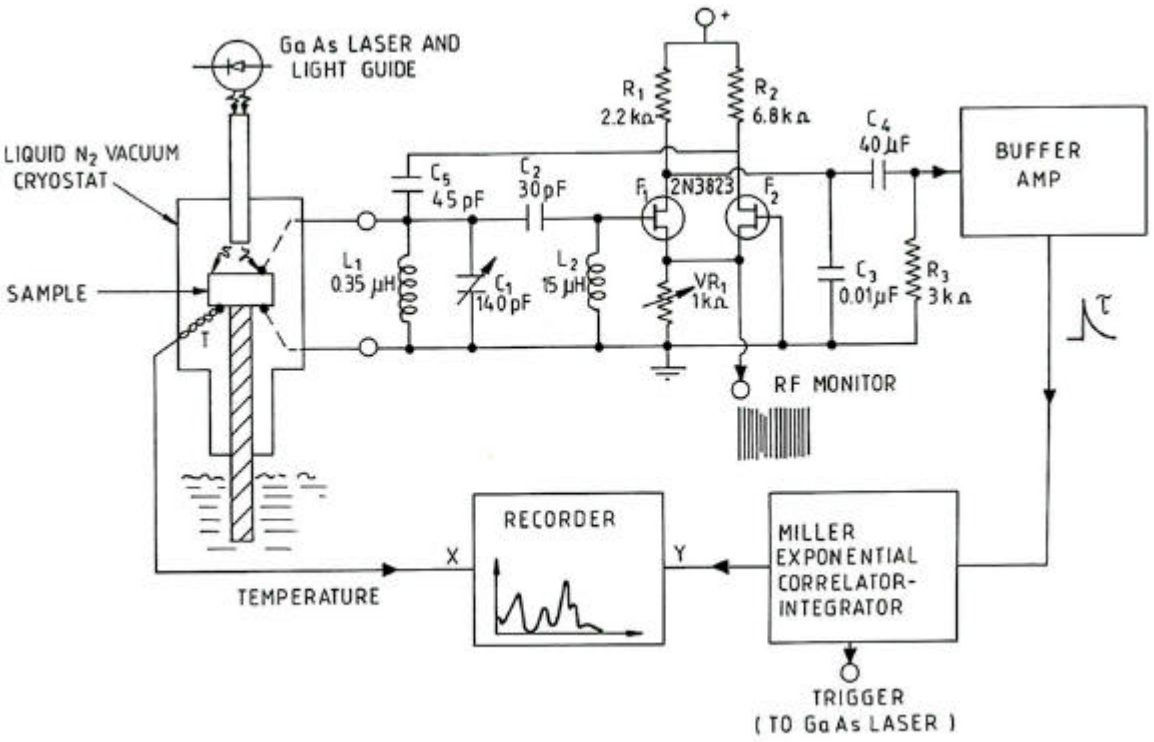

Figure 3.22: Schematic of overall ODLTCS spectrometer system using the marginal oscillator detector.

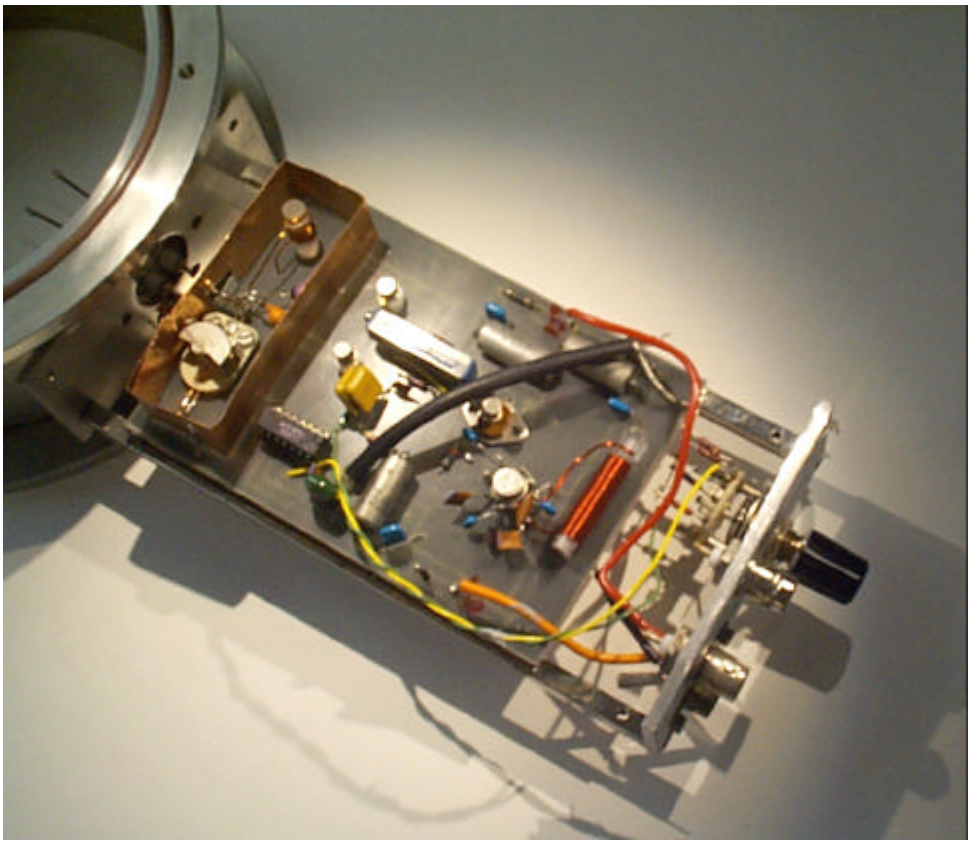

Figure 3.23: A photograph of the marginal oscillator detector circuit mounted adjacent to the sample cryostat. The entire detector was enclosed within a metal box which acted as a electromagnetic shield.

Additional circuitry included the Miller correlator. This circuit had been built by others previously and was in the form of a separate module which was mounted in a bin rack located in the vicinity of the main experimental apparatus.

The measurement cryostat consists of a small aluminium cup which accommodates a sample holder of the type described in Section 3.2. Two electrically insulated feed-throughs provide electrical contact between the detector and marginal oscillator circuit. Upon insertion of

the sample holder a small aluminium lid is placed over the aluminium cup. This provided a good thermal shield to reduce the effects of temperature hysteresis. At the centre of the lid is a hole of diameter 7 mm which allowed the insertion of the light guide. The guide itself is made of a perspex rod. To improve the transmission of photons, both ends of the rod were carefully hand polished. The light source is a type SG3001 stacked-diode GaAs laser with a peak emission at 904 nm. Typically, the laser is operated at a peak average power of 80 W with a pulse duration of approximately 1 μsec. The laser pulse is triggered by a square pulse produced by the Miller correlator circuitry.

The cryostat was fitted with a copper cold finger which could be lowered in and out of a dewar of LN_2. This enabled temperature scanning from room temperature down to ~ 80 K. The temperature gradient could roughly be controlled by the degree of submersion of the copper cold finger into the LN_2. For measurement at higher temperatures a gas torch was used to heat the cold finger.

Sample temperature is monitored via a copper/constantan thermocouple which is located in a small groove at the base of the aluminium cup. Indium foil was used to ensure good thermal contact between the cold finger, thermocouple and sample. The thermocouple signal is feed to the *x* input of a data logger. A complete view of the constructed system is shown in Figure 3.24.

To obtain an estimate of the sensitivity of the marginal oscillator radiofrequency output voltage as a function of shunt resistance across the tank circuit, the output was plotted for various loading resistors, R_L, at constant d.c. potential at the common sources of F_1 and F_2 (see Figure 3.25). These static characteristics are useful for obtaining an estimate of the equivalent shunting resistance of the sample that can be made. However, as can be seen from the relative insensitivity of the marginal oscillator radiofrequency output to R_L, values beyond ~ 14 kΩ and below ~ 2.8 kΩ, this characteristic has limited application. Below 2.8 kΩ the oscillation was quenched. For samples with low R_L values the value of R_L can be boosted by placing a conductive element in series with the device near the marginal oscillator circuit.

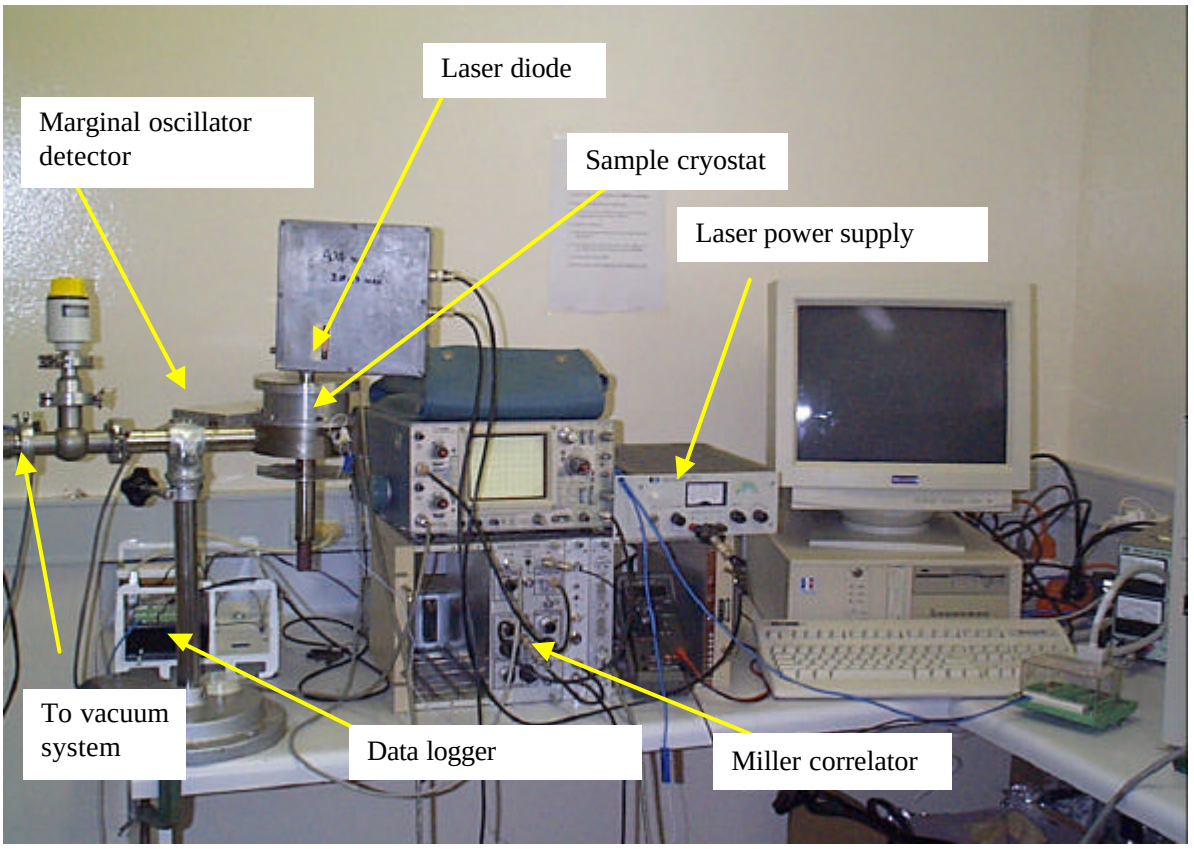

Figure 3.24: Completed Optical Deep Level Transient Conductance Spectrometer with computer data acquisition.

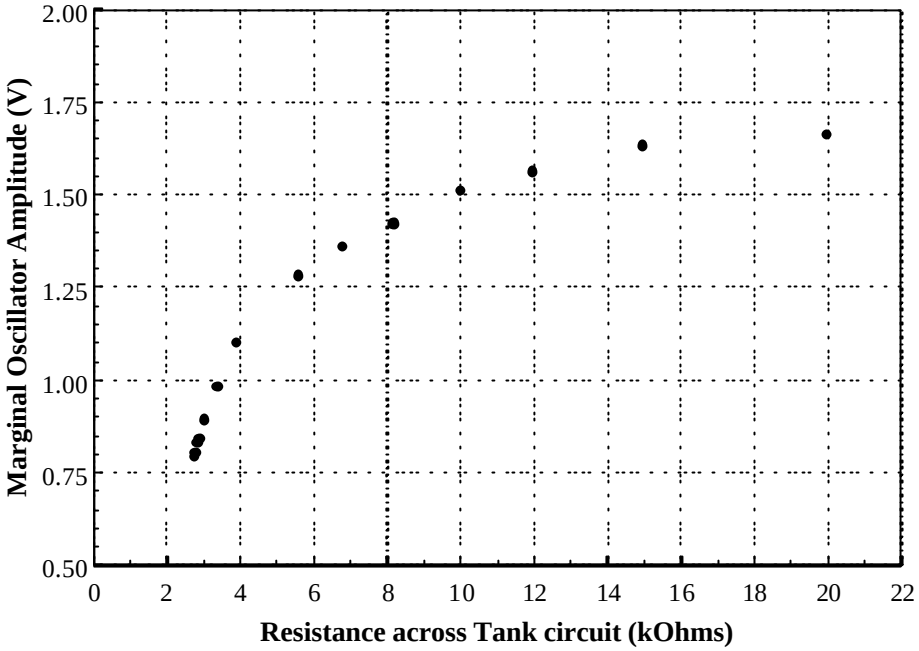

Figure 3.25: Marginal oscillator output as a function of shunt tank load resistance.

In operation, the optimum conditions for marginal oscillator detection were determined by observing the photo-decay signal and maximising it by adjusting VR_1. In practice, this adjustment is not very critical.

The volume of semiconductor within which the 904 nm light pulses effectively generates carriers is dependent on the absorption coefficient of silicon at the particular temperature of interest. Over the temperature range from 77 K to 300 K the absorption coefficient varies by almost a factor of four times for 904 nm light [225]. Both the absorption coefficient and the non-linear absorption of carriers in the bulk would make the calculation of trap density difficult. Partial trap occupancy due to the intensity of the source and the low capture cross section of the traps is also of concern if trying to determine the trap density. Brotherton [226] has examined some of these factors for back illuminated silicon barriers. Of course these concerns not only

impact on the ability to determine trap density from ODLTCS but also relate to the sensitivity of the method for observing various trap levels.

3.6.3 Measurement of Deep Level Defects in the Irradiated Detector Test Structures

The U5b detector was measured using the ODLTCS technique. The measurement was performed approximately six months after the irradiation by neutrons. It was anticipated that room temperature annealing of the defect distribution within the silicon bulk had ceased.

The ODLTCS measurement was performed over a temperature range of 300 K to 80 K. The spectrum obtained is shown in Figure 3.26. The spectrum bears a close resemblance to DLTS spectrums obtained in silicon irradiated at low neutron fluence (see for example [7]). The spectrum consisted of an isolated peak at a temperature of about 100 K and a broad feature located over a temperature interval of 150 - 260 K. This feature appeared to be made up of more than one closely spaced and unresolved peaks.

To estimate the energy level of the isolated peak at a temperature about 100 K, the ODLTCS measurement was repeated using correlator time constants of 2, 5, 7, 10 and 20 ms. An activation energy of E_c - 0.18 eV was determined. The peak was thus identified as the well known A-centre. A determination of the energy levels of the defects associated with the broad spectral feature required mathematical deconvolution. A means of performing this task was developed and is described in the following chapter.

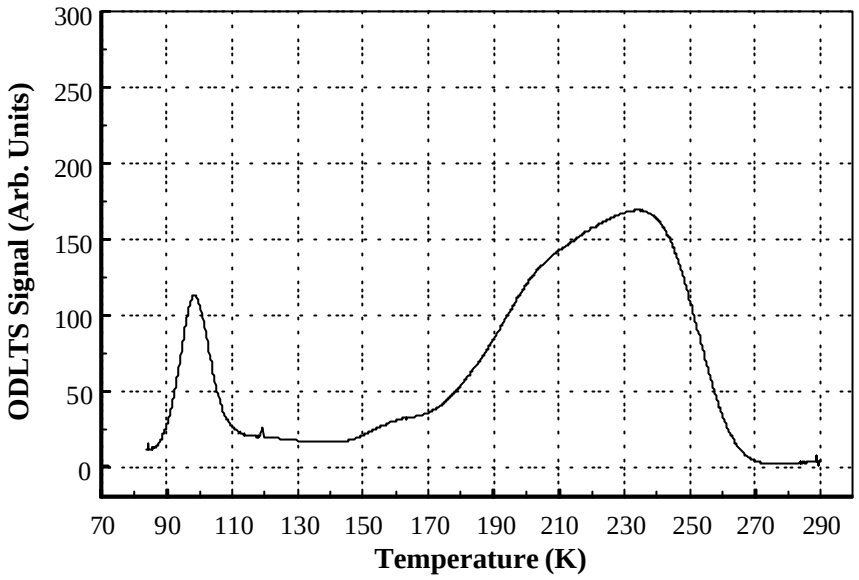

Figure 3.26: ODLTCS defect spectrum obtained from a silicon detector irradiated by an equivalent 1 MeV neutron fluence of 3.2×10^{13} cm^{-2}.

3.6.4 Discussion of the ODLTCS Technique

It has been shown that the ODLTCS technique can successfully be applied to the characterisation of deep-level defects of highly irradiated silicon. The defect concentration in this material was considerably larger than 0.1 of the background impurity concentration. Such material cannot be characterised using the conventional capacitance based DLTS.

It should be noted that the marginal oscillator detector conductance mode does not require high electric fields, as is often the case in conventional DLTS. Therefore the possibility of complicating Poole-Frenkel (field-sensitive emission) effects on the measurement of trap activation energy is diminished. Furthermore, the use of high-frequency oscillators (~ 40 MHz compared with 1 MHz in the common commercial capacitance bridges used for DLTCS) enables the measurement of deep level defects at higher scanning temperatures (higher emission

rates) thus avoiding freeze-out of the shallow background levels at low temperatures, an effect which limits the usefulness of DLTS [227].

The lack of an applied voltage eliminates the possibility of electric field disturbance of the defect state behaviour. Additionally, the high reverse current usually present in such highly irradiated detectors is absent. In many junctions techniques where capacitance or current transients are to be measured a high sample reverse current can cause considerable problems.

A disadvantage of ODLTCS is the inability to provide a direct measurement of trap concentration. This arises because of the absence of knowledge of the primary photocarrier concentration, diffusion kinetics of the carriers, non-linear generation of carriers with depth because of light absorption, and degree of partial traps filling. In addition, the amplitude of the conductance signal is also determined by the carrier recombination lifetime, a further unknown quantity. However, despite this drawback the qualitative comparison of relative trap concentration can be useful.

Although trap concentrations may not be measurable, trapping cross sections can be estimated by measuring the prefactor in Equation 3.30 (intercept on emission axis for T^{-1} as it approaches zero).

It would be advantageous if the circuit could be modified to accommodate the reverse biasing and pulse injection to the sample so as to provide a means of defining the sensitive volume and hence allow determination of trap concentrations. Although a variety of alterations to the existing circuit where tried, no viable change could be obtained. The marginal oscillator was quenched in all attempts.

Further development of the marginal oscillator detector circuit could be directed towards the use of higher frequency oscillators using high Q tank circuits, possibly of the tuned cavity type. Le Cleach [228] has reported the use of a contactless microwave photoconductive technique which may demonstrate some of the advantages of a higher frequency system. An amplitude limited oscillator reported by Robinson [257], has the advantages of lower noise and

greater insensitivity to microphonics than the simpler oscillator reported here. They should be investigated together, using an electronically variable conductance calibrator for sensitivity determination.

This technique is now available for the study of radiation induced defects in highly damaged detector grade silicon.

3.7 Conclusion

The preliminary study of this thesis was mostly directed to developing measurement techniques for the characterisation of radiation detector materials. As part of this program it was shown that the presence of a MOS capacitor will lead to an under estimation of N_{eff} as a result of an additional capacitance contribution to the junction depletion capacitance.

It was also shown that for an accurate determination of N_{eff} in a square junction device based on high resistivity silicon that the Copeland peripheral capacitance correction is not adequate. A numerical solution was used to obtain an improved correction factor for detectors with square junction areas from 0.09 cm^2 to 1 cm^2. It may be possible to obtain confirmation of this result by performing a computer simulation of the electric field profile about the corner and perimeter regions of the junction. From this the capacitance contribution could be determined. Semiconductor device simulation tools such as DESSIS of the TCAD program suite should be capable of solving this problem.

In terms of the post irradiation measurements, similar results were obtained as those reported previously in the literature (as discussed in Chapter 2). Following neutron irradiation *C-V* measurements for profiling the effective impurity concentration and junction built in bias were not possible. This result was shown to be caused by the frequency dependence of the measured capacitance in the presence of a deep level acceptor impurity located about the mid bandgap of the n-type bulk.

Measurement of the reverse current following irradiation allowed a determination of the reverse current damage constant. Agreement of this parameter with published literature was only possible after determination of the equivalent 1 MeV neutron fluence in silicon experienced by each detector. This was a time consuming process and only possible due to the relatively simple kinematics of the monoenergetic neutron production reaction employed in the irradiation. Although reasonable agreement was observed following correction, a remaining variability in α between different detectors irradiated at different angle from the beam line axis was seen. This may have been due to a failure to consider the variation in the neutron yield of the $Li^7(p,n)Be^7$ reaction as a function of angle. The experimental neutron flux was monitored in the 0° angle only and the inverse square law used to determine the flux at different radial distances from the target. A consideration of the effect of the device under test (including mounting components) in terms of neutron beam attenuation and neutron energy moderation was not done. Nor was the effect of room scattered neutrons taken into account. Such experimental factors are extremely difficult to quantify from a theoretical perspective. From these points of view it would be advantageous to have a simple and reliable monitor capable of responding directing in terms of the equivalent 1 MeV neutron fluence in silicon. Such a monitor could be used to characterise the neutron field prior to insertion of the device to be irradiated. Or alternatively the monitor could be mounted close to the device under test during the irradiation to provide an on-line assessment of the equivalent 1 MeV neutron fluence in silicon. The development of such a monitor was a second focus of work completed for this thesis.

Experimental observation of the radiation induced deep level defects using the DLTS technique was not possible. This technique becomes invalid for the case of high defect concentrations. To counter this limitation the alternative technique called Optical Deep Level Transient Conductance Spectroscopy was employed. While this technique had been developed for the characterisation of deep level defects in semi insulating materials it was shown to operate successfully for the case of highly irradiated silicon based detector test structures. The A-centre defect was successfully identified in a detector which had been irradiated by a 1 MeV

equivalent neutron fluence of 10^{13} $n \cdot cm^{-2}$. This neutron fluence is two orders of magnitude in excess of the neutron fluence at which the conventional DLTS technique fails.

Chapter 4

Evolution of Deep Level Defects in Neutron Irradiated Silicon Detectors with Room Temperature Annealing

4.1 Introduction

A detailed physical mechanism at a microscopic level which adequately describes the change in N_{eff} in silicon with neutron (or charged particle) irradiation, as well as during the subsequent room temperature annealing is yet to be obtained. Deep level defects are known to play a dominant role. This was seen experimentally in the previous chapter where the *C-V* characteristics of the detectors became frequency dependent as a result of the introduction of deep level defects with irradiation by 1 MeV neutrons. The identity of the defects responsible has not been determined. One possible reason why this has not been achieved is the lack of characterisation techniques for observing the deep level defects in highly irradiated material.

Following on from the previous chapter, the ODLTCS technique is used here to observe the evolution of the deep level defect spectrum in silicon detector test structures following neutron irradiation, and as a function of the subsequent room temperature annealing. The aim is to identify the key defects involved in the changes to N_{eff} with room temperature annealing.

A further objective of this work is to use the principles of defect engineering to postulate on means by which the detector silicon bulk could be radiation hardened. Defect engineering involves the intentional addition and/or intentional omission of particular impurities in the starting silicon in order that the formation of beneficial electrically active defects is enhanced, and the formation of detrimental electrically active defects is reduced. Two impurities which may affect the radiation hardness of silicon are oxygen and nitrogen. The reasons why oxygen and nitrogen might offer an improvement to the radiation hardness of silicon are discussed in the next section. This is followed by an experimental study into the behaviour of radiation

induced deep level defects in both oxygenated and nitrogenised silicon as well as silicon containing the standard residual impurities.

4.2 Possible Mechanisms of Defect Engineering in Silicon

Impurities play a prominent role in the formation of radiation induced defects in silicon. Well known examples are the vacancy oxygen V-O defect, and the vacancy phosphorus V-P defect. Mechanisms by which impurities may improve the radiation hardness of silicon have been observed experimentally. It was reported in 1963 that in silicon which contained a high oxygen content, a reduced introduction rate of mid band defects was observed under high energy electron irradiation [6,7]. This was explained as a result of the effective trapping of silicon vacancies by interstitial oxygen atoms to form V-O defect [8]. Associated with V-O defect is an electrical state at E_c - 0.18 eV. This state is relatively benign in terms of the effect it has on the electrical properties of the material. The trapping of vacancies by oxygen occurred preferentially to the capture of vacancies by other impurities. This reduces the production rate of other defects, such as the divacancy defect, which are associated with mid band electrical states and therefore highly detrimental to the electrical properties of the material. Hence by reducing the rate of mid centre accumulation the material was radiation hardened.

This particular result was obtained in *n*-type silicon with a phosphorus concentration of 10^{15} - 10^{16} cm^{-3}. The corresponding resistivity was of the order of 1 Ω·cm. The material also contained high concentrations of other residual impurities. For this reason it does not immediately follow that higher oxygen content would lead to improved radiation hardness in high purity detector grade silicon. Experimental investigation of oxygenated high purity silicon is warranted.

Another impurity which has been shown to affect the behaviour of crystallographic defects in silicon is nitrogen. Solute trapping of nitrogen during silicon crystal growth has been used to increase the physical strength of low oxygen content wafers where nitrogen has been reported to

be more effective than oxygen for pinning dislocations and suppressing slip and warp during silicon wafer processing [9,10]. Additionally, the concentration of swirls and other lattice defects were found to be reduced in nitrogenised silicon [11]. The relevance of nitrogen inclusion as a means of improving the radiation hardness of detector grade silicon is not known. Experimental investigation of nitrogenised silicon is also warranted.

4.3 Experimental Methods and Materials

In the study undertaken here the radiation induced defects created in detector test structures manufactured from oxygenated silicon as well as nitrogenised silicon are compared to defects in detector test structures manufactured from silicon with the standard residual impurities. The ODLTCS technique is used to track the evolution of individual defects as a function of room temperature annealing in all of the different silicon types. The experimental program contained the following elements:

1. Exposure of detector test structures manufactured from silicon containing different residual impurities to 1 MeV neutrons at a fluence sufficient to induce inversion of the conduction type within the detector bulk.
2. Measurement of the radiation induced deep level defects using the ODLTCS technique.
3. Measurement of the evolution of the deep level defect spectrum as a function of room temperature annealing.
4. Comparison of the defect evolution results with known changes to N_{eff}.

4.3.1 Detector Test Structures

The detector test structures under study were supplied by Dr Lemeulluer of the ROSE collaboration. A total of four detectors were used. All detectors were produced from *n*-type silicon grown using the Float Zone technique at Belovadice in Prague. The silicon of two of the

detectors contained the standard residual impurities typical of high purity silicon. The silicon of a third detector contained an additional nitrogen component at a concentration of approximately 10^{15} cm^{-3}. The silicon of a fourth detector contained an additional oxygen component at a concentration of approximately 10^{16} cm^{-3}. All detectors had p^+nn^+ structure. The substrate thickness was 300 μm. Junctions were produced by either diffusion technology at 'ITE' in Warsaw, or by ion implantation technology at 'Si-NTEF' in Oslo. The detectors with ion implanted junctions also had a guard ring structure surrounding the *p-n* junction window. The junction window in all detectors had an area of 5×5 mm^2. A centrally located circular gap in the front side aluminium metallisation was present to allow the passage of infrared photons directly into the silicon. The diameter of this circle was approximately 2 mm. The rear side was metallised with aluminium formed in a cris-cross grid pattern to enable the incidence of photons directly onto the rear silicon surface without increasing the surface resistivity of the rear Al contact.

In Table 4.1 is a complete list of the detector details as well as the labelling scheme used to identify each detector.

Table 4.1: Details on the detector test structures under study.

Detector	Silicon	Resistivity, (kΩ·cm)	Junction type	Guard rail
L2	Standard	2.87	Diffused	No
L5	Nitrogen ~ 10^{15} cm^{-3}	4.58	Diffused	No
L9	Standard	1.75	Ion implanted	Yes
L11	Oxygen ~ 10^{16} cm^{-3}	2.21	Ion implanted	Yes

Basic electrical characterisation of the detectors using the techniques described in Chapter 3 was undertaken prior to neutron irradiation.

4.3.2 Neutron Irradiation

Neutron irradiation was performed using the fast neutron facility described in Chapter 3. Protons of energy 2.7 MeV were made incident on a lithium metal target of thickness 190 keV. Neutrons produced in the forward direction had energies between 0.805 MeV to 0.995 MeV.

The detectors were mounted in a stack at a distance of 5 mm from the target face. Each detector was individually wrapped in aluminium foil to protect against the water spray used for target cooling. Irradiation was performed in two 12 hour stages performed on two consecutive nights. Prior to commencing the second irradiation stage the order of detectors in the stack was reversed so as to achieve a more uniform neutron fluence between all detectors.

Neutron production was monitored using a neutron long counter located along the beam line axis at a distance of 277 cm from the target face. The neutron fluence at the point of the detectors was determined using the inverse square law. The neutron damage KERMA factors for silicon were used to normalise the neutron fluence in terms of the equivalent 1 MeV neutron fluence, $\Phi_{eq,1MeV,Si}$. Details of the neutron fluence over the two irradiations is reported in Table 4.2. The fluence variation between different detectors was not more than 5%.

Table 4.2: Measured neutron fluence in terms of $\Phi_{eq,1MeV,Si}$.

Detector	Equivalent 1 MeV neutron fluence, (cm^{-2})
L2	7.5×10^{13}
L5	7.4×10^{13}
L9	7.6×10^{13}
L11	8.0×10^{13}

Following irradiation the detectors were promptly transported from the target area to the semiconductor laboratory. During the transfer the detector temperatures did not exceed 23°C as measured by a mercury thermometer located within the transport container. Once in the

laboratory the detectors were placed within a perspex desiccator cabinet which was continuously purged with dry nitrogen. The cabinet temperature was maintained at 22°C or less for the course of the measurement program to ensure that no accelerated annealing of the radiation damage occurred.

4.3.3 ODLTCS Measurement Program

The ODLTCS measurements were commenced immediately following transfer of the detectors to the semiconductor laboratory. The operation of the ODLTCS apparatus was described in Chapter 3.

While it is not possible to determine the concentration of defects using ODLTCS, the relative peak height can be used to make comparisons of the relative defect concentration within the different detectors under study. For each measurement particular care was taken in the mounting of the detector within the cryostat. This was to ensure that the infrared photon intensity incident at the detector face was the same for each measurement. A specially designed jig allowed placement of the detector relative to the photon source to within 500 μm. The photon intensity at the sample position was measured twice weekly using an infrared photon detector. A variability of no greater than 3 % was seen in 12 measurements.

Power to the ODLTCS instrumentation was not interrupted during the measurement program. This was to ensure that all components were at the correct operating temperature at all times.

The ODLTCS data was taken in a downward temperature scan. More commonly in a DLTS type measurement the data is taken in an upward temperature scan. This avoids interference to the sample signal by microphonic noise from cryocooler pumps which are operated during the downward temperature scan only. No such pumps were used here but rather a simple arrangement consisting of a dewer of LN_2. It was preferable to take data in the

downward temperature scan due to the more uniform temperature scan rate which could be achieved.

Scans were performed from room temperature to approximately 80 K. The average rate was 0.1 Ks^{-1}. At this rate only minimal temperature hysteresis was seen. This was based on additional measurements at a scan rate of 0.01 Ks^{-1} where no spectral peak shifts in temperature were observed relative to those in the spectrums obtained with a scan rate of 0.1 Ks^{-1}.

A correlator rate window time constant of 5 ms was used.

Each measurement took 50 minutes to perform. This included the time to warm the detector back to room temperature and remove and replace the detector with another. All four detectors could be measured within 3.5 hours.

The first series of measurements were commenced 1 hour after neutron irradiation. Measurements were performed on a periodic basis until changes in the deep level defect spectra had ceased. This occurred after 1000 hours post irradiation. Nineteen separate ODLTCS spectrums were obtained for each detector. The time interval between each measurement was increased with time post irradiation. The detailed measurement schedule is shown in Figure 4.1.

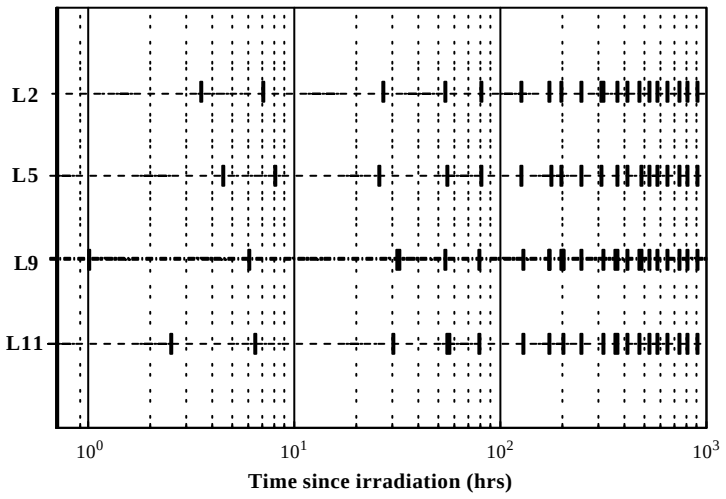

Figure 4.1: ODLTCS measurement program for the four detectors L2, L5, L9 and L11.

4.4 ODLTCS Results

Evolution of the ODLTCS spectra within the first 60 hrs of room temperature annealing is shown in Figure 4.2 for each of the four detectors. Similar spectral features were seen in all detectors. Each consisted of an isolated peak at a temperature of about 100 K in addition to a broad feature over the temperature interval of 160 K - 260 K. This broad feature appeared to be made up of more than one closely spaced but unresolved peaks.

Based on the calculated activation energy of E_c - 0.18 eV, the defect associated with the 100 K peak was identified as the A-centre. The amplitude of this peak in the detectors with the standard residual impurities (L2 and L9), was similar. In L5, the nitrogenised detector, the peak amplitude was significantly less than in all other detectors. Conversely, in L11, the oxygenated detector, the peak amplitude was significantly greater than in the other detectors.

The A-centre peak of L11 in the 25 hr measurement can be seen to be distorted. This was found to be due to an erratic electrical contact between the detector and the spring contact of the sample holder. Movement of the electrical contact occurred at low temperatures as a result of thermal contractions in the teflon feed through which supports the wire. The problem was eliminated by substituting the teflon with a ceramic material with greater rigidity.

In the L11 spectrum obtained at 56 hrs the 100 K peak signal appeared to exceed the maximum supply rail voltage leading to clipping. For further measurements attenuation of the correlator output signal was required to accommodate this component. This was achieved by changing the gain of the correlator circuitry. The gain change was done for measurement of L11 as the detector temperature passed below 120 K. At higher temperatures the gain was kept at the same setting used in measurement of detectors L2, L5 and L9.

a)

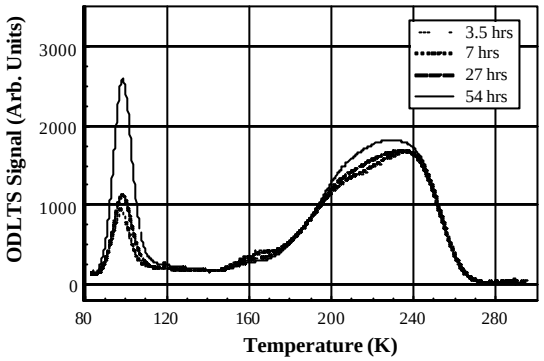

b)

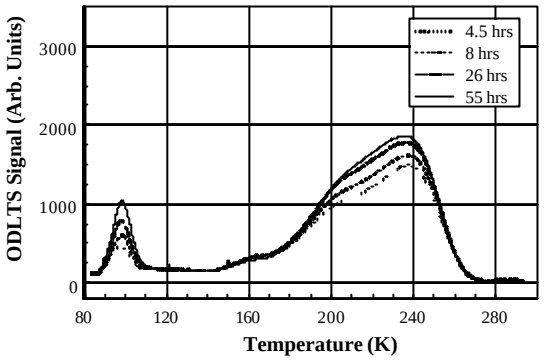

c)

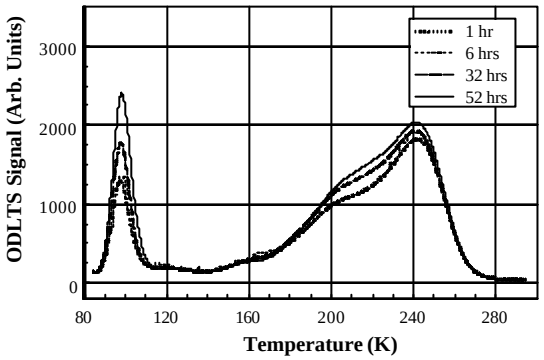

d)

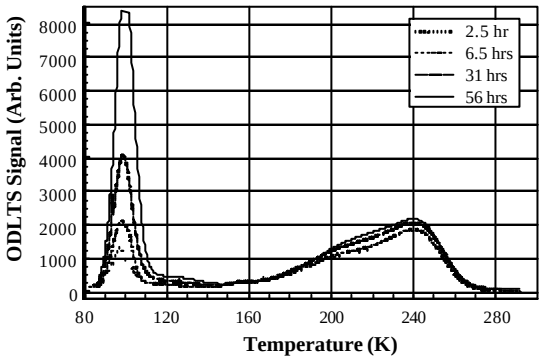

Figure 4.2: ODLTCS spectrums obtained within the first 60 hours following irradiation. The graphs are for detectors: a) L2, (standard), b) L5 (nitrogenised), c) L9, (standard), and d) L11, (oxygenated).

In terms of evolution with time the signal strength of the A-centre was seen to increase substantially in all detectors. This indicates the continued formation of the V-O complex with room temperature annealing. The kinetics of growth was examined and is discussed below.

Considerable evolution of the multi peak feature about 160 K - 260 K as a function of room temperature annealing was also observed in all detectors. The complete evolution of this feature over the entire measurement period is shown in Figure 4.3 for detector L9. To understand the physics of these changes it was necessary to resolve the individual contribution of the hidden peaks which make up this broad feature.

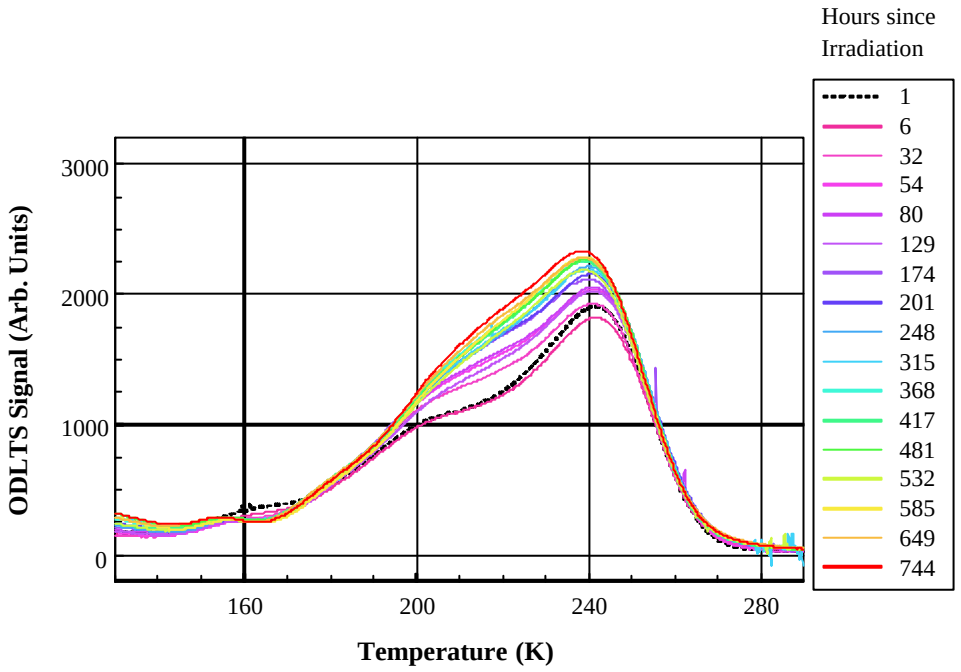

Figure 4.3: Evolution of the broad feature in the ODLTCS spectra of detector L9 with room temperature annealing.

4.4.1 Peak Fitting of the ODLTCS Spectra

A hidden peak is one located in the data which is not responsible for a local maximum. Various methods are available for the detection of such peaks. The method used here was the residual method. A residual is the difference in the *y*-value between a curve data point and the sum of the corresponding peaks evaluated at that same *x*-value of the curve. By placing peaks in such a way that their total area is equal to the area of the curve (or spectrum), the hidden peak is revealed by the residual.

Extraction of the physically correct hidden peaks using the residual method requires that some priori information regarding the physical form or shape of the hidden peak is known (otherwise an infinite number of solutions could be obtained). In the ODLTCS measurement the peak shape is dependent on the response function of the exponential correlator circuitry. For the Miller correlator used here [186], the response function has been derived [181]. It is given by:

$$R(t) = \frac{A}{b}\left\{\frac{t}{t+t_c} + \frac{t_c}{t+t_c}\exp\left[-\frac{b(t+t_c)}{t}\right] - \exp\left[-\frac{bt_c}{t}\right]\right\} \qquad (4.1)$$

where: t_c = time constant of the electronically generated exponential decaying wavefunction,

b = $t_{corr} \times t_c^{-1}$,

t_{corr} = time period over which correlation is performed,

t = the carrier detrapping lifetime given by:

$$t = e_n^{-1} = \frac{g}{s\langle v\rangle N_s}\exp\left[\frac{E_t}{kT}\right]$$

$$= \frac{A}{T^2}\exp\left[\frac{E_t}{kT}\right] \qquad (4.2)$$

where: E_t = activation energy of the trap,

T = temperature,

k = Boltzmann constant.

The function $R(t)$ will be a maximum for $t = t_c$ only when b has a value of 2.05. This is established by setting the value of t_{corr} within the correlator circuitry.

Using the well known parameters of the A-centre the correlator response function was plotted as a function of temperature. The result is shown in Figure 4.4. A corrleator time constant of 5 ms was used. The curve (shown as a solid line), is seen to be relatively symmetrical about the temperature mid point. Some skewing to the higher temperature side is evident. Apart from this small degree of asymmetry the peak appeared to have a shape similar to that of a gaussian curve. For this reason a gaussian curve was used to model $R(t)$. This significantly simplified the peak fitting procedure on account of the availability of commercial software which uses gaussian curve fitting [229]. Ideally the exact form of $R(t)$ would have been used. However this would have necessitated the development of complex computer code.

A fitted gaussian curve to the simulated correlator response for the A-centre defect is also shown in Figure 4.4 (dotted line). Recalling the mathematical form of a gaussian curve:

$$y = a_o \exp\left[-\frac{1}{2}\left(\frac{x-a_1}{a_2}\right)^2\right] \qquad (4.3)$$

where: a_o = curve peak amplitude,

a_1 = x value at curve peak amplitude,

a_2 = peak width.

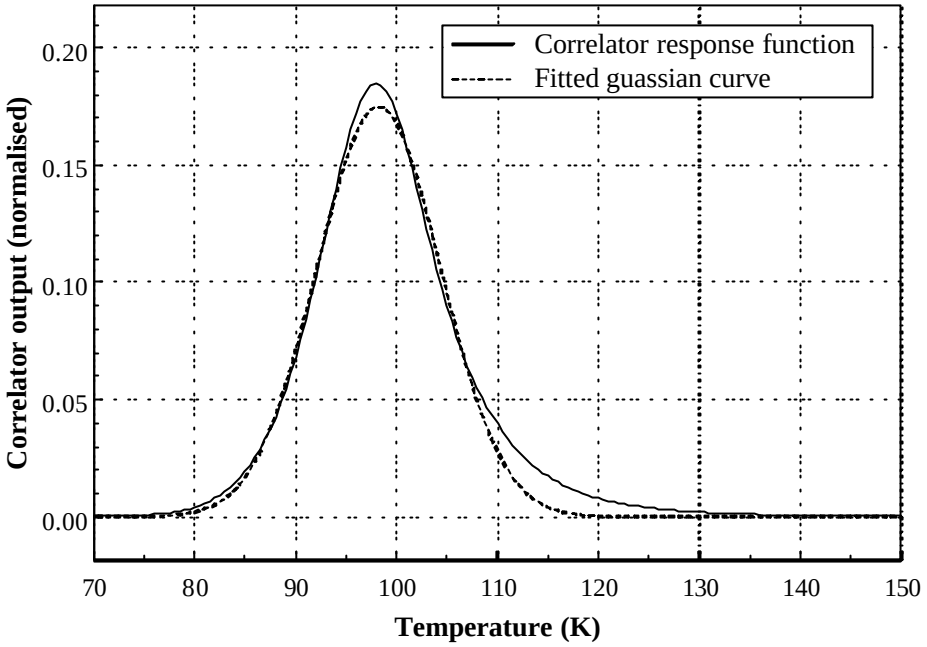

Figure 4.4: Theoretical correlator response function in addition to a fitted gaussian curve.

The parameters of the gaussian curve deviated from the true correlator function, $R(t)$ by 0.4 % in temperature, 4.6 % in peak amplitude and 5.2 % in peak width. As a first approximation this was considered adequate.

To provide additional physical information to impose on the fitting procedure, the temperature dependence of the correlator response function width was determined. This was done by modelling the correlator response function using parameters of the divacancy and other defects known to exist in neutron irradiated silicon. The width parameter of the fitted gaussian curve was identified and is plotted as a function of temperature in Figure 4.5. A linear dependence of the $R(t)$ peak width with temperature was found. This physical restraint could now be imposed on the peak fitting procedure to ensure a physically valid solution was obtained.

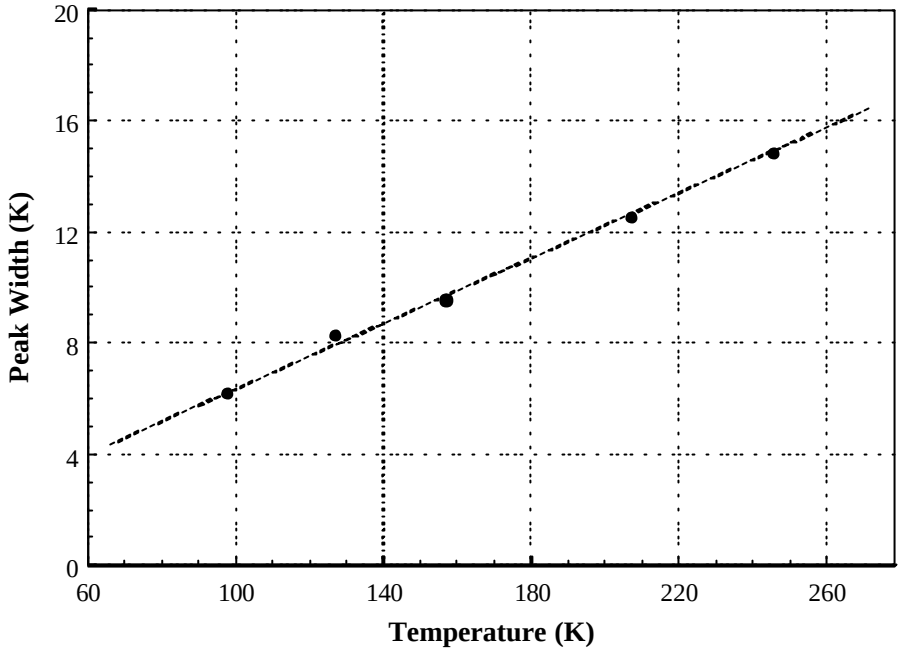

Figure 4.5: Correlator response function peak width as a function of temperature.

Peak fitting was performed on the ODLTCS spectrums of all four detectors. The steps used were as follows:

1. Gaussian curves were placed at points in the ODLTCS spectrum where local maximum were present. (The peak width was fixed using the temperature dependence of the $R(t)$ peak width).
2. Hidden peaks were identified based on the residual between the ODLTCS data stream and the initial fitted peaks.
3. An additional gaussian curve was placed at the point of an identified hidden peak. (The peak width was again fixed using the temperature dependence of the $R(t)$ peak width).
4. In an iterative process the parameters of each peak (i.e. temperature mid point and amplitude), where adjusted so as to minimise the residuals.

In all spectra seven peaks were identified. An example result for detector L2 is shown in Figure 4.6. The seven identified peaks are seen at temperatures of 98 K, 127 K, 158.7 K, 163 K, 203 K, 220.8 K and 242.6 K.

If additional peaks were forced into the fitting procedure they appeared following the iterative procedure to be present with amplitudes of less than 1 % of the amplitude of the smallest of the seven main peaks. For this reason it was considered adequate to model the spectrum evolution by the seven main peaks only.

The fitting procedure was carried out on all measured spectra. The peak amplitudes were extracted as a relative measure of the defect concentration. In addition the peak mid point temperature was determined. All data was collated as a function of room temperature annealing.

These results are now discussed on a peak by peak basis.

4.4.2 Peak Evolution with Room Temperature Annealing

Peak 1

Peak 1 was observed at a temperature of 98 K. This peak was previously associated with the A-centre. The evolution of peak amplitude with room temperature annealing in all detectors is plotted in Figure 4.7. A considerable scatter in the data can be seen that does not seem to correlate with any understandable physical process. An explanation for the results was sought. It is worth noting at this point that the behaviour of the other peaks in the spectrum was considerably less complicated.

Figure 4.6: Peak fitting of the ODLTCS spectrum using the residual method. The hidden peaks are Peaks 4,5 and 6.

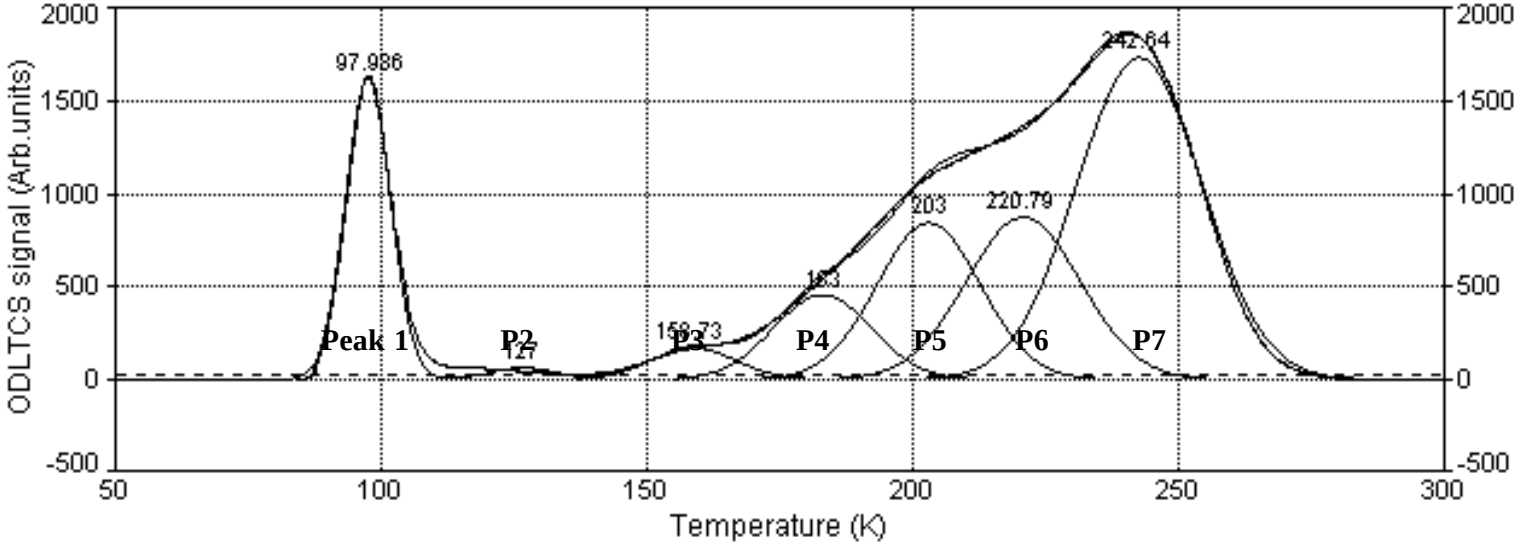

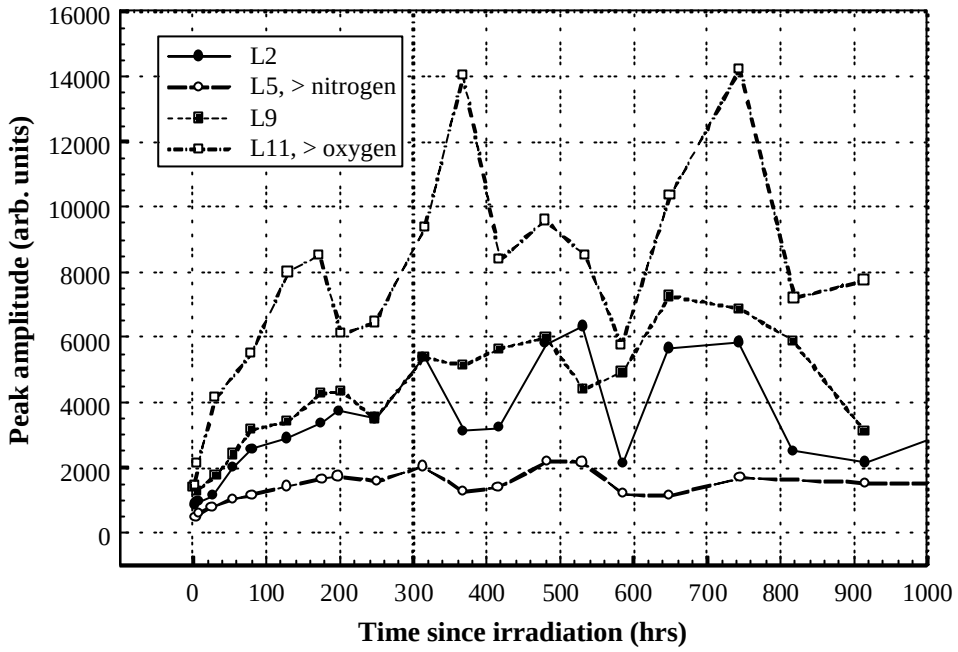

Figure 4.7: Evolution of Peak 1 amplitude with room temperature annealing.

In the first step in understanding the Peak 1 behaviour a locally weighted least squares regression fit was made to each data set. The resulting curves are plotted in Figure 4.8. Four important features are noted:

1. In all detectors the peak amplitude was found to increase substantially during the first 400 hours of room temperature annealing.
2. The amplitude of the peak in L2 and L9 (the detectors with standard residual impurities), was similar.
3. The amplitude of the peak in L11 (the oxygenated detector) was a factor of two greater than in L2 and L9.
4. The amplitude of the peak in L5 (the nitrogenised detector) was approximately four times less than that in L2 and L9.

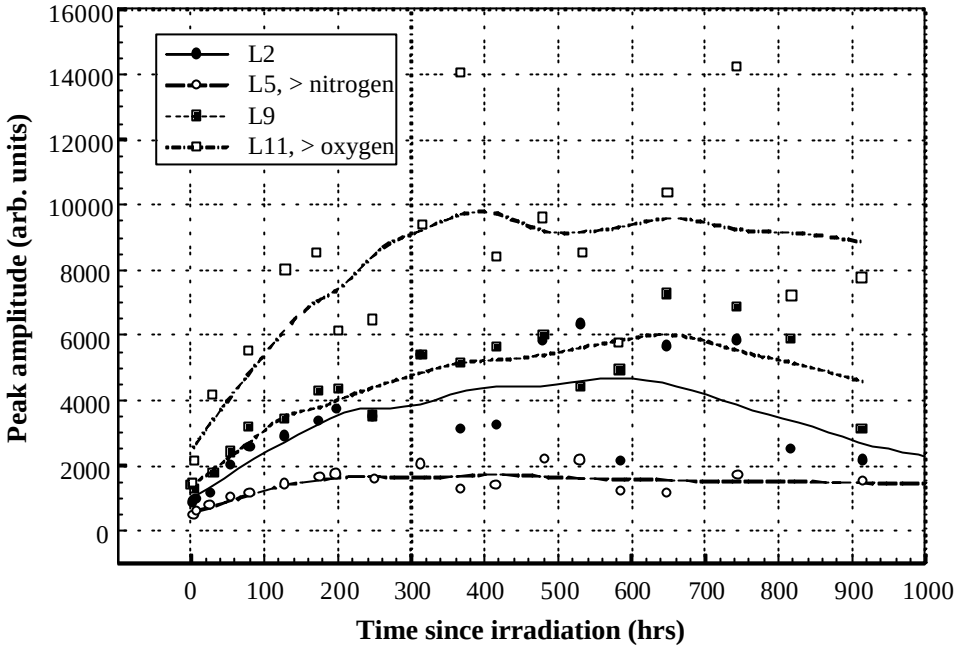

Figure 4.8: Peak 1 data with a locally weighted least-squares linear regression fit.

The presence of oxygen and nitrogen had a substantial effect on the peak amplitude.

In Figure 4.9 the Peak 1 data is separated into individual graphs for each detector. For detector L2, shown in Figure 4.9-a), the peak amplitude over the first 200 hrs increases a factor of six times from the first measurement performed immediately following irradiation. Evolution of the trend back to zero time after irradiation shows that the peak amplitude is almost zero at the end of irradiation. This result indicates that the peak is associated with a defect which is not produced in a primary process but rather a secondary process as a result of room temperature annealing. The same behaviour was exhibited in L5, L9 and L11.

Beyond 200 hrs of room temperature annealing it was evident that the amplitude in L2 begins to fluctuate between two extremes notated in Figure 4.9 a) by a solid line for the upper level and a dotted line for the lower level. This behaviour was not unique to detector L2, similar behaviour was seen in L5, L9 and L11.

a) L2 (standard)

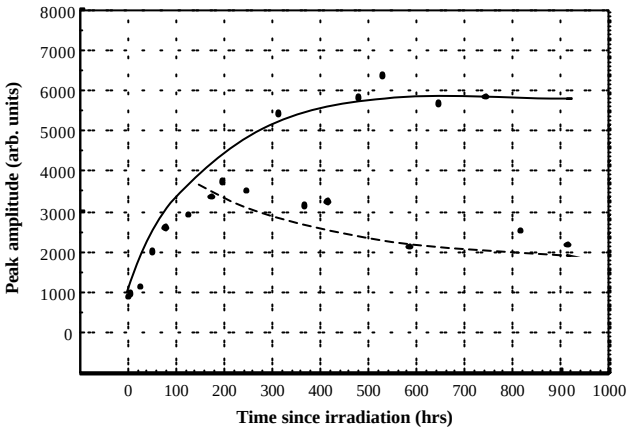

b) L5 (nitrogenised)

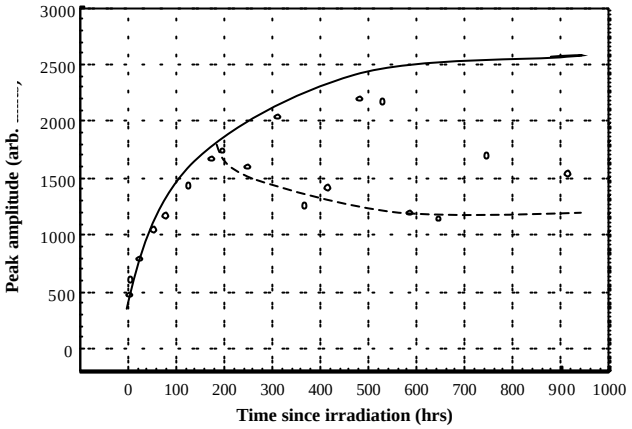

c) L9 (standard)

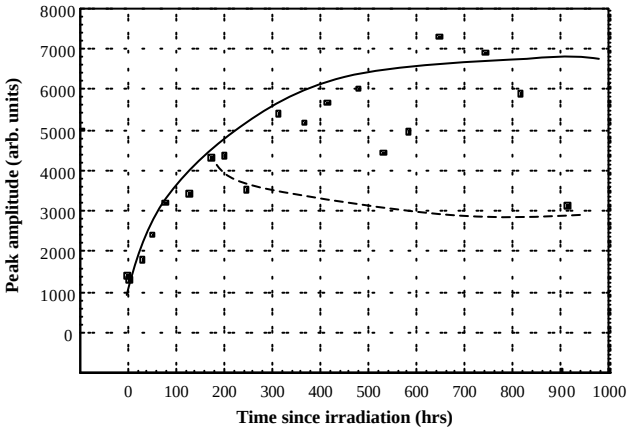

d) L11 (oxygenated)

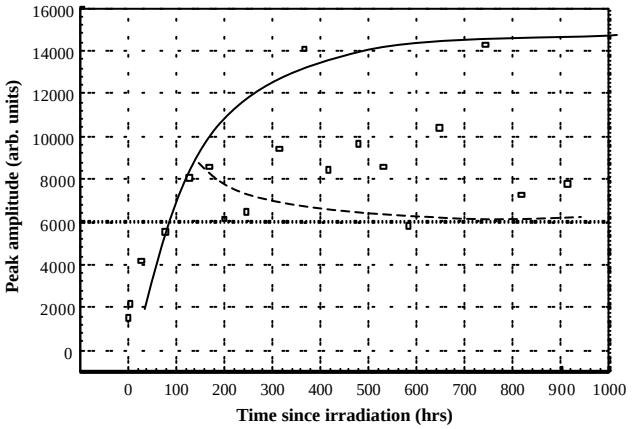

Figure 4.9: Amplitude evolution of peak 1 in a) L2 (standard), b) L5 (nitrogenised), c) L9 (standard), d) L11 (oxygenated).

It was initially suspected that the fluctuating amplitude of Peak 1 was due to an uneven injection of electron hole pairs within the detector as a result of a corresponding fluctuation in the intensity of the photon source. Measurement of the intensity of the photon source during the measurement program had shown that the photon intensity at the sample position was stable to within 3 % as measured by a photo detector placed within the sample cryostat. This would not seem likely to cause amplitude variations of the magnitude seen here. Further, corresponding variations in the amplitude of other peaks in the same ODLTCS spectrum were not apparent. The output from a laser diode is known to vary with temperature. Here however the GaAs laser diode was not situated within the cryostat and as such the diode temperature was immune to changes in the temperature. The photon pulse width was also examined and found to be stable. For these reasons it was concluded that fluctuations in the e-h injection were not responsible for the observed fluctuations in the Peak 1 amplitude.

Another possible explanation that was considered was the sample cooling rate. If the sample cooling rate was too great then differential cooling of the detector may have occurred. This however seems unlikely to affect the results in the way seen for two reasons; 1) Firstly, the sensitive volume of the detector for the ODLTCS measurement is dependent upon the penetration distance of the infrared photons within the material. For photons with a wavelength of 904 μm the absorption coefficient of silicon at 100 K is ~ 100 cm^{-1}. The penetration depth, given by the inverse of the absorption coefficient, is 10 μm. The thermal conductivity of silicon at 100 K is 9.13 $W{\cdot}cm^{-1}{\cdot}K^{-1}$ [230]. Thermal asymmetry through this thin region of material at a cooling rate of 0.1 Ks^{-1} is therefore not expected. 2) Secondly, even if thermal asymmetry was present, it would still be the case that all of the sensitive sample volume would eventually pass through the maximum peak emission temperature. If differential cooling was present then reduction in the peak amplitude could be expected but this would be compensated by a broadening of the peak width such that the peak area remained the same. This was not observed. In lower amplitude peaks, the peak width was reduced in a corresponding fashion.

With measurement anomalies ruled out it, a physical solution at the microscopic level was sought. (Note that the following measurements were undertaken about 1200 hrs after irradiation when room temperature annealing of the defects had ceased). A series of seven ODLTCS measurements were performed by repetitively cycling the sample temperature between 130 K and 80 K. In doing so the random fluctuation in the peak amplitude was removed and a systematic behaviour observed. The measured peaks in each of the seven measurements are shown in Figure 4.10. It can be seen that the peak amplitude approaches a maximum value in an asymptotic manner. In a plot of the peak amplitude versus measurement number, see Figure 4.11, this behaviour is more clearly evident.

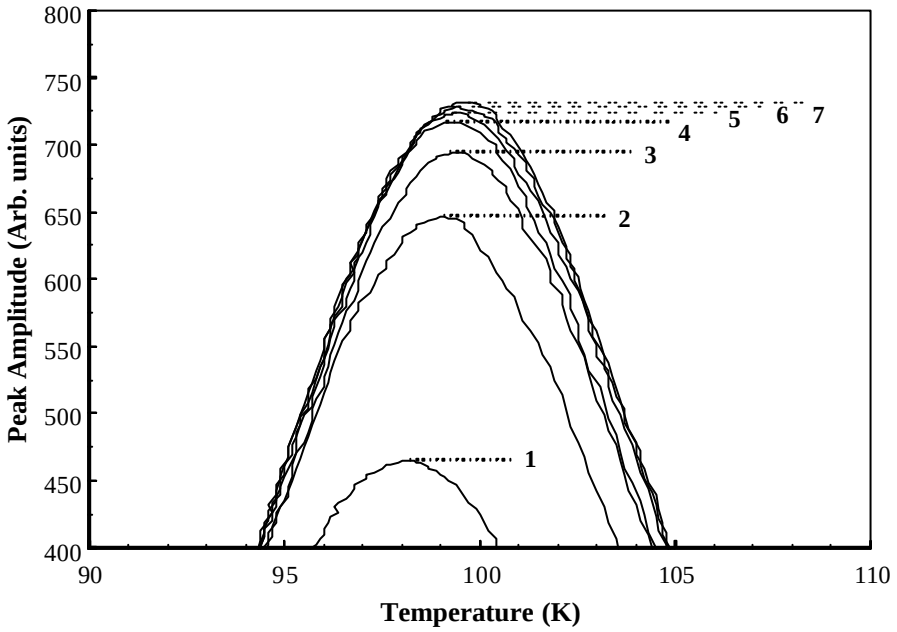

Figure 4.10: ODLTCS Peak 1 amplitude obtained in seven consecutive measurements. Each curve is labelled with the measurement number.

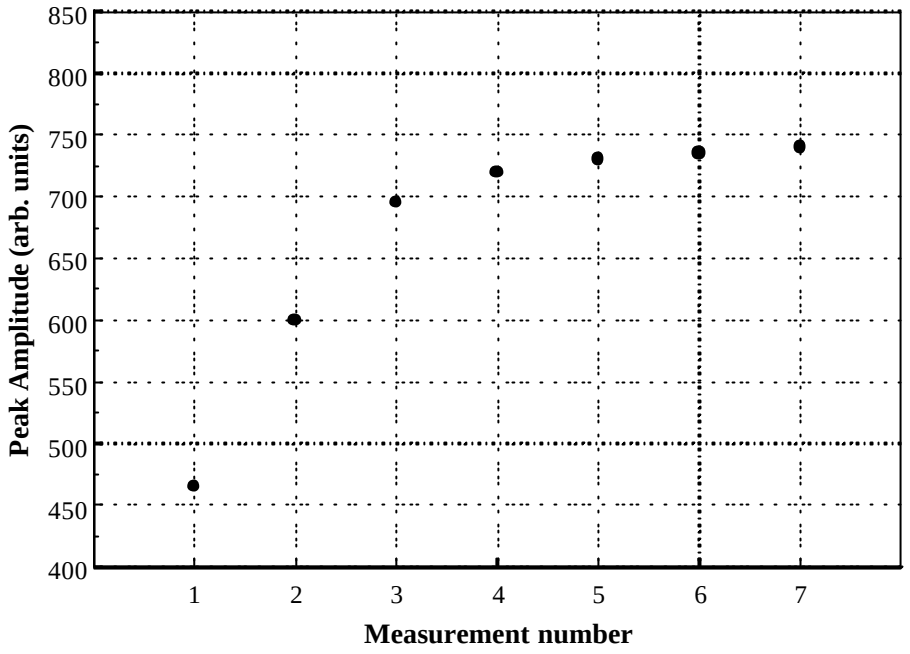

Figure 4.11: Peak 1 amplitude as a function of measurement number in a series of repeated measurements during which time the sample temperature did not exceed 130 K.

The observed behaviour could be reproduced simply by warming the detector back to room temperature before re-cooling and repeating the measurement cycle. No difference was obtained if the light source was left on or off during the warm up to room temperature and re-cooling phase.

In Figure 4.10 it can also be seen that as the peak amplitude increased, so too did the peak temperature mid point. In Figure 4.12 a plot of the peak height versus the peak mid point temperature shows a definite systematic movement of the peak towards higher temperatures as the amplitude increases. This result demonstrates that Peak 1 consists of two closely spaced peaks. The higher temperature component is associated with a metastable defect. The state in which the metastable defect is found is dependent on the thermal history of the material. The

longer the detector remains at a low temperature, about 100 K, the higher the likelihood that the defect will be in the state which gives rise to the Peak 1 contribution.

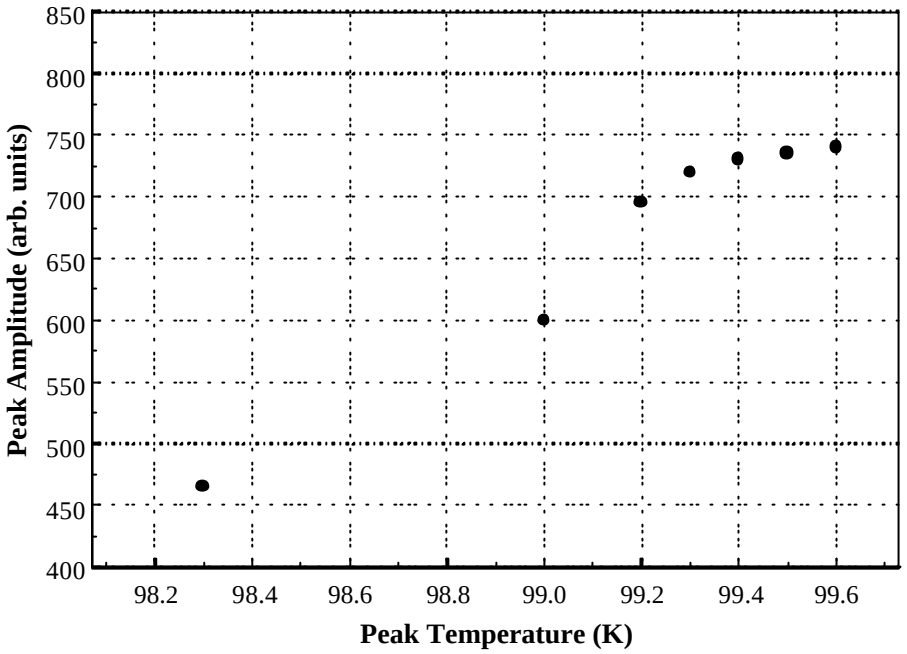

Figure 4.12: Peak 1 amplitude versus Peak 1 temperature mid point.

Metastability can occur whenever the stable configuration of a defect changes with its charge state and a substantial barrier exists for conversion from one configuration to another. Metastability in the form of bistability has been seen with the A-centre using DLTS [231]. The observations were ascribed to the carbon related centre C_s-C_i [232,233]. Those studies found that under illumination of radiation damaged silicon at a temperature of less than 50 K with 1.16 eV photons that the G17 EPR signature associated with the C_s-C_i defect disappeared and was replaced by a new EPR centre labelled L7. This new EPR centre was found to be associated with the C_s-Si_i-C_i defect. The new centre was converted back by heating the silicon in the absence of the photon source.

The C_s-C_i / C_s-Si_i-C_i defects are dominant in carbon-rich, low oxygen content silicon. The concentration of the defect is insignificant in silicon containing a high oxygen content [234].

The ODLTCS spectra seen here are not consistent with this result. It can be seen in Figure 4.9 that the greatest degree of variability in the A-centre peak amplitude occurred in L11, the oxygenated detector. The carbon content in L11 was not thought to be greater than within the other detectors. This is supported by similarly measured concentrations of other carbon related defects in all detectors (presented later in this chapter). The metastability observed here occurred at a temperature of 100 K as opposed to below 50 K as observed by others. It would therefore appear that the metastability observed here is associated with the V-O defect and not the carbon related centres as described by others.

An assignment of the source of the metastability is not important in terms of operation of silicon microstrip detectors. The energy level associated with the A-centre is relatively shallow in comparison to that of other mid band states. For this reason will not have any meaningful impact on the performance of the detectors.

The metastability is however unexpected and has not been reported by other experimenters.

Peak 2

Peak 2 was identified at a temperature of 127 K. The amplitude of the peak was found to be very low in all detectors. An increase in the peak amplitude was seen as a function of room temperature annealing. The increase was greatest in L11 (oxygenated), and least in L5 (nitrogenised). The statistical fluctuation in the amplitude corresponded directly with the statistical fluctuation in the amplitude of Peak 1 in all detectors. For this reason it was concluded that the peak was erroneous, caused by a remaining residual from Peak 1. This can be understood by recalling that the gaussian curve used to fit the correlator response was not an exact fit. The correlator function, $R(t)$, is not symmetrical about the peak temperature and displays a skewness towards the higher temperature side. A gaussian fit to this curve would have induced a small residual on the higher temperature side of the peak. It appears that this residual was identified by the peak fitting program and assigned an erroneous peak. The

amplitude of the peak was extremely small and was clearly a result of the very large amplitude of Peak 1.

Peak 3

Peak 3 was observed at a temperature of ~ 155 K. Significant changes in the peak amplitude were observed with room temperature annealing. The amplitude evolution is shown in Figure 4.13. Similar behaviour was observed in all four detectors. In the first 200 hrs the amplitude can be seen to decrease. This is followed by relative stability for the remaining 800 hrs of observation.

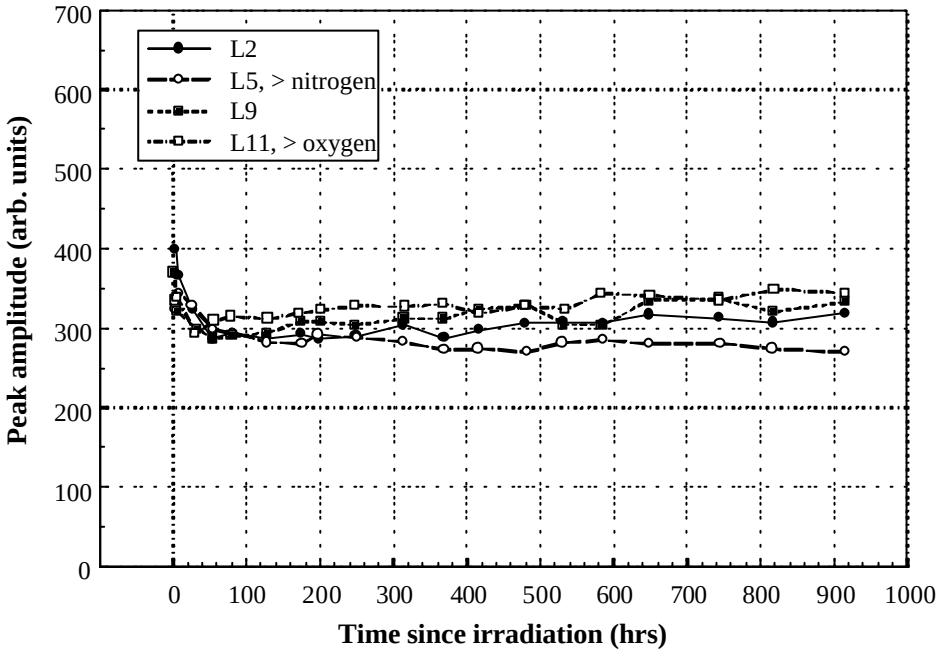

Figure 4.13: Peak 3 amplitude evolution as a function of room temperature annealing.

In Figure 4.14 the amplitude evolution of Peak 3 in detector L2 (standard) shows that a decrease in peak amplitude of ~ 25 % occurs during the first 100 hrs. This trend suggests that Peak 3 is actually composed of two closely spaced overlapping peaks. The amplitude of one component is rapidly decreasing with time and anneals out after the first 100 hours. The amplitude of the second component is relatively stable with room temperature annealing. Further evidence to support this hypothesis is an observed shift in the peak mid point temperature as a function of room temperature annealing. In Figure 4.15 it can be seen that the peak temperature shifts from an initial temperature immediately after irradiation of 159 K to a temperature of 155 K after 100 hrs of room temperature annealing. Beyond 100 hrs the Peak 3 mid point temperature remains constant for the duration of the observation period.

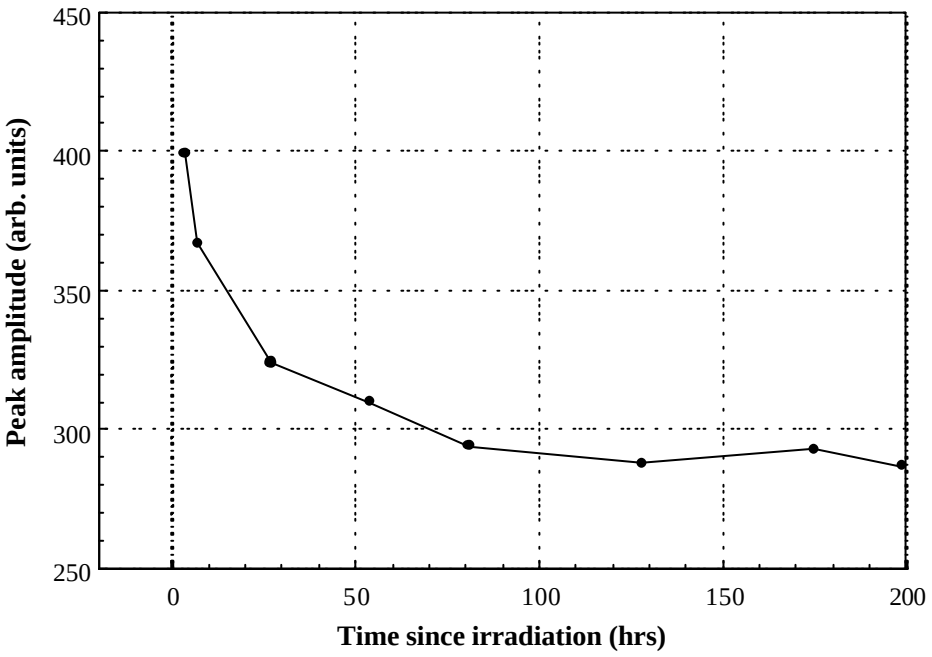

Figure 4.14: Peak 3 evolution with room temperature annealing in detector L2 (standard).

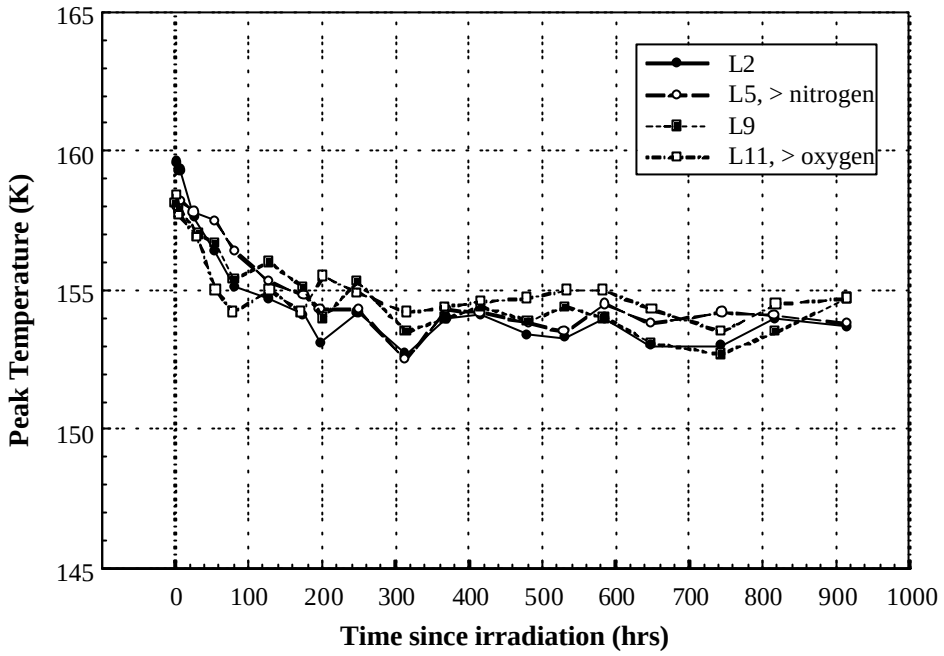

Figure 4.15: Shift in Peak 3 temperature as a function of room temperature annealing.

The stable fraction of Peak 3 is most likely produced on the time scale of the irradiation, suggesting it is a primary defect. This is deduced by an extrapolation of the amplitude data between 900 hrs and 100 hrs back to the zero time after irradiation. The activation energy calculated from Peak 3 data, obtained at the end of the room temperature annealing period, gave a value of $|0.24\ eV|$. The absolute value is given here since the band edge from which the energy is measured cannot be determined from the ODLTCS measurement. By taking into account the time constant of the rate window employed in the measurement, comparison with the literature suggests this peak is associated with the divacancy defect in the $V\text{-}V^{(--/-)}$ charge state [203]. In neutron irradiated silicon the divacancy is produced predominantly in a primary process. It is stable at temperatures well above room temperature.

No significant difference in the amplitude of the divacancy component between the oxygenated, nitrogenised or standard impurity content silicon detectors was seen. This indicates that oxygen and nitrogen have no part to play in the creation rate of the divacancy. And further,

oxygen and nitrogen have no effect on the room temperature stability of the defect, at least during the 1000 hour period of observation.

The higher temperature component of Peak 3 decayed rapidly following irradiation. The amplitude evolution of Peak 3 in detector L2 over the first 200 hrs of room temperature annealing was shown in Figure 4.14. With the amplitude of the stable high temperature component subtracted from the Peak 3 data, the evolution of the higher temperature component would appear to follow the simple exponential behaviour described by:

$$A(t) = A_0 \exp\left[-\frac{t}{t}\right] \qquad (4.4)$$

where: A_0 = amplitude at time $t = 0$,

t = decay time constant.

The Peak 3 amplitude data, corrected for the stable component, at times less than 100 hrs, was used in a plot of (ln A) versus t. The time constant was then found from the negative inverse of the curve slope. For detector L2, L5 and L9 an average time constant of 10 hrs was obtained. The time constant within L11 (oxygenated) and L5 (nitrogenised) could not be accurately obtained due to insufficient data. The data for L5 and L11 suggested that the annealing occurred at an increased rate in these materials.

In a comparison with the literature the annealing time constant of 10 hrs is similar to the time constant for the annealing of the carbon interstitial defect, C_i. The defect is associated with the well known Si-G12 signature in electron paramagnetic resonance studies [235-237]. The C_i defect has also been linked to infrared local vibrational bands at 920 cm^{-1} and 931 cm^{-1} [238] as well as a photoluminescence feature at 856 meV [239]. DLTS studies have shown that the C_i defect induces a donor state at E_v + 0.27 eV [234]. An acceptor state has also been attributed at E_c - 0.12 eV [234]. A peak associated with this lower energy level cannot be seen in the

ODLTCS spectra as it would appear below the minimum temperature scanned in these measurements.

The temperature at which Peak 3 appears in the experimental ODLTCS spectra is consistent, when the different rate window settings are taken into account, with the reported peak temperature in DLTS spectra of the C_i defect [234]. It is concluded that the annealing component of Peak 3 is the carbon interstitial.

The C_i defect is known to form at temperatures of as low as 4 K through the capture of a mobile silicon interstitial at the site of an immobile carbon substitutional atom according to the Watkins replacement mechanism [235]. The C_i defect is mobile at or near room temperature [235,238]. It has been reported to anneal as a result of being captured at the site of other impurities including O, N, P, Ga, Be, Li and C_s [240]. In high purity detector grade silicon studied here it is unlikely that capture would occur at sites of Ga, Be or Li on account of the low concentration of such impurities in this high purity material. Trapping at O, N, P and C_s could be expected. The decay time of C_i is much shorter in CZ silicon than in FZ silicon [239]. This behaviour has been attributed to the ability of oxygen to compete with other impurities to trap the mobile C_i species and thereby increase the rate of reduction of C_i. The inability to measure the time constant in L11 is consistent with this result.

The reduced decay time constant in L5 (nitrogenised) also suggests that nitrogen, at the concentration present within L5, has a role to play in the annealing of the C_i defect. The most probable explanation is that nitrogen competes with the other impurities to trap the mobile C_i defect in an analogous fashion to oxygen. Another less probable explanation is that the presence of nitrogen inhibits the initial production of the C_i defect by competing for the Si_i defects. Better data at times immediately following irradiation would be required to resolve this question. Most helpful would be EPR data in which the C_i EPR Si-G12 signature could be used to directly measure the production and decay of the C_i defect in both standard and nitrogenised silicon.

Peak 4

Peak 4 was identified at a temperature of 163 K. The evolution of peak amplitude with room temperature annealing is shown in Figure 4.16.

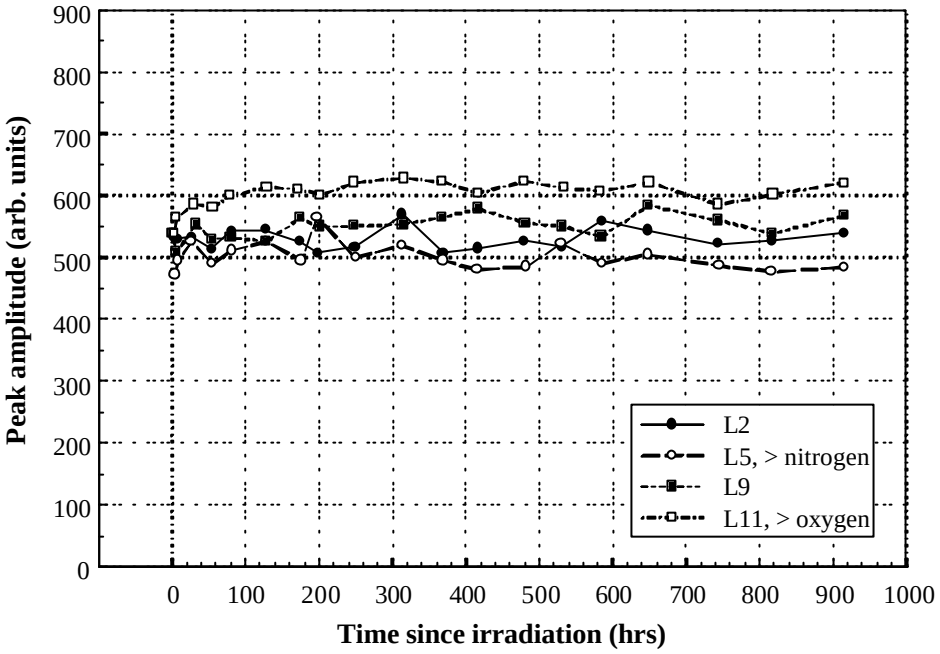

Figure 4.16: Peak 4 evolution as a function of room temperature annealing.

In all detectors no significant change in peak amplitude was seen throughout the observation period. Extrapolation of the trend back to the time of irradiation indicates that the associated defect was produced on the time scale of the irradiation. From this it may be assumed that the associated defect was produced in a primary process. Primary defects are known to include silicon interstitials, vacancies and divacancies. Since divacancies are immobile, it is not possible for them to interact with other immobile impurities. The other two species are mobile and thus capable of interacting with other impurities present within the material. Vacancies are present many days after irradiation as indicated by the continued formation of the A-centre

defect seen experimentally by the growth of Peak 1 as a function of time. It is therefore unreasonable to expect that the Peak 4 defect is due to a vacancy impurity complex. This leaves a divacancy or silicon interstitial association. Apart from the substitutional carbon production, the only other defect associated directly with the silicon interstitial is an aluminium interstitial. This result was found in low resistivity silicon with a high Al content [241]. It is not likely that the concentration of Al in the detector grade silicon studied here was sufficiently high that aluminium defects would be present. Another possible source of Al is the metallisation on both the front and rear sides of the detectors. During device processing the Al metallisation layers are formed by an evaporative process under high vacuum conditions. The device is kept at room temperature. Diffusion of Al into the Si bulk is therefore not possible.

It is therefore concluded that Peak 4 is associated with the divacancy.

Further experimental evidence to support this conclusion is available from the literature. Using TSC two peaks were identified in high purity silicon which gave rise to defects with energy states at $|0.20 - 0.24|$ eV and at $|0.24 - 0.28|$ eV [242]. These were assigned as the divacancy in the V-V$^{(--/-)}$ charge state and the divacancy in the V-V$^{(0/+1)}$ charge state respectively. The corresponding situation in the ODLTCS spectra would be that Peak 4 corresponds to the V-V$^{(0/+1)}$ defect and the stable fraction of Peak 3 corresponds to the V-V$^{(--/-)}$ charge state.

A divacancy related defect was also reported using TSC at an energy of E_v + 0.35 eV by two independent workers [243,244]. In both papers the divacancy in the more commonly reported V-V$^{(--/-)}$ charge state was also measured at an energy of E_c - 0.26 eV.

Peak 5

Peak 5 was identified at a temperature of 203 K. The evolution with room temperature annealing is shown in Figure 4.17. The same behaviour was seen in all detectors. Two trends

were identified. Firstly, the defect responsible appeared to be produced via a secondary process on a short time scale. This was most evident in the data of detector L11 (oxygenated).

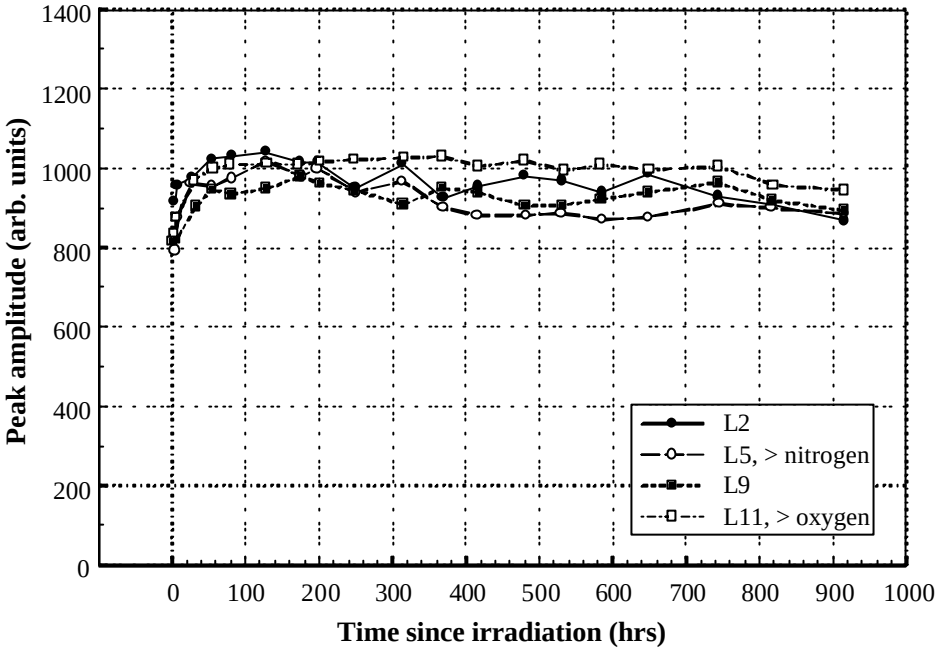

Figure 4.17: Peak 5 evolution as a function of room temperature annealing.

An expanded plot of Peak 5 evolution with room temperature annealing in L11 is shown in Figure 4.18. The trend appears to be that of the saturating exponential function:

$$A(t) = A_{\infty}\left[1 - \exp\left(-\frac{t}{t}\right)\right] \qquad (4.5)$$

where: $A(t)$ = the amplitude as a function of time, t,

A_∞ = the amplitude at the time when $t >> t$,

t = time constant of the growth.

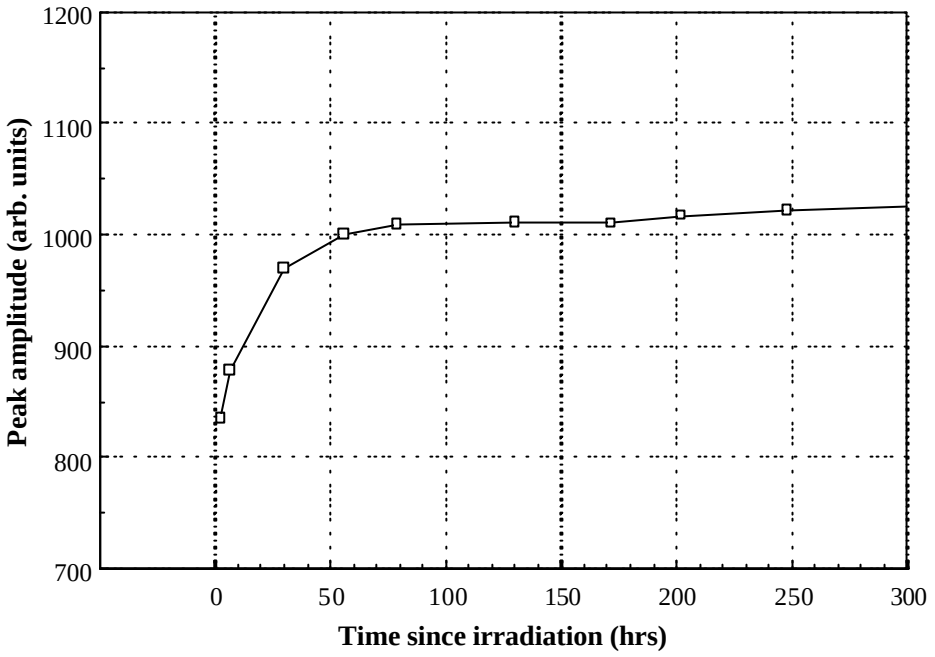

Figure 4.18: Peak 5 evolution with room temperature annealing in detector L11 (oxygenated).

The time constant can be extracted by plotting :

$$\ln\left[\frac{A_\infty - A(t)}{A_\infty}\right] \quad \text{versus} \quad \frac{t}{t}$$

This plot was made and an average time constant for the four detectors of 19.6 hrs determined. The defect activation energy was measured to be $|0.32\ eV|$.

A review of the literature does not give a definite assignment for this defect. A possible assignment is P_s-C_i. This defect was observed by Asom et al. [234] with an electron trap at an energy of E_c - 0.29 eV. The defect is produced via the capture of mobile C_i defects at the site of substitutional phosphorus atoms. The defect is primarily observed in silicon with low oxygen content, low carbon content and high phosphorus content [234].

The experimental results obtained here showed a similar concentration of this defect in the oxygenated detector as well as within the other three detectors. This is not inconsistent with the above finding since the concentration of oxygen in the oxygenated detector was of the order of $10^{16}\ cm^{-3}$ which is still quite low in comparison to what can be found in silicon grown using the CZ technique where oxygen content may be as high as $10^{18}\ cm^{-3}$. The material referred to by Asom et al. [234], was not high purity but rather electronic grade silicon and while it was referred to as low oxygen silicon, the actual oxygen content was not provided.

The material under study here was high purity silicon and for this reason contained a low carbon content. The phosphorus content would also be low. This is not consistent with the Asom finding although it may explain why the defect was found to be a minor carbon related defect as opposed to the premier carbon related defect as reported by Asom et al.

The kinetics of growth of this defect is consistent with the experimental finding for Peak 3 in which C_i defects were found to be liberated with a time constant of 10 hrs.

An altogether different defect assignment to Peak 5 is that of V_2O. This defect was initially reported in irradiated silicon by Awadelharim et al., with an energy state at $|0.30\ eV|$ [244]. The defect has also been reported more recently with a measured energy level at E_c - 0.35 eV [203]. Formation of this defect is understood to proceed via the capture of a mobile vacancy at the site of a V-O centre. This would necessitate the availability of vacancies as a function of time after irradiation. The growth of Peak 1 indicates that this is the case.

A definite assignment between the P_s-C_i and the V_2O could not be made.

From a time of 100 hrs post irradiation, at the end of the growth stage, a small trend was noted whereby the peak amplitude decreased with time. A linear fit was made to each curve to determine the rate of this trend. The fractional decrease in amplitude between times 100 hrs and 1000 hrs for each detector is tabulated in Table 4.3.

Table 4.3: Fractional decrease of Peak 5 amplitude measured between 100 and 1000 hrs.

Detector	Fractional decrease
L2 (standard)	12.3 %
L5 (nitrogenised)	11.4 %
L9 (standard)	7.78 %
L11 (oxygenated)	6.73 %

If the defect is correctly assigned as P_s-C_i then a mechanism by which this decrease could proceed may be of the form:

$$P_s\text{-}C_i + X$$

The identity of X can only be speculated. It would need to be a defect species which was liberated at a relatively slow rate with room temperature annealing. One possibility is a vacancy which are released from densely damaged defect clusters.

If rather the correct defect assignment was V_2O then decay in the peak intensity might be associated with the formation of a higher order vacancy oxygen related defect of the form V_3O. This defect would be formed through the capture of a mobile vacancy at the site of a V_2O defect.

Peak 6

Peak 6 was identified at a temperature of 219 K. In all detectors considerable changes were observed with room temperature annealing. The evolution with room temperature annealing is shown in Figure 4.19.

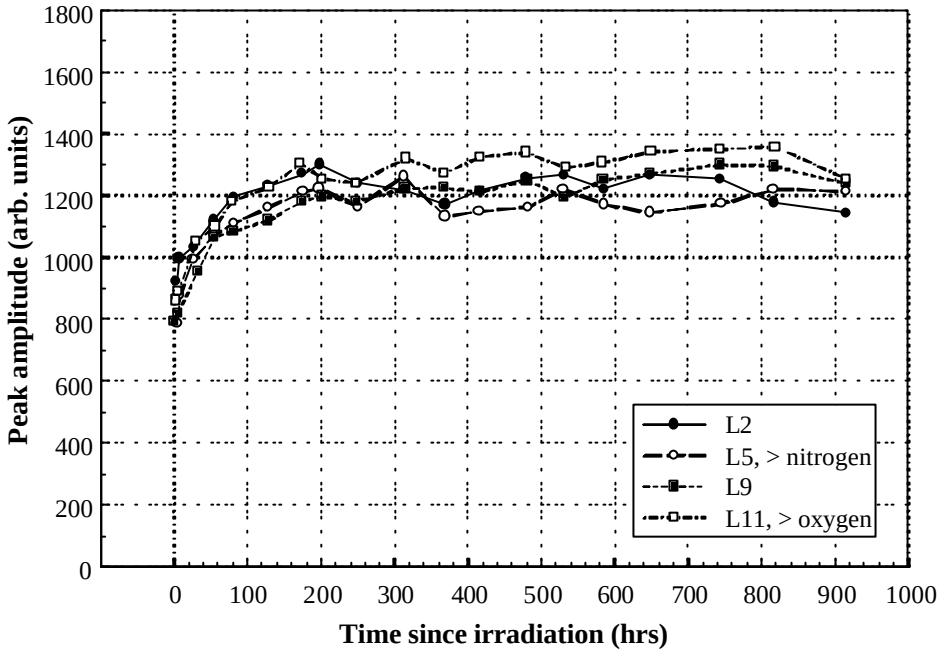

Figure 4.19: Peak 6 evolution as a function of room temperature annealing.

By 200 hrs the peak amplitude was observed to increase by 50 % of the value measured immediately after irradiation. The behaviour appeared to follow the saturating exponential equation given by:

$$A(t) = A_{\infty}\left[1 - \exp\left(-\frac{t}{t}\right)\right] \qquad (4.6)$$

t was determined in the same manner as it was for Peak 5. The plot is shown in Figure 4.20. The average time constant was found to be 52.4 hrs with variations from this number no greater than 4 %.

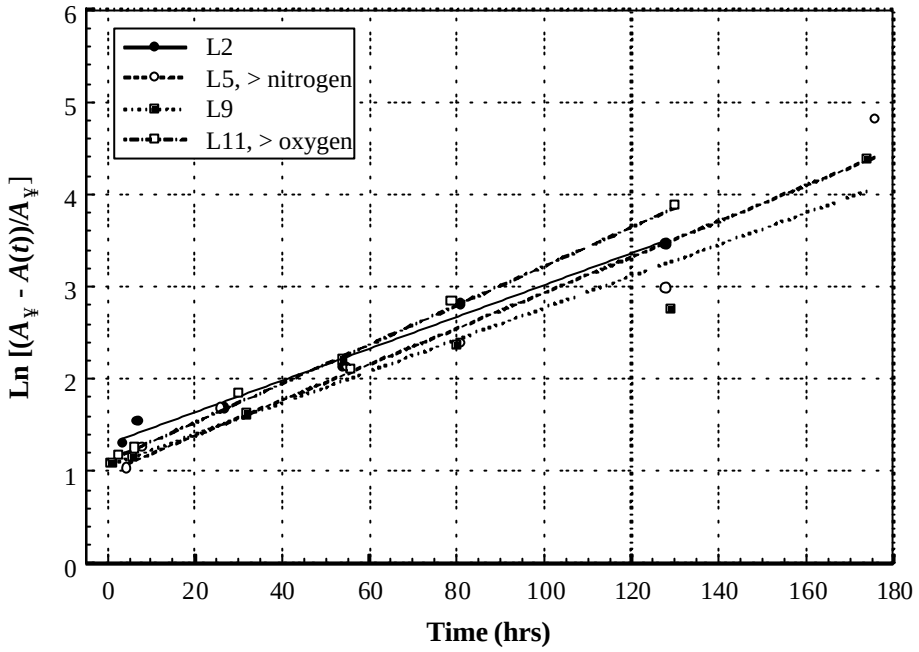

Figure 4.20: Determination of the time constant for the growth of Peak 6.

The time constant for peak growth and the location of the peak in the ODLTCS spectra suggests in comparison with the literature that Peak 6 is associated with the C_i - O_i complex [234]. This defect induces a hole trap at E_v + 0.35 eV [255]. It is also associated with photoluminescence at 789 meV and vibrational absorption at 865 cm^{-1} and 1135 cm^{-1} [258]. It is formed at room temperature following the capture of mobile C_i defects by immobile interstitial oxygen. It has been reported that the defect is only produced in CZ silicon [240]. Although in that particular work the silicon studied contained a high concentration of carbon. Substitutional carbon is well known to successfully compete with interstitial oxygen for the mobile interstitial

carbon. The capture ratio for C_i by C_s and O_i is ~ 3:1 [240]. Unless oxygen is present at similar concentrations to carbon the C_i - O_i defect will not form at measurable levels.

The rate of formation of C_i - O_i is also dependent on the availability of C_i. It was found in the analysis of Peak 3 that C_i defects are liberated by the capture of silicon interstitials at the site of substitutional carbon. A time constant for release of C_i of 10 hrs was measured.

Peak 7

Peak 7 was identified at a temperature of 240 K. The evolution with room temperature annealing is shown in Figure 4.21. The same behaviour was seen in all detectors. Peak amplitudes differed considerable between different detectors. The amplitude in detectors L9 and L11 was similar. In L5 the amplitude was approximately 85 % that of the first two detectors. While in L2 the amplitude was about 75 % that of the first two detectors.

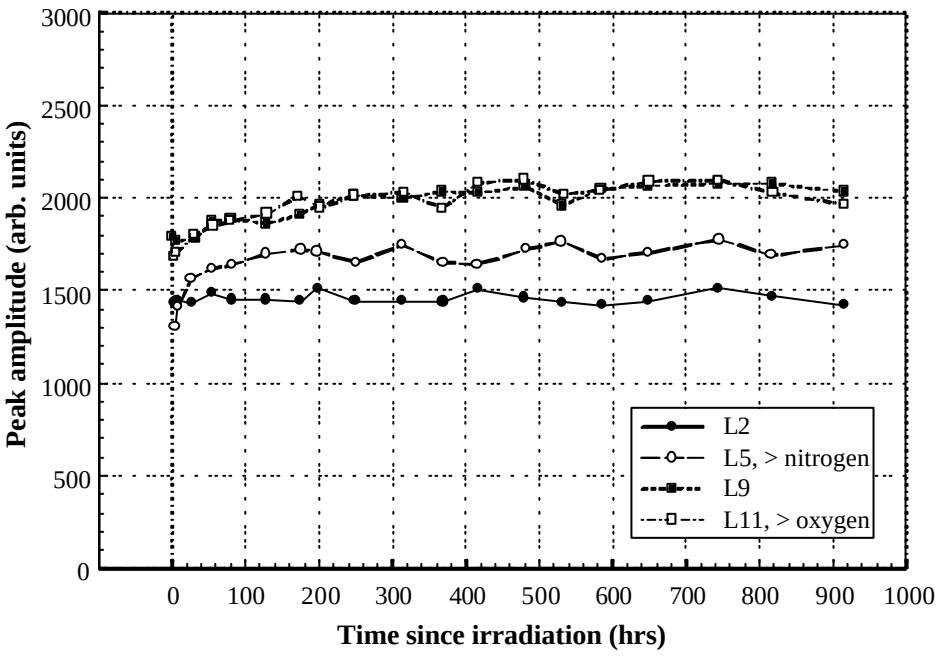

Figure 4.21: Peak 7 evolution as a function of room temperature annealing.

The average temperature of Peak 7 in detectors L9 and L11 was 242 K, while the average in detectors L5 and L2 was 239.3 K. This suggests that Peak 7 is in fact made up of two unresolved closely spaced peaks. The higher temperature component was greater in L9 and L11 as evidenced by the higher peak amplitude shown in Figure 4.21 and the higher average temperature.

In other DLTS studies peaks located about this temperature have been assigned as either the divacancy in the single minus charge state $V\text{-}V^{(-/0)}$, or the E-centre V-P, or a combination of both. The $V\text{-}V^{(-/0)}$ defect has been associated with an acceptor level at E_c - 0.41 eV [243,245]. The V-P defect has been associated with an acceptor level at E_c - 0.44 eV [243,245]. Similar energies have been quoted by many others and although they vary it is always the case that the $V\text{-}V^{(-/0)}$ energy is less than that associated with V-P. Applying this information to the Peak 7 data it would appear that for the proposed two closely spaced peaks that the lower temperature component is associated with the $V\text{-}V^{(-/0)}$ defect, and the higher temperature component is associated with the V-P defect. The activation energy is not the only component which determines the peak temperature, the pre-factor of Equation 4.3 also has an influence. Its effect is however only minor and generally the activation energy gives a good indication of the peak temperature.

In the previous analysis Peak 3 was attributed to the divacancy in the $V\text{-}V^{(--/-)}$ charge state. The rate of introduction was found to be the same in all detectors. This is consistent with accepted view that the divacancy is produced in a primary process. This being the case, the difference in amplitude in Peak 7 can be explained by the varying concentration of the E-centre component.

The production of the E-centre is understood to occur via the capture of vacancies by substitutional phosphorus atoms. The Peak 1 analysis showed that vacancies are present for many days after irradiation. It should thus be expected that V-P would continue to be formed after irradiation while vacancies are still present and the substitutional phosphorus concentration is not exhausted. Evidence of this continued formation was seen in detectors L5, L9 and L11

which were those detectors with the highest Peak 7 amplitude. No growth with room temperature annealing was seen in detector L2. This was consistent with the observation that the average temperature of Peak 7 in L2 was the lowest of the four detectors. This would indicate that phosphorus was present in a lower concentration in L2 than within the other 3 detectors.

Close correlation of the V-P component with the effective impurity concentration was not seen. This does not conflict with the above argument since the effective impurity concentration in high purity detector grade silicon is achieved through compensation of the phosphorus concentration by boron according to:

$$N_{eff} = |[P] - [B]| \qquad (4.7)$$

The implication here being that for two samples of silicon with the same effective impurity concentration the phosphorus concentrations can be considerably different.

In summary, the lower amplitude of Peak 7 in detector L2 is explained by a smaller concentration of phosphorus which has resulted in the lower production of V-P defects. No measurable growth of the V-P centre was seen in detector L2 and the peak temperature lower reflecting the dominance of the V-$V^{(--/-)}$ component.

Unfortunately no data on the P and B content in each of the four detectors was available to further support this conclusion.

4.5 Comparison of ODLTCS Peak Evolution with Changes to N_{eff}

In search of a mechanism by which silicon might be radiation hardened against the detrimental effects of room temperature annealing of N_{eff}, a comparison was made between the magnitude and time properties of the changes to N_{eff} with the ODLTCS peak evolution data. As discussed extensively in Chapter 2, the effect of room temperature annealing on N_{eff} in type inverted silicon detectors leads to a short term annealing stage where N_{eff} is reduced by approximately 45 % over a period of about 200 hrs. This is followed by a reverse anneal where

N_{eff} increases by approximately 200 % from the minimum reached in the short term anneal over a period of approximately 200 days.

In the ODLTCS spectra the most significant changes to peak magnitude was associated with Peak 1 and Peak 6. Smaller but non-negligible changes were also seen in the magnitudes of Peak 3 and Peak 5. Peak 1 is the A-centre, made up of a combination of predominantly the V-O defect and to a lessor extent the C_i-C_s defect. The energy level associated with this defect is located at E_c - 0.18 eV. The state behaves as an electron trap. The location of the energy state is well into the upper half of the bandgap and well above the Fermi level in type inverted silicon. The electron occupancy of the trap is therefore low. For this reason this defect is not likely to play a role in alteration and evolution of N_{eff}. The relative proximity of the energy state to the band edge also limits the effect the state will have on carrier generation and hence the detector reverse current. In summary the A-centre is relatively benign.

Peak 6 was seen to increase in magnitude by approximately 50 % over a period of about 200 hrs. This is in close correlation with the short term annealing of N_{eff}. It is not possible from the ODLTCS measurement to determine whether the defect associated with Peak 6 is an electron or hole trap. It is however well established within the literature that Peak 6 is associated with a hole trap at an energy level of E_v + 0.36 eV. The energy level measured in the ODLTCS data was also $|0.36$ eV$|$. The hole trapping behaviour would support a hypothesis that this defect is associated with the short term annealing of N_{eff} whereby the silicon *p*-type conductivity decreases. If so, a means by which the silicon could be radiation hardened against the detrimental change to N_{eff} would be through the promotion or enhancement in the formation rate of this defect. A more detailed examination of how this might be achieved is given in the next section.

Peak 3 was also seen to evolve on a time scale of the short term reverse anneal of N_{eff}, albeit a smaller change in magnitude of about 15-25 %. The peak was found to be associated with two components. One component was the divacancy in a charge state of V-$V^{(--/-)}$. This defect was stable and did not evolve with room temperature annealing. The second component was the mobile C_i defect. This defect is associated with a hole trap with an energy state at $|0.27$

eV| [234]. In the ODLTCS results the defect was observed to anneal out with a time constant of 10 hrs. Removal of this defect would have lead to an increase in the *p*-type conductivity. The relatively low magnitude of Peak 3 indicates that the defect is present within the irradiated silicon at a relatively low concentration in comparison to that of other defects with larger peak amplitudes. In addition, the defect annealed with a very short time constant of only 10 hrs. These two observations indicate that this defect could make at most only a minor contribution to the short term annealing of N_{eff}.

In terms of identifying a defect responsible for (or associated with) the long term reverse annealing of N_{eff} the results obtained here are less encouraging. The period over which ODLTCS measurements were performed was 100 hrs or 42 days. In this period of time the expected increase in N_{eff} according to Bates et al. [128], is approximately 60 %. No peaks in the ODLTCS spectra were observed to change by this magnitude during this time period.

The most significant long term trend was observed in Peak 5 where an average amplitude decrease in all detectors was 10 %. Peak 5 was attributed to either the P_s-C_i or V_2O defect. A number of papers have been published in which it is claimed that the V_2O defect is responsible for the long term anneal of N_{eff} [246,247]. A small change in the defect concentration based on the change to the peak height in the ODLTCS data, as well as a failure to make a positive identification of the V_2O defect means that the experimental data obtained here offers only limited support to this possibility. If this assignment is correct the radiation hardening of the silicon by increasing the oxygen content of the silicon could be possible. The mechanism, which has been suggested previously by MacEvoy [247], is via the decreased production the V_2O defect as a result of the gettering of vacancies by the oxygen atoms in the formation of the V-O defect.

No other peaks in the ODLTCS spectra were observed to evolve with room temperature annealing on the time scale of the reverse annealing of N_{eff}. It may be that the evolution is a complicated function of many small changes in different defects. The data obtained here was not sufficiently robust to formulate such an explanation.

Another possibility was that the responsible defect was unobservable by ODLTCS on account of the limited temperature interval scanned. The minimum temperature was 80 K. For a correlator time constant of 5 ms the region of the band gap in which defects are detectable extends from the middle of the band in both directions to points 0.16 eV from the conduction and valence band edges. For this reason a defect with an energy state outside of this observable interval should not be precluded.

Some additional evidence which lends support to the possibility that a relatively shallow level energy state is responsible for the long term room temperature annealing of N_{eff} is the behaviour of the reverse current. The reverse current reduction with room temperature annealing suggests that the net concentration of deep level defects is significantly reduced with time. (Note also that an alternative explanation for the radiation induced reverse current is via 'intercentre charge transfer' [248]). No evidence of a significant reduction in deep level defect concentration was seen in the ODLTCS spectra. If however a relatively shallow level acceptor type impurity was being introduced then an increase in the reverse current would not be expected.

The simplest candidate for a shallow level impurity is boron. Boron is the standard *p*-type shallow level impurity in high purity silicon. As a result of irradiation the boron electrical state can become inactive due to the displacement of the boron atom substitutional site to a interstitial site [249-253]. It is possible that during the subsequent room temperature annealing phase that the boron electrical state is reactivated as a result of the restoration of the boron atom to a substitutional site. This would occur through the capture of a mobile vacancy at the site of the interstitial boron atom. Such a mechanism was proposed by Wunstorf et al. in 1996 [254]. Confirmation of this result could be obtained using photo luminescence.

4.6 A Mechanism for Radiation Hardening Silicon by Defect Engineering

The correlation between the growth of Peak 6 and the short term reverse anneal of N_{eff} suggests that an increased rate of production of the associated defect could be a means by which the silicon radiation hardness could be improved.

The evolving component of Peak 6 is the C_i-O_i defect. As mentioned previously the defect is formed via the capture of the mobile C_i defect at the site of an immobile interstitial oxygen atom. The C_i defect is produced following the ejection of substitutional carbon by the highly mobile silicon interstitials. The C_i-O_i defect is formed at room temperature [255], and is stable at temperatures of up to 600 K [259]. It is associated with a vibrational absorption line at 865 cm^{-1} and 1125 cm^{-1} [258], a photoluminescence line at 789 meV and an electron paramagnetic resonance signature known as Si-G15 [259].

The availability of both oxygen atoms and carbon interstitials is a prerequisite for the formation of the C_i-O_i defect. Since O_i is immobile and present in the material prior to and after irradiation, the rate of creation of C_i-O_i will increase with an increased oxygen concentration in the starting material. For carbon the situation is more complicated. This is on account of an experimental finding that C_i defects are preferentially trapped at immobile C_s sites as opposed to O_i sites [255]. In order that oxygen could successfully compete with the C_s to trap the mobile C_i defects it is necessary that the oxygen concentration in the starting silicon is well in excess of the carbon concentration. In addition, the carbon content in the starting silicon would need to be low so as too minimise capture of C_i defects at the C_s sites. Conversely, if the concentration of carbon was too low then the availability of C_s for the production of C_i may become exhausted. This could result in the creation of unwanted defects such as C_i-O_i-Si_i. This defect has been observed in silicon irradiated by 2 MeV electrons only once the fluence exceeds 10^{16} cm^{-2} [256]. Associated with the creation of C_i-O_i-Si_i defect is a decline in the concentration of the C_i-O_i defect. It would therefore be necessary that the carbon concentration is carefully optimised. For example, using this 2 MeV electron irradiation result of Brozel et al.[256], and the assumption that the carbon content in the material studied is similar to what is found in standard high purity silicon, the limitation in the supply of C_i can be estimated for neutron irradiation by equating the equivalent deposition of NIEL between 1 MeV neutrons and 2 MeV electrons. In the electron case the fluence at which point the C_i-O_i-Si_i defects began to be produced was 10^{16} cm^{-2}. For 1 MeV neutrons, or high energy protons, the corresponding fluence is 6×10^{14} cm^{-2}. This is similar to what is expected in the lifetime of ATLAS. In this simple analysis the exhaustion of carbon

would not be anticipated. This is under the assumption that the carbon content in the electronic grade silicon studied by Brozel et al. [256], was similar to that in the high purity silicon. This is not necessarily the case and further consideration of this point should be made prior to the preparation of silicon for ATLAS.

Experimental verification of an improvement in the radiation hardness of oxygenated silicon to changes in N_{eff} under charged hadron irradiation was recently reported by the ROSE collaboration [260].

Another consequence of the proposed mechanism of defect engineering is the effect of a higher oxygen concentration on the production of other defects. It was seen that the concentration of the A-centre was significantly enhanced in the oxygenated material. Associated with the V-O defect is the energy state at E_c - 0.18 eV. The relatively shallow energy in comparison to that of the true mid band states renders the V-O defect harmless in terms of the electrical properties of the material as pointed out in section 4.5.

4.7 The Nitrogenised Detector

Some discussion is also required regarding the ODLTCS results for the nitrogenised detector. The most obvious difference in the ODLTCS spectral evolution between the nitrogenised detector and the other detectors related to Peak 1. The main finding was that:

- The Peak 1 amplitude in the nitrogenised detector was approximately 50 % of the amplitude of Peak 1 in L2 and L9, the detectors with standard impurities.

This result suggests that the presence of nitrogen inhibits the production of the V-O defect during room temperature annealing. Since vacancies are produced as a primary defect, the rate of production would be unaffected by the presence of nitrogen. The mechanism by which the production rate of V-O defect is produced is most probably associated with a trapping mechanism of mobile vacancies at sites of immobile nitrogen atoms.

To understand this result from a microscopic level consider some known facts regarding the physical behaviour of nitrogen in silicon. Firstly nitrogen, a group IV element, behaves drastically different in crystalline silicon to other group IV elements such as phosphorus, arsenic

or antimony. While these elements provide electrically active shallow donor states, donor like electrical activity attributable to nitrogen in silicon has not been seen for limits of detectability of 10^{12} cm^{-3} [261], in either *n* or *p*-type silicon [262], or at most, less then 1% of the nitrogen concentration displays a donor nature [263]. The solid solubility of nitrogen in silicon is only $(4.5\pm1.0)\times10^{15}$ cm^{-3} [264], a value of at least two orders of magnitude less than that of other light elements such as oxygen or carbon. Combined, the low electrical activation and low solid solubility of nitrogen in silicon explains the negligible importance of this impurity as a donor in silicon.

The electrically active group IV impurities exist in the silicon lattice at substitutional sites. Only limited experimental evidence is available which would suggest nitrogen is also substitutionally located. Electron paramagnetic resonance (EPR) has revealed the presence of a number of signatures associated with nitrogen. An EPR centre labelled 'Si-SL5' was identified as possibly being due to substitutionally located nitrogen in silicon [265,266]. This signal has been found in nitrogen implanted silicon following rapid annealing (using pulsed laser annealing). The EPR signature provides evidence that this centre consists of a nitrogen atom located at a substitutional site within the silicon lattice and distorted off centre along a <111> direction. Theoretical calculations support the stability of such a configuration [266,267].

Other experimental evidence supports an alternate structural configuration for nitrogen. In melt doped silicon, infrared absorption measurements have revealed the presence of nitrogen containing centres with bands reported at 963 and 764 cm^{-1} [262,270-272]. The incorporation of N^{15} instead of the more abundant isotope of N^{14} gave absorption frequencies of 937 and 748 cm^{-1} [273]. This shift correlates with calculations for localised mode vibrations of diatomic molecules of nitrogen bonded to silicon [273]. It was suggested that a molecular form of nitrogen could exist at interstitial sites within the silicon lattice [274]. In comparison to the Si-O bond in oxygen doped silicon, no sub peaks were observed on the 963 cm^{-1} band associated with interactions with the various naturally occurring silicon isotopes. This demonstrates that the Si-N bond is weak and that the nitrogen pair behaves almost as if it is isolated from the silicon

lattice [262]. The present understanding is that this centre consists of two paired nitrogen atoms behaving as if molecular nitrogen and only loosely coupled to the silicon lattice via weak Si-N bonds. While the exact bonding nature is not clear, three possibilities exist. The nitrogen atoms exist at two adjacent silicon lattice sites (N_sN_s), or the nitrogen pair is located in one substitutional site $(N_2)_s$, or the pair is located at an interstitial site $(N_2)_i$. The third possibility is unlikely based on evidence provided by a low temperature electron irradiation study [275].

In the case of the substitutional nitrogen centre, the low temperature annealing study revealed the transformation of this centre into the paired centre described in the preceding paragraph [265]. Results of selective N^{14} and N^{15} incorporation during crystal growth showed that nitrogen atoms are mixed completely in the melt and paired nitrogen atoms are incorporated into the single crystal through the growth interface [262]. These two results in addition to the lack of observation of the EPR SL5 centre in melt grown silicon indicate that under equilibrium processes, the nitrogen pair is the more stable configuration for nitrogen in silicon. In comparison to the configuration of other group IV impurities found as single atoms located in clearly substitutional sites, the lack of a shallow donor level associated with nitrogen in silicon can be appreciated. It has been postulated that the improved physical hardness of nitrogen doped silicon is associated with the physical size of the nitrogen molecule acting as a large obstacle for dislocation movement [262].

The large physical size of the nitrogen complex could also explain the reduced production of the A-centre defect. The nitrogen complex may act as an obstacle in the diffusion of mobile defect species throughout the material. Significant distortions of the silicon lattice caused by the presence of the di-nitrogen complex induces significant potential wells at which point mobile defect could be trapped. The trapping of the mobile vacancies at the potential well sites would cause a reduction in the availability of vacancies and therefore a reduction in the formation of the V-O defect.

Apart from the behaviour of the Peak 1 feature, no other differences in the ODLTCS spectral evolution were seen between the nitrogenised detector and the other detectors.

4.8 Conclusion

It is important to note, prior to a statement of the conclusions, that the process of peak fitting using guassian peak shapes to model the correlator output was not ideal. The non-guassian shape of real data, and the possibility of local short range interactions in defect clusters which can alter the peak shape of the observed defects, are two factors that could affect the peak fitting process. Despite these possible sources of error, which it should also noted are common to other deep level defect characterisation techniques such as conventional DLTS, the peak assignments were very carefully matched against a considerable bank of data compiled in the literature. Definitive assignments quoted in the literature have usually been obtained through intercomparison of DLTS type data with EPR type results.

The physical process of defect filling and emptying in response to some external stimulus is identical for both the ODLTCS and the conventional DLTS technique. The techniques differ only by the way in which the signal is extracted from the sample. In ODLTCS it is a change in the sample conduction induced by additional carriers emitted from the emptying defect, while in DLTS it is a change in the capacitance of the junction induced by the additional carriers emitted from the emptying defect.

The main experimental findings are summarised as follows:

- ODLTCS was found to be a useful technique for observing the evolution of the deep level defect spectrum during room temperature annealing in silicon detectors irradiated by ~ 1 MeV neutrons to as fluence of $7.5\times10^{13}\,cm^{-2}$.
- Metastability was observed in the A-centre. This defect is known to consist of a combination of the V-O defect and the C_s-C_i defect. Metastability of the C_s-C_i defect has been reported at temperatures below 50 K. The prevalence of the ODLTCS measured metastability in the oxygenated detector, and the fact it occurred at a temperature of ~ 100 K suggests that some form of metastability is associated with the V-O defect.

- Comparison of the ODLTCS spectral evolution due to room temperature annealing with characteristic evolution of N_{eff} with room temperature annealing was made. Changes in the C_i-O_i defect concentration correlated strongly with the short term annealing of N_{eff}.
- Based on the C_i-O_i finding it may be feasible to enhance the advantageous short term annealing stage by maximising the formation of this defect. This would lead directly to improved radiation hardness of the silicon. It was postulated that this would be achieved by increasing the oxygen content in the starting silicon and carefully optimising the carbon content. This mechanism is supported be recently reported work which found that for charged hadron irradiation the damage to N_{eff} was three times less in oxygenated silicon and worse in silicon with a high carbon content [260].
- A small correlation was found between the evolution of a deep level defect signature and the detrimental long term annealing of N_{eff}. The associated defect was assigned as either the P_s-C_i or V_2O or defect.
- Since no strong correlation between the evolution of a deep level defect and the evolution of N_{eff} was observed, it was suggested that a shallow level electrical state maybe involved. The most practical assignment is boron. Under irradiation the substitutional boron atom, which is associated with a shallow level acceptor state, is dislodged to a interstitial site and the electrically activity deactivated. Under the action of room temperature annealing it is proposed that the boron atom reverts to a substitutional site and in doing so re-activates the electrical activity. This mechanism has been proposed previously by Wunstorf et al. [254].
- The formation of the V-O defect was reduced in nitrogenised silicon. The mechanism proposed to explain this effect is associated with the trapping of mobile vacancies within the potential well surrounding the di-nitrogen complex.
- The presence of nitrogen in silicon has negligible influence on the creation and evolution of other deep level defects observed using ODLTCS.

Chapter 5

A Reference Dosimeter for Monitoring Bulk Radiation Damage in Silicon Devices Exposed to Neutrons

5.1 Introduction

It is well known that displacement damage in neutron irradiated silicon is highly dependent on the neutron energy. This was observed experimentally in Chapter 3 where the reverse current increase in the neutron irradiated detector test structures was found to differ between detectors irradiated at different angles, and hence with a different energy spectrum of neutrons. In a spread of neutron energies from a low of 0.57 MeV to a maximum of 0.88 MeV a variation in α (the reverse current damage constant defined in equation 2.1), of 30 % was observed. Even larger variations in α can be found in the literature as shown in the tabulation in Table 2.1 of Chapter 2. Again, the variation can be attributed to differences in the neutron spectrum of the facility at which the measurement was performed.

Both of these points demonstrate the difficulty in making intercomparison of radiation hardness results obtained at different facilities with different neutron spectra, or even within the same facility at different points in the irradiation rig. A direct intercomparison of results can be facilitated by normalising the irradiating conditions using the silicon damage KERMA via the equivalent 1 MeV neutron fluence in silicon methodology. The procedure required is however quite cumbersome and further, it is not always possible for reasons outlined in the following section.

It was suggested in the conclusion of Chapter 3 that a simple and reliable dosimeter which was capable of responding directly in terms of the equivalent 1 MeV neutron fluence in silicon could be used as a simple alternative. Such a device could be combined with the device under

test and inserted into the radiation field to allow a direct assessment of the radiation damaging field. The response of these dosimeters at other facilities would permit a direct comparison of the radiation hardness test results between the two different facilities. Since ideally the response would be in terms of the equivalent 1 MeV neutron fluence, device radiation hardness results obtained with the dosimeter could also be compared with the existing database of results obtained over the many years of electronic device radiation hardness testing. The dosimeter could also be used to provide on-line monitoring of neutron damage during operation. For example, the dosimeter could be mounted with the microstrip detectors within ATLAS to monitor the accumulated neutron damage in real time during the experimental program.

The dosimeter proposed for this purpose is a PIN Dosimeter Diode manufactured from detector grade silicon. This type of device has been used previously for monitoring the damaging efficacy of fast neutron fields in silicon based devices in terms of the equivalent 1 MeV neutron fluence [276,277]. In both of those studies the device was calibrated in a neutron field with a known spectrum and then used as a dosimeter in second neutron field which had a similar spectrum. The dosimetric performance of the device in a field with a dissimilar spectrum to the calibration spectrum was not investigated. To provide confidence that a PIN Dosimeter Diode is capable of responding accurately in terms of the equivalent 1 MeV neutron fluence in any arbitrary neutron field it is necessary to show first that the dosimeter response is independent of the type of neutron energy spectrum used for calibration. That is, the dosimetric response should be the same regardless of the neutron energy spectrum of the calibration field. The purpose of this chapter is to test experimentally whether this is the case.

The work begins by a brief examination of the equivalent 1 MeV neutron fluence methodology and its use in electronic device radiation hardness testing.

5.2 Equivalent 1 MeV Neutron Fluence in Silicon

The equivalent 1 MeV neutron fluence in silicon is the fluence of 1 MeV neutrons which would have the same damage effect in silicon as the particular wide energy neutron spectrum of interest. In ASTM E722-94 [196] this parameter is defined for any arbitrary material and arbitrary monoenergetic energy as the equivalent monoenergetic neutron fluence, $\Phi_{eq,Erefmat}$. It is given by:

$$\Phi_{eq,Eref,mat} = \frac{\int_0^\infty \Phi(E) F_{D,mat}(E) dE}{F_{D,Eref,mat}} \qquad (5.1)$$

where: $\Phi(E)$ = incident neutron energy spectrum,

$F_{D,mat}(E)$ = neutron displacement damage function for the irradiated material as a function of energy (damage KERMA), and

$F_{D,Eref,mat}$ = displacement damage reference value for the irradiated material at the reference energy, E_{ref} (damage KERMA at E_{ref}).

While the energy at which the equivalent fluence is normalised is essentially arbitrary, the use of 1 MeV gained wide spread acceptance within the electronics radiation hardness testing community. The material of interest is in most cases silicon.

Calculation of $\Phi_{eq,1MeV,St}$ requires knowledge of both the silicon displacement damage function, $F_{D,Si}(E)$, and the neutron energy spectrum, $\Phi(E)$, at the point of irradiation. The silicon displacement damage function is often referred to as the displacement damage cross section, *D*. This quantity is equivalent to the Non Ionizing Energy Loss (NIEL). *D* is quantified in units of MeV·mb, where as NIEL is quantified in units of keV·cm^2·g^{-1}. For silicon, with an atomic

density of 28.086 g·mol^{-1}, the relation between D and NIEL is 100 MeV·mb = 2.144 keV·cm^2·g^{-1}. The NIEL value may also be referred to as the 'damage KERMA' where KERMA is an acronym for Kinetic Energy Released per Mass Absorber.

For silicon, theoretical treatments of $F_{D,Si}(E)$ [7-17] have contributed to an accepted formulation within ASTM E722-94 [196]. In this document $F_{D,Si}(E)$ is referred to as the Silicon Displacement KERMA Function, $K_{D,Si}(E)$. $K_{D,Si}(E)$ is identical to $F_{D,Si}(E)$. The units of $K_{D,Si}(E)$ are MeV·mb. The $K_{D,Si}(E)$ tabulation in ASTM E722-94 extends from a neutron energy of 0.11750×10^{-8} MeV to 19.9500 MeV. This energy range adequately covers the U-235 fission neutrons. A plot of $F_{D,Si}(E)$ is shown in Figures 5.1 and 5.2. Due to the existence of a sharp resonant feature in the neutron cross section around 1 MeV in silicon, $K_{D,Si}(E)$ at 1 MeV is assigned an average value of $F_{D,1MeV,Si} = 95 \pm 4$ MeV·mb [196,290]. The resonant feature is most clearly evident in Figure 5.2.

Some neutron fields, such as those produced by high energy accelerators and spallation neutron sources as well as space environments, may contain neutrons with energies in excess of 20 MeV. At such energies the silicon displacement KERMA function is known with less certainty. Work continues to be published for these higher energies [286,287]. The most up to date nuclear cross sections from which $F_{D,Si}(E)$ is calculated is available [291].

It should also be noted that tabulations of the displacement damage functions of other semiconductor materials have been determined. Most notable amongst them is GaAs [196,288,289,292].

The neutron energy spectrum, $\Phi(E)$, can be measured using neutron detectors with an energy dependent response. Proton recoil spectrometers, time of flight techniques or foil activation analysis can be used. For neutron fields characterised by a range of neutron energies and neutron fluxes, generally only the foil activation technique can be used for an accurate determination of $\Phi(E)$.

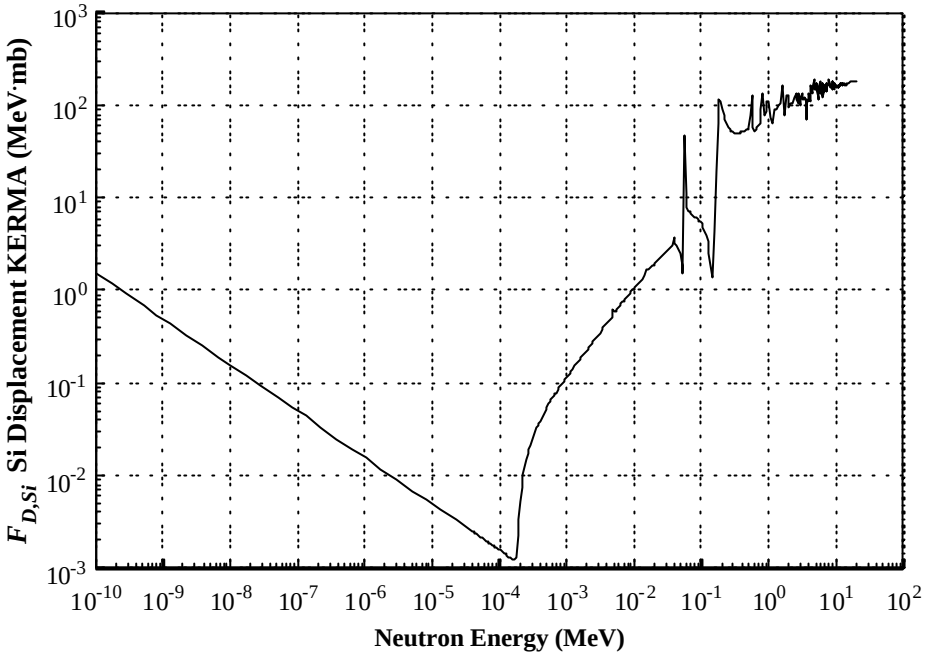

Figure 5.1: Silicon Displacement KERMA, $F_{D,Si}$ (E) taken from ASTM E722-94 [196].

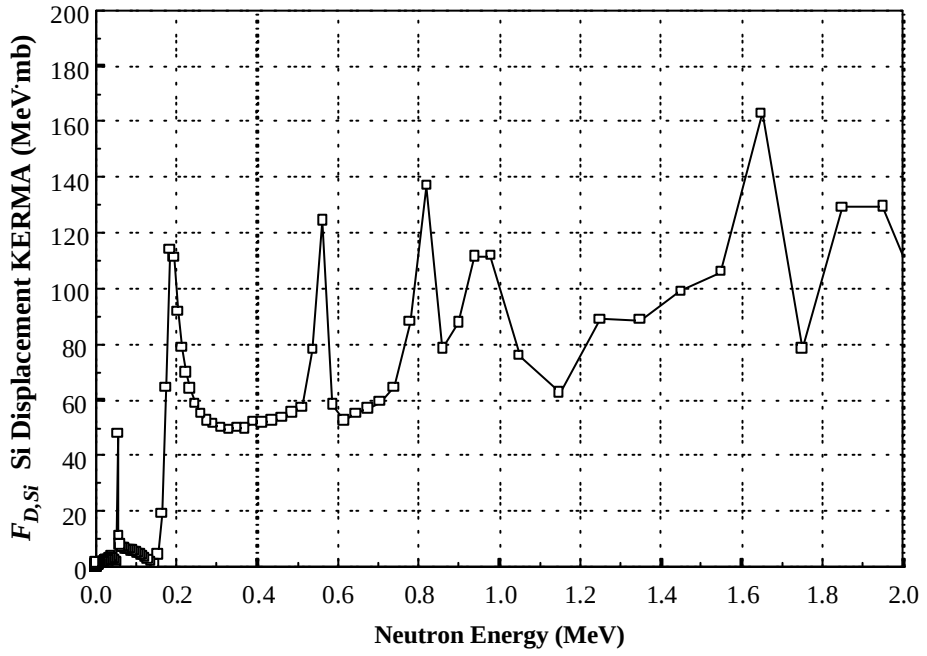

Figure 5.2: Silicon Displacement KERMA, $F_{D,Si}$ (E) taken from ASTM E722-94 [196].

The resonant feature about a neutron energy of 1 MeV is clearly shown.

The foil activation technique involves the simultaneous irradiation of a set of foils at the same point within the radiation field. Neutron activation products are then identified from the gamma emissions and the neutron fluence at particular energies determined from known response functions for each foil. $\Phi(E)$ is then determined using spectral adjustment codes such as SAND II [293] or LSM-M2 [294]. Both of these codes require some prior knowledge of the spectrum shape. More recently a process was described by Williams et al [295] in which prior knowledge of the spectrum shape is not required. More extensive details on the selection and use of activation foils is given in ASTM E720-94 [296] and ASTM E721-94 [297],

It is important to note that the foil activation technique is extremely time consuming and many difficulties must be overcome including:

- Radiological handling difficulties with some foils (particularly U-235 and Pu-239).
- Fluence levels in some neutron fields may be too low to produce an adequate response in some foils with short half-life.
- High gamma ray background can affect foil response.
- Difficulty in the correct placement of foils to ensure equal exposure of all foils, and
- A high economic cost of foils and gamma spectroscopy equipment for foil readout.

Limitations of the foil activation technique include:

- For each set of foil measurements $\Phi(E)$ is only determined at one single point within the radiation field. An extrapolation of $\Phi(E)$ to other points within the field can be done using a neutron transport calculation. This requires more time and additional uncertainties may be introduced. In some situations due to incomplete information regarding the make up and dimensions of materials present, a transport calculation may not be possible [284].

- The inclusion of the device under test (DUT) may itself induce perturbations to the field by acting as a neutron energy moderator. Measurement of $\Phi(E)$ in the presence of the DUT may be different to that measured in its absence.

- The techniques described by the ASTM standards [196,296,297] are not applicable for neutron energies in excess of 20 MeV. Such high energy neutrons are found in spallation neutron sources and space radiation fields.

- In some fields, due to limited accessibility, a measurement of $\Phi(E)$ and hence $\Phi_{eq,1MeV,Si}$ may not be possible at all. Examples of such situations are encountered in high energy physics where the radiation field can only be predicted prior to experimental construction and full device testing not possible before the field is created. Space radiation environments are also not easily ascertained.

- Activation foils cannot be used with good accuracy when the neutron fluence is less than $10^{11}\,\mathrm{cm}^{-2}$.

- Most importantly, activation foils do not allow the neutron field to be monitored on-line.

The difficulties and limitations of the foil activation technique beckon a simple alternative for determination of $\Phi_{eq,1MeV,Si}$.

A PIN Dosimeter Diode offers such an alternative.

5.3 PIN Dosimeter Diodes

A PIN Dosimeter Diode can be used for a direct measure of $\Phi_{eq,1MeV,Si}$ within a neutron field. The device consists of a simple p^+in^+ diode type structure. The *'i'* region is usually manufactured from a wide substrate of high resistivity *n*-type silicon. It is sometimes referred to as the base region. The sensitivity of the device to neutrons is based on the accumulation of displacement damage within the silicon.

The theory of the PIN Dosimeter Diode response to neutrons was initially studied by Swartz et al. [298]. The response was determined for a device with a base manufactured from low resistivity silicon of order 10 - 40 Ω·cm. It was found that under conditions of high level injection that the resistivity of the base could be modulated. The continuity equation was solved in an analytical form taking into account that $\Delta n_{\text{injected}} >> n,p$ (where $\Delta n_{\text{injected}}$ is the carrier concentration in excess of the equilibrium carrier concentrations n and p). It was shown under these conditions that:

$$\frac{\Delta V_F}{\Delta \Phi} \sim t \cdot w^2 \qquad (5.2)$$

where: ΔV_f = forward voltage shift following irradiation,

Φ = fast neutron fluence,

t = minority carrier lifetime in the base region,

w = diode width.

The dependence of t on the neutron fluence is described by the well known relation:

$$\frac{1}{t} = \frac{1}{t_o} + k\Phi \qquad (5.3)$$

where: t_o = initial minority carrier lifetime,

k = damage constant.

Due to the modulation of the base conductivity, response could be determined independently of the base resistivity. Detection of the displacement damage is made by measuring the diode forward voltage before and after neutron exposure. If measured at constant current, the forward voltage drop across the device can be expected to increase with neutron exposure due to the reduction of the minority carrier lifetime. Within a particular neutron fluence range, the forward voltage shift is directly proportional to the neutron fluence, thus providing a linear dosimetric response. The device was found to be useful only up to a maximum neutron fluence of ~ 2×10^{11} cm^{-2}.

In order to extend the measurable fluence limit, work was performed by Rosenfeld et al. [276,299]. To improve the response to NIEL the continuity equation was solved for the case of intermediate injection and also taking into account the concentration of carriers in the base region. This required a consideration of the change of resistivity of the base as a function of fast neutron fluence. The introduction of a higher resistivity silicon allowed an improvement of the initial sensitivity at low fast neutron fluence as well as an extension to the upper fluence limit [299].

The merits of PIN Dosimeter Diode identified in various papers by various authors [276,277,298,299,300-307] are:

- *Simple readout*; No need for latent processing such as is the case for activation foils.
- *High spatial resolution*; The sensor volume is small (approximately 3-5 mm^3).
- *Wide range of response*; The measurable neutron fluence spans 5 orders of magnitude. The minimal detectable fluence is 10^8 cm^{-2} [307]. The maximum detectable fluence is ~ 10^{13} cm^{-2} [299].
- *Variable sensitivity*; The device sensitivity can be altered by changing the width of the diode base region.

- *Response independent of device orientation*; Early versions of PIN Dosimeter Diodes did display some sensitivity to the device orientation however this was found to be due to the large nickel contacts employed at the time [301]. Such contacts are no longer in use and the spatial response dependence is now absent.

- *Dose rate independent*; No dose rate dependence has been observed for dose rates of up to 10^7 Rad·s^{-1} [301] and 10^8 Gy·s^{-1} [302].

- *Minimal response variation within a batch of devices*; A uniform sensitivity of not worse than 6.4 % was observed in a single batch production of 72 devices [299]. (If required, device sensitivity can be made more uniform by pre-irradiating with fast neutrons to a fluence of 10^{11} cm^{-2} followed by a brief high temperature anneal [304]).

- *Devices may be reusable*; Thermal annealing permits the displacement damage to be removed from the device bulk thus permitting reuse.

- *Remote Recovery*; A new technique using current annealing was been proposed to permit remote recovery of the PIN Dosimeter Diode. This would eliminate the need to physically replace a highly irradiated device [276].

- *Mechanism of response identical to mechanism of damage in actual electronic devices.* The mechanism of response is the reduction in minority carrier lifetime within high resistivity silicon.

5.3.1 PIN Dosimeter Diode Response in Fields with Dissimilar Neutron Spectra

The PIN Dosimeter Diode can be calibrated in neutron fields in which $\Phi_{eq,1MeV,Si}$ is known. Despite the many merits of the device, their wide spread application in radiation hardness testing has not occurred. One possible reason for a reluctance to use the device is uncertainty of the dosimetric response in neutron fields in which the spectra is dissimilar to the calibration spectra. In the two papers describing the applications of PIN Dosimeter Diodes for direct

determination of $\Phi_{eq,1MeV,Si}$, the neutron energy spectrum of the calibration field was similar to or identical to the energy spectrum of the test field. That is:

$$\Phi_c(E) \approx \Phi_t(E) \qquad (5.4)$$

where: $\Phi_c(E)$ = is the neutron energy spectrum of the calibration neutron field, and

$\Phi_t(E)$ = is the neutron energy spectrum of the test neutron field.

In 1994 Rosenfeld et al. [276] calibrated PIN Dosimeter Diodes in terms of $\Phi_{eq,1MeV,Si}$ within a reactor produced neutron field at the KINR facility in the Ukraine. The devices were then used to monitor $\Phi_{eq,1MeV,Si}$ within other reactor neutron fields where some moderation was present. A detailed description of $\Phi_c(E)$ and $\Phi_t(E)$ was not provided in the original paper. $\Phi_t(E)$ did not differ significantly from $\Phi_c(E)$ [308].

In another study in 1994, by Oliver [277], PIN Dosimeter Diodes were used for measurement of $\Phi_{eq,1MeV,Si}$ within various reactor neutron fields with average neutron energies of about 1 MeV. The PIN Dosimeter Diodes were initially calibrated using neutrons from a Cf-252 source. The average energy of the emitted neutrons from Cf-252 is 2.140 ± 0.014 MeV [309,310]. Again in this case $\Phi_t(E)$ did not deviate significantly from $\Phi_c(E)$.

In order to answer the question proposed in the introduction, a set of PIN Dosimeter Diodes were calibrated in a neutron field $\Phi_c(E)$ and used to monitor the displacement damage in a test field $\Phi_t(E)$ where $\Phi_c(E) \neq \Phi_t(E)$.

5.4 Experimental

5.4.1 Description of the PIN Dosimeter Diodes Under Test

The PIN Dosimeter Diodes used in this study were obtained from 'SPA Detector' Pty. Ltd., Ukraine. They were manufactured from a high purity *n*-type silicon substrate with an approximate volume of 5 mm^3. A rectifying junction was formed at one surface by boron implantation to create a thin p^+ layer. Ohmic contacting at the opposing side to the junction was aided by a thin n^+ layer formed by phosphorus implantation. Electrical contact leads were soldered to the p^+ and n^+ layers. The entire device was encapsulated in a thin polymer to provide physical protection to the delicate electrical contacts and silicon surfaces.

A total of eleven diodes were used.

5.4.2 Selection of the Calibration and Test Neutron Field

Apart from the initial requirement that $\Phi_t(E) \neq \Phi_c(E)$, the additional selection criteria for both the calibration and test neutron fields were that:

1. the neutron energy spectrum was well known,
2. the neutron flux was sufficient to provide a dosimetric response in PIN Dosimeter Diodes within a reasonably short period of time, and
3. the field contained minimal contamination by other NIEL radiations (e.g. gamma radiation).

First consider selection of the calibration field.

The availability of a source of neutrons with an average energy well in excess of 1 MeV which meet the selection criteria could not be identified. No spallation type neutron sources are available in Australia.

On the low energy side it was important to consider that the minimum neutron energy required to produce a displacement via a scattering process in silicon is ~ 190 eV. Silicon displacements at lower neutrons energies can also occur as a result of neutron induced reactions.

The accuracy of such reactions while reliable is subject to change as improved data becomes available. It was decided that an epithermal neutron field would be the most sensible neutron field for calibration.

Such a neutron field exists in the form of a Boron Neutron Capture Therapy (BNCT) neutron beam. BNCT has been proposed as a means of treating deeply seated cancer tumours. Such facilities are characterised by a minimal flux of both fast and thermal neutrons. The peak neutron energy is generally within the energy range of 1 keV to 20 keV [311]. The enhanced epithermal neutron energy is achieved through a combination of moderation and filtering of a source of ^{235}U fission neutrons or a spallation neutron source. The neutron energy spectrum of such facilities is well characterised in order to permit an accurate computation of the proposed therapy dose. In the interests of reducing patient exposure to unnecessary radiation, lead shielding is used to significantly reduce the gamma radiation component. The BNCT field thus satisfies the selection criteria above.

Now consider selection of a test field.

The test field was chosen so as to satisfy the selection criteria used to choose the calibration field in addition to a source with average energy well above 10 keV (so as to differentiate it from the calibration field).

The neutron field selected was that produced using a 3 MV Van de Graaff and the $Li^7(p,n)Be^7$ reaction. Such a neutron source is characterised by almost monoenergetic neutrons the energy of which is selected by altering the incident proton energy, angle and target thickness. The flux is highly controllable via the proton current on target. An acceptably low level of gamma radiation is produced.

5.4.3 Calibration of the PIN Dosimeter Diodes within the BNCT Neutron Field

Six of the eleven PIN Dosimeter Diodes were calibrated using the HB11 filtered epithermal neutron beam at the High Flux Reactor (HFR) located in Petten at the European Commission Joint Research Centre (JRC) [312]. Assistance in this task was provided by M. Carolan [312].

The neutron energy spectrum of this facility is shown in Figure 5.3. It can be seen that the average neutron energy is well below 1 MeV.

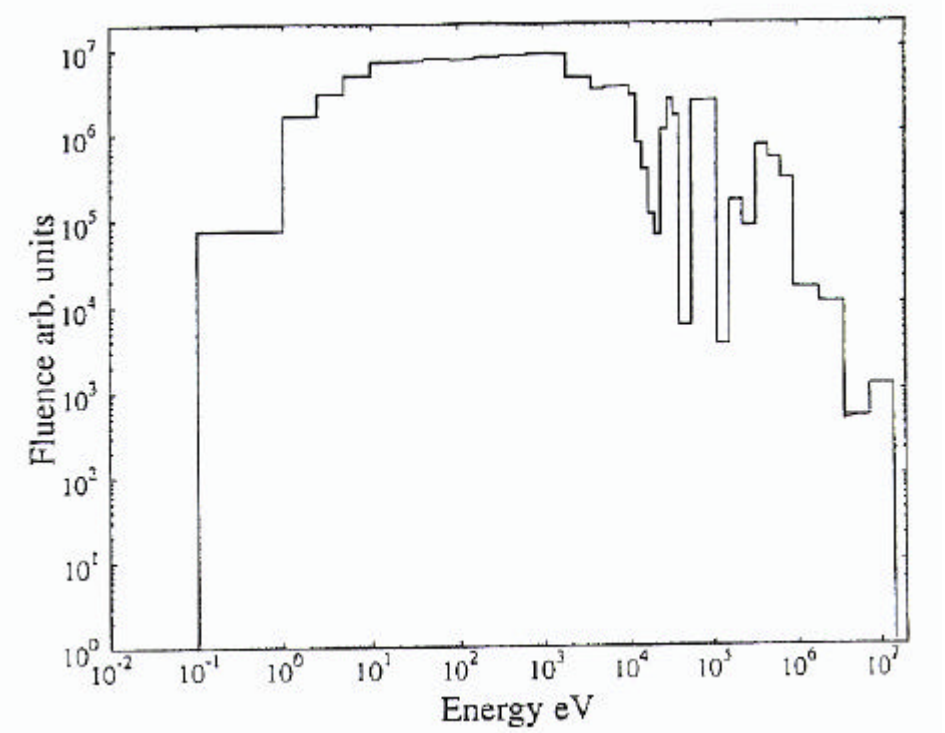

Figure 5.3: Neutron energy spectrum of the Boron Neutron Capture Therapy (BNCT) epithermal beam of the high flux reactor at Petten.

The experimental assembly for the irradiation involved attaching all of the PIN Dosimeter Diodes to a thin (~ 2 mm) aluminium sheet using adhesive tape. This aluminium sheet was then clamped in the beam so that the axis of the beam was normally incident on the sheet of aluminium holding the devices. The diodes were separated from one another by a 2 cm gap. No absorbent or scattering materials were placed between the beam port and the diodes. Two irradiations were performed. One irradiation was performed with an 8 cm collimator and another was performed with a 15 cm collimator in place. The distance from the collimator face

to the point where the diodes were irradiated was 20 cm in both cases. The range of temperatures that existed during these irradiations was from 21.8 °C to 23 °C. All diode readout measurements were adjusted for any temperature differences between the initial and final readouts. The reactor power was set at 45 MW during both irradiations. The first exposure in the 8 cm diameter field was for 20 min 10 sec. The exposure in the 15 cm diameter field was for 20 min 0 sec.

Activation foils were used to measure reaction rates on all axes for comparison with Monte Carlo predictions. For this purpose pairs of measurements were performed using bare and cadmium covered gold foils. All foil activations were measured by the Petten counting laboratory using a sodium iodide or high purity germanium detector. The raw activity data were then corrected for decay and self shielding and the specific activities determined.

$\Phi_{eq,1MeV,Si}$ experienced by each device was determined by convolving the neutron spectrum with the silicon damage function and normalising in terms of damage by 1 MeV neutrons according to Equation 5.1.

The diode readout was performed using a dedicated pulse reader circuit. The circuit provided a pulsed constant current of 1 mA with a pulse width of 1 ms and a period of 11.2 ms. This current pulse was used to forward bias the diode being measured. The voltage across the diode junction was connected to the inputs of a FET operational amplifier. The signal from this amplifier was then feed to a detector circuit from which the output voltage was measured using a Keithely digital voltmeter. The voltmeter had a reading resolution of ± 0.1 mV. Repeated measurements of a standard 100 ohm resistor placed across the test points showed a variability of approximately ± 4 mV in the output voltage over a time period of several days. Throughout the course of the measurements at the Petten HFR a standard 100 Ω resistor was used to check on this drift in the circuit. Since the data of interest for the measurements is the difference between the diode threshold voltage before and after the irradiation a small drift that affects both of these readings does not yield significant errors in the final result. The observed changes in the reader output when measuring the 100 ohm standard occurred over the course of days.

With few exceptions all measurements before and after irradiation were separated by no more than several hours. Short term fluctuations in the readout of the diodes arising from noise or other instabilities of undetermined origin were less than 1 mV. The diodes were connected directly to the reader circuit to avoid any voltage drop arising due to resistance of leads and to keep the readout procedure reproducible.

To ensure that the temperature during the PIN Dosimeter Diode readout was as constant as possible lead blocks were placed in contact with the outer surface of the device encapsulation. One block was placed above and one below the diode. During the interval between readouts these blocks were left on the readout bench and were therefore in thermal equilibrium with the ambient temperature in the Reactor Containment Building (RCB). Throughout the series of measurements this temperature was observed to be 22 $\pm$ 1° C. The RCB temperature was monitored via built in thermocouples. The temperature of the lead blocks used to stabilise the temperature of the PIN dosimeter diodes was measured using a mercury thermometer that was placed in direct contact with them. The readings on the thermometer were observed to agree with the RCB thermocouples to within 0.2 ° C. As far as possible the diodes were handled using forceps to avoid heating them with body heat from the experimenters fingertips.

The average response for all PIN Dosimeter Diodes tested was found to be 6.21×10^{-9} $mV\cdot cm^{-2}$. The maximum variation of any individual diode from this average value was not more than 7.5 %. The uncertainty in the calibration figures was estimated to be 10%. This was mostly attributed to the uncertainties in the knowledge of $\Phi_c(E)$. The individual calibration factors are listed in Table 5.1.

Five additional PIN Dosimeter Diodes were used. They were not individually calibrated at the Petten facility. The average calibration value of 6.21×10^{-9} $mV\cdot n\cdot cm^{-2}$ was assumed (they were from the same manufacturing batch as the six calibrated diodes). With a maximum variation in any of the individual diode calibration factors from 6.21×10^{-9} $mV\cdot n\cdot cm^{-2}$ of not more than 5 %, it was assumed that the uncertainty in the assumed calibration factor for the new five diodes would be no greater than 15 %.

Table 5.1: PIN Dosimeter Diode experimental data.

Pin ID	A[C]	B	C[C]	D	E[C]	F	G[C]	H	I[C]	J	K[C]
Calibration ($mV \cdot n \cdot cm^{-2}$)	6.06×10^{-9}		6.25×10^{-9}		6.56×10^{-9}		6.40×10^{-9}		6.25×10^{-9}		5.74×10^{-9}
Assumed Calibration ($mV \cdot n \cdot cm^{-2}$)		6.21×10^{-9}		6.21×10^{-9}		6.21×10^{-9}		6.21×10^{-9}		6.21×10^{-9}	
Pre. Irrad. Forward Voltage (V)	1.457	1.289	1.318	1.377	1.501	1.450	1.725	1.488	1.874	1.242	1.743
Post Irrad. Forward Voltage (V)	1.783	1.645	1.693	1.790	1.902	1.882	2.177	1.889	2.266	1.577	2.085
Change in Forward Voltage, ΔV_f (mV)	326	356	375	413	401	432	452	401	392	335	342
$\Phi_{eq,1MeV,Si}$ (n/cm^2) measured at 'pin'	5.25×10^{10}	5.73×10^{10}	6.04×10^{10}	6.65×10^{10}	6.46×10^{10}	6.96×10^{10}	7.28×10^{10}	6.46×10^{10}	6.31×10^{10}	5.39×10^{10}	5.51×10^{10}
Distance of 'pin' from target (cm)	14.57	14.33	14.13	14.01	13.93	13.9	13.93	14.01	14.13	14.33	14.57
Angle of 'pin' from beam line centre (±1°)	17.4	14.1	10.7	7.2	3.6	0	3.6	7.2	10.7	14.1	17.4
$\Phi_{eq,1MeV,Si}$ (n/cm^2) normalised to 13.9 cm from target	5.77×10^{10}	5.90×10^{10}	6.24×10^{10}	6.76×10^{10}	6.49×10^{10}	6.96×10^{10}	7.31×10^{10}	6.56×10^{10}	6.52×10^{10}	5.55×10^{10}	6.05×10^{10}

The response of the calibrated PIN dosimeter diodes was now measured in the fast neutron test field, $\Phi_t(E)$.

5.4.4 Irradiation of the PIN Dosimeter Diodes in the Test Neutron Field

The experiment was set up at the monoenergetic fast neutron facility described in Chapter 3. A schematic of the experimental arrangement is shown in Figure 5.4. The PIN Dosimeter Diodes were arranged in a stack and mounted on a thin aluminium backing plate. In Figure 5.4 the diodes are labelled from A to K. The 'Petten' calibrated diodes are identified by a superscript, 'C'. The stack was arranged with the individually calibrated diodes and those with the assumed calibration placed consecutively. The stack was mounted perpendicular to the beam line with the central axis of the beam line passing through the centrally located diode. The distance between the stack and the neutron source was 13.9 cm. This arrangement permitted mapping of the neutron field out to a maximum angle of 17° as measured from the beam line axis.

To permit an independent verification of $\Phi_{eq,1MeV,Si}$ six ion implanted silicon detectors were irradiated in the same field simultaneously. The aim was to use the change in the reverse current as a measure of the equivalent 1 MeV neutron fluence. These devices were placed at a distance of 1.89 cm from the target face and orientated perpendicular to the beam central axis. See Figure 5.4.

A new lithium target was prepared. The target thickness was estimated to be 1.88 ± 0.2 $mg \cdot cm^{-2}$. Neutrons were produced by bombarding the target with 2.6 MeV protons with an average beam current of 24.0 μA. During the irradiation the neutron flux was monitored using the neutron long counter which was placed 4.11 m from the neutron source. The beam current on the target was measured and the accumulated charge determined using a current to frequency converter and a counter/timer unit.

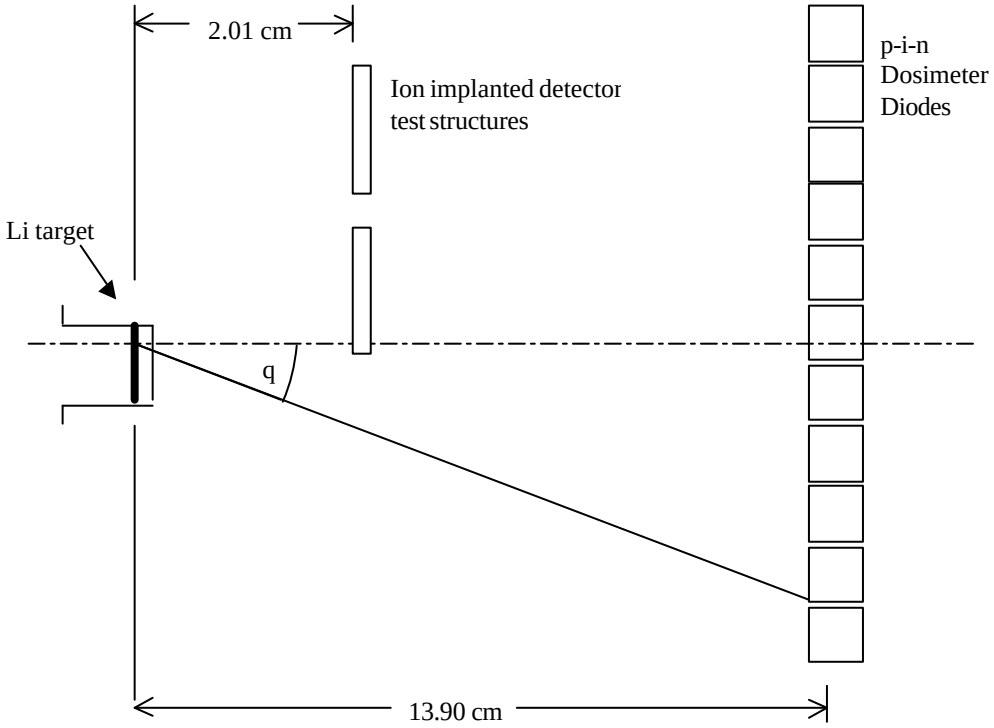

Figure 5.4: Experimental set-up during the fast neutron irradiation of the PIN Dosimeter Diodes and the ion implanted radiation test structures using 2.6 MeV protons and $Li^7(p,n)Be^7$. The subscript c indicates the diodes that were individually calibrated in the Petten epithermal neutron beam.

The PIN Dosimeter Diodes and ion implanted silicon detectors were irradiated simultaneously. After the first 188 minutes the PIN Dosimeter Diodes were removed from the beam. The integrated beam current during this period was 0.2165 C. Irradiation of the ion implanted silicon detectors was continued for another 821 minutes. The total integrated beam current was 1.162 C.

The neutron long counter response was monitored as a function of integrated beam current. In Figure 5.5 the long counter response is shown as a function of integrated beam current. During the 1009 minute irradiation fluctuations in the neutron yield of no greater than 4 % were

observed for counting integration times of 1 minute. A decrease in the neutron yield of not more than 1 % as measured from the beginning of the irradiation to the end of the irradiation for counting integration times of ~ 10 minutes. This indicates that lithium metal target loss due to overheating was negligible and the neutron field remained the same thoughout the entire irradiation period.

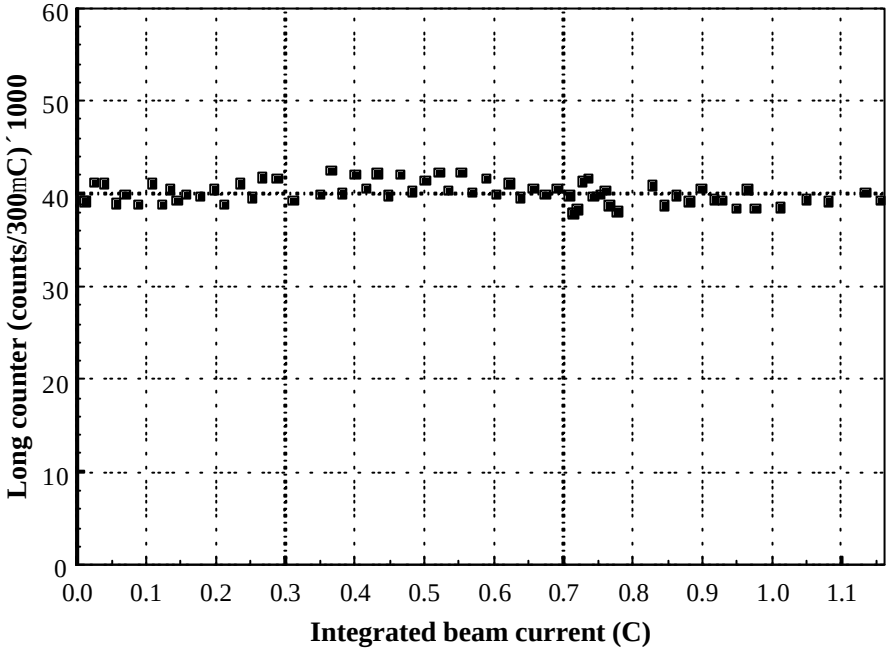

Figure 5.5: Neutron long counter response as a function of integrated beam current.

5.4.5.1 PIN Dosimeter Diode Response

Following irradiation the PIN Dosimeter Diodes were stored at room temperature. Readout was performed 14 hours after irradiation. The readout procedure was the same as that used in the Petten calibrations. The results of the pre and post irradiation are listed in Table 5.1.

$\Phi_{eq,1MeV,Si}$ was determined for devices A^C, C^C, E^C, G^C, I^C and K^C using the individually measured calibration figures. For devices B, D, F, H and J the average calibration figure was used.

A graphical representation of the data is shown later in this chapter in Figure 5.10. A discussion of the results is also left to later in this chapter.

5.4.5.2 Independent Determination of $F_{eq,1MeV,Si}$

For a verification of $\Phi_{eq,1MeV,Si}$ as measured by the PIN Dosimeter Diodes, $\Phi_{eq,1MeV,Si}$ was determined using three independent methods. In the first method the irradiation conditions were used in conjunction with the experimentally measured nuclear cross sections of the $Li^7(p,n)Be^7$ and $Li^7(p,n)Be^{7*}$ reactions to reconstruct the neutron energy spectrum, $\Phi_t(E)$. The silicon damage function and Equation 5.1 was than used to determine $\Phi_{eq,1MeV,Si}$ at varies points within the radiation field.

In the second method, an experimental approach was employed based on the changes of the electrical properties of the silicon detectors. The reverse current damage constant is a well quantified parameter understood in terms of $\Phi_{eq,1MeV,Si}$. Changes in the detector reverse current can thus be used to determine $\Phi_{eq,1MeV,Si}$.

In the third method, $\Phi_{eq,1MeV,Si}$ was estimated from the neutron fluence as measured by a calibrated neutron long counter. This method was restricted to the 0° direction of the beam through the PIN Dosimeter Diode stack.

The individual determinations are now described.

5.4.5.2.1 $F_{eq,1MeV,Si}$ from $Li^7(p,n)Be^7$ Reaction Kinetics

The neutron yield as a function of proton energy can be determined from the experimental differential cross sections ($d^2\sigma/d\Omega dE_p$) for the $Li^7(p,n)Be^7$ reaction and for the $Li^7(p,n)Be^{7*}$ reaction. However, a determination of $\Phi_{eq,1MeV,Si}$, requires that the neutron yield be known as a function of neutron energy. The neutron energy spectrum was reconstructed using the following approach:

First begin by considering the number of neutrons, *N* emitted per second into the solid angle, *dW*, by *p* protons per second incident upon an element of target of thickness, *dx*:

$$dN = pD_{Li}\left(\frac{ds\left(E_p\right)}{d\Omega}\right)d\Omega dx \qquad (5.5)$$

where: p = number of protons per second,

D_{Li7} = atomic density of Li^7,

E_p = proton energy, and

$d\sigma(E_p)/d\Omega$ = differential cross section as a function of proton energy in the laboratory frame of reference.

A known relationship exists between the proton energy loss and the target thickness, and also between the proton energy and the emitted neutron energy. Equation 5.5 can be rewritten as:

$$dx = \left(\frac{dx}{dE_p}\right)\left(\frac{dE_p}{dE_n}\right)dE_n \qquad (5.6)$$

where: E_n = neutron energy.

The differential cross sections are usually expressed for the centre of mass frame of reference. Conversion to the laboratory frame of reference is done using:

$$\left(\frac{ds}{d\Omega}\right)=\left(\frac{ds}{d\Omega'}\right)\left(\frac{d\Omega'}{d\Omega}\right) \qquad (5.7)$$

where: ′ indicates centre of mass frame of reference.

The number of protons per second incident upon the target, *p*, is given by:

$$p=\frac{I_p}{e} \qquad (5.8)$$

where: I_p = the proton current, and

e = the electronic charge of the proton.

Using Equations 5.6, 5.7, and 5.8, Equation 5.3 can be rewritten as:

$$\frac{d^2N}{dE_n d\Omega}=\frac{I_p}{e}D_{Li7}\left(\frac{ds}{d\Omega'}\right)\left(\frac{d\Omega'}{d\Omega}\right)\left(\frac{dx}{dE_p}\right)\left(\frac{dE_p}{dE_n}\right) \qquad (5.9)$$

I_p is known from the experimental conditions. e is equal to 1.602×10^{-19} C. D_{Li7} is the natural abundance of the Li^7 isotope (92.41 %) multiplied by the atomic density of Li metal (4.644×10^{22} cm^{-3}) which gives 4.292×10^{22} cm^{-3}. The nuclear cross sections, ($d\sigma/d\Omega'$), were taken from the summary of Liskien and Paulsen [313]. In this summary the differential cross sections are given as a function on angle. A comprehensive set of cross section data is available for the $Li^7(p,n)Be^7$ reaction at 0°. The data set is significantly less comprehensive at angles of 5°, 10°, 15°, 20° and up to 180°. For this reason results obtained at angles other than the 0° angle will be determined with less certainty. For the $Li^7(p,n)Be^{7*}$ reaction the cross section data is only available in angular increments of 5°. It will however be shown that the neutrons from the 1st excited state reaction make an insignificant contribution to $\Phi_{eq,1MeV,Si}$ and can thus be neglected.

The terms ($d\Omega'/d\Omega$) as well as (dE_p/dE_n) can be calculated using the expressions of Winter and Schmid [314]:

$$\frac{d\Omega'}{d\Omega} = \frac{g}{x}\left(m \pm x\right)^2 \qquad (5.10)$$

$$\frac{dE_p}{dE_n'} = \frac{\left(m_{Li}+m_n\right)^2}{m_p m_n}\times\left(m \pm x\right)^{-1}\times\left(m \pm x \pm \frac{m_{Li}(m_{Li}+m_n-m_p)}{m_p m_n}\times\frac{E_{th}}{xE_p}\right)^{-1} \qquad (5.11)$$

$$g^2 = \frac{m_p m_n}{(m_{Li}+m_n-m_p)m_{Li}}\times\frac{E_p}{(E_p-E_{th})} \qquad (5.12)$$

$$x^2 = \frac{1}{g^2}-1+m^2 \qquad (5.13)$$

where: m = cosine of the angle of neutron emission in the laboratory frame,

m_n = neutron mass number,

m_p = proton mass number,

m_{Li} = ^{7}Li mass number,

E_{th} = reaction threshold energy (1.881 MeV for the ground state reaction and 2.378 MeV for the 1st excited state).

The term (dx/dE_p) is the inverse of the energy loss, expressed by Livingston and Bethe [315] in the c.g.s system as:

$$-\frac{dE_p}{dx} = \frac{2\pi e^4 z^2 DZ}{E_p} \times \frac{m_p}{m_n}\left(\log\left(\frac{4E_p m_e}{I_e m_p} \right) - \log\left(1-b^2\right) - b^2 \right) \qquad (5.14)$$

The energy of the protons in this work was less than 3 MeV. Thus terms with b^2 can be neglected. An average ionisation potential of I_e = 60 eV was used [316].

In the 0° angle of the laboratory frame of reference the cross section of the $Li^7(p,n)Be^7$ reaction close to the threshold is sharply peaked. The total energy loss of the protons in the lithium target was thus determined from the neutron yield, measured using the long counter, as a function of proton energy from the threshold up to 2.15 MeV. This data is plotted in Figure 5.6. The peak neutron intensity occurs when the proton energy loss in the target is such that all protons have sufficient energy to exceed the reaction threshold at all points though the lithium metal. The energy loss is then estimated from the proton energy at which the peak neutron intensity occurs minus the reaction threshold. The peak neutron yield occurs at a proton energy

of 2.10 MeV. The target thickness in terms of proton energy loss in lithium metal is thus 220 ± 10 keV. Using Equation 5.14, the corresponding energy loss for 2.6 MeV protons will be 183 ± 8.3 keV. Protons with energy from 2.417 MeV to 2.600 MeV can be expected.

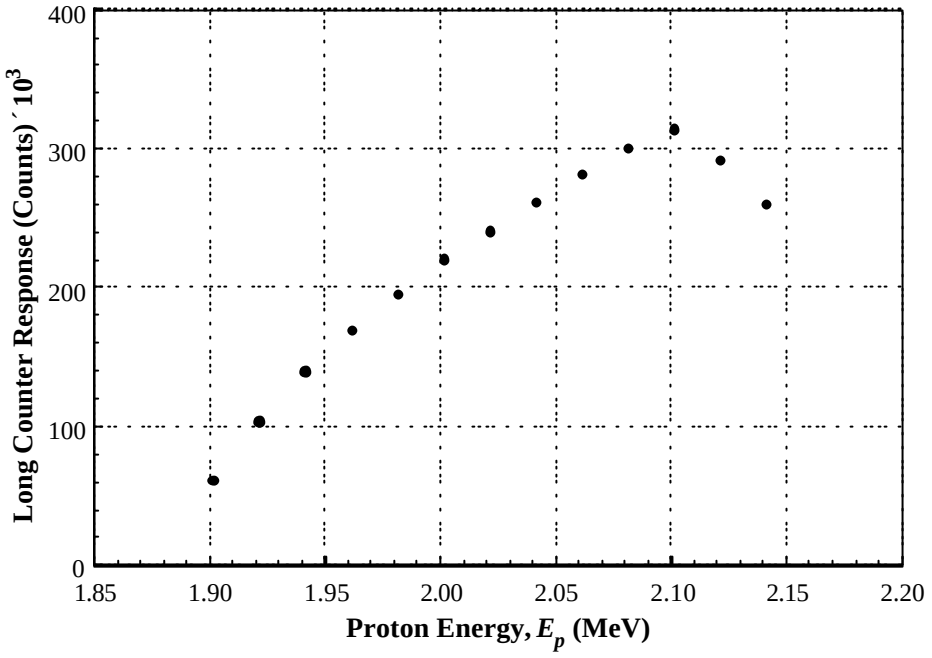

Figure 5.6: Proton energy loss in the Li target determined from the neutron long counter response at energies about the sharply peaked threshold of the $Li^7(p,n)Be^7$ reaction in the forward direction.

No attenuation of the proton beam was expected within the lithium target (the number of protons removed due to nuclear reaction is minimal). The effect of proton energy variation due to machine voltage fluctuations was also neglected. (At 3 MeV the proton energy FWHM is only 6 keV [317]).

The neutron yield was calculated using Equation 5.9 for the 0° direction as measured in the laboratory frame of reference. The results are shown in Figure 5.7. Two energy groups can be seen, one about 0.25 MeV and another about 0.8 MeV. The group about 0.25 MeV is associated with the $Li^7(p,n)Be^7$ reaction. The jagged features of this curve are due to the uncertainties in the experimental cross sections taken from ref. [313].

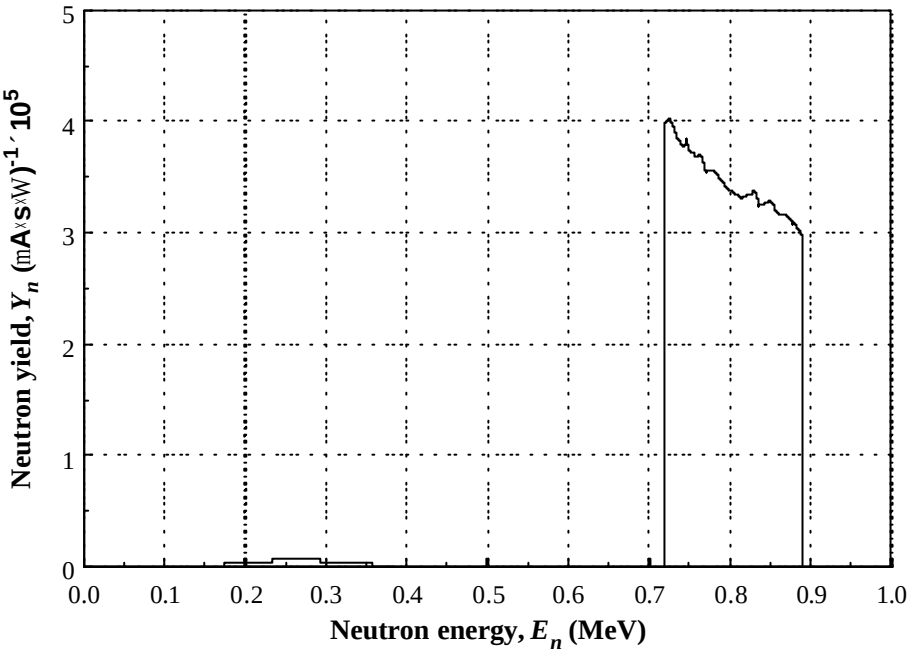

Figure 5.7: Neutron energy spectrum for the 0° direction and laboratory frame of reference.

It can be seen that the neutron yield contribution of the $Li^7(p,n)Be^{7*}$ reaction is minimal in comparison to the $Li^7(p,n)Be^7$ reaction. Also, at neutron energies of about 0.25 MeV and 0.80 MeV the magnitude of the silicon damage is similar (see Figure 5.8). For these reasons the

contribution to silicon damage due to $Li^7(p,n)Be^{7*}$ neutrons can be neglected in the calculation of $\Phi_{eq,1MeV,Si}$.

The calculated neutron yield for the $Li^7(p,n)Be^7$ reaction was then used together with the neutron damage KERMA values in silicon to calculate $\Phi_{eq,1MeV,Si}$ in the zero degree direction according to Equation 5.1. Due to the limited data set of $F_{D,Si}(E)$ as a function of neutron energy and the non regular neutron energy intervals in the data, a smooth curve was fitted to the $F_{D,Si}(E)$ data. The curve was re-scaled to neutron energy intervals of 1 keV. The fitted curve and actual $F_{D,Si}(E)$ data from ASTM E722-94 is shown together in Figure 5.8.

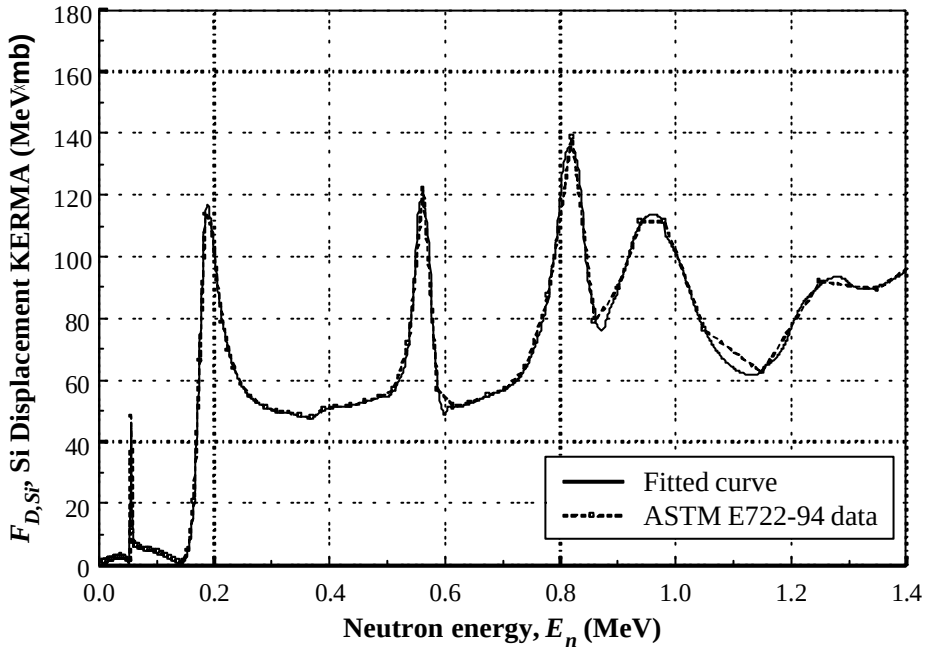

Figure 5.8: Si Displacement KERMA values from ASTM E722-94 [196], and a smooth curve fitted to this data. Fitted curve re-scaled to increments of 1 keV in neutron energy.

$\Phi_{eq,1MeV,Si}$ was calculated for a 188 minute irradiation at a distance of 13.9 cm. Conversion of neutron yield to the neutron fluence at 13.9 cm was done using the inverse square law. The r^{-2} dependence of the neutron flux was measured using the neutron long counter. The secondary neutron component from floor and wall scattered neutrons was considered negligible as the samples were positioned in close proximity to the target.

Using the same methodology as just described, the neutron fluence was determined at angles of 5°, 10°, 15° and 20°. The neutron energy spectrum for these angles is shown in Figure 5.9. The 1st exicted state contribution was neglected on the same basis as for the calculation in the 0° direction.

A tabulation of results can be found in Table 5.2.

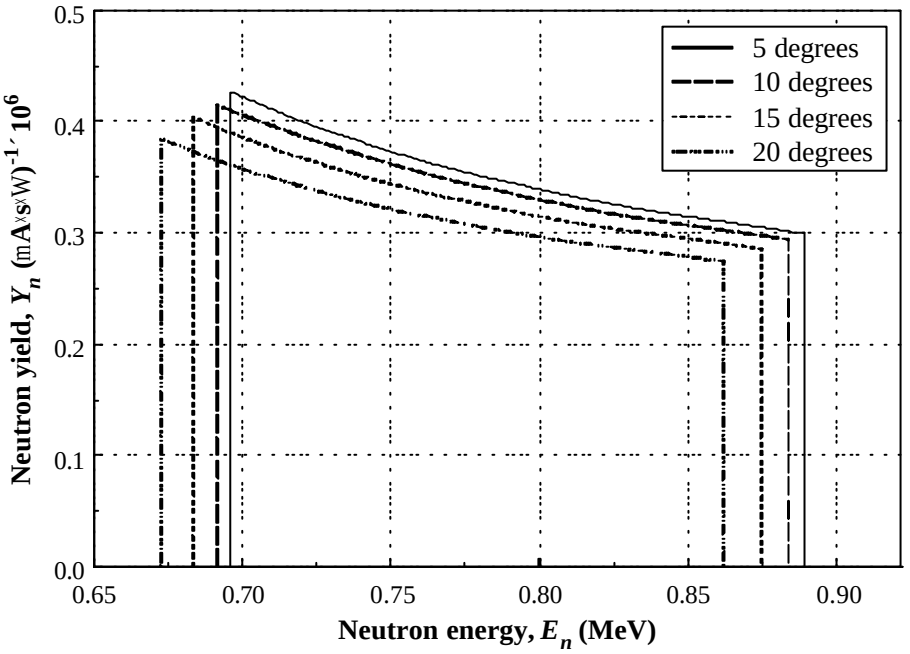

Figure 5.9: Neutron energy spectrum for the 5°, 10°, 15° and 20° directions and laboratory frame of reference.

Table 5.2: $\Phi_{eq,1MeV,Si}$ determined from neutron yield calculations.

Angle	$\Phi_{eq,1MeV,Si}$	$\Delta\Phi_{eq,1MeV,Si}$
0°	8.13×10^{10}	$\pm 1.22\times10^{10}$
5°	8.29×10^{10}	$\pm 1.66\times10^{10}$
10°	7.92×10^{10}	$\pm 1.58\times10^{10}$
15°	7.39×10^{10}	$\pm 1.47\times10^{10}$
20°	6.68×10^{10}	$\pm 1.34\times10^{10}$

5.4.5.2.2 $F_{eq,1MeV,Si}$ Determined from Ion Implanted Si Detectors

Post irradiation the reverse current of the ion implanted silicon detectors was measured. The first measurement was made 14 days after neutron irradiation. In the precluding time, post irradiation and pre measurement, the detectors were stored at room temperature. A Keithley 237 high voltage source and measurement unit was used. Measurement was performed at room temperature and corrected to 20°C using:

$$I(T_2) = I(T_1)\left(\frac{T_2}{T_1}\right)^2 \exp\left[\frac{E}{2k}\left(\frac{T_1 - T_2}{T_1 T_2}\right)\right] \qquad (5.15)$$

where: $I(T_2)$ = Equivalent current at temperature T_2,

$I(T_1)$ = Measured current at temperature T_1,

T_2 = Corrected temperature, (20°C),

T_1 = Measurement temperature,

k = Boltzmann constant,

E = 1.2 eV [318].

To understand the current per unit detector volume, the current was determined at the point at which the detector was just fully depleted. Full depletion was determined from measurements of the detector front and rear side response to 5.4 MeV alpha particles.

The equivalent 1 MeV neutron fluence was then determined using:

$$\frac{\Delta I}{vol} = a_{1MeV,Si}\Phi_{eq,1MeV,Si} \qquad (5.16)$$

Up until a period of about 1 month from the time of irradiation, the value of the reverse current damage constant is highly dependent on the amount of time that has passed since irradiation. A value of $\alpha_{1MeV,Si}$(14 days) = 3.75×10^{-17} A·cm^{-1} was used from the literature review given in Chapter 2. This value was taken from an average of the literature reported values where the time post irradiation was well considered (see tabulation in Chapter 2).

The results obtained were adjusted to a distance of 13.9 cm using the inverse square law. Results are listed in Table 5.3.

Due to the large uncertainty in α_{1MeV}(14 days), the above procedure was repeated at 50 days post irradiation. At this time the agreement between different values for α_{1MeV} reported in the literature is ~ 3 %.

Results for the reverse current measurements at 50 days are also listed in Table 5.3.

5.4.5.2.3 $F_{eq,1MeV,Si}$ Determined from Neutron Long Counter Response

The third independent determination of $\Phi_{eq,1MeV,Si}$ was made using the neutron long counter. This type of detector is characterised by an approximately uniform detection efficiency for

neutrons with energies from 10 keV to 3 MeV. The absolute neutron detection efficiency is high with excellent discrimination against gamma radiation [319-321].

For the neutron field produced in this experiment the range of neutron energies incident upon the detector face was 0.698 MeV to 0.891 MeV (excluding the low energy group associated with the $Li^{7}(p,n)Be^{7*}$ reaction). The relative detection efficiency of the neutron long counter over this energy interval varies by less than 1 % [321]. It was thus assumed that the relative detection efficiency for this range of neutron energies could be approximated as uniform without introducing any significant errors.

Table 5.3: Ion implanted detector test structure reverse current measurements.

*a) **Pre Irradiation***

Detector	I_o (nA)	I_o (nA) @ 20°C
U4-a	200	154
U4-b	199	153
U4-c	193	149
U5-a	182	140
U5-b	189	146
U5-c	193	149

b) 14 days after irradiation.

Detector	I_1 (μA)	Temperature (°C)	I_1 (μA) @ 20°C	ΔI (μA) @ 20°C	$\Phi_{eq,1MeV,Si}$ * (n/cm^2)	Distance from target (cm)	Angle from beam centre line	$\Phi_{eq,1MeV,Si}$ * (n/cm^2)×10^{13} **At 'pin' stack**
U4-a	4.9	25.6	3.02	2.87	2.36×10^{13}	1.89	0° ± 4.5°	8.16×10^{10}
U4-b	4.6	25.3	2.91	2.76	2.27×10^{13}	1.93	11.9° ± 4.2°	7.85×10^{10}
U4-c	3.6	25.2	2.30	2.15	1.77×10^{13}	2.05	22.9° ± 3.8°	6.12×10^{10}
U5-a	2.1	23.1	1.60	1.46	1.21×10^{13}	2.27	33.5° ± 3.3°	4.18×10^{10}
U5-b	1.45	22.9	1.13	0.981	0.807×10^{13}	2.51	41.1° ± 2.5°	2.79×10^{10}
U5-c	1.50	23.0	1.16	1.01	0.829×10^{13}	2.79	47.3° ± 2.1°	2.87×10^{10}

c) 50 days after irradiation

Detector	ΔI (μA) @ 20°C	$\Phi_{eq,1MeV,Si}$ + (n/cm^2)	$\Phi_{eq,1MeV,Si}$ + (n/cm^2)×10^{13} **At 'pin' stack**
U4-a	2.18	2.24×10^{13}	7.75×10^{10}
U4-b	2.11	2.17×10^{13}	7.50×10^{10}
U4-c	1.70	1.75×10^{13}	6.05×10^{10}

All currents were measured at the detector full depletion voltage.

* Calculated using $\alpha = 3.75\times10^{-17}$ A·cm^{-1} and $vol = 0.00324$ cm^{-3}.

+ Calculated using $\alpha = 3.0\times10^{-17}$ A·cm^{-1} and $vol = 0.00324$ cm^{-3}

The absolute detection efficiency of the long counter was determined using a calibrated $Am^{241}Be$ neutron source. Details on the calibration as a well as a measure of the angular dependence of the detection efficiency were reported elsewhere by this author [322]. The results of this work showed that one count per second corresponded to a fast neutron flux of 0.231 $s^{-1}\cdot cm^{-2}$ at the front face of the long counter. The largest uncertainty in the calibration was attributed to the wide range of neutron energies from the $Am^{241}Be$ neutron source which exceeded the region of uniform detection efficiency as a function of neutron energy. An uncertainty of 15 % was assigned.

During the present experiment the neutron long counter front face was positioned at 4.11 m from the neutron target. The central axis of the detector was aligned with the central axis of the beam line. During the 188 minute irradiation 4.397×10^{8} counts were recorded. The corresponding neutron fluence was thus 9.563×10^{7} cm^{-2}.

In order to determine $\Phi_{eq,1MeV,Si}$ consideration of the KERMA factors for neutrons between 0.698 MeV to 0.891 MeV was required. The minimum and maximum KERMA factors for this energy range is 56.44 MeV·mb and 135.85 MeV·mb respectively. The average KERMA factor is 87.89 MeV·mb. By weighting according to the neutron yield as a function of neutron energy a more accurate estimate of the effective KERMA value for the incident neutron flux was found to be 86.39 MeV·mb. (In both of these cases the KERMA factors were taken from the fitted curve shown in Figure 5.8).

$\Phi_{eq,1MeV,Si}$ as measured by the neutron long counter was determined to be:

$$\Phi_{eq,1MeV,Si} = \frac{F_{D,Si}(0.698 to 0.891 MeV)}{F_{D,Si}(1 MeV)} \times 9.563 \times 10^{7} \qquad (5.17)$$

$$= 8.696\times10^{7}\ cm^{-2}$$

where: $F_{D,Si}$(0.698 to 0.891 MeV) = 86.39 MeV·mb (the effective KERMA factor for incident neutrons),

$F_{D,Si}$(1 MeV) = 95 MeV·mb.

Accounting for the separation between the long counter and the PIN Dosimeter Diode stack and using the inverse square law dependence, $\Phi_{eq,1MeV,Si}$ as measured by the neutron long counter at a 0° angle was 7.49×10^{10} cm^{-2}.

The greatest uncertainty in this determination was in the uncertainty of the neutron long counter absolute efficiency calibration.

5.5 Discussion of Results

$\Phi_{eq,1MeV,Si}$ as measured by the PIN Dosimeter Diodes, along with $\Phi_{eq,1MeV,Si}$ determined by the neutron yield calculation, the reverse current increase in the ion implanted silicon detectors, and the neutron long counter, are shown as a function of angle from the beam line axis in Figure 5.10. All fluence values were adjusted to a distance of 13.9 cm from the neutron source using the inverse square law.

For the PIN Dosimeter Diodes, neutron yield calculations and reverse current measurements, a maximum value of $\Phi_{eq,1MeV,Si}$ was found at an angle of 0°. At angles away from 0° the value of $\Phi_{eq,1MeV,Si}$ decreased. This was not an obvious result due to the dependence of $\Phi_{eq,1MeV,Si}$ on the $F_{D,Si}(E)$ function and not $\Phi(E)$ alone. All results were found to agree within the assigned uncertainties for each individual determination.

The angular uncertainty bars for the silicon ion implanted detector reverse current determinations of $\Phi_{eq,1MeV,Si}$ are due to the wide angle presented to the neutron field by the

significant area of the individual detector windows relative to the lateral distance from the target. (The detector junction had an area of 3 mm × 3 mm).

The PIN Dosimeter Diode result at 0° was also found to agree within the experimental uncertainties with the value obtained by the neutron long counter.

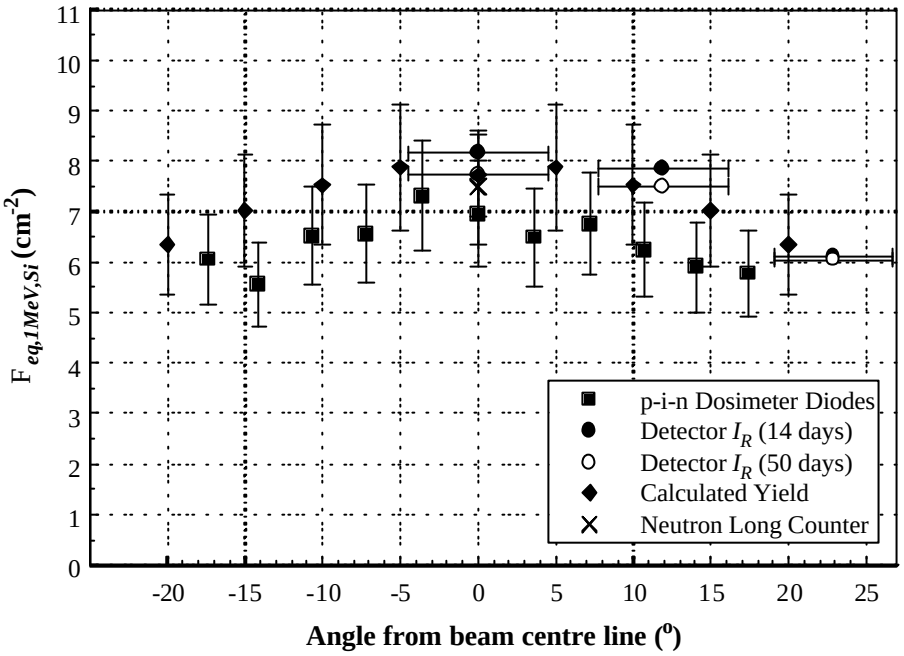

Figure 5.10: $\Phi_{eq,1MeV,Si}$ as determined by the PIN Dosimeter Diodes, the neutron yield calculation, the reverse current increase in the radiation detectors and the neutron long counter response.

5.6 Conclusion

The agreement of within 15 % of the PIN Dosimeter Diode measurements of $\Phi_{eq,1MeV,Si}$ and the three independent determinations of $\Phi_{eq,1MeV,Si}$ at all points mapped in the neutron field

indicates that the diodes response was valid. It is thus shown that PIN Dosimeter Diodes which have been calibrated in an epithermal neutron beam in terms of $\Phi_{eq,1MeV,Si}$ can be used to measure $\Phi_{eq,1MeV,Si}$ in a fast neutron field. The PIN Dosimeter Diode response is not dependent on the type of neutron spectrum used for calibration.

It is therefore demonstrated that a PIN Dosimeter Diode is a reliable sensor for a direct measurement of $\Phi_{eq,1MeV,Si}$ in any arbitrary neutron field capable of producing displacement damage in silicon based devices. Since the technology required to produce a PIN Dosimeter Diode is well known and widely available such a sensor would be suitable for use as a standard reference sensor for monitoring displacement damage effects in silicon based devices exposed to neutrons.

Chapter 6

A Radiation Damage Monitoring System for Silicon Devices Exposed to Mixed Radiation Fields

6.1 Introduction

In many applications electronic devices operate in mixed radiation fields. In such fields the reliable prediction of a device's performance is extremely difficult. This is due to the different damage mechanisms associated with the exposure of the device to the varied components of the field.

A priori radiation hardness testing can be undertaken in the usual way. For reliable results it is important that the mixed radiation field of the testing environment is identical or similar to that of the real environment. This may not always be achievable and the results obtained can be an unreliable indicator of performance. In some applications a considerable uncertainty in the mixed radiation field may be apparent. For example, the inner regions of HEP collider experiments prior to accelerator commissioning. The simulation of device performance in a poorly understood field is highly speculative and unreliable. Also, when radiation hardness testing is performed at different facilities, differences in the individual radiation fields makes the inter-comparison of results between facilities quite difficult. From these perspectives a means of measuring and standardising the damage in electronic devices exposed to mixed radiation fields is an important goal.

The purpose of this study was to develop such a capability in the form of a standard Radiation Damage Monitoring System (RDMS) for silicon devices, which will be universal in any mixed radiation field. Such a system would have three main areas of application:

1. For the characterisation of a mixed radiation field in terms of the capacity to cause radiation damage to electronic devices. Such information would then permit the appropriate selection of suitably radiation hard components.

2. For radiation hardness testing programs. Here, a universal means of comparing results obtained at different facilities with different mixed radiation fields would be provided.

3. On-line monitoring of radiation damage to electronic devices within the actual operating field. This capability, used in conjunction with priori radiation hardness testing results, would permit the on-line assessment of electronic system degradation as a function of exposure. In this way the possible failure of critical devices could be anticipated well before it occurs and corrective actions undertaken.

In this chapter a RDMS is designed and evaluated for the on-line monitoring of damage to electronic components in a mixed radiation field containing high energy electrons and soft *x*-ray synchrotron radiation. Such a radiation field is found within the silicon vertex detector (SVD) of the High Energy Physics *Belle* experiment at KEK, Japan [13]. Details of KEK, the *Belle* experiment, and the radiation field within *Belle* were described in Chapter 1.

6.2 Design of a Radiation Damage Monitoring System (RDMS) for Mixed Radiation Fields

As discussed in Chapter 1, the most important electronic materials which are also vulnerable to radiation damage, are silicon and silicon dioxide. Other semiconductor materials are also vulnerable although their use in radiation environments is less wide spread. For this reason the system to be designed here will concentrate on silicon based devices.

The level of vulnerability of an electronic device to radiation damage is dependent on the type of radiation and its energy as well as individual device construction. Susceptibility to radiation damage will therefore vary between different device types in different radiation fields.

For this reason it is important that the response of the RDMS is universal to all silicon / silicon dioxide based device types and in all mixed radiation fields.

The various types of particles, particle energy ranges, and the variety of interactions that can occur within a device in a mixed radiation field would make the design of a universal RDMS seem at first glance to be a difficult proposal. In practise however, considerable simplification can be made on account of the fact that only two mechanisms of damage are important. The first is displacement damage, and the second is ionisation damage. As discussed previously, displacement damage is associated with non ionising energy loss (NIEL) of incident radiation within the silicon bulk. The device effects are understood in terms of the displacement KERMA in silicon. Where as ionisation damage is associated with ionising energy loss (IEL) within the silicon dioxide. It is responsible for the build up of charge within the oxide layers of CMOS devices. Such effects are understood in terms of the dose in SiO_2 [323].

The same kind of radiation can contribute to both IEL and NIEL, but with different efficiency. The quantity of energy deposited in either form is dependent upon the type of incident radiation and its energy. A suitable radiation damage monitoring system should be capable of responding independently to both IEL and NIEL. Two separate sensors are thus required, one which responds to IEL, and a second which responds to NIEL. Existing dosimeters such as TLDs and ionisation chambers are not capable of discriminating between the two forms of dose.

Additional requirements of the RDMS sensors are as follows:

1. The response of the IEL sensor should be independent of NIEL effects. Similarly, the response of the NIEL sensor should be independent of IEL effects.

2. Since the damage effects in silicon based devices by IEL is due to the dose in SiO_2, the response of the IEL sensor should be in terms of the dose in SiO_2. Similarly, since the damage effects in silicon devices by NIEL is due to the dose in Si, the response of

the NIEL sensor should be in terms of the NIEL dose in silicon. This is best represented by $\Phi_{eq,1MeV,Si}$.

3. For applications in radiation fields with considerable uncertainties both sensors would need a wide range of response.
4. Within the dose range of application the sensors would need to be well calibrated and have a response function which does not change with exposure to the field.
5. For applications with physical limitations in space, such as within the inner regions of high energy physics detectors or within Earth orbiting satellites, the sensors would need to be small and require minimal services. Integration with other components would also be advantageous.
6. For true on-line monitoring the readout of the sensors should not depend on latent processing.

The unique radiation field associated with the *Belle* experiment at KEK provided an opportunity to design and test the most suitable sensor types for a universal RDMS. The initial attempts by the *Belle* collaboration to design a RDMS are shown to have underestimated the strong influence of NIEL effects and the associated device degradation in a mixed radiation field.

6.3 Radiation Monitoring System of the *Belle* SVD

The radiation field within the *Belle* experiment will consist of a high flux of synchrotron radiation in the energy range of 5 - 15 keV in addition to a high flux of leptons with GeV energies.

In the initial design phase of the *Belle* SVD, most attention was placed on radiation damage to the detector system due to the deposition of ionising energy. IEL is responsible for a build up

of charge within the gate oxide of MOS transistors thus causing a shift of the threshold voltage and eventual degradation of the signal to noise ratio, S/N. These are critical parameters of the front-end electronics. In the microstrip detectors the ionisation energy will cause a build-up of charge in the insulating oxide between the p^+ and n^+ strips. This build up can lead to a decrease of the inter-strip resistance and an increase of the inter-strip capacitance thereby increasing the amplifier noise. Special methods such as *p*-stop layers between strips can reduce these effects [324].

Monte Carlo simulations have given the maximum ionisation doses in the SVD at up to 50 kRad·yr^{-1} in a worst case scenario [325]. Ninety nine percent of this dose is due to the high energy electron contribution [326]. The expected electron flux, in this worst case scenario, is approximately 2×10^{12} cm^{-2}·yr^{-1}. The same simulations predict an average ionising dose of 6 kRad·yr^{-1} with a corresponding electron flux of 2.3×10^{11} cm^{-2}·yr^{-1}. In another simulation an average ionising radiation dose of 10 kRad·yr^{-1} was calculated [13].

In the background simulations the effects of NIEL from the high energy electrons in the Double Sided Strip Detectors (DSSD) was not taken into account. Although the simulated doses are based only on the ionising component, the effect of non-ionising energy loss can be considerable in silicon exposed to high energy electrons. It was recently demonstrated that highly energetic electrons, (~ 500 MeV), produce a similar amount of damage in silicon per fluence as 1 MeV neutrons and high energy protons [327]. This result was inferred from the increase of the reverse current measured in silicon strip detectors of the OPAL detector at the LEP collider at CERN. GeV energy electrons in *Belle* should be similarly if not more damaging than 500 MeV electrons. If this is the case, at the particle flux predicted above, both IEL and NIEL damage should be expected within the SVD components.

Due to the uncertainty in the radiation environment, it was proposed by the *Belle* collaboration that a radiation monitoring system be incorporated into the SVD. (Similar systems had been successfully implemented in the OPAL detector of the LEP collider at CERN [328]). The *Belle* radiation monitoring system was designed to perform two tasks;

1. To detect an unanticipated increase of the dose rate within the SVD associated with an accidental beam malfunction. In such instances, an alarm would be triggered to allow for harm reduction strategies to be employed (i.e. dump the beam).
2. To monitor the integrated dose with time so as to provide a regular assessment as to the level of exposure to radiation experienced by the DSSD and CMOS electronics.

A radiation monitoring system was proposed and constructed by the High Energy research groups at the University of Sydney and the University of Melbourne [329]. The system consisted of 8 self contained units which will be bonded into various locations within the SVD. Each individual unit consists of a small brass box containing a pair of Hamamatsu S3590-08 photodetectors.

The photodetectors will be operated in an unbiased mode. The signal from the monitors is an analog DC voltage which is proportional to the current induced in the photodetector by the IEL of the incident radiation. This signal is not integrated or shaped by any electronics and sent "as it is" to the data acquisition system which is able to register DC voltage. Integration of the signal can be done later by software. The only external electronics connected to the detectors will be DC level discriminators and fast logic circuitry for alarm signal production.

The proposed photodetector sensor would be capable of measuring the radiation dose associated with IEL within silicon. It will not be capable of monitoring the dose associated with NIEL in silicon and hence not capable of identifying NIEL damage to the DSSD detectors. Additionally, if NIEL in silicon is significant throughout the SVD, then the photodetectors themselves may also be susceptible to the effects of NIEL.

6.4 Experimental Program

An experimental program was undertaken with three main objectives;

1. Assess the reliability of a photodetector for the measurement of the radiation dose associated with IEL in silicon within a mixed radiation field containing high energy electrons.
2. Assess the performance of an alternate sensor for the measurement of the radiation dose associated with IEL in SiO_2. The tested sensor is a MOSFET.
3. Determine the suitability of a PIN Dosimeter Diode for measurement of radiation dose associated with NIEL in silicon within a mixed radiation field containing high energy electrons.

Results will be used to design an alternative RDMS for the *Belle* SVD. The universality of the RDMS in other mixed radiation fields will also be addressed.

6.4.1 Radiation Hardness of the Hamamatsu S3590-08 Photodetector

The Hamamatsu S3590-08 is a silicon based depletion layer photodetector with p^+nn^+ structure. It has an active area of 10 mm × 10 mm and a maximum depletable thickness of 300 μm. A schematic of the photodetector is shown in Figure 6.1. A photodetector can be operated in either the photoconductive or the photovoltaic mode. In the photoconductive mode the photodetector functions in a similar fashion to a silicon strip detector. A reverse bias is applied to the *p-n* junction to provide full depletion of the device bulk. *e-h* pairs created by incident radiation within this region are acted upon by the electric field and move in response. This causes a signal to flow in the external circuit. In this mode signal detection is characterised by a high speed of response, a low capacitance (giving good S/N ratio), and good response linearity. As the reverse bias is increased towards the full depletion voltage the reverse current also increases. This has the effect of limiting the sensitivity of the device to weakly ionising signals.

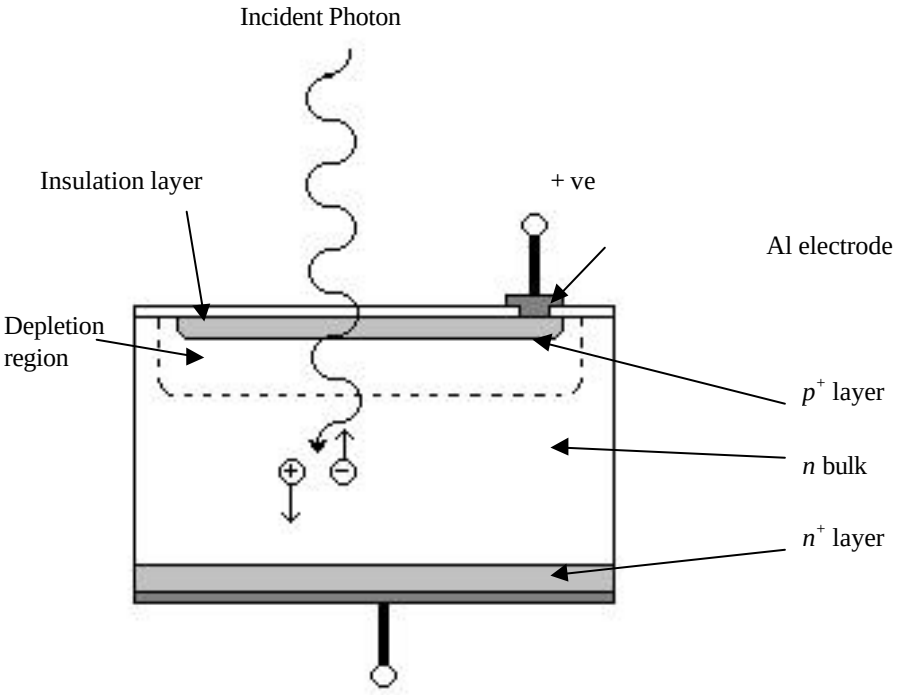

Figure 6.1: A depletion layer photodetector with p^+nn^+ structure. (Similar to the Hamamatsu S3590-08).

In the photovoltaic mode no external reverse bias is applied to the *p-n* junction. Some depletion will occur as a result of the *p-n* junction built in bias. Under ionising radiation, *e-h* pairs can be created both within and outside the depletion region. When charge is produced within both regions the signal will consist of two components. The first is the drift component which is associated with charge deposited within the depletion region. The second is the diffusion component associated with charge deposited outside of the depleted region but within a diffusion length of it.

The lower reverse current in the photovoltaic mode increases the minimum sensitivity of the photodetector. This was considered an important requirement for the *Belle* radiation monitor. Thus the photovoltaic mode was selected by the system designers.

This reliance of the photodetector signal generation on the diffusion length of minority carriers in the photovoltaic mode may however predispose the photodetector to damage in a field where NIEL is expected. The diffusion length of the minority carriers, L, is given by $(D \cdot t)^{½}$ where D is the diffusion constant and t is the lifetime of the minority carriers. It is well known that t is reduced as a function of accumulated NIEL in silicon.

In order to evaluate the suitability of the photodetector in the mixed radiation field of the *Belle* SVD, the response to ionising radiation was studied before, during and after exposure to a 20 MeV electron field and a 1 MeV neutron field. The 20 MeV electron irradiation was performed to test if high energy electrons were capable of causing sufficient displacement damage to degrade the photodetector response. An electron fluence similar to that expected within *Belle* was used. The 1 MeV neutron irradiation was used to model the *Belle* GeV energy electron environment as the damage in silicon is expected to be similar [327].

Due to the photo-sensitivity of the photodetector in the visible and infrared region, all measurements were performed within a light tight experimental chamber. The ambient background current (dark noise) was periodically measured. An average of 0.030 nA with a variability of ~ 4 % was observed. This background current was subtracted from all measurements.

6.4.1.1 Response of a Photodetector to a 20 MeV Electron Field

Exposure of the photodetector to 20 MeV electrons was done in an electron field produced using a Varian 2100C clinical linear accelerator at the St. George Cancer Care Centre, Sydney, Australia.

The experimental arrangement for this irradiation is shown in Figure 6.2. The photodetector was attached to a current pre-amplifier and covered with a thin copper foil housing. This was done to eliminate the photodetector response to ambient background light. To expose the photodetector to a high electron flux, the package was mounted at the minimum possible distance of 50 cm from the virtual electron source (Point A in Figure 6.2). The field size was collimated to a 10×10 cm^2 size as measured at Point B, 1 m from the electron source. The electron beam was delivered in 4 μs pulses at a rate of 300 Hz.

The read-out system in all tests consisted of a current pre-amplifier circuit. The circuit produced a voltage signal directly proportional to the photodetector current. It is shown in Figure 6.3. A trim pot with 4 different resistive loads permitted a wide range of voltage measurements. The DC voltage was measured with a Keithley digital multimeter (model DMM177). The photocurrent was monitored on-line during the irradiation from the accelerator control room via a 20 m interconnect cable.

Stability of the LINAC output and the electron fluence were monitored with a transmission ionisation chamber. Uniformity of the flux during the irradiation was found to be better than 2%.

The electron fluence was calculated from the dose measured in water at a distance of 1 m from the virtual electron source. The fluence at the point of irradiation was calculated using the inverse square law.

The electron fluence and ionising dose in silicon were also measured independently using the Hamamatsu photodetector at the point of irradiation using:

$$D(Si) = \frac{I_d w_{Si} t_{ir}}{e r_{Si} V_{Si}} \qquad (6.1)$$

where: I_d = photodetector current,

w_{Si} = average energy required to produce an electron-hole pair, 3.62 eV,

t_{ir} = irradiation time,

e = 1.6×10^{-19} C,

r_{Si} = density of silicon,

V_{Si} = sensitive volume of the photodetector ($1\times1\times0.03$ cm^3),

$D(Si)$ = ionising dose in silicon.

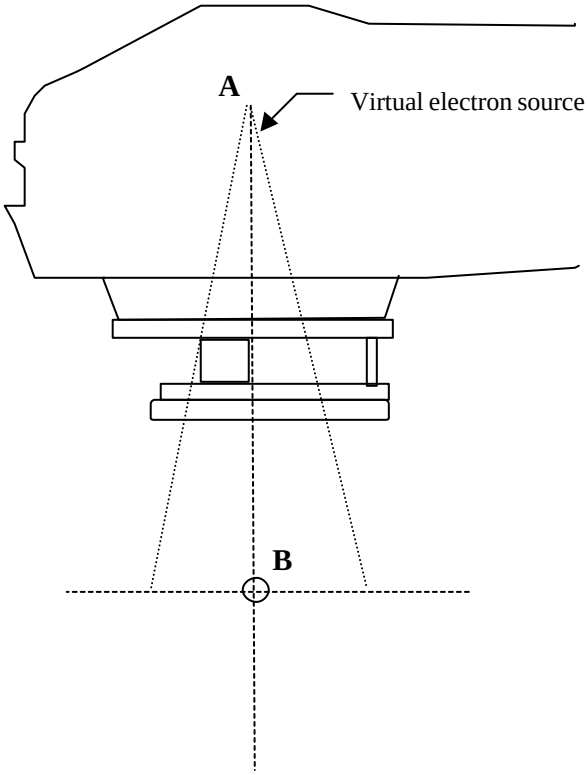

Figure 6.2: Experimental arrangement for the 20 MeV electron irradiation using a Varian 2100C clinical linear accelerator.

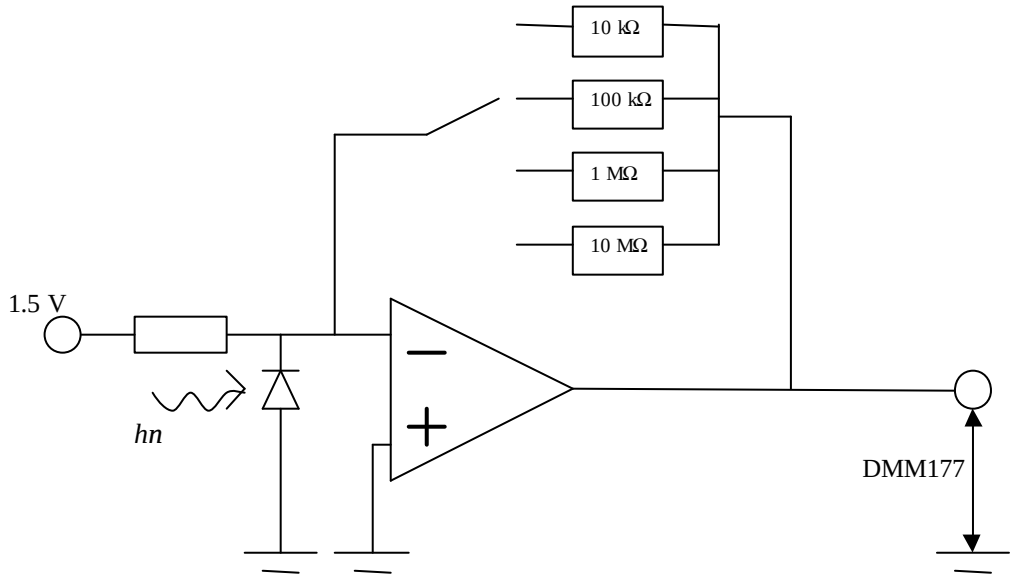

Figure 6.3: Photodetector preamplifier circuit.

The minority carrier lifetime in the photodetector silicon bulk was determined from the reverse current characteristics to be ~1.5 ms. Using a diffusion constant for holes of 10 $cm^2 \cdot s^{-1}$ [20], the corresponding minority carrier diffusion length is ~ 1.2 mm. This is much greater than the device thickness of 300 μm, so that the charge collection volume of the unirradiated photodetector in the photovoltaic mode corresponded to the geometrical volume, V_{Si}, of the photodetector.

The electron flux was calculated at the point of irradiation from the measured D(Si) in the photodetector using the energy deposited by a minimum ionising particle (mip) in 300 μm of silicon. A flux of 9.57×10^8 $cm^{-2} \cdot s^{-1}$ was calculated. The fluence calculated using this technique and from the ionisation chamber measurements were within 15 %.

A calibration of the LINAC at the point of irradiation of 1.56 kRad (Si) per 1 minute of irradiation was obtained. This calibration was done at the beginning of the irradiation when the photodetector was undamaged.

The irradiation was carried out over a period of 91 minutes.

The response of the photodetector as a function of cumulative absorbed dose in silicon is shown in Figure 6.4. It can be seen that after a dose of 50 kRad, which is the ionisation dose expected within the *Belle* SVD per year in a worst case scenario, the response is degraded by ~ 15%.

This initial result shows that use of a photodetector as an ionising radiation sensor in a high energy electron field is unreliable. The response of the photodetector will continually be degraded as a function of use.

From tabulations of the electron displacement KERMA in silicon, 20 MeV electrons are less damaging than the GeV energy electrons expected within the *Belle* SVD. A plot of the electron displacement KERMA in silicon by Summers et al. [330] is shown in Figure 6.5. The increasing displacement KERMA as a function of electron energy is associated with the relativistic boost to the electron mass which permits a higher transfer of kinetic energy from the electron to a silicon nucleus. Reliable tabulations of the displacement KERMA in silicon for electrons with energies above 200 MeV is not available [331]. The displacement KERMA for GeV electrons can however be approximated by extrapolating existing data to higher energies. In this approximation, the ratio of displacement KERMA in silicon of 1 GeV electrons to that of 20 MeV electrons is 1.37. Thus an increased level of damage of this order would be expected in a GeV energy electron field. The photodetector response in the *Belle* SVD could thus be expected to be degraded at a faster rate than for the 20 MeV electron irradiation results measured here.

6.4.1.2 Response of a Photodetector to a 1 MeV Neutron Field

In order to estimate the photodetector response in a GeV energy electron field a second Hamamatsu S3590-08 was exposed to 1 MeV neutrons.

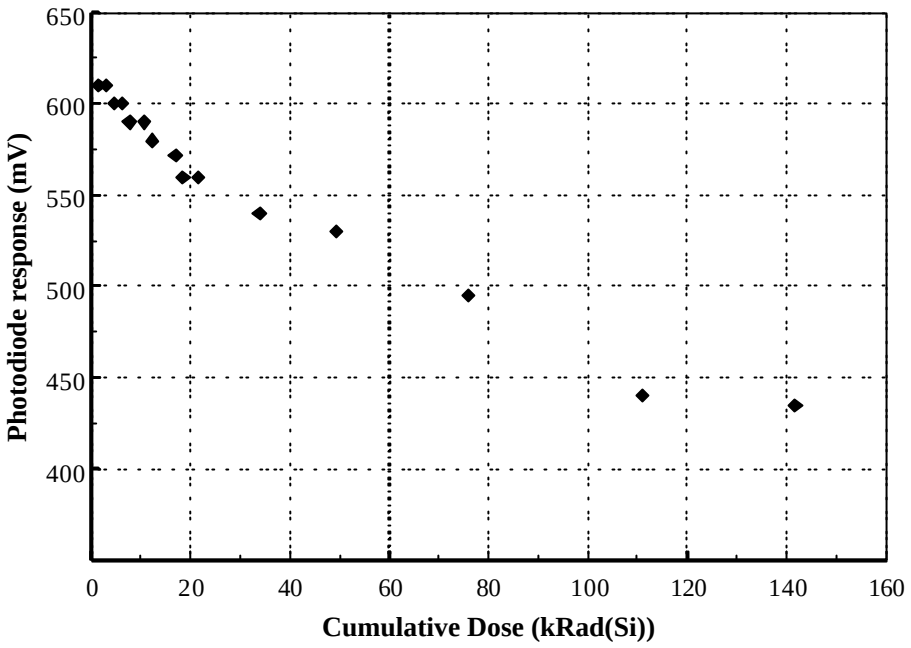

Figure 6.4: Hamamatsu S3590-08 photodetector response to 20 MeV electrons.

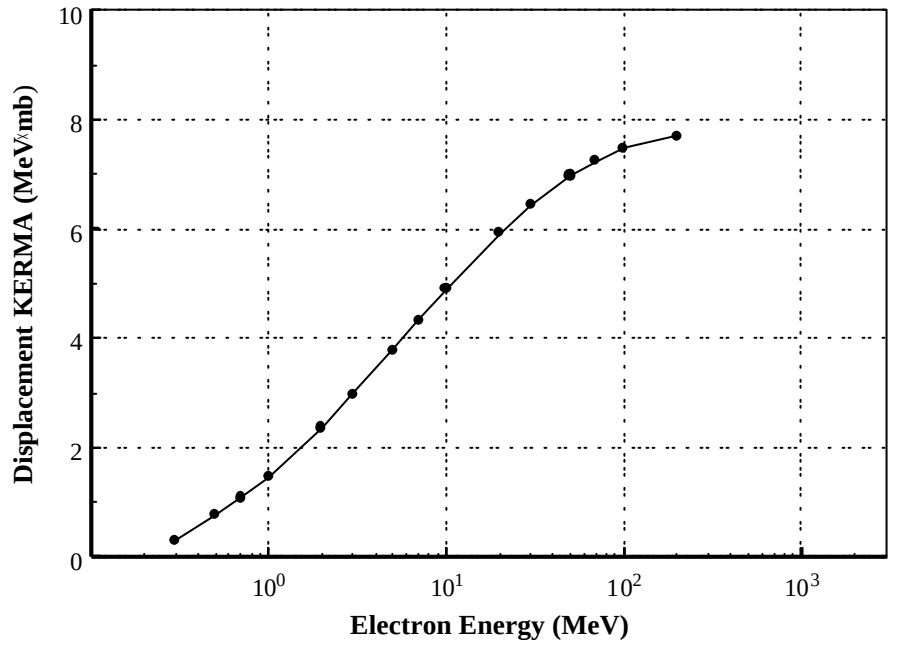

Figure 6.5: Electron displacement KERMA in silicon. Data taken from Ref. [330].

The displacement KERMA in silicon for electrons and neutrons in silicon is shown together in Figure 6.6. For 1 MeV neutrons the damage factor is 95 MeV·mb and for GeV electrons extrapolation of the curve gives, to a first order approximation, a value of 9 MeV·mb. In this approximation, GeV energy electrons are ~ 0.10 times as damaging as 1 MeV neutrons.

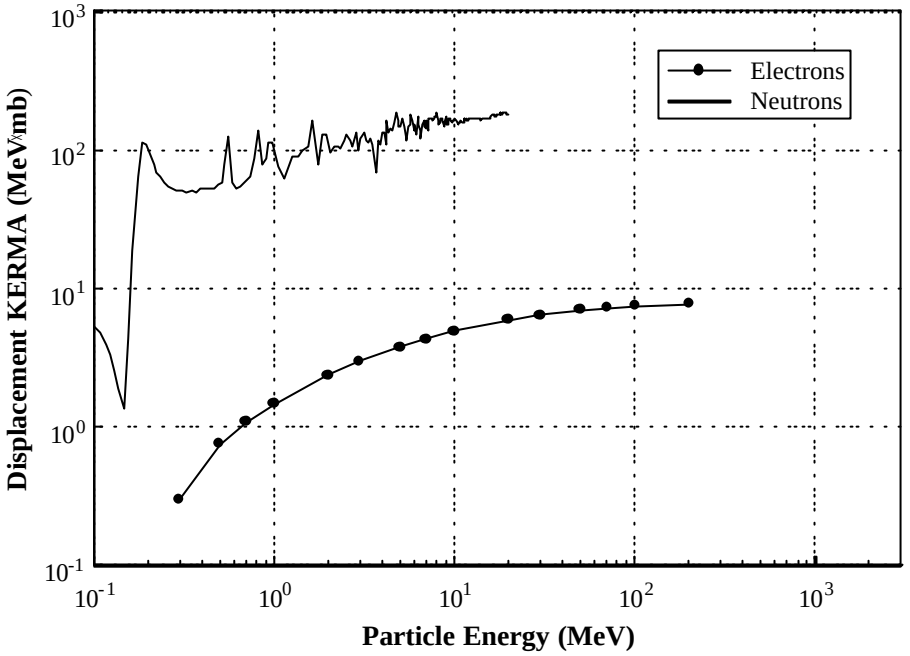

Figure 6.6: Electron and Neutron Displacement KERMA in silicon as a function of energy. Date taken from Refs [297,330].

The experimental findings of Lauber et al. [327] do not agree with this approximation. Lauber et al observed that the reverse current damage constant for 500 MeV electrons was equal to 1.1×10^{-17} A·cm^{-1}. The reverse current damage constant for 1 MeV neutrons is 2.5×10^{-17} A·cm^{-1} [332]. Thus 500 MeV electrons were found to be 0.44 times as damaging as 1 MeV neutrons.

The discrepancy between calculation and experimental results suggest that the Summer calculations may not be reliably extrapolated to higher energies to approximate the GeV energy electron displacement KERMA in silicon. Based on the Lauber et al. result it is reasonable to model a GeV energy electron field with 1 MeV neutrons.

6.4.1.2.1 Photodetector Response to Ionising Radiation Prior to Neutron Irradiation

The photodetector response was tested with three different ionising radiations: Sr-90 beta particles, *x*-ray photons (50 keV), and 940 nm infrared photons.

A Sr-90 beta source with an activity of ~ 0.1 mCi (37 MBq) was used. Sr-90 is a pure beta emitter. The maximum beta particle energy is 546 keV and the average energy is 196 keV. The daughter product of Sr-90 beta decay is Y-90 which is also a pure beta emitter. On account of the fact that the source is of sufficient age, the concentration of Y-90 is in equilibrium with the concentration of Sr-90. The beta particles of Y-90 have a maximum energy of 2.284 MeV and an average energy of 935 keV. Such electrons are minimum ionising particles (m.i.p.'s) in silicon.

The Sr-90 source was contained in the tip of a narrow metal cylinder. To ensure a reproducible dose rate at the photodetector, a mounting jig was designed and constructed. The engineering permitted the precise positioning of the Sr-90 source and photodetector giving a fixed and accurate separation between the two.

A photodetector response of 0.082 μA to the Sr-90 (Y-90) beta particles was observed.

The photodetector response to *x*-ray photons of energy 50 keV was measured at an orthovoltage machine located at the Illawarra Cancer Care Centre, Wollongong, Australia. Energies closer to the synchrotron *x*-ray energies expected in the SVD were not available.

The machine photon source was mounted above the 'patient bed'. A small perspex block was designed to house the photodetector within a small aluminium light tight enclosure. The aluminium had a thickness of 40 μm and was assumed to not cause any significant attenuation

of the photon flux. Any small attenuation could be ignored considering that an absolute measurement was not essential as final results will be reported in terms of the relative change in photodetector response to the *x*-rays, measured before and after neutron irradiation using the same measurement conditions.

Movement of the machine head allowed the distance of separation between the virtual photon source and the photodetector to be varied. Measurement was performed with distances of separation of 30 cm and 81 cm. This gave a measurement at a high and low photon flux. The dose rate at the 30 cm point was 125 rad·min^{-1}. This figure was supplied by the facility staff.

The photodetector output was monitored on-line from within the accelerator control room via a 10 m interconnect cable. A response of 2.929 V and 0.384 V was measured at the 30 cm and 81 cm positions respectively. The response was inversely proportional to the square of the distance between the source and the detector. According to facility staff an inverse square dependence of the photon flux with the distance of separation had been independently measured. This was an important verification that the photodetector signal was not saturated at the dose rates employed.

Infrared photons were used to better simulate the response of the photodetector to the 5-15 keV synchrotron radiation expected in *Belle*. Such radiation was considered appropriate on account of the similarity in the optical absorption properties of silicon to low 5-15 keV photon energies, as expected in the *Belle* SVD, and to photons of wavelength ~ 940 nm. Figure 6.7 shows the optical absorption coefficients in silicon. For 5-15 keV the optical absorption coefficient varies from 514 cm^{-1} to 27 cm^{-1}. For 940 nm photons it is equal to ~ 200 cm^{-1} [333].

The photon source was a commercially available high power GaAs infrared emitter (Kodenshi model: OPE5794). The emitter is characterised by a peak wavelength of 940 nm, and a beam angle of 34°. The emitter was powered by a constant current source designed around a LM 317 voltage regulator integrated circuit. The circuit is shown in Figure 6.8. Currents of 1 to 3 mA were used.

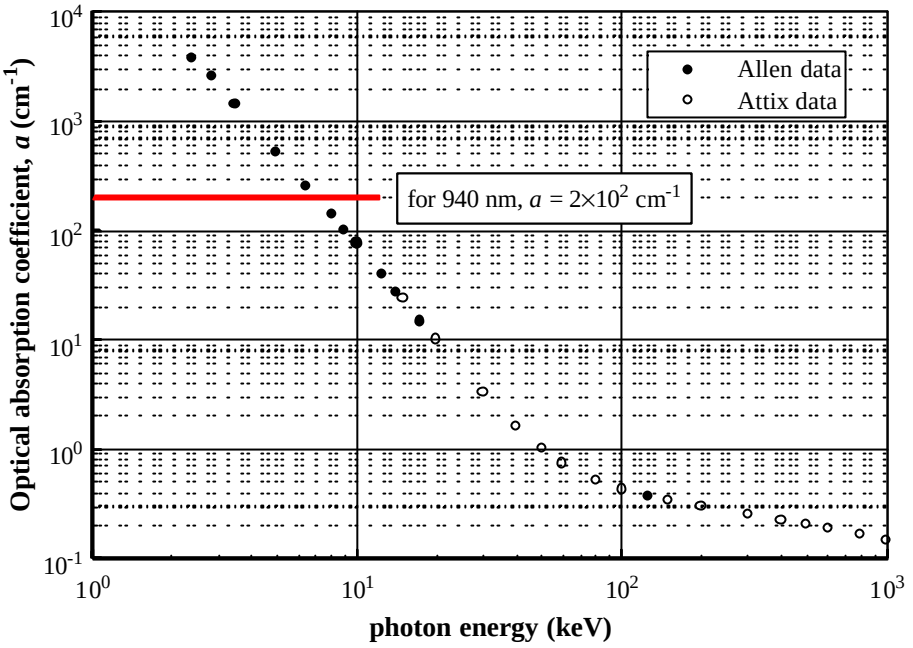

Figure 6.7: Optical absorption coefficient for x-ray photons in silicon. Data taken from Allen [334], and Attix [335]. The optical absorption coefficient for 940 nm photons is 2×10^2 cm^{-1} [333].

The experimental holder used in the Sr^{90} source measurements was adapted to accommodate the emitter at a reproducible position from the photodetector. The distance of separation was 9.8 cm. Again, all measurements were performed in a light free chamber.

The results obtained are described in the post irradiation analysis.

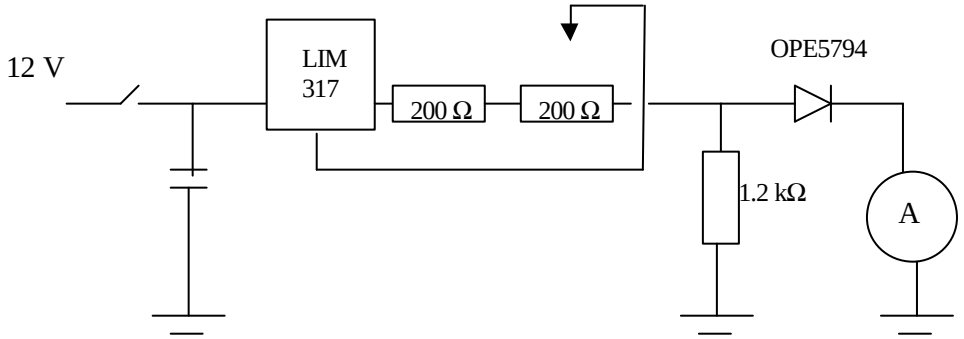

Figure 6.8: Photo-emitter constant current source.

6.4.1.2.2 1 MeV Neutron Irradiation of the Photodetector

Neutron irradiation was performed at the fast neutron facility described in Chapter 3. The neutrons were produced on a Li^7 target bombarded by 2.7 MeV protons with an average beam current at the target of 22 μA. The neutron energy in the forward direction was ~ 1 MeV. The Hamamatsu photodetector, enclosed within a thin walled aluminium canister, was located at a distance of 5 mm from the target. The canister protected the photodetector from a water spray used for target cooling. Measurement of the neutron fluence was made using a neutron long counter located at a distance of 3 m from the neutron source. Additionally, a PIN Dosimetric Diode, calibrated in terms of the 1 MeV equivalent neutron fluence, was placed at the same point as the photodetector.

Irradiation was performed over a period of ~ 8 hrs. The total neutron fluence was ~ $2.3\times10^{12}\,cm^{-2}$. The maximum uncertainty in this fluence was 20 %.

The photodetector response was not measured on line during irradiation. The irradiation was however periodically interrupted and the response of the photodetector to the $\lambda \sim 940$ nm photons measured.

6.4.1.2.3 Photodetector Response to Ionising Radiation During and After Neutron Irradiation

Response to 940 nm photons was measured at an equivalent 1 MeV neutron fluence of 1.9×10^{10}, 2.8×10^{11}, 1.8×10^{12} and 2.3×10^{12} cm^{-2}.

The observed degradation of the photodetector response is shown in Figure 6.9. After a fluence of $\sim 1\times10^{12}$ a degradation of around 25 % has occurred.

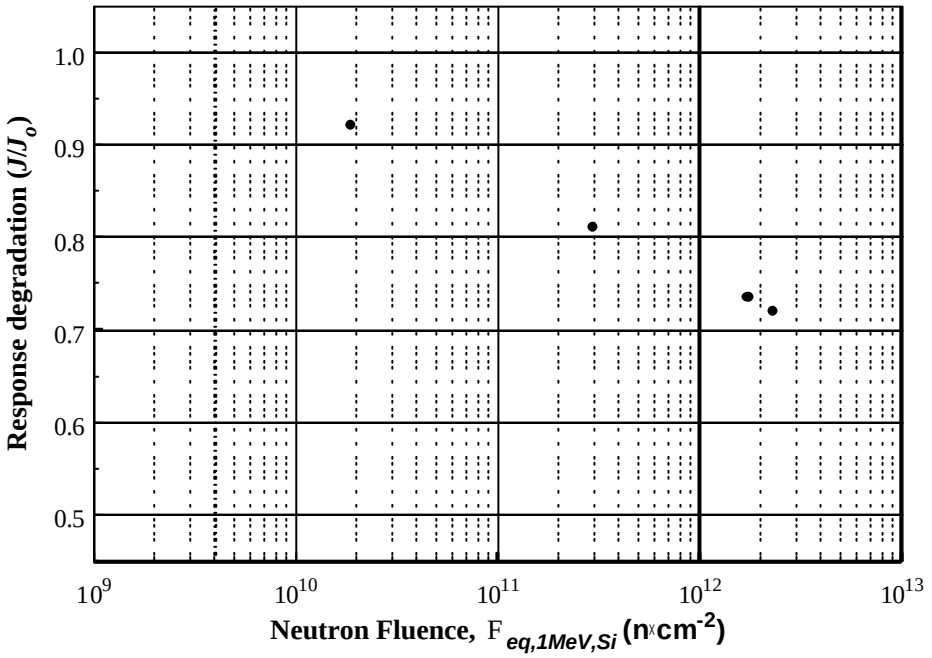

Figure 6.9: Photodetector response degradation to 940 nm photons as a function of neutron irradiation. The $\Phi_{eq,1MeV,Si}$ neutron fluence was measured using a PIN Dosimeter Diode mounted adjacent to the photodetector.

The response of the photodetector to the Sr-90 beta source was measured on the day after neutron irradiation. Measurement conditions were kept the same as for the pre irradiation measurements. The photodetector response was degraded by a factor of 27 times after the total neutron fluence of 2.3×10^{12} cm^{-2}.

The response to the 50 keV *x*-ray photons was measured 36 hrs after irradiation. Conditions were kept the same as for the pre irradiation measurements. At the 30 cm and 81 cm positions, a response of 0.704 V and 0.098 V was measured. The average response degradation was 4.1 times.

All results obtained here further demonstrate that the photodetector is not radiation hard to the effects associated with NIEL in silicon and is thus an unreliable sensor for IEL in a radiation field where NIEL is expected.

The differing degradation of the photodetector response to the infrared photons, 50 keV *x*-rays and Sr-90 beta particles can be explained by the differing contribution of diffusion charge to the photodetector signal. In all cases the ionising radiation was incident upon the front face (junction side) of the photodetector. For the photon sources, the photon flux is exponentially attenuated within the absorbing medium. The photon penetration depth is defined as the inverse of the optical absorption coefficient, a^{-1}. For the 940 nm photons, a^{-1} is equal to 50 μm. In this case a significant proportion of the *e-h* pairs will be produced in the depleted region. As such, a significant portion of the signal will be due to charge drift. For the 50 keV *x*-ray photons, a^{-1} is approximately 1 cm. In this case significant portions of energy will be deposited in both regions. Thus both mechanisms of signal formation will be important. For the Sr-90(Y-90) beta particles, which may be approximated as mips in silicon, the *e-h* generation rate will be linear throughout the device. Here the largest fraction of *e-h* pairs will be produced in the undepleted region. Thus the signal will be most significantly affected by a radiation induced reduction to the minority carrier diffusion length.

The response of the photdetector is expected to be most significantly degraded for ionising radiation which deposits the largest fraction of radiation within the undepleted region of the photdetector bulk.

This explanation was considered more thoroughly from a charge transport perspective.

6.4.1.2.4 Charge Transport in a Photodetector Damaged by 1 MeV Neutrons

For the case of photons incident on the front side of the photodetector the induced signal and its dependence on neutron damage can be derived from the charge transport equations.

Consider a photon flux, F_o, incident upon the front face of the detector. Under the condition that the front contact layer is much thinner than a^{-1}, the generation rate of carriers, G, as a function of distance, x, into the device is given by Equation 6.2 (see Blood and Orton [181]). For photons in the region of 940 nm photons, a^{-1} is ~ 50 μm which is much greater than the typical contact thickness of a photodetector.

$$G(x) = TF_0 a e^{-ax} \qquad (6.2)$$

where: T = transparency of the front contact (which is equal to the flux of photons which are not reflected),

a = optical absorption coefficient of the silicon bulk (which is dependent on the photon energy).

Sze derives the total current density using the one-dimensional diffusion equation under the condition that the photon generated minority carrier concentration is much greater than the equilibrium minority carrier concentration [20]. It is given by:

$$J_{tot.} = -qF_0T\left[1 - \frac{e^{-ax_d}}{1+aL}\right] \qquad (6.3)$$

where: x_d = the depletion layer depth,

L = the minority carrier diffusion length.

For the case of a p^+nn^+ structure the minority carriers are holes. Therefore $L_p = (D_p \cdot t_p)^{½}$.

The dependence of t_p on the neutron fluence is usually parameterised according to:

$$\frac{1}{t_p} = \frac{1}{t_{po}} + K\Phi \qquad (6.4)$$

where: t_{po} = the initial, unirradated, minority carrier lifetime,

K = the minority carrier lifetime damage constant.

Substitution of Equation 6.4 and the minority carrier lifetime definition into Equation 6.3 gives:

$$J_{tot.} = -qF_0T\left[1 - \frac{e^{-ax_d}}{1 + a\left(\frac{D_p}{\frac{1}{t_{po}} + K\Phi}\right)^{\frac{1}{2}}}\right] \qquad (6.5)$$

The diffusion constant, D_p, is a slowly varying function with the impurity concentration [20]. Equation 6.5 predicts that as the neutron fluence increases, the total current density for identical ionising conditions will be reduced. For typical values of the diffusion constant, D_p, and the initial minority carrier lifetime, t_{po}, the current density will be dependent upon the depletion region width, x_d, the optical absorption coefficient, a, and the neutron damage constant, K.

In the photovoltaic mode the depletion region width, x_d, for conditions of no external bias is dependent upon the doping concentrations within the p^+ and n regions. For a single sided abrupt junction (p^+n) as is the case for the Hamamatsu S3590-08, the depletion width can be approximated by:

$$x_d \approx \sqrt{\frac{2e_o e_{Si} V_{bi}}{qN_D}} \qquad (6.6)$$

where V_{bi} is given by;

$$V_{bi} = \frac{kT}{q}\ln\left(\frac{N_A N_D}{n_i^2}\right) \qquad (6.7)$$

Using the values of $N_A=10^{21}$ cm^{-3}, $N_D=2\times10^{12}$ cm^{-3}, and T=295 K, the built in bias, V_{bi}, is 0.773 V and, x_d, is 22.5 μm. A minority carrier lifetime of 1.4 ms was determined experimentally from the reverse *I-V* characteristics of the unirradiated photodetector. For photons of wavelength ~ 940 nm, the optical absorption coefficient in silicon is ~ 200 cm^{-1} [333]. The minority carrier lifetime damage constant for 1 MeV neutrons, K_n, was taken to be 7.7×10^{-8} cm$^2\cdot$s^{-1}. This was obtained from:

$$a = \frac{qn_i K_n}{2} \qquad (6.8)$$

where a was assumed to be 9×10^{-17} A·cm^{-1}. a is the reverse current damage constant immediately after irradiation before room temperature annealing has occurred.

The photodetector degradation given by $J(\Phi_n)/J_o$ was plotted as a function of Φ_n. In Figure 6.10 the plot is shown along with the experimentally measured data. A good agreement was obtained.

Photons which interact with the photodetector but are not incident upon the device junction surface have a lower probability of depositing *e-h* pairs within the depleted region. In this situation the device response can be expected to be reduced further. In the SVD of *Belle* the incidence of photons to the photodetector sensors will depend on the orientation of the photodetector relative to the photon source. Not all photons will be incident on the junction face. As such, the results presented are for a best case scenario.

This result confirms that the photodetector signal degradation is associated with the reduction of the minority carrier lifetime as a result of the deposition of NIEL within the silicon bulk.

Most of the ionising radiation within the *Belle* SVD will be made up of high energy electrons, the response degradation of the photodetector to Sr-90 beta particles is the most important result. The reduction in response by 27 times is a serious weakness.

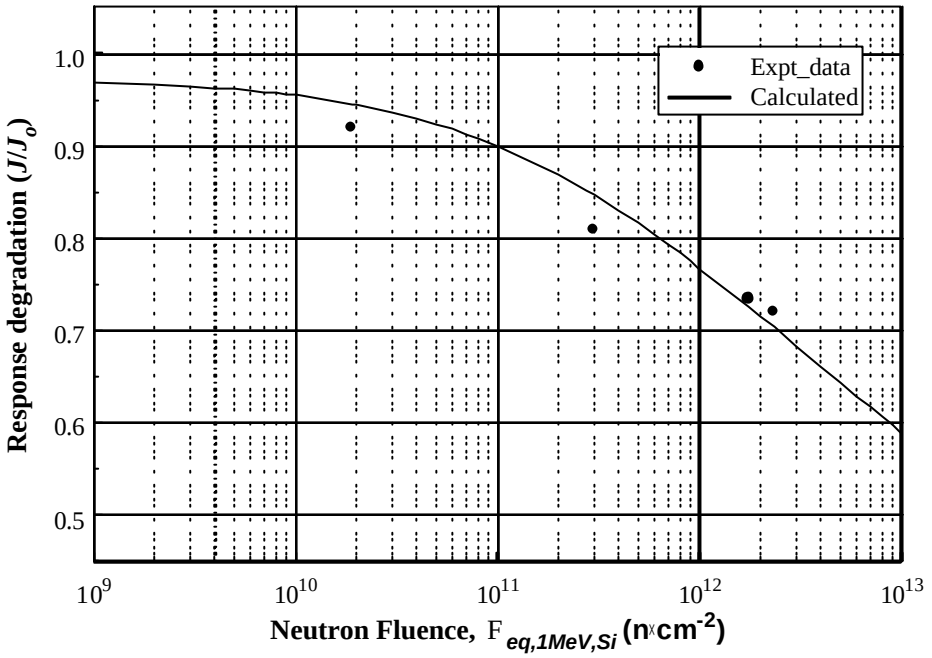

Figure 6.10: Calculated response degradation of the photodetector to the 940 nm photons as a function of neutron irradiation.

The conclusion from this experiment and the 20 MeV electron irradiation experiment is that an ionisation dose monitor based on a photodector would be unreliable for applications within a field containing high energy electrons. The apparent radiation levels would continuously be

underestimated as a function of time due to the continued degradation of the charge collection characteristics of the device.

An alternative sensor based on a MOSFET structure was investigated.

6.4.2 MOSFETs for Ionising Dose Monitoring

The use of a MOSFET structure as a radiation monitor was first proposed by Andrew Holmes-Siedle [336]. The mechanism of dosimetric response in such a device is based on the same effect that causes damage in CMOS LSI electronics. As mentioned previously, with increasing ionising dose, the charge stored within the oxide layer increases. This gives rise to a shift in the threshold voltage of the transistor, which can easily be measured.

The device consists of an insulating layer of silicon dioxide which acts as the gate insulation of a metal-oxide-semiconductor (MOS) structure. A schematic of a MOSFET is shown in Figure 6.11.

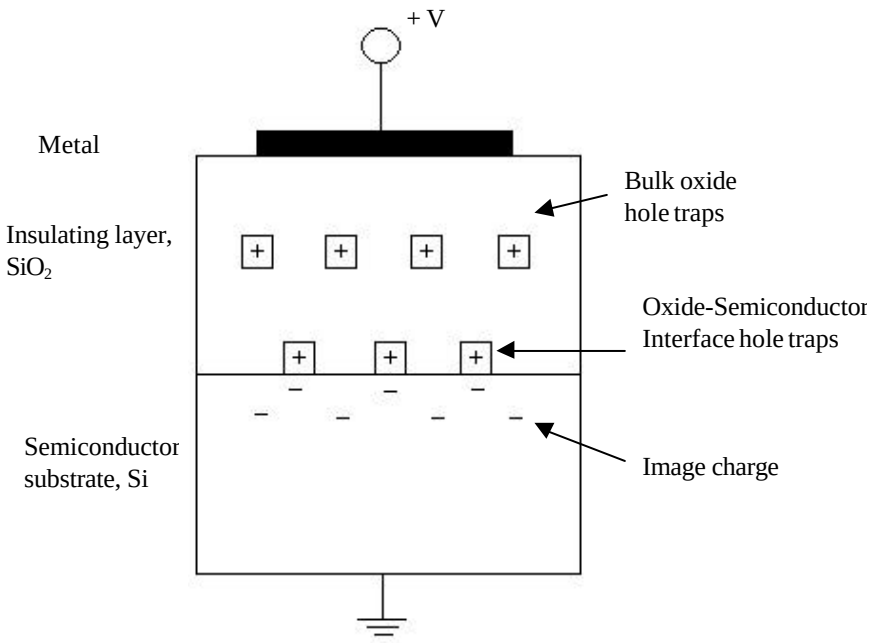

Figure 6.11: Simple schematic of a metal-oxide-semiconductor (MOS) structure. Also shown are interface and bulk trapping states.

The accumulation of oxide charge with exposure to ionising radiation occurs under two different mechanisms. In the first, known as the "low field mode," hole traps are created in the oxide side of the oxide-semiconductor interface. In the second, known as the "high field mode," hole traps are created within the bulk of the oxide layer. When a positive voltage is applied to the metal contact, *e-h* pairs created by the incident ionising radiation move in response to the electric field. Electrons are able to escape the insulation layer but holes become trapped. The resulting excess of positive charge within the oxide layer induces an image charge within the silicon bulk adjacent to the SiO_2-Si interface. In terms of the macroscopic device properties, this charge induces a shift in the threshold voltage, ΔV_t, of the MOS transistor. For a useful range of dose, the shift, ΔV_t, is proportional to the radiation induced charge within the oxide layer which in turn is proportional to the radiation dose accumulated by the device.

A typical channel current versus threshold voltage curve of a MOS transistor and the shifted curve after irradiation is shown in Figure 6.12. In a normal readout system a constant drain current of order 10 mA is used and the threshold voltage is measured before and after irradiation. The observed shift in ΔV_t is the dosimetric parameter which can be calibrated in terms of the actual radiation dose.

For the "high field mode," a linear behaviour exists between the threshold voltage shift, ΔV_t, and the absorbed radiation dose, D, given by [337]:

$$\Delta V_t = R \cdot A \cdot D \qquad (6.9)$$

where: R = constant dependent on the radiation induced carrier generation rate within the oxide,

A = probability of charge trapping by the oxide hole traps,

D = absorbed radiation dose.

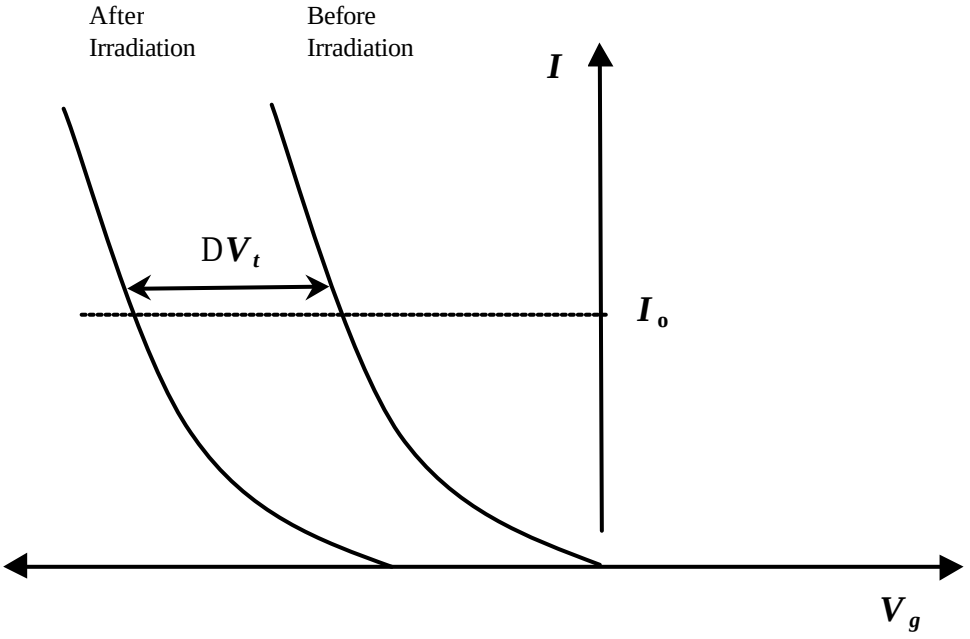

Figure 6.12: Channel current versus threshold voltage curve of a MOS transistor and the shifted curve after irradiation.

For the "low field mode," the relationship between the threshold voltage shift, ΔV_t, and the absorbed radiation dose, D, is only approximately linear. The relationship is of the form:

$$\Delta V_t = kD^n \qquad (6.10)$$

where: k = a constant factor similar to R above,

n = measure of response linearity with absorbed dose, D.

The value of *n* varies about 1 depending upon the dose range and the oxide thickness [337]. For operation in the low field mode it is important that the MOSFET response is carefully calibrated.

The response sensitivity under both mechanisms of charge accumulation can be changed by altering the thickness of the gate oxide and metal layer.

More extensive details on the use of a MOSFET device for radiation dose measurement is available in a comprehensive review by Holmes-Siedle and Adams [337]. In this paper the MOSFET is referred to as a RADFET. [337].

6.4.2.1 Response of a MOSFET to a High Energy Electron Field

Following preliminary calibrations in terms of ionisation dose to the SiO_2 layer it was proposed that this detector could be used for the characterisation of IEL in a high energy electron field. The requirements of the sensor were that it responded in a reliable fashion to the accumulation of ionising energy dose deposited by high energy electrons. And secondly that the response was not degraded as a function of non-ionising energy dose.

The MOSFET sensors used were REM RADFET TOT500 type devices, supplied by Radiation Experiments and Monitors (REM), Oxford, UK. The device integrates four *p*-channel dosimeters onto a single die approximately 1 mm x 1 mm in size, with the die connected on top of a thin circuit board.

Two different oxide thickness were used, 0.93 μm and 0.13 μm. The thicker oxide provides greater sensitivity to ionising dose, giving a dosimeter that is sensitive within the low Rad(Si) range. This RADFET was designated as type ‘R’. The thinner oxides give a dosimeter suitable to higher doses, in the kRad(Si) range. This RADFET was designated type ‘K’.

To obtain calibration curves for the RADFET system under high energy electrons in terms of dose in silicon, four such devices were exposed to a 20 MeV electron field. Irradiation was performed at the Varian 2100C facility described previously. Four RADFETs, TOT500 (2 in DIL package, 2 in CC-3 package) were irradiated. The shift of the threshold voltage under a constant current was measured. All measurements were done during a 3 hour irradiation. The spread in the change in threshold voltage, ΔV_t, as a function of the dose in silicon, D(Si), was found to be less than 3% for different RADFETs from the same batch. Figure 6.13 shows the response curves for both 'R' and 'K' type RADFETS in the 20 MeV electron field in terms of dose in silicon. The analytical expressions derived from the calibration curves for the 'K' type RADFET is $D = 40.23\times(\Delta V_t)^{1.250}$, where D is the dose measured in kRad(Si), and ΔV_t is the voltage shift in Volts. For the 'R' type RADFETs, $D = 1.81\times(\Delta V_t)^{1.304}$.

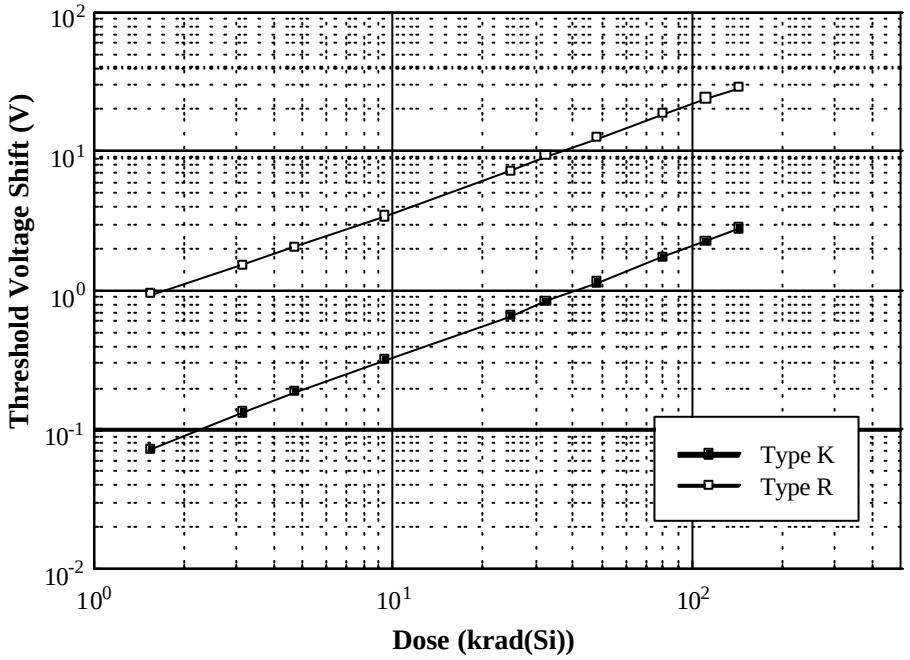

Figure 6.13: Response of the RADFETs to the 20 MeV electron field. The response is shown in terms of the absorbed dose in silicon.

The sensitivity of both devices did not change during the 20 MeV electron dose of 100 kRad(Si). This dose corresponds to an electron fluence of ~ 5×10^{12} cm^{-2}. It was anticipated before testing that the sensitivity would not be changed for doses of this magnitude. This was based on previous experimental studies on similar devices tested with electrons in the energy range of 30 keV – 30 MeV [334], as well as with protons in the energy range 10 MeV – 40 MeV [335]. (Protons of energy > 10 MeV are similarly damaging to 1 MeV neutrons).

Satisfactory performance in the 20 MeV electron field to doses equivalent to 3 years of operation at *Belle* in a worst case scenario was considered a satisfactory verification that the RADFET was sufficiently radiation hard. The negligible sensitivity of the MOSFET to NIEL can be attributed to the low resistivity of the silicon used for MOSFET construction, and hence the low minority carrier lifetime [338].

The measurable dose ranged from 10 to 2.5×10^{6} Rad(Si) for the RADFETs in a high energy electron field using both 'K' and 'R' type devices.

Temperature stability of the RADFET dosimeters was investigated at a readout current of 160 μA. Before electron irradiation, the average temperature instability coefficient of change in threshold voltage was found to be approximately -2 $mV\cdot°C^{-1}$ for type 'R', and 0.7 $mV\cdot°C^{-1}$ for type 'K' dosimeters. The stability of the 'K' type dosimeters did not change much after irradiation, and was consistent, at 0.8 $mV\cdot°C^{-1}$, for all of the 'K' type dosimeters tested. The 'R' type dosimeters, however, had varying responses, ranging from -8 $mV\cdot°C^{-1}$ to -3 $mV\cdot°C^{-1}$ and an average value of -5 $mV\cdot°C^{-1}$. This represents a dose dependence of approximately 15 $Rad(Si)\cdot°C^{-1}$ at the beginning of the irradiation, which is negligible for the expected dose range in the present application.

6.4.3 PIN Dosimeter Diodes for Non Ionising Dose Monitoring

For the *Belle* experiment no allowance was made for the monitoring of radiation dose associated with NIEL in silicon. This was largely based on the assumption that high energy electrons, at the fluences expected in the *Belle* SVD, would not create any significant radiation hardness concerns for the DSSDs. It has been shown here that the NIEL anticipated for a particle flux in a worst case scenario ($\Phi_e \sim 2\times10^{12}$ el·cm^2), will cause damage leading to degradation in the performance of a photodetector based ionising radiation monitor. The susceptibility of the DSSDs to the worst case scenario particle fluence will largely depend on the displacement KERMA of GeV energy electrons in silicon. Using the approximate value of 10 MeV·mb obtained by extrapolating the electron displacement KERMA in silicon of Summers to GeV energies (see Figure 6.5), such electrons will be ~ 0.1 times less damaging then 1 MeV neutrons. It would thus be anticipated that changes to the DSSD reverse current will occur. Only minimal alteration to the effective impurity concentration of the DSSD silicon bulk could be expected. Type inversion of the DSSD silicon bulk would not occur.

The reliability of the displacement KERMA in silicon at high electron energies is questionable. It does not agree with experimental measurements at 500 MeV electron fields [334]. Also, the scenario presented here does not address the possibility of an unanticipated beam malfunction which could lead to a sudden increase in the radiation level within the SVD. Such an incident occurred in the OPAL e^+e^- collider experiment. The result was that part of the detector became irreversibly non-functional.

The inclusion of a NIEL damage sensor within the *Belle* SVD is beneficial for monitoring accumulated NIEL damage in the DSSDs under normal operating conditions. It will also allow the assessment of damage in the DSSDs in the event of a catastrophic increase in the radiation levels associated with a beam malfunction. With the trend in lepton colliders towards higher beam energies and higher beam currents it is inevitable that radiation damage to DSSD type devices in future e^+e^- collider experiments will become increasingly apparent as is currently the case for hadron colliders.

It is reasonable to assume that the most appropriate sensor for the monitoring of damage in silicon strip detectors is one based on the same type of material. That is, high resistivity silicon. The PIN Dosimeter Diode examined in Chapter 5 was manufactured from such material. The sensitivity of this device to dose associated with NIEL in silicon is well known in 1 MeV neutron applications. In this previous chapter it was shown that the response of the device in terms of the equivalent 1 MeV neutron fluence, $\Phi_{eq,1MeV,Si}$, was not dependent upon the energy spectrum of the neutron field used for calibration. This result infers that the PIN Dosimeter Diode dosimetric response is associated with the accumulation of NIEL as predicted by the neutron displacement KERMA in silicon. It is proposed here that a PIN Dosimeter Diode, calibrated in terms of $\Phi_{eq,1MeV,Si}$ could be used to monitor NIEL damage in silicon devices exposed to high energy electrons. The response of the device in the high energy electron field would be in terms of $\Phi_{eq,1MeV,Si}$. This would permit immediate assessment of electron damage in DSSD type devices by comparison with radiation hardness results understood in terms of $\Phi_{eq,1MeV,Si}$.

6.4.3.1 Response of PIN Dosimeter Diode to a 20 MeV Electron Field

The response of a PIN Dosimeter Diode, calibrated in terms of $\Phi_{eq,1MeV,Si}$ was measured in a 20 MeV electron field.

To provide an independent verification of $\Phi_{eq,1MeV,Si}$ in this field, an ion implanted silicon detector test structure was also irradiated. The change of the detector reverse current of this device is well understood in terms of $\Phi_{eq,1MeV,Si}$.

The experimental arrangement of the electron irradiation was the same as for the photodetector electron irradiation described in section 6.4.1.1. The irradiation was performed in two stages. In the first stage both devices were exposed to the electron field at the same point for 25 minutes. In the second stage the ion implanted detector structure was removed from the beam. The PIN Dosimeter Diode was irradiated for a further 25 minutes. Uniformity of the electron flux in both stages of irradiation was found to be better than 2%.

The temperature of the ion implanted detector test structure was monitored during irradiation using a thermocouple sensor. The sample temperature before, during and at the end of the irradiation was 30°C ± 1°C. No heating occurred as a result of direct irradiation by the electron beam. The room temperature was measured to be 22°C. The localised heating of the sample to 30°C was caused by a halogen light globe located in the accelerator head. No corrective action was taken to remove this heat source due to the necessary illumination for another experiment performed simultaneously with this work.

The reverse current characteristics of the ion implanted detector test structure was measured 12 hrs after irradiation. During the intermediate period the device was stored at room temperature. The results from before and after electron irradiation are shown in Figure 6.14. In both cases the reverse current was normalised to a temperature of 20°C. The reverse current at full depletion as a result of irradiation was observed to increase by a factor of 30. The full depletion voltage of 79 V was measured using rear contact projected 5 MeV alpha particles. No change in the full depletion voltage was observed.

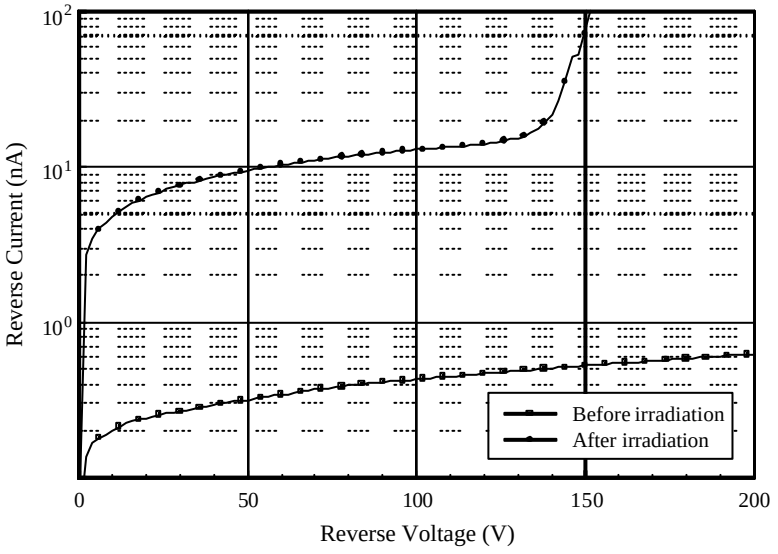

Figure 6.14: Reverse current of the Ion implanted Si detector test structure before and 12 hrs after irradiation with 20 MeV electrons.

The increase in the reverse current was attributed to bulk radiation damage on account of an observed linearity between the change in reverse current and the square root of the reverse voltage. A plot is shown in Figure 6.15.

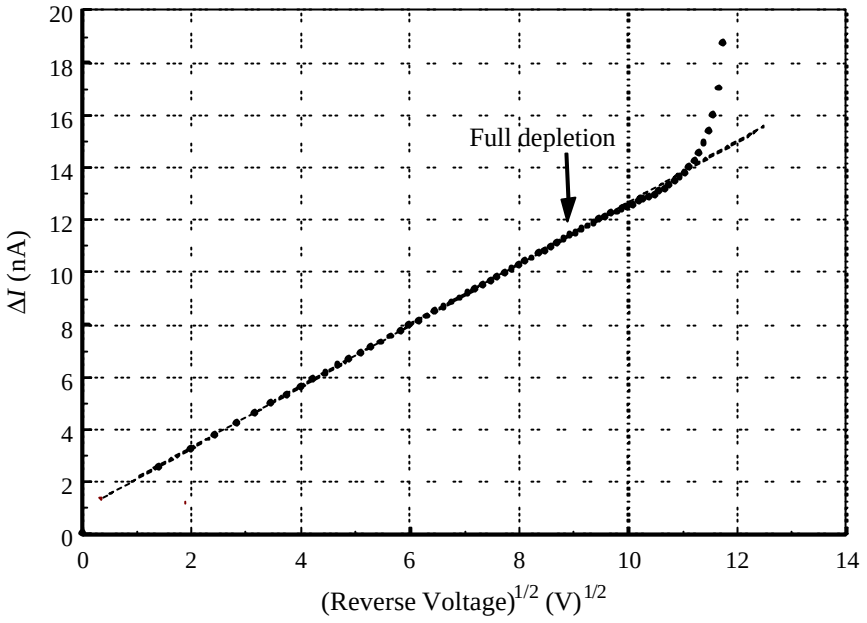

Figure 6.15: Radiation induced reverse current plotted as a function of the square root of the reverse voltage.

Repeated measurement of the reverse current was done to determine the effect of RT annealing (see Figure 6.16). Significant reverse current annealing was observed with time following irradiation. The reverse current measured at full depletion, as a function of time, is shown in Figure 6.17. All measurements have been corrected to 20°C. Over a period of 30 days, the reverse current was seen to decrease by 35% from the value measured 12 hrs after irradiation. After approximately 60 days the reverse current became constant and no further reductions where observed in an additional 30 days of testing.

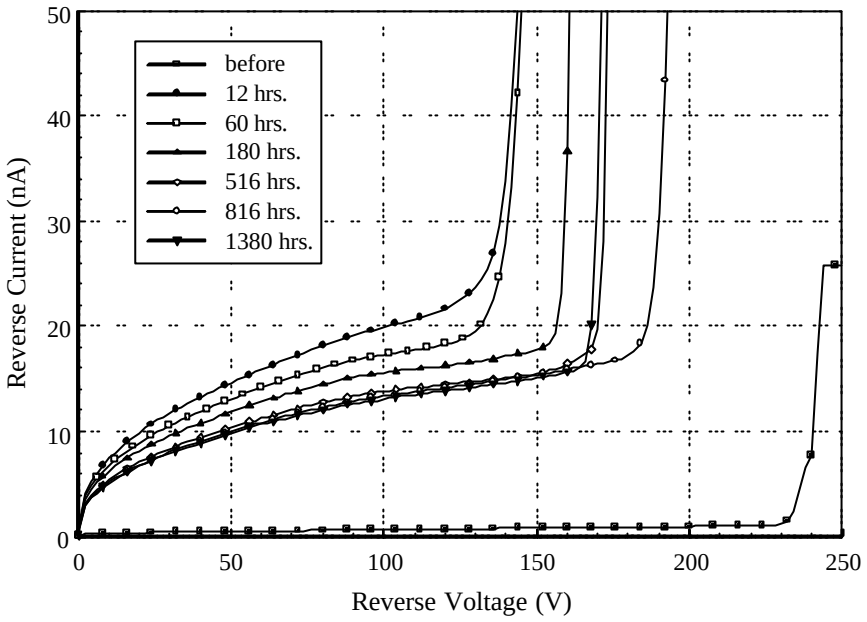

Figure 6.16: Reverse current measured at various times following electron irradiation. Measurements performed at 25°C.

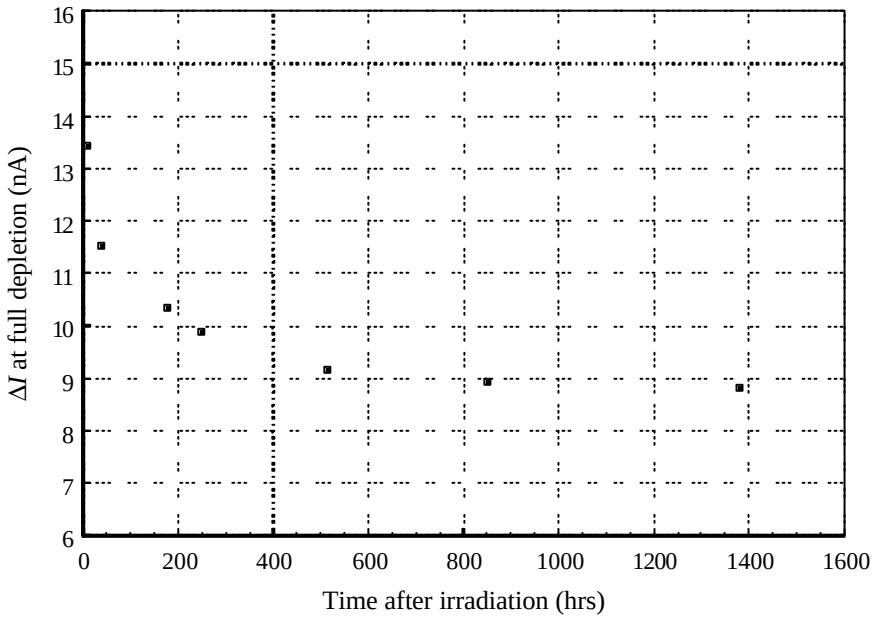

Figure 6.17: Reverse current measured at full depletion as a function of time after irradiation. Reverse current was normalised to 20°C.

The detector reverse current increase with irradiating particle fluence is parameterised according to:

$$\frac{I - I_o}{Vol} = a \ \Phi \qquad (6.11)$$

where: I_o = reverse current before irradiation,

I = reverse current after irradiation,

Vol = full depletion volume of the detector,

Φ = particle fluence.

To simulate the equivalent 1 MeV neutron fluence, $\Phi_{eq,1MeV,Si}$, of this electron irradiation, the reverse current damage constant for 1 MeV neutrons ($\alpha = 2.5\times10^{-17}$ A·cm^{-1} [332]) was used. Using $I–I_o = 8.7$ nA, $vol = 7.5\times10^{-3}$ cm^3, $\Phi_{eq,1MeV,Si}$, is equal to 4.6×10^{10} cm^{-2}.

The PIN Dosimeter Diode showed a good linear response as a function of fluence of the 20 MeV electron beam. The forward bias voltage of the PIN Dosimeter Diode was measured before and immediately after irradiation in water at a temperature of 21°C in order to avoid a temperature error. A forward voltage shift of 317±15 mV was observed for the total irradiation time of 50 minutes. Using the known sensitivity of the diode in terms of 1 MeV(Si) neutrons the forward voltage shift corresponded to an equivalent neutron fluence of 7.46×10^{10} n·cm^{-2}. For comparison with the detector reverse current result, correction for the differing times of exposure was required. The ion implanted detector was irradiated for 25 minutes only. Hence $\Phi_{eq,1MeV,Si}$ as measured by the PIN Dosimeter Diode for the period of irradiation experienced by the detector was 3.73×10^{10} cm^{-2}. This value is within 20% of $\Phi_{eq,1MeV,Si}$ determined from the detector reverse current.

This good agreement supports the suitability of PIN Dosimeter Diodes for the measurement of damage in high energy electron fields in terms of the equivalent 1 MeV neutron fluence.

6.4.4 Construction of the RDMS

Based on the results obtained for the RADFET sensor and the PIN Dosimeter Diode sensor, a RDMS based on these sensors was proposed for the *Belle* SVD. The proposal was accepted by the *Belle* collaboration. With sensors already developed and tested, the RDMS required only the electronic readout system.

The readout system was designed and constructed by technical staff from the Centre of Medical Radiation Physics. The developed system allows the simultaneous readout of 32×2 channels on-line with automatic data logging to a computer. The basic operation of the reader is to pass a constant current of 160 μA through the RADFET and 1 mA through the PIN Dosimeter Diodes followed by reading of the corresponding threshold voltage, V_t, and forward voltage, V_F, respectively. During the irradiation all pins of the RADFETs and PIN Dosimeter Diodes are grounded. It is important to have a duty cycle much longer than the readout time for the RADFET to avoid a change of sensitivity due to the voltage on the gate. The readout for the RADFET and PIN Dosimeter Diode sensors was made in a pulsed mode. Initial delay in sampling was about 1 ms to avoid any fast transients in the RADFET and PIN Dosimeter Diodes.

The system is currently designed with a long ribbon cable interconnect (the *Belle* experiments require a 10 m cable from the SVD to the control room). A PC board with calibrated resistors is used for testing channels during the device operation or installation. Special adaptors connect the RADFETs and PIN Dosimeter Diodes to the reader to allow readout scanning of individual sensors. Parallel readout of the 32 R/K RADFET pairs or PIN Dosimeter Diodes can occur simultaneously. Any channel can be read manually using the built-in digital display. The whole unit fits in a standard 3 unit 19” rack enclosure. The logger used is a TempScan/1100. A photograph of the developed readout electronics is shown in Figure 6.18.

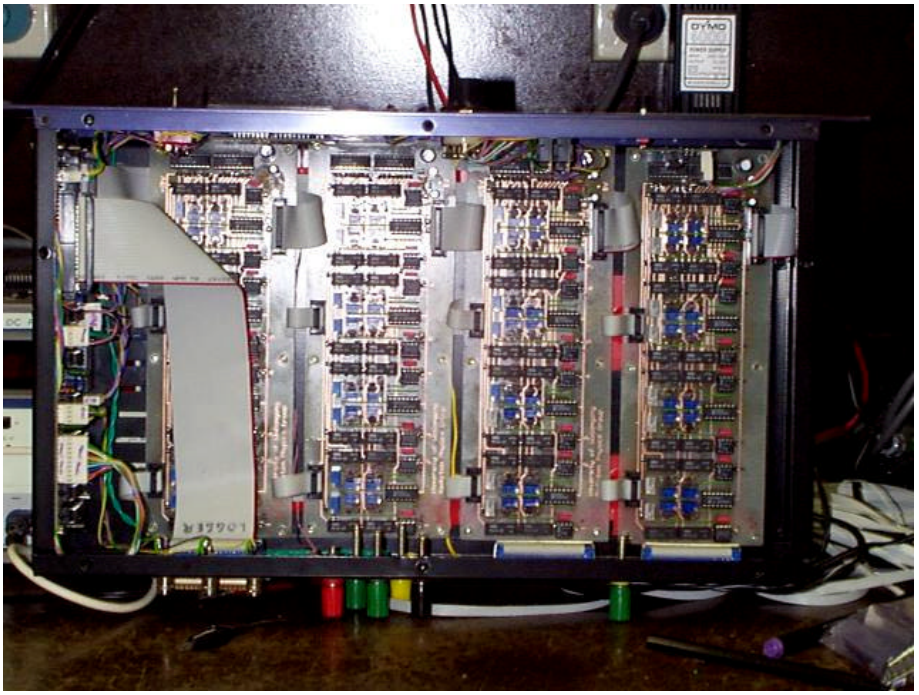

Figure 6.18: Readout electronics of the RDMS installed within the *Belle* SVD.

The system sensors were incorporated into various points within the *Belle* SVD. At the time of writing only preliminary results were available and are not discussed here. Suffice to say that it is working well. Based on the results a system was requested by staff at SLAC in the United States.

6.5 Conclusion and Discussion

Radiation damage monitoring of silicon devices within mixed radiation fields requires separate determination of the ionising damage and displacement damage.

In a mixed radiation field containing synchrotron radiation and high energy electrons it is impossible to predict displacement KERMA in silicon by relying upon the ionising dose rate only.

The application of photodetectors for radiation damage monitoring in a radiation field similar to that within the *Belle* SVD can lead to an error in the determination of the integral ionising dose. The error is due to the bulk damage in the silicon caused by the deposition of non-ionising energy. Although such a system is suitable for the monitoring of uncontrollable beam losses [339] where a fast beam dump is required. The monitoring system with a photodetector sensor requires power for the readout preamplifier that demands additional cables and could not be used in the limited space close to the SVD readout electronics.

An alternative damage monitoring system should satisfy the following criteria;

- a capacity to measure both ionising and non ionising damage separately,
- Sensors should be capable of independently measuring damage in terms of ionizing dose in SiO_2 and non-ionizing dose in terms of a 1 MeV(Si) equivalent neutron fluence,
- the sensors should have a wide range of response due to uncertainties in the radiation field,
- sensor response should be well calibrated within the expected dose range,
- sensors should be small in size and preferably passive.

In this study such a system was designed based on MOSFET sensors for measuring the ionising energy losses in SiO_2 and PIN Dosimetric Diodes for monitoring the non-ionising energy losses in the silicon. The MOSFET sensor is based on the SiO_2-Si interface while the PIN Dosimeter Diode is based on high purity silicon. This is ideal because the mechanisms of response are identical to the mechanisms of damage within the CMOS gate oxide of electronics and silicon bulk of the detectors.

It was demonstrated that in the case of predicting the degradation of silicon detectors in a 20 MeV electron field it is possible to standardise the damage in terms of the equivalent 1 MeV (*Si*) neutron fluence, $\Phi_{eq,1MeV,Si}$. This improves the PIN Dosimeter Diodes universality beyond standardisation of neutron fields containing different neutron energy spectra.

The advantages of these sensors include passive operation, small size and the suitability for incorporation into a hybrid electronic system. The wide dose range in ionizing dose measurements is achieved by the simultaneous readout of MOSFETs with different oxide thickness as in the REM RADFETs. The PIN Dosimetric Diodes are manufactured on the base of high resistivity silicon [299] and have a large dynamic range enabling the measurement without annealing of the equivalent 1 MeV (Si) neutron fluence up to 7×10^{12} cm^{-2}. These advantages allow the consideration of this radiation damage monitoring system based on MOSFETs and PIN Dosimetric Diodes as a possible standard for the characterisation of any mixed radiation field.

Chapter 7

Summary

This thesis was concerned with the issue of radiation hardness of silicon and silicon based devices for applications in harsh radiation environments. The main contributions were in two areas. The first was the study of deep level defects in highly neutron irradiated silicon detectors and the observation of deep level defect evolution as a function of room temperature annealing. The second was the development of a radiation damage monitoring system for electronic devices in mixed radiation fields.

In Chapter 1 a basic overview was given of experimental high energy physics and silicon based microstrip detectors for charged particle detection.

In Chapter 2 an extensive review was given of radiation effects in silicon with particular emphasis on the radiation hardness of microstrip detectors.

In Chapter 3 an experimental study was undertaken into neutron damaged silicon detector test structures. While the initial aim of this phase of work was to develop good experimental techniques for use in the studies to follow, two useful results in the area of device characterisation were also obtained. Both related to the accurate measurement of N_{eff} in a square junction device with a planar structure. In the first it was found that the presence of a bond pad introduced an additional capacitance component. This was found to be associated with a MOS capacitor which was formed between the bondpad, SiO_2 interface and semiconductor bulk. Under reverse biasing of the detector junction an inversion layer was formed at the interface of the semiconductor region and the SiO_2 causing a significant change to the detector capacitance as a function of voltage. The second related to the lateral expansion of the depletion region peripherally to the junction area. The Copeland correction for this effect was found to be inadequate on account of the fact that it was derived for a circular junction area. A new factor

was determined to account for this affect on a square geometry like that of the detectors under study.

In Chapter 3 the technique of Optical Deep Level Transient Conductance, Spectroscopy (ODLTCS) was found to be a suitable means of detecting and measuring radiation induced deep level defects in high purity silicon which had undergone type inversion at a neutron fluence of 10^{13} cm^{-2}. This was important as the conventional characterisation tool based on capacitance transients is not able to characterise defects in silicon irradiated by 1 MeV neutrons to a fluence in excess of only 10^{11} cm^{-2}.

In Chapter 4 the ODLTCS technique was used to observe the evolution of the deep level defect spectrum in neutron irradiated silicon detectors as a function of room temperature annealing. The detectors had been irradiated by 1 MeV neutrons to a fluence of ~ 7.5×10^{13} cm^{-2}. This was a sufficient fluence to cause type inversion of the *n*-type bulk. The individual defect signatures were identified through mathematical deconvolution of the spectra and comparison of the defect parameters with the literature. The detectors had been manufactured from silicon containing different impurities concentrations. Oxygenated silicon, nitrogenised silicon and silicon containing the standard residual impurities were studied.

Comparison of the spectral evolution with room temperature annealing of N_{eff} was made. A strong correlation between the growth of the C_i-O_i defect was found with the short term annealing stage of N_{eff}. Based on this finding it was suggested that the promoted growth of this defect could enhance the short term annealing of N_{eff} leading to improved radiation hardness of the silicon. This could be achieved by increasing the oxygen content in the starting silicon and carefully optimising the carbon content. This mechanism was supported by recently reported work which found that for charged hadron irradiation the damage to N_{eff} was three times less in oxygenated silicon and worse in silicon with a high carbon content [260].

No strong correlations were observed between the evolution of any deep level defects and the long term reverse annealing stage of N_{eff}. This suggested that the responsible defect had an energy state of less than 0.16 eV as measured from the conduction or valence band edge. This

supported the hypothesis that the defect was the shallow level boron impurity. Small correlations were found with another defect identified as either the P_s-C_i or V_2O defect.

Study of the nitrogenised detector showed that the presence of nitrogen in silicon inhibits the production of the V-O defect. The mechanism proposed to explain this effect is associated with the trapping of mobile vacancies within the potential well surrounding the di-nitrogen complex.

Metastability was observed in the A-centre. This defect is known to consist of a combination of the V-O defect and the C_s-C_i defect. Metastability of the C_s-C_i defect has been reported at temperatures below 50 K. The prevalence of the ODLTCS measured metastability in the oxygenated detector, and the fact it occurred at a temperature of ~ 100 K suggests that some form of metastability is associated with the V-O defect. This defect is not thought to play a dominant role in either the radiation induced reverse current of change in N_{eff} with irradiation or the subsequent room temperature annealing.

The final two chapters, Chapter 5 and 6, were dedicated to the development of a Radiation Damage Monitoring System for electronic devices in mixed radiation fields. For such a system two sensors were required. The first would be capable of responding to dose associated with IEL in SiO_2, and the second to dose associated with NIEL in silicon.

In the first stage of this development (Chapter 5), it was shown that a PIN Dosimeter diode which was calibrated in an epithermal neutron beam in terms of $\Phi_{eq,1MeV,Si}$ can be used to measure $\Phi_{eq,1MeV,Si}$ in a fast neutron field. The use of the PIN Dosimeter Diode for measuring $\Phi_{eq,1MeV,Si}$ in neutrons fields with different neutron spectra was then extended to high energy electron fields. Based on these findings it is reasoned that a PIN Dosimeter Diode could provide a universal means of measuring dose associated with NIEL in silicon when exposed to any mixed radiation field in terms of $\Phi_{eq,1MeV,Si}$.

For the IEL sensor two alternatives were tested. The first was a photodetector sensor based on silicon. It was shown that use of this sensor type in a mixed radiation field containing high energy electrons (20 MeV) would lead to an increasing underestimate of the level of IEL dose.

This is a result of the effect of damage associated with the deposition of NIE within the photodetector silicon substrate and its effect on the minority carrier lifetime. The performance of the device in a GeV electron field such as *Belle* at the KEK *B*-Factory could be expected to be even worse. The second IEL dose sensor was a MOSFET based on the SiO_2-Si interface. This device was found to be radiation hard to the effects of NIEL and suitable for a wide range of IEL dose measurement in a mixed radiation field.

Based on the MOSFET and PIN Dosimeter Diode a RDMS was developed for use in the on-line monitoring of damage within a mixed radiation field. The system was installed within the *Belle* SVD at the KEK *B*-factory as well as within the lepton collider at SLAC in the US.

REFERENCES

[1] "ATLAS Technical Design Report," CERN/LHCC/97-16&17, ISBN 92-9083-102-2 and 92-9083-103-0 (1997).

[2] G. Gorfine, "Studies of Radiation Levels in the Large Hadron Collider and of Radiation Damage to Silicon Detectors," Ph.D. Thesis, Centre for High Energy Physics, University of Melbourne (1994).

[3] F. Lemeilleur, M. Glaser, et al., "Electrical properties and charge collection efficiency for neutron irradiated p-type and n-type silicon detectors," *CERN ECP* 92-72 (1992).

[4] T. Ohsugi, T. Kondo, et al., "Radiation damage in silicon microstrip detectors," *Nucl. Instru. & Meth. in Phys. Res. Section A*, Vol. 265, pp. 105-111 (1988).

[5] P.A. Aarnio, M. Huhtinen, M. Pimia, K. Kaita, M. Laakso, A. Numminen and P. Ryytty, "Damage observed in silicon diodes after low energy pion irradiation," *Nucl. Instru. & Meth. in Phys. Res. Section A*, Vol. 360, pp. 521-531 (1995).

[6] E. Sondar and L.C. Templeton, "Gamma irradiation of silicon II levels in p-type float-zone material," *J. Appl. Phys.*, Vol. 34, No. 11, p. 3295 (1963).

[7] G.D. Watkins and J.W. Corbett, "Defects in irradiated silicon: Electron paramagnetic resonance and electron-nuclear double resonance of the Si-E centre," *Phys. Rev.*, Vol. 134, No. 5A, p. 1359 (1964).

[8] I.D. Konozenko, A.K. Semenyuk, V.I. Khivrich, "Radiation defects created by Co60 γ-rays in p- and n-type Si of high purity," *Phys. Stat. Sol.*, Vol. 35, p. 1043 (1969).

[9] T. Abe, K. Kikuchi, S. Shirai and S. Muraka, "Semiconductor silicon", Edited by H.R. Huff and Y. Takeishi (1981).

[10] K. Sumino, I. Yonenaga, M. Imai and T. Abe, *J. Appl. Phys.*, Vol. 54, p. 5016 (1983)

[11] T. Abe, H. Harada and J. Chikawa., "Defects in semiconductors II", Edited. by S. Mahajan et al., p. 1 (1983).

[12] J.A. Lauber, S. Gascon-Schotkin, R.G. Kellogg and G.R. Martinez, "Energy dependence of damage to Si PIN diodes exposed to β radiation," *Nucl. Inst. and Meth. in Phys. Res. Section A*, Vol. 396, pp. 165-171 (1997).

[13] "The KEK Accelerator Technical Design Report," *KEK-Report* 94-2, June (1995).

[14] A. Bondar, "The BELLE Detector," *Nucl. Instr. & Meth. A*, Vol. 408, p. 64-76 (1998).

[15] G. Bertolini. and A. Coche, "Semiconductor Detectors," North-Holland publishing company, Amsterdam (1968).

[16] G. Dearnaley and D.C. Northrop, "Semiconductor Counters for Nuclear Radiations," 2nd edition, E. & F.N. Spon limited London (1966).

[17] G.F. Knoll, "Radiation Detection and Measurement," 2nd edition, New York : Wiley (1989).

[18] J. Kemmer, "Fabrication of low noise silicon radiation detectors by the planar process," *Nucl. Instr. & Meth. in Nucl. Res. Section A*, Vol. 169, pp. 499-502 (1980).

[19] J. Kemmer, "Improvement of detector fabrication by the planar process," *Nucl. Instr. & Meth. in Nucl. Res. Section A*, Vol. 226, pp. 89-93 (1984).

[20] S.M. Sze, "Semiconductor Devices : Physics and Technology," published by John Wiley & Sons, ISBN 0-471-87424-8 (1985).

[21] C. Kittel, "Introduction to Solid State Physics," 6th edition, published by John Wiley & Sons (1986).

[22] EMIS DataReview Series No. 4, "Properties of Silicon", published by The Institution of Electrical Engineers (INSPEC) (1988).

[23] J.J. Wortman, and R.A. Evans, "Young's Modulus, Shear Modulus, and Poisson's ratio in Silicon and Germanium," *J. Appl. Phys.*, Vol. 36, pp. 153-156 (1965).

[24] C. Herring, "Fundamental Formulas of Physics, Elastic Constants," edited by D.H. Menzel, New York (1960).

[25] R.G. Rhodes, "Imperfections and Active Centres in Semiconductors," Pergamon Press, Oxford, U.K. (1964).

[26] J.S. Blakemore, "Solid State Physics," Cambridge: Cambridge University Press (1985).

[27] C. Jacoboni and L. Reggiani, *Adv. Phys*. (GB), Vol. 28, No. 4 (1979).

[28] G. Restelli and A. Rota, "Semiconductor Detectors," edited by Bertolini and Coche, published by North-Holland, Chapter 1.4, p. 75 (1968).

[29] S.M. Sze and J.C. Irvin, "Resistivity, Mobility and Impurity Levels in GaAs, Ge and Si at 300° K," *Solid State Electron*, Vol. 11, p. 599 (1968).

[30] M.I. Reinhard, "Neutron Transmutation Doped Silicon for Radiation Detector Applications," Honours thesis, University of Wollongong (1994).

[31] D. Alexiev, K.S.A Butcher and T.L. Tansley, "NTD Silicon for the Production of Radiation Detectors, " *Nucl. Instrum. & Meth. in Phys. Res. Part B*, Vol. 69, pp. 510-516 (1992).

[32] W. Von. Ammon and H. Herzer, "The production and availability of high resistivity Si for detector applications," *Nucl. Instr. & Meth. in Nucl. Res. Section A*, Vol. 226, p. 94 (1984).

[33] P. Dreier, "High resistivity silicon for detector applications," *Nucl. Instr. & Meth. in Nucl. Res. Section A*, Vol. 288, pp. 272-277 (1990).

[34] EMIS DataReview Series No. 4, RN = 15704, "Properties of Silicon," published by The Institution of Electrical Engineers (INSPEC) (1988).

[35] EMIS DataReview Series No. 4, RN = 17819, "Properties of Silicon," published by The Institution of Electrical Engineers (INSPEC) (1988).

[36] E. Belau, R. Klanner, G. Lutz, et al., "Charge Collection in Silicon Strip Detectors," *Nucl. Instr. & Meth. in Nucl. Res. Section A*, Vol. 214, pp. 253-260 (1983).

[37] U. Kotz, K.U. Posnecker, E. Gatti, et al., "Silicon Strip Detectors with Capacitive Charge Division," *Nucl. Instr. & Meth. in Nucl. Res. Section A*, Vol. 235, pp. 481-487 (1980).

[38] R. Sonnenblick, N. Cartiglia, B. Hubbard, et al., "Electrostatic simulations for the design of silicon strip detectors and front-end electronics," *Nucl. Instr. & Meth. in Nucl. Res. Section A*, Vol. 310, pp. 189-191 (1991).

[40] G. Batignani, et al., *Nucl. Instr. & Meth. in Nucl. Res. Section A*, Vol. 310, p. 165 (1991).

[41] G. Batignani, et al., *Nucl. Instr. & Meth. in Nucl. Res. Section A*, Vol. 326, p. 183 (1993).

[42] R. Brenner, H. Harr, A. Rudge, et al., *Nucl. Instr. & Meth. in Nucl. Res. Section A*, Vol. 326, pp. 189-197 (1993).

[43] J. Kemmer, and G. Lutz, *Nucl. Instr. & Meth. in Nucl. Res. Section A*, Vol. 260, p. 124 (1987).

[44] A. Bischoff, N. Findeis, D. Hauff, et al., *Nucl. Instr. & Meth. in Nucl. Res. Section A*, Vol. 326, pp. 27-37 (1993).

[45] R.E. Davis, W.E. Johnson, et al., "Neutron-Bombarded Geranium Semiconductors," *Phys. Rev.*, Vol. 74, p. 1255 (1948).

[46] H.M. James & K. Lark-Horowitz, *Z. Phsick. Chem.* (Leipzig), Vol. 198, p. 107 (1951).

[47] K. Lark-Horowitz, E. Bleuler et al., "Deuteron-Bombarded Semiconductors," *Phys. Rev.*, Vol. 73, p. 1256 (1948).

[48] W.E. Johnson and K. Lark-Horowitz, "Neutron Irradiated Semiconductors," *Phys. Rev.*, Vol. 76, p. 442 (1949).

[49] J.H. Crawford and K. Lark-Horowitz, "Fast neutron bombardment effects in germanium," *Phys. Rev. Lett.*, p. 815 (1950).

[50] W.H. Brattain and G.L. Pearson, "Changes in conductivity of germanium induced by alpha-particle bombardment," *Phys. Rev*., Vol. 80, No. 5, p. 846 (1950).

[51] J.W. Cleland, J.H. Crawford et al., "The effects of fast neutron bombardment on the electrical properties of germanium," *Phys. Rev*., Vol. 83, No. 2, p. 312 (1951).

[52] P. Rapport, *Phys. Rev*., Vol. 94, p. 1409A (1954).

[53] J.J. Loferski and P. Rappaport, "Electron Voltaic Study of Electron Bombardment Damage and its Thresholds in Ge and Si," *Phys. Rev. Lett.*, p. 1861 (1955).

[54] F. Seitz, *Discussions Faraday Soc*., Vol. 5, p. 271 (1949).

[55] M. Becker, H.Y. Fan et al., "Infrared absorption of Nucleon-Bombarded Silicon I," *Phys. Rev*., Vol. 55, p. 730 (1952).

[56] H.Y. Fan, A.K. Ramadas, "Infrared absorption in neutron irradiated silicon," *J. Phys. Chem. Solids*, Vol. 8, pp. 272-274 (1959).

[57] H.Y. Fan & A.K. Ramadas, "Infrared absorption and photoconductivity in irradiated silicon," *J. Appl. Phys*., Vol. 30, No. 8, p. 1127 (1959).

[58] D.E. Hill, "Electron bombardment of silicon," *Phys. Rev*., Vol. 114, No. 6, pp. 1414-1420 (1959).

[59] G. Rupprecht and C.A. Klein, "Energy levels in neutron-irradiated n-type silicon," *Phys. Rev*., Vol. 116, No. 2, pp. 342-343 (1959).

[60] J.H. Crawford, Jr., J.W. Cleland, "Nature of bombardment damage and energy levels in semiconductors," *J. Appl. Phys*., Vol. 30, No. 8, p. 1204 (1959).

[61] G.K. Wertheim, "Recombination properties of bombardment defects in semiconductors," *J. Appl. Phys*., Vol. 30, No. 8, pp. 1166-1174 (1959).

[62] R.W. Beck, E. Paskell and C.S. Peet, "Some effects of fast neutron irradiation on carrier lifetimes in silicon," *J. Appl. Phys*., Vol. 30, No. 9, pp. 1437-1439 (1959).

[63] E. Schulz-DuBois, M. Nisenoff et al., *Phys. Rev*., Vol. 121, p. 1561 (1961).

[64] W. Kaiser, P.H. Keck and C.F. Lange, "Infrared Absorption and Oxygen Content in Silicon and Germanium," *Phys. Rev*., Vol. 101, No. 4, p. 1264 (1956).

[65] G.D. Watkins, J.W. Corbett, et al., "Spin resonance in electron irradiated silicon," *J. Appl. Phys*., Vol. 30, No. 8, p. 1198 (1959).

[66] G. Bemski and W.M. Augustyniak, "Annealing of Electron Bombardment Damage in Silicon Crystals," *Phys. Rev*., Vol. 108, No. 3, p. 645 (1957).

[67] G.K. Wertheim and D.N.E. Buchanan, "Electron Bombardment Damage in Oxygen Free Silicon," *J. Appl. Phys*., Vol. 30, No. 8, p. 1232 (1959).

[68] G.K. Wertheim, "Neutron-Bombardment Damage in Silicon," *Phys. Rev*., Vol. 111, No. 6, p. 1500 (1958).

[69] R.A. Dugdale, "Report of the Conf. on defects in crystalline solids," *Phys. Soc.* London, p. 246 (1955).

[70] V. Vard, *Proc. Phys. Soc.* (London) Vol. 55, p. 222 (1943).

[71] R. Truell, "Nature of defects arising from fast neutron irradiation of silicon single crystals," *Phys. Rev*., Vol. 116, No. 4, pp. 890-892 (1959).

[72] B.R. Gossick, "Disordered regions in semiconductors bombarded by fast neutrons," *J. Appl. Phys*., Vol. 30, No. 8, p. 1214 (1959).

[73] J.W. Corbett and G.D. Watkins, "Silicon divacancy and its direct production by electron irradiation," *Phys. Rev. Lett*., Vol. 7, No. 8, pp. 314-316 (1961).

[74] L.J. Cheng, J.C. Corelli, et al., "1.8-, 3.3- 3.9- bands in irradiated Si: Correlations with the divacancy," *Phys. Rev*., Vol. 152, No. 2, p. 761 (1966).

[75] I.D. Konozenko, A.K. Semenyuk, V.I. Khivrich, "Radiation defects created by Co^{60} γ-rays in p- and n-type Si of high purity," *Phys. Stat. Sol*., Vol. 35, p. 1043 (1969).

[76] J.W. Corbett, G.D. Watkins et al., "Production of divacancies by electron irradiation of silicon," *Phys. Rev*., Vol. 138, No. 2A, p. 555 (1965).

[77] J.W. Corbett, G.D. Watkins et al., "Defects in irradiated silicon. 2. Infrared absorption of the Si-A centre," *Phys. Rev*., Vol. 121, No. 4, p. 1015 (1961).

[78] J.W. Corbett, R.S. McDonald and G.D. Watkins, "The configuration and diffusion of isolated oxygen in silicon and germanium," *J. Phys. Chem. Solids*, Vol. 25, pp. 873-879 (1964).

[79] J.C. Corelli, G. Oehler et al., "Annealing of infrared defect absorption bands in 40 MeV electron-irradiated silicon," *J. Appl. Phys*., Vol. 36, No. 5, p. 1787 (1965).

[80] A.K. Ramdas and M.G. Rao, "Infrared absorption spectra of oxygen-defect complexes in irradiated silicon," *Phys. Rev*., Vol. 142, No. 2, p. 451 (1966).

[81] L.J. Cheng and P. Vajda, "11.6 um oxygen-associated absorption bands in neutron irradiated silicon," *J. Appl. Phys.*, Vol. 40, p. 4679 (1969).

[82] G.D. Watkins and J.W. Corbett, "Defects in irradiated silicon. 1. Electron spin resonance of the Si-A center," *Phys. Rev*., Vol. 121, No. 4, p. 1001 (1961).

[83] E. Sondar and L.C. Templeton, "Gamma irradiation of silicon II levels in p-type float-zone material," *J. Appl. Phys*., Vol. 34, No. 11, p. 3295 (1963).

[84] G.D. Watkins and J.W. Corbett, "Defects in irradiated silicon: Electron paramagnetic resonance and electron-nuclear double resonance of the Si-E centre," *Phys. Rev*., Vol. 134, No. 5A, p. 1359 (1964).

[85] H.J. Stein, "Electrical studies of neutron irradiated p-type silicon: Defect structure and annealing," *J. Appl. Phys*., Vol. 39, No. 11, p. 5283 (1968).

[86] H.J. Stein, "Comparison of neutron and gamma irradiated n-type Si: Impurity and irradiation-temperature dependence," *Phys. Rev*., Vol. 163, No. 3, p. 790 (1967).

[87] H.J. Stein, "Electrical studies of neutron-irradiated n-type Si: Defect structure and annealing," *Phys. Rev*., Vol. 163, No. 3, p. 803 (1967).

[88] N.D. Wilsey, R.L. Statler & B.J. Faraday, "Defect clusters in electron irradiated silicon," *IEEE Trans. on Nucl. Sci.*, Vol. 16, p. 1238 (1969).

[89] G.C. Messenger, "Displacement damage in Si and Ge transistors," *IEEE Trans. on Nucl. Sci*., Vol. 12, p. 53 (1965).

[90] H.W. Kraner, "Radiation damage in silicon detectors," *Nucl. Instru. & Meth. in Phys. Res. Section A*, Vol. 225, pp. 615-618 (1984).

[91] P. Borgeand et al., "The effects of radiation on the energy resolution of ion-implanted silicon detectors," *Nucl. Instru. & Meth. in Phys. Res. Section A*., Vol. 211, pp. 363-367 (1983).

[92] E. Fretwurst, R. Grube, G. Lindstrom and J. Nagel, "Development of large area silicon detectors," *Nucl. Instru. & Meth. in Phys. Res. Section A*, Vol. 253, pp. 467-477 (1987).

[93] M. Nakamura, Y. Tomita, K. Niwa and T. Kondo, "Radiation damage test of silicon multistrip detectors," *Nucl. Instru. & Meth. in Phys. Res. Section A*, Vol. 270, pp. 42-55 (1988).

[94] M. Campanella, N. Croitoru, et al., "The effect of radiation on ion-implanted silicon detectors," *Nucl. Instru. & Meth. in Phys. Res. Section A*, Vol. 243, pp. 93-97 (1986).

[95] H. Dietl, T. Gooch, D. Kelsey, R. Klanner, A. Loffler, M. Pepe and F. Wickens, "Radiation damage in silicon strip detectors," *Nucl. Instru. & Meth. in Phys. Res. Section A*, Vol. 253, pp. 460-466 (1987).

[96] M. Hasegawa, T. Ohsugi, T. Kondo, et al., "Radiation damage of silicon junction detectors by neutron irradiation," *Nucl. Instru. & Meth. in Phys. Res. Section A*, Vol. 277, pp. 395-400 (1989).

[97] E. Beuville, W. Kraner, et al., "Measurements of degradation of silicon detectors and electronics in various radiation environments," *Nucl. Instru. & Meth. in Phys. Res. Section A*, Vol. 288, pp. 68-75 (1990).

[98] J. Hauffe, W. Eyrich, M. Kirsch, M. Moosburger and F. Stinzing, "Annealing of silicon strip detectors after irradiation," *Nucl. Instru. & Meth. in Phys. Res. Section A*, Vol. 366, pp. 79-84 (1995).

[99] H.J. Ziock, C.M. Hoffman, et al., "Measurement of proton induced radiation damage to CMOS transistors and PIN diodes," *IEEE Trans. on Nucl. Sci.*, Vol. 37, No. 3, p. 1238 (1990).

[100] M. Edwards, G. Hall and S. Sotthibandhu, "Neutron radiation damage studies of silicon detectors," *Nucl. Instru. & Meth. in Phys. Res. Section A*, Vol. 310, pp. 283-286 (1991).

[101] E. Fretwurst, G. Lindstrom, R. Wunstorf, "Silicon detector developments for calorimetry: Technology and radiation damage," *Nucl. Instru. & Meth. in Phys. Res. Section A*, Vol. 288, pp. 1-12 (1990).

[102] F. Lemeilleur, M. Glaser, P. Jarron, et al., "Neutron-induced radiation damage in silicon detectors," *IEEE Trans. on Nucl. Sci.*, Vol. 39, No. 4, p. 551 (1992).

[103] K. Gill, G. Hall, S. Roe, S. Scotthibandhu, R. Wheadon, P. Giubellino and L. Ramello, "Radiation damage by neutrons and photons to silicon detectors," *Nucl. Instru. & Meth. in Phys. Res. Section A*, Vol. 322, pp. 177-188 (1992).

[104] W. Shockley and W.T. Read, *Phys. Rev*. Vol. 87, p. 835 (1952).

[105] F. Lemeilleur, M. Glaser, et al., "Neutron, proton, and gamma irradiations of silicon detectors," *IEEE Trans on Nucl. Sci*., Vol. 41, No. 3, p. 425 (1994).

[106] P. Giubellino, G. Panizza, G. Hall, S. Sotthibandhu, H.J. Ziock, et al., "Study of the effects of neutron irradiation on silicon detectors," *Nucl. Instru. & Meth. in Phys. Res. Section A*, Vol. 315, pp. 156-160 (1992).

[107] Z. Li, W. Chen and H.W. Kraner, "Effects of fast neutron radiation on the electrical properties of silicon detectors," *Nucl. Instru. & Meth. in Phys. Res. Section A*, Vol. 308, pp. 585-595 (1991).

[108] S.J. Bates, B. Dezillie, C. Furetta, M. Glaser and F. Lemeilleur, "Proton Irradiation of Various Resistivity Silicon Detectors," *Proceedings of RADECS 95*, p. 487 (1996).

[109] R. Wunstorf, E. Fretwurst, G. Lindstrom, et al., "Results on radiation hardness of silicon detectors up to neutron fluences of 10^{15} n/cm^2," *Nucl. Instru. & Meth. in Phys. Res. Section A.* Vol. 315, pp. 149-155 (1992).

[110] Z. Li, H.W. Kraner, V. Eremin, et al. "Investigation of the oxygen vacancy (A-centre) defect complex profile in neutron irradiated high resistivity silicon junction particle detectors," *IEEE Trans. on Nucl. Sci.* Vol. 39, No. 6, p.1730 (1992).

[111] E. Barberis, D. Pitzl, H.J. Ziock, et al., "Temperature effects on radiation damage to silicon detectors," *Nucl. Instru. & Meth. in Phys. Res. Section A*, Vol. 326, pp. 373-380 (1993).

[112] F. Lemeilleur, S.J. Bates, A. Chilingarov, C. Furetta, M. Glaser, E.H.M. Heijne, P. Jarron, C. Leroy and I. Trigger, "Study of characteristics of silicon detectors irradiated with 24 GeV/c protons between -20°C and 20°C," *CERN-ECP*/94-8 (1994).

[113] E. Borchi, R. Macii, C. Leroy, C. Manoukian-Bertrand, C. Furetta, et al., "Leakage current, annealing, and deep defect production studies in neutron irradiated n-type silicon-detectors," *Nucl. Instru. & Meth. in Phys. Res. Section A*., Vol. 301, pp. 215-218 (1991).

[114] A. Baldini, E. Borchi, M. Bruzzi and P. Spillantini, "Electrical and spectroscopic analysis of neutron irradiated silicon detectors," *Nucl. Instru. & Meth. in Phys. Res. Section A*, Vol. 315, pp.182-187 (1992).

[115] F. Lemeilleur, M. Glaser, et al., "Electrical properties and charge collection efficiency for neutron irradiated p-type and n-type silicon detectors," *CERN ECP* 92-72 (1992).

[116] C. Leroy, M. Glaser, P. Jarron, F. Lemeilleur, et al., "Study of electrical properties and charge collection of silicon detectors under neutron, proton and gamma irradiations," *CERN ECP* 93-12 (1993).

[117] E. Fretwurst, G. Lindstrom, R. Wunstorf, et al, "Radiation hardness of silicon detectors for future colliders," *Nucl. Instru. & Meth. in Phys. Res. Section A*, Vol. 326, pp. 357-364 (1993).

[118] M. Bruzzi, A. Baldini, E. Borichi, and I. Lukianov, "Defect complexes in neutron irradiated silicon detectors evaluation and effects," *Nucl. Instru. & Meth. in Phys. Res. Section A*, Vol. 326, pp. 344-349 (1993).

[119] R. Bardos, E. Fretwurst, M. Glaser, G. Gorfine, G. Moorhead, G. Taylor, et al., "Neutron irradiation of silicon diodes at temperatures of 20°C and -20°C," *Nucl. Instru. & Meth. in Phys. Res. Section A*, Vol. 326, pp. 365-372 (1993).

[120] A. Holmes-Siedle, M. Robbins, et al., "Radiation tolerance of single sided silicon microstrips," *Nucl. Instru. & Meth. in Phys. Res. Section A*, Vol. 339, pp. 511-523 (1994).

[121] T. Angelescu et al., "Radiation hardness studies on silicon detectors in fast neutron fields," *Nucl. Instru. & Meth. in Phys. Res. Section A*, Vol. 357, pp. 55-63 (1995).

[122] M. Bosetti, C. Furetta, C. Leroy, S. Pensotti, P.G. Rancoita, M. Rattaggi, M. Redaelli, A. Seidman and G. Terzi, "Systematic study of neutron irradiation effects on the

performance of FZ and MCZ silicon detectors," *Nucl. Instru. & Meth. in Phys. Res. Section A*, Vol. 345, pp. 250-255 (1994).

[123] V. Eremin, A. Ivanov, E. Verbitskaya, Z. Li and H.W. Kraner, "Elevated temperature annealing of the neutron induced reverse current and corresponding defect levels in low and high resistivity silicon detectors," *IEEE Trans on Nucl. Sci.*, Vol. 42, No. 4, p. 387 (1995).

[124] C. Li and Z. Li, "Characterisation of high fluence neutron induced defect levels in high resistivity silicon detectors using a laser deep level transient spectroscopy (L-DLTS)," *Nucl. Instru. & Meth. in Phys. Res. Section A*, Vol. 342, p. 137 (1994).

[125] RD2 Collaboration, "Some recent results of the silicon detector radiation damage study by the RD2 collaboration," *Nucl. Instru. & Meth. in Phys. Res. Section A*, Vol. 360, pp. 41-49 (1995).

[126] D. Dorfan, *Nucl. Instru. & Meth. in Phys. Res. Section A*, Vol. 342, p. 143 (1994).

[127] S.J. Bates, B. Dezillie, C. Furetta, M. Glaser, F. Lemeilleur and E. Leon-Florian, "Proton irradiation of silicon detectors with different resistivities," *CERN-ECP*/95-18 (1995).

[128] S.J. Bates, D.J. Munday, et al. (RD2), "Recent results of radiation damage studies," *Nucl. Instru. & Meth. in Phys. Res. Section A*, Vol. 344, pp. 228-236 (1994).

[129] S. Bates, D.J. Munday, et al., "Study of neutron irradiated silicon counters with a fast amplifier," *Nucl. Instru. & Meth. in Phys. Res. Section A*, Vol. 337, pp. 57-65 (1993).

[130] H.J. Ziock, et al., "Temperature dependence of radiation damage and its annealing in silicon detectors," *IEEE Trans on Nucl. Sci.*, Vol. 40, No. 4, p. 344 (1993).

[131] M. Bosetti, C. Furetta, C. Leroy, S. Pensotti, P.G. Rancoita, M. Rattaggi, M. Redaelli, M. Rizzatti, A. Seidman and G. Terzi, "Effect on charge collection and structure of n-type silicon detectors irradiated with large fluences of fast neutrons," *Nucl. Instru. & Meth. in Phys. Res. Section A*, Vol. 343, pp. 435-440 (1994).

[132] Z. Li, "Investigation on the long-term radiation hardness of low and medium resistivity starting materials for RT silicon detectors in high energy physics," *Nucl. Instru. & Meth. in Phys. Res. Section A*, Vol. 360, p. 445 (1995).

[133] F. Lemeilleur, M. Glaser, C. Leroy, et al., "Charge transport in silicon detectors," *CERN/ECP* 93-21 (1993).

[134] Z. Li, V. Eremin, et al., "Investigation of the type inversion phenomena: Resistivity and carrier mobility in the space charge region and electrical neutral bulk in neutron

irradiated silicon p^+-n junction detectors," *IEEE Trans on Nucl. Sci.*, Vol. 40, No. 4, p. 367 (1993).

[135] F. Lemeilleur et al., "Neutron-induced radiation damage in silicon detectors," *CERN/ECP* 91-21 (1993).

[134] V. Eremin and Z. Li., "Carrier drift mobility study in neutron irradiated high purity silicon," *Nucl. Instru. & Meth. in Phys. Res. Section A*, Vol. 362, pp. 383-343 (1995).

[135] M. Edwards, G. Hall and S. Sotthibandhu, "Neutron radiation damage studies of silicon detectors," *Nucl. Instru. & Meth. in Phys. Res. Section A*, Vol. 310, pp. 283-286 (1991).

[136] E. Fretwurst, G. Linstom, R. Wunstorf, et al., "Radiation hardness of silicon detectors for future colliders," *Nucl. Instru. & Meth. in Phys. Res. Section A*, Vol. 326, pp. 357-364 (1993).

[137] M. Kurokawa, T. Motobayashi, et al., "Radiation damage factor for ion implanted silicon detectors irradiated with heavy ions," *IEEE Trans on Nucl Sci.*, Vol. 42, No. 3, p. 4 (1995).

[138] G. Hall, "Radiation damage to silicon detectors," *Nucl. Instru. & Meth. in Phys. Res. Section A*, Vol. 368, pp. 199-204 (1995).

[139] H.J. Ziock, et al., "Temperature dependance of the radiation induced change of depletion voltage in silicon PIN detectors," *Nucl. Instru. & Meth. in Phys. Res. Section A*, Vol. 342, pp. 96-104 (1994).

[140] Z. Li, H.W. Kraner, "Fast neutron radiation effects in silicon detectors fabricated by different thermal oxidation processes," *IEEE Trans on Nucl. Sci.*, Vol. 39, No. 4, p. 577 (1992).

[141] G.N. Taylor, et al., *Nucl. Instru. & Meth. in Phys. Res. Section A*, Vol. 383, pp. 144-154 (1996).

[142] Z. Li, "Modeling and simulation of neutron induced changes and temperature annealing of N_{eff} and changes in resistivity an high resistivity silicon detectors," *Nucl. Instru. & Meth. in Phys. Res. Section A*, Vol. 342, p. 105 (1994).

[143] G. Hall, "Detector radiation damage studies for a silicon microstrip tracker at LHC," *IEEE Trans on Nucl. Sci.*, Vol. 41, No. 4, p. 767 (1994).

[144] A. Holmes-Siedle, M. Robbins, et al., "Radiation tolerance of single sided silicon microstrips," *Nucl. Instru. & Meth. in Phys. Res. Section A*, Vol. 339, pp. 511-523 (1994).

[146] Z. Li, L. Dou, V. Eremin, H.W. Kraner, et al., "Study of the long term stability of the effective concentration of ionized space charge (Neff) of neutron irradiated silicon

detectors fabricated by various thermal oxidation processes," *IEEE Trans. on Nucl. Sci.*, Vol. 42, No. 4, p. 219 (1995).

[147] W. Dabrowski, "Radiation damage in Si detectors and front-end electronics," *Nucl. Phys. B (Proc. Suppl.*), Vol. 44, pp. 463-467 (1995).

[148] R. Wheadon, RD20, "Radiation damage studies on single-sided and double-sided silicon microstrip detectors," *Nucl. Instru. & Meth. in Phys. Res. Section A*, Vol. 348, pp. 449-453 (1994).

[149] S.U. Pandey, et al., "Studies of ionizing radiation effects on silicon drift detectors," *Nucl. Instru. & Meth. in Phys. Res. Section A*, Vol. 361, p. 457 (1995).

[150] K. Gill, "Radiation damage studies of n-side silicon microstrip detectors," *Nucl. Phys. B (Proc Suppl.)*, Vol. 44, pp. 475-479 (1995).

[151] G. Gorfine, "Studies of radiation levels in the large hadron collider and of radiation damage to silicon detectors," *Ph.D. Thesis, School of Physics, University of Melbourne,* Australia (1994).

[152] P. Aarnio and M. Huhtinen, "Hadron fluxes in inner parts of LHC detectors," *Nucl. Instru. & Meth. in Phys. Res. Section A*, Vol. 336, p. 98 (1993).

[153] J.G. Kelly and P.J. Griffin, "Comparison of Measured Silicon Displacement Damage Ratios with ASTM E-722 and NJOY Calculated Damage," *Proc. 7th ASTM-Euratom Symp. Reactor Damage*, p. 711, G. Tsotridis, R. Dierckx, P.D'Hondt, Eds., Kluwer Academic Publishers, Dordrecht, The Netherlands (1992).

[154] M. Huhtinen and P. Aarnio, "Pion induced displacement damage in silicon devices," *Nucl. Instru. & Meth. in Phys. Res. Section A*, Vol. 335, p. 580 (1993).

[155] I. Lazanu, S. Lazanu, U. Biggeri, E. Borichi and M. Bruzzi, "Non-ionising energy loss of pions in thin silicon samples," *Nucl. Instru. & Meth. in Phys. Res. Section A*, Vol. 388, pp. 370-374 (1997).

[156] C. Furetta et al., *Nucl. Phys. B*, (Proc. Suppl.), Vol. 44, p. 503 (1995).

[157] K. Riechmann, K.T. Knopfle and V.M. Pugatch, "Pion and proton induced radiation damage to silicon detectors," *Nucl. Instru. & Meth. in Phys. Res. Section A*, Vol. 377, pp. 276-283 (1996).

[158] J.A.J. Mathews, P. Berdusis, et al., "Bulk radiation damage in silicon detectors and implications for LHC experiments," *Nucl. Instru. & Meth. in Phys. Res. Section A*, Vol. 381, pp. 338-348 (1996).

[159] P.A. Aarnio, M. Huhtinen, M. Pimia, K. Kaita, M. Laakso, A. Numminen and P. Ryytty, "Damage observed in silicon diodes after low energy pion irradiation," *Nucl. Instru. & Meth. in Phys. Res. Section A*, Vol. 360, pp. 521-531 (1995).

[160] S.J. Bates, C. Furetta, M. Glaser, F. Lemeilleur, C. Soave and E. Leon-Florian, "Damage induced by pions in silicon detectors," *CERN-ECP*/95-03 (1995).

[161] S.J. Bates, C. Furetta, M. Glaser, F. Lemeilleur, et al., "Pion induced damage in silicon detector," *Nucl. Instru. & Meth. in Phys. Res. Section A*, Vol. 379, pp. 116-123 (1996).

[162] G.N. Taylor, "Radiation damage in silicon detectors," *Proceedings of the 4^{h} Australian experimental high energy physics meeting and workshop*, ANSTO, 11th-12th Dec. (1995).

[163] N. Bacchetta, D. Bisello, A. Candelori, A. Giraldo, M. Loreti, D. Pantano and A. Pellizzari, "Radiation induced bulk damage in silicon diodes with pions and protons," *Nucl. Instru. & Meth. in Phys. Res. Section A*, Vol. 388, pp. 318-322 (1997).

[164] H. Feick, E. Fretwurst, G. Lindstrom and M. Moll, "Long term damage studies using silicon detectors fabricated from different starting materials and irradiated with neutrons, protons, and pions," *Nucl. Instru. & Meth. in Phys. Res. Section A*, Vol. 377, pp. 217-223 (1996).

[165] U. Biggeri, E. Borichi, M. Bruzzi, E. Catacchini, S. Lazanu and G. Parrini, "Evaluation of charged pions induced damage in the CMS silicon forward tracker," *Nucl. Instru. & Meth. in Phys. Res. Section A*, Vol. 388, pp. 345-349 (1997).

[166] G.D. Watkins, "Radiation Damage in Semiconductors" Dunod: Paris, p. 97 (1965).

[167] R. Wunstorf, "Systematische untersuchungen zur strahlenresistenz von silizium-detektoren für die verwendung in hochenergiephysik-experimenten," *Ph. D Thesis Interner Bericht, DESY FH1K*-92-01 (1992).

[168] C. Li and Z. Li, "Characterisation of high fluence neutron induced defect levels in high resistivity silicon detectors using a laser deep level transient spectroscopy (L-DLTS)," *Nucl. Instru. & Meth. in Phys. Res. Section A*, Vol. 342, p. 137 (1994).

[169] M. Bosetti, C. Leroy, "DLTS measurements of energetic levels, generated in silicon detectors," *Nucl. Instru. & Meth. in Phys. Res. Section A*, Vol. 361, pp. 461-465 (1991).

[170] I.I. Kolkovskii and V.V. Luk'yanitsa. "Characteristic features of the accumulation of vacancy- and interstitial-type radiation defects in dislocation-free silicon with different oxygen contents," S.C.'s, Vol. 31, No. 4, p. 340 (1997).

[171] E. Borchi, M. Bruzzi and M.S. Mazzoni, "Thermally stimulated nand leakage current analysis of neutron irradiated silicon detectors," *Nucl. Instru. & Meth. in Phys. Res. Section A*, Vol. 310, pp. 273-276 (1991).

[172] L.W. Song & G.D. Watkins, "EPR identification of the single acceptor state of interstitial carbon in silicon," *Phys. Rev*., Vol. B42, No. 9, p. 5759 (1990).

[173] G.D. Watkins and K.L. Brower, "EPR-observation of the isolated interstitial carbon atom in silicon," *Phys. Rev. Lett.*, Vol. 36, p. 1329 (1990).

[174] L.C. Kimberling, P. Blood and W.M. Gibson, "Defects and Radiation Effects in Semiconductors," *IOP Conference proceedings*, No. 46, p. 273 (1979).

[175] M.T. Asom et al., "Interstitial defect reactions in silicon," *Appl. Phys. Lett.*, Vol. 51, No. 4, p. 256 (1987).

[176] A. Chantre and L.C. Kimberling, "Configurational multistable defect in silicon," *Appl. Phys. Lett.*, Vol. 48 (1986).

[177] G.E. Gellison, "Transient capacitance studies of an electron trap E_c–E_t = 0.105 eV in phosphorus doped silicon," *J. Appl. Phys*., Vol. 53, No. 8, p. 5715 (1982).

[178] P.V. Kuchinskii, V.M. Lomako and L.N. Shakhlevich, "Configurationally bistable defects in silicon," *J. ETP Lett*., Vol. 43, No. 9, p. 544 (1986).

[179] L.W. Song, B.W. Benson and G.D. Watkins, "Identification of a bistable defect in silicon: The carbon interstitial-carbon substitutional pair," *Appl. Phys. Lett.*, Vol. 51, No. 15, p. 1155 (1987).

[180] SPO Detector Pty. Ltd., Ukraine.

[181] P. Blood and J.W. Orton, "The electrical characterization of semiconductors: majority carriers and electron states," *Academic Press*, ISBN 0-12-528627-9 (1992).

[182] A.M. Goodman, "Metal-semiconductor barrier height measurement by the differential capacitance method – one carrier system," *J. of Appl. Phys*., Vol. 34, No. 2, p. 329 (1963).

[183] J.A. Copeland, "Diode edge effect on doping-profile measurement," *IEEE Trans. on Electron Devices*, Vol. ED-17, No. 5, pp. 404-407, (1970).

[184] K.W. Sexton, K.M. Horn et al., "Relationship between IBICC imaging and SEV in CMOS IC's," *IEEE Trans. on Nucl. Sci*., Vol. 40, No. 6, p. 1787 (1993).

[185] D.V. Lang, *J. Appl. Phys*., Vol. 45, p. 3023 (1974).

[186] G.L. Miller, D.V. Lang and L.C. Kimberling, "A correlation method for semiconductor transient signal," *J. Appl. Phys*, Vol. 46, No. 6, pp. 2638-2644 (1975).

[187] D.K. Schroder, "Semiconductor material and device characterisation," *John Wiley & Sons*, ISBN 0-471-51104-8 (1990).

[189] J.W. Chen and A.G. Milnes, "Energy levels in silicon," *Ann. Rev. Mater. Sci.*, Vol. 10, pp. 157-228 (1980).

[190] T. Schulz, "Investigation on the long term behaviour of damage effects and corresponding defects in detector grade Si after neutron irradiation," Ph.D. Thesis, University of Hamburg (1995).

[191] Verbitskaya et al., *Sov. Phys. S.C.* Vol. 26, No. 11, p. 1101 (1992).

[192] Nagasawa and M. Sculz, *J. Appl. Phys*., p. 835 (1975).

[193] H.F. Wolf "Si semiconductor data," *International series of monographs on semiconductors.* (1969).

[194] J.B. Marion and J.L. Fowler, "Fast neutron Physics: Part 1," Interscience publishers, INC., New York, (1960).

[195] H.J. Ziock, et al., "Temperature dependence of radiation damage and its annealing in silicon detectors, " *IEEE Trans. on Nucl. Sci.*, Vol. 40, No. 4, p. 344 (1993).

[196] ASTM E 722 – 94, "Standard Practice for Characterizing Neutron Energy Fluence Spectra in Terms of an Equivalent Monoenergetic Neutron Fluence for Radiation-Hardness Testing of Electronics," *1996 Annual Book of ASTM Standards*, Vol. 12.02, pp. 318-333 (1996).

[197] L. Vismara, "Radiation damage effects on silicon detectors, " presented at the Conf. on advanced technology and particle physics, Como, Italy (1988).

[198] Z. Li, W. Chen and H.W. Kraner, "Effects of fast neutron radiation on the electrical properties of silicon detectors," *Nucl. Instr. and Meth. in Phys. Res. Section A*, Vol. 308, p. 585 (1991).

[199] E. Borichi, et al., "Deep-level transient spectroscopy measurements of majority traps in neutron irradiated n-type silicon detectors," *Nucl. Instr. and Meth. in Phys. Res. Section A*, Vol. 279, pp. 277-280 (1989).

[200] Z. Li, et al., "Investigation of the oxygen vacancy (A-centre) defect complex profile in neutron irradiated high resistivity silicon junction particle detectors," *IEEE Trans on Nucl. Sci*., Vol. NS-39, No. 6, p. 1730 (1992).

[201] M. Bosetti, C. Leroy, "DLTS measurements of energetic levels, generated in silicon detectors," *Nucl. Instr. and Meth. in Phys. Res. Section A*, Vol. 361, pp. 461-465 (1991).

[202] E. Fretwurst, C. Dehn, H. Feick, P. Heydarapoor, G. Lindstrom, M. Moll, C. Schutze, and T. Shulz, "Neutron induced defects in silicon detectors characterized by DLTS and TSC methods," *Nucl. Instr. and Meth. in Phys. Res. Section A*, Vol. 377, pp. 258-264 (1996).

[203] M. Moll, H. Feick, E. Fretwurst, G. Lindstrom and C. Schutze, "Comparison of defects produced by fast neutrons and ^{60}Co-gammas in high-resistivity silicon detectors using deep-level transient spectroscopy," *Nucl. Instr. and Meth. in Phys. Res. Section A*, Vol. 388, pp. 335-339 (1997).

[204] B.S. Avset, "Measurements on a hole trap in neutron-irradiated silicon," *Nucl. Instr. and Meth. A*, Vol. 388, pp. 361-364 (1997).

[205] W.E. Phillips and J.R. Lowney, "Analysis of non-exponential transient capacitance in silicon diodes heavily doped with platinum," *J. Appl. Phys.*, Vol. 54, No. 5 (1983).

[206] A.C. Wang and C.T. Sah, "Determination of trapped charge emission rate from non-exponential capacitance transients due to high trap densities in semiconductors," *J. Appl. Phys.*, Vol. 55, p. 565 (1984).

[207] D. Stievenard, M. Lanou, et al., "Transient capacitance spectroscopy in heavily compensated semiconductors," *Solid-State Electron.* Vol. 28, p. 485 (1985).

[208] G. Goto, S. Yanagisawa, O. Wada and H. Takanashi, "Determination of deep-level energy and density profiles in inhomogeneous semiconductors,"*Appl. Phys. Lett.*, Vol. 23, pp. 150-151 (1973).

[209] N.M. Johnson, "Measurement of semiconductor-insulator interface states by constant-capacitance, deep-level transient spectroscopy," *J. Vac. Sci. Tech.*, Vol. 21, pp. 303-314 (1982).

[210] J.A. Pals, "Properties of Au, Pt, Pd and Rh levels in silicon measured with a constant capacitance technique," *Solid-State Electron*, Vol. 17, pp. 1139-1145 (1974).

[211] E. Borchi, M. Bruzzi and M.S. Mazzoni, "Thermally stimulated nand leakage current analysis of neutron irradiated silicon detectors," *Nucl. Instr. and Meth. in Phys. Res. Section A*, Vol. 310, pp. 273-276 (1991).

[212] A. Baldini, E. Borchi, M. Bruzzi and P. Spillantini, "Electrical and spectroscopic analysis of neutron irradiated silicon detectors," *Nucl. Instr. and Meth. in Phys. Res. Section A*, Vol. 315, pp. 182-187 (1992).

[213] A. Baldini and M. Bruzzi, "Thermally stimulated current spectroscopy: Experimental techniques for the investigation of silicon detectors," *Rev. Sci. Instrum.*, Vol. 64, No. 4, p. 932 (1993).

[214] M. Bruzzi, “TSC data-analysis on heavily irradiated silicon detectors,” *Nucl. Instr. and Meth. in Phys. Res. Section A*, Vol. 352, pp. 618-621 (1995).

[215] H. Feick, E. Fretwurst et. al., “Analysis of TSC spectra measured on silicon pad detectors after exposure to fast neutrons, ” *Nucl. Instr. and Meth. in Phys. Res. Section A*, Vol. 388, pp. 323-329 (1997).

[216] C. Li and Z. Li, “Characterisation of high fluence neutron induced defect levels in high resistivity silicon detectors using a laser deep level transient spectroscopy (L-DLTS),” *Nucl. Instr. and Meth. in Phys. Res. Section A*, Vol. 342, pp. 137 (1994).

[217] Z. Li, C.J. Li, V. Eremin and E. Verbitskaya, “Investigation on the N_{eff} reverse annealing effect using TSC/I-DLTS: relationship between neutron induced microscopic defects and silicon detector electrical degradations, ” *Nucl. Instr. and Meth. in Phys. Res. Section A*, Vol. 377, p. 265 (1996).

[218] Z. Li, G. Ghislotti, H.W. Kraner, C.J. Li, B. Nielsen, H. Feick and G. Lindstroem, “Microscopic analysis of defects in a high resistivity silicon detector irradiated to 1.7E15 $n \cdot cm^{-2}$,” *IEEE Trans. on Nucl. Sci.*, Vol. 43, No. 3, p. 1590 (1996).

[219] D. Alexiev, K.S.A. Butcher, T.L. Tansley, “A deep-level transient-conductance spectrometer for high-resistivity semiconductors using a marginal oscillator detector,” *Jpn. J. Appl. Phys.*, Vol. 31, Part 1, No. 6A, pp. 1909-1914 (1992).

[220] S. T. Lai, B. D. Nener, D. Alexiev and K. S. A. Butcher, *Jpn. J. Appl. Phys.*, Vol. 33, p. 199 (1994).

[221] S. T. Lai, D. Alexiev, C. Schwab and I. Donnelly, *Nucl. Instr. and Meth. in Phys. Res. Section A*, Vol. 395 p. 76 (1997).

[222] S. T. Lai, B. D. Nener, D. Alexiev, L. Faraone, T. C. Ku and N. Dytlewski, *J. Appl. Phys*. Vol. 77, p. 2985 (1995).

[223] D. Alexiev, K. S. A. Butcher and T.A. Tansley, *Jpn. J. Appl. Phys*. Vol. 32. p. 1855 (1993).

[224] J. D. Idione and J. R. Brandenberger, *Rev. Sci. Instrum.* Vol. 42, p. 715 (1971).

[225] S. M. Sze, "Physics of Semiconductor Devices," 2nd edition, Wiley, New York, p. 750 (1981).

[226] S. D. Brotherton, *J. Appl. Phys.* Vol. 55, p. 3636 (1984).

[227] L.C. Kimberling, J.L. Benton, *Appl. Phys. Lett*., Vol. 39, p. 410 (1981).

[228] X. Le Cleach, *Solid State Communication*, Vol. 85, p. 799 (1993).

[229] "PeakFit™: Peak separation and analysis software," *Jandel Scientific Software*, Version 4 (1995).

[230] M.N. Wybourne, "Thermal Conductivity of Si," Rn=15711, In Properties of Silicon, EMIS Data Review Series No. 4, ISBN 0 9=85296 475 7, p. 37 (1988).

[231] G.E. Gellison, Jr, *J. Appl. Phys.*, Vol. 53, p. 5715 (1982).

[232] L.W. Song, X.D. Zhan, B.W. Benson and G.D. Watkins, "Bistable interstitial-carbon-substitutional-carbon pair in silicon," *Phys. Rev. B*, Vol. 42, pp. 5765-5784 (1990).

[233] L.W. Song, X.D. Zhan, B.W. Benson and G.D. Watkins, "Bistable Defect in Silicon: The Interstitial-Carbon-Substitutional-Carbon Pair," *Phys. Rev. Lett.*, Vol. 60, No. 5, pp. 460-463 (1988).

[234] M.T. Asom, L.C. Kimerling, et al., "Interstitial defect reactions in silicon," *Appl. Phys. Lett*. Vol. 51, No. 4 (1987).

[235] G.D. Watkins, Radiation Damage in Semiconductors, (*Dunod: Paris*) p. 97 (1965).

[236] G.D. Watkins, K.L. Brower, "EPR observation of the isolated interstitial carbon atom in silicon," *Phys. Rev. Lett.* Vol. 36, No. 22 (1976).

[237] K.L. Brower, "EPR of a Jahn-Teller distorted <111> carbon interstitial in irradiated Si," Phys. Rev. B, Vol. 15, No. 8, p. 3836 (1977).

[238] R.C. Newman and A.R. Bean, *Radiation Effects*, Vol. 8, pp. 189-193 (1971).

[239] R. Woolley, E.C. Lightowlers, et al., "Electronic and vibrational absorption of interstitial carbon in silicon," Defects in semiconductors – Ed. H.J.von Bardeleben. *Mat. Sci. Forum*, Vol. 10-12, pp. 929-934 (1986).

[240] G. Davies, "Carbon-related processes in crystalline silicon," *Mat. Sci. Forum.*, Vol. 38-41, pp. 151-158 (1989).

[241] G.D. Watkins, "A microscopic view of radiation damage in semiconductors using EPR as a probe," *IEEE Trans. on Nucl. Sci.*, Vol. 16, No. 6, p. 13 (1969).

[242] U. Biggeri, E. Borichi, et al., "Studies of deep levels in high resistivity silicon detectors irradiated by high fluence fast neutrons using a thermally stimulated current spectrometer," *IEEE Trans. on Nucl. Sci* ., Vol. 41, No. 4, p. 964 (1994).

[243] E. Borchi, M. Bruzzi and M.S. Mazzoni, "Thermally stimulated current analysis of neutron irradiated silicon," *Phys. Stat. Sol.* (a), Vol. 124, p. K27 (1991).

[244] O.O. Awadelkarim and B. Monemar, *J. Appl. Phys*. Vol. 64, p. 6306 (1988).

[245] S.D. Brotherton and P. Bradley, *J. Appl. Phys.*, Vol. 53, p. 5730 (1982).

[246] J. Matheson, M. Robbins, S. Watts, G. Hall and B. MacEvoy, "A microscopic explanation for type inversion and the annealing behaviour of radiation damaged silicon detectors," *Nucl. Instr. and Meth. in Phys. Res. Section A*, Vol. 371, pp. 575-577 (1996).

[247] B.C. MacEvoy, "Defect evolution in silicon detector material," *Nucl. Instr. and Meth. in Phys. Res. Section A*, Vol. 388, pp. 365-369 (1997).

[248] S.J. Watts et al., "A new model for generation-recombination in silicon depletion regions after neutron irradiation," *IEEE Trans. on Nucl. Sci* ., Vol. 43, No. 6, p. 2587-2594 (1994).

[249] G.D. Watkins, "EPR of a trapped vacancy in boron-doped silicon," *Phys. Rev. B*, Vol. 13, No. 6, pp. 2511-2517 (1976).

[251] A.R. Bean, S.R. Morrison, R.C. Newman and R.S. Smith, "Electron irradiation damage in silicon containing high concentrations of boron," *J. Phys C: Solid State Phys.*, Vol. 5, pp. 379-400 (1972).

[252] G.D. Watkins, "Defects in irradiated silicon: EPR and electron-nuclear double resonance of interstitial boron," *Phys. Rev. B*, Vol. 12, No. 12, pp. 5824-5839 (1975).

[253] P.M. Mooney, L.J. Cheng, M. Suli, J.D. Gerson and J.W. Corbett, "Defect energy levels in boron-doped silicon irradiated with 1-MeV electrons," *Phys. Rev. B*, Vol. 15, No. 8, pp. 3836-3843 (1977).

[254] R. Wunstorf, W.M. Bugg, J. Walter, F.W. Garber and D. Larson, "Investigations of donor and acceptor removal and long term annealing in silicon with different boron/phosphorus ratios," *Nucl. Instr. and Meth. in Phys. Res. Section A*, Vol. 377, pp. 228-233 (1996).

[255] L.I. Murin, "On the electrical activity of the C_i - O_i complex in silicon," *Phys. Stat. Sol., (a)*, Vol. 101, p. K107 (1987).

[256] M.R. Brozel, R.C. Newman and D.H.J. Totterdell, "Interstitial defects involving carbon in irradiated silicon," *J. Phys C: Solid State Phys.*, Vol. 8, pp. 243-248 (1975).

[257] F.N.H. Robinson, *J. Sci. Instrum.*, Vol. 36, p. 481 (1959).

[258] G. Davies, E.C. Lightowlers, et al., "A model for radiation damage effects in carbon-doped crystalline silicon," *Semicond. Sci. Technol.*, Vol. 2, pp. 524-532 (1987).

[259] G. Davies et al., *Phys. C. Solid State Phys.*, Vol. 19, p. 841 (1986).

[260] G. Lindstrom, et al., RD48 (ROSE collaboration), "Developments for radiation hard silicon detectors by defect engineering - Results by the CERN RD48 (ROSE) collaboration," *ROSE Technical Note*, Vol. TN/2000/06 (2000).

[261] W. Kaiser and C.D. Thurmond, "Nitrogen in Silicon," *J. Appl. Phys.*, Vol. 30, No. 3 p.427 (1959).

[262] T. Abe, H. Harada, N. Ozawa and K. Adomi, "Deep level generation-annhillation in nitrogen doped float zoned silicon", *Materials Research Society*, Vol. 59, "Oxygen,

carbon, hydrogen and nitrogen in crystalline silicon", Ed. By J.C. Mikkelson Jr, S.J. Pearton, J.W. Corbett and S.J. Pennycook (1986).

[263] M. Tajina, T. Masui, T. Abe and T. Nozaki, *Jap. J. Appl. Phys.*, Vol. 20, L423 (1981).

[264] Y. Yatsurgi, N. Akiyama, Y. Endo and T. Nozaki., *J. Electrochem. Soc.*, Vol. 120, p. 975 (1973).

[265] K.L. Brower, *Phys. Rev. B.*, Vol. 26, p. 6040 (1982).

[266] K.L. Brower, *Phys. Rev. Lett.*, Vol. 44, p. 1627 (1980).

[267] H.P. Hjalmarson, D.R. Jennison and J.R. Binkley., "Off-centre nitrogen and oxygen in silicon", *Materials Research Society*, Vol.59, "Oxygen, carbon, hydrogen and nitrogen in crystalline silicon," Ed. By J.C. Mikkelson, Jr, S.J. Pearton, J.W. Corbett and S.J. Pennycook (1986).

[268] H.J. Stein, "Nitrogen in crystalline silicon," *Materials Research Society*, Vol.59, "Oxygen, carbon, hydrogen and nitrogen in crystalline silicon", Ed. By J.C. Mikkelson, Jr, S.J. Pearton, J.W. Corbett and S.J. Pennycook (1986).

[269] H.J. Stein, "Infrared absorption band for substitutional nitrogen in silicon", *Appl. Phys. Lett.* Vol. 47, No. 12, p. 1339 (1985).

[270] T. Abe, K. Kikuchi, S. Shirai and S. Muraka, "Semiconductor silicon," edited by H.R. Huff and Y. Takeishi. (1981).

[271] H.J. Stein, "Vibrational absorption bands for implanted nitrogen in crystalline silicon," *Appl. Phys. Lett.*, Vol. 43, No. 3, p. 296 (1983).

[272] Y. Yatsurgi, N. Akigama, Y. Endo and T. Nozaki., *J. Electrochem. Soc.*, Vol. 120, p. 985 (1973).

[273] T. Abe, T. Masui, H. Harada and J. Chikawa, *Proc. 3rd Int. Symp. VLSI Sci. Technol. Toronto, Canada (1985), Electrochem. Soc.*, Pennington NJ, USA, Vol. 85-7 (1985).

[274] P.V. Pavlov, E.I. Zorin, P.I. Telelbaum and A.F. Khkhow, *Phys. Stat. Sol. A*, Vol. 35, p. 11 (1976).

[275] M. Sprenger, E.G. Sieverts, S.H. Muller and C.A.J. Ammerluon, "Electron paramagnetic resonance of a nitrogen related centre in electron irradiated silicon," *Solid State comm.*, Vol. 51, No. 12, p. 951 (1984).

[276] A. Rosenfeld, V. Khivrich, et al. "Use of Ukrainian semiconductor dosimeters in a CERN particle accelerator field," *IEEE Trans. on Nucl. Sci.*, Vol. 41, No. 4, pp. 1009-1013 (1994).

[277] M.A. Oliver. "PIN diode and neutron spectrum measurements at the army pulse radiation facility," *IEEE Trans. on Nucl. Sci.*, Vol. 41, No. 6, p. 2132 (1994).

[278] J. Lindhard and P.V. Thompson, "Sharing of Energy Dissipation between Electronic and Atomic Motion," *Proceedings of the Symposium on Radiation Damage in Solids and Reactor Materials*, Int. Atomic Energy Agency, Venice, p. 65 (1962).

[279] A.R. Sattler, "Ionization Produced by Energetic Silicon Atoms within a Silicon Lattice," *Phys. Rev*., Vol. 138, No. 6A, pp. 1815-1821 (1965).

[280] E.C. Smith, D. Binder, et al., "Theoretical and experimental determinations of neutron energy deposition in silicon," *IEEE Trans. on Nucl. Sci.*, Vol. 13, No. 6, p. 11, (1966).

[281] A.R. Sattler and L. Vook, "Partition of the Average Energy Deposited in Silicon as a function of Incident Neutron Energy," *Phys. Rev*., Vol. 155, No. 2, pp. 211-217 (1967).

[282] R.R. Speers, "Neutron energy dependence of excess charge carrier lifetime degradation in silicon," *IEEE Trans. on Nucl. Sci.*, Vol. 15, p. 9 (1968).

[283] J.M. McKenzie, "Reactor Equivalence of an Arbitrary Neutron Spectrum by Multi-source Synthesis," *IEEE Trans. on Nucl. Sci.*, Vol. 20, pp. 18-25 (1973).

[284] V.C. Rogers, L. Harris Jr., D.K. Steinmann and D.E. Bryan, "Silicon Ionization and Displacement kerma for Neutrons from Thermal to 20 MeV," *IEEE Trans. on Nucl. Sci.*, Vol. 22, No. 6, pp. 2326-2329 (1975).

[285] W.R. Van Antwerp, J.E. Youngblood, "Calculated and measured displacement in silicon for monoenergetic neutrons," *IEEE Trans. on Nucl. Sci.*, Vol. NS-24, No. 6, pp. 2521-2526 (1977).

[286] R.E. Macfarlane, D.W. Muir and F.M. Mann, "Radiation Damage Calculations with NJOY," *J. of Nucl. Mat.*, Vol. 122 & 123, pp. 1041-1046 (1984).

[287] "Nuclear Data for Neutron and Proton Radiotherapy and for Radiation Protection," *ICRM* Report 63, USA (2000).

[288] T.F. Luera, J.G. Kelly, H.J. Stein et al., "Neutron damage equivalence for silicon, silicon dioxide, and gallium arsenide," *IEEE Trans. on Nucl. Sci.*,, Vol. 34, pp. 1557-1563 (1987).

[289] A.M. Ougouag, J.G. Williams, et al., "Differential displacement KERMA cross sections for neutron interactions in Si and GaAs," *IEEE Trans. on Nucl. Sci.*, Vol. 37, No. 6, pp. 2219-2228 (1990).

[290] A.L. Namenson, E.A.Wolicki, G.C.Messenger. "Average silicon neutron displacement KERMA factor at 1MeV," *IEEE Trans. on Nucl. Sci.*, Vol. 39, p. 1018 (1982).

[291] A.J. Koning, "Processing and Validation of Intermediate Energy Evaluated Data Files," *A report by the Working Party on International Evaluation Co-operation of the NEA Nuclear Science Committee*, NEA/WPEC, Vol. 14 (2000).

[292] P.J. Griffin, J.G. Kelly, et al., "Neutron damage equivalence in GaAs," *IEEE Trans. on Nucl. Sci*., Vol. 38, No. 6, pp. 1216-1224 (1991).

[293] W.N. McElroy, S. Berg, T.B. Crockett and R.J. Tuttle, *Nucl. Sci. Eng.*, Vol. 36, p. 15 (1969).

[294] F.W. Stallmann, "LSM-M2: A Computer Program for Least Squares Logarithmic Adjustment of Neutron Spectra," NUREG/CR-4349, Nuclear Regulatory Commission, Washington, DC (1985).

[295] J.G. Williams, P.J. Griffin, J.G. Kelly and J.T. Figueroa, "Estimation of 1-MeV Equivalent Neutron Fluence from Dosimetry Responses without Spectrum Unfolding" *IEEE Trans. on Nucl. Sci.*,, Vol. 41, No. 6, pp. 2147-2151, (1994).

[296] ASTM E 720 – 94, "Standard Guide for Selection and Use of Neutron-Activation Foils for Determining Neutron Spectra Employed in Radiation-Hardness Testing of Electronics," *1996 Annual Book of ASTM Standards*, Vol. 12.02, pp. 296-307 (1996).

[297] ASTM E 721 – 94, "Standard Guide for Determining Neutron Energy Spectra from Neutron Sensors for Radiation-Hardness Testing of Electronics," *1996 Annual Book of ASTM Standards*, Vol. 12.02, pp. 307-317 (1996).

[298] J.M. Swartz and M.O. Thurston, "Analysis of the effect of fast-neutron bombardment on the current-voltage characteristics of a conductivity-modulated p-i-n diode," *J. Appl. Phys*., Vol. 37, No. 2, p. 745 (1965).

[299] A. B. Rosenfeld, I.E. Anokhin, L.I. Barabash et al., "P-I-N diodes with a wide measurement range of fast neutron doses," *Rad. Prot. Dos*., Vol. 33, No. 1/4, pp. 175-178 (1990).

[300] O.J. Mengali, E. Paskell, R.W. Beck and C.S. Peet, *Proceedings of the second conference on Nuclear Radiations Effects on Semiconductor Devices, Materials and Circuits* (1959).

[301] J.M. Swartz and L. Browne, "Experimental calibrations of a silicon rectifier developed as a fast neutron sub-miniature dosimeter," *IEEE Trans. on Nucl. Sci*., Vol. 10, p. 63 (1963).

[302] G. Kramer, "The semiconductor Fast-Neutron Dosimeter – It's Characteristics and Applications," *IEEE Trans. on Nucl. Sci*, Vol. 13, No. 1, pp. 104-110 (1966).

[303] M.O. Thurston, J.M. Swartz, et al., "A silicon fast neutron dosimeter with a wide sensitivity range," Neutron monitoring, IAEA Vienna (1967).

[304] R.R. Speers, "Neutron energy dependence of excess charge carrier lifetime degradation in silicon," *IEEE Trans. on Nucl. Sci*, Vol. 15, p. 9 (1968).

[305] Z. Prouza, A. Skubal, J. Bohacek and J. Trousil, "Interpretation of the response of dosimetric Si-diode," *Jad. Energ.*, Vol. 28, pp. 318-323 (1982).

[306] A. Rozenfeld, V. Khivrich, O. Zinets et al., "Development of Semiconductor Sensors for Dosimetry of Mixed Radiation Fields," *Radiation Protection in Australia*, Vol. 12, No. 4, pp. 156-163 (1994).

[307] J. Morin, J.C. Arnoud, J. David and P. Zyromski, "Widening the Range in Measuring Neutron Fluences with PIN Silicon Diodes," *Third European Conference on Radiation and its Effects on Components and Systems, RADECS 95'*, Arcachon, France, pp. 476-480 (1995).

[308] Private communication with A. Rosenfeld.

[309] Proc. IAEA Panel Neutron Standard Reference Data, Vienna, Austria, November 20-24, 1972, CONF-721127, pp. 362, International Atomic Energy Agency, Vienna, (1973).

[310] Proc. IAEA Consultants' Mtg. Promt Fission Neutron Spectra, Vienna, Austria, August 25-27, 1971, pp. 169, International Atomic Energy Agency, Vienna, (1972).

[311] O.K. Harling, J.A. Bernard and R.G. Zamenhof, "Neutron Beam Design, Development, and Performance for Neutron Capture Therapy," *Proceedings of an international workshop on Neutron Beam Design*, etc., March 29-31, (1989) Massachussetts.

[312] Private communication with Martin Carolan. Details on the Petten facility and pin dosimeter diode calibration were provided by Martin Carolan.

[313] H. Liskien and A. Paulsen, "Neutron Production Cross Sections and Energies for the Reactions ^{7}Li(p,n)^{7}Be and ^{7}Li(p,n)^{7}Be*," *Atomic Data and Nuclear Data Tables*, Vol. 15, pp. 57-84 (1975).

[314] Winter and Schimd, *EUR* 3908e (1968).

[315] M.S. Livingston and H. Bethe, *Rev. Mod. Phys.*, Vol. 9, p. 263 (1937).

[316] W. Whaling. "Handbook of Physics," Edited by S. Flugge, Springer-Verlag, Berlin, Vol. 34, p. 193 (1958).

[317] Private Communication with John Fallon, Physics Division, ANSTO.

[318] A.O. Hansen and J.L. McKibben, "A Neutron Detector Having Uniform Sensitivity from 10 keV to 3 MeV," *Phys. Rev.*, Vol. 73, No. 8, p. 673 (1947).

[319] J.De Pangher, "Double Moderator Neutron Dosimeter," *Nucl. Instr. and Meth. in Phys. Res. Section A*, Vol. 5, pp. 61-74 (1959).

[320] J.De Pangher, “A Reproducible Precision Polyethylene Long Counter for Measuring Fast Neutron Flux,” Presented at the American Physical Society, Washington, D.C. (1961).

[321] J.M. Adams, A.T.G. Ferguson and C.D. McKenzie, “An Activation Technique for the Absolute Calibration of a Long Counter,” United Kingdom Atomic Energy Authority Report AERE – R 6429 (1970).

[322] M. Reinhard, Technical Report AP/TN (In preparation).

[323] P. S. Winokur, F. W. Sexton, D. M. Fleetwood, et al. “Implementing QML for radiation hardness assurance,” *IEEE Trans. Nucl. Sci*., Vol. 37, No. 3, p. 1794, (1990).

[324] Sadrodizinsky, “Silicon Strip Detectors in High Luminosity Applications,” *IEEE Trans. Nucl. Sci*., Vol. 45, No. 3, (1998).

[325] A. Bozek, S.K. Sahu, H. Ozaki and S. Uno, “Simulation Study of Beam-backgrounds on Silicon Vertex Detector at KEK B-factory,” *BELLE note 174*, May (1997).

[326] A. Bozek, private communication with A Rosenfeld.

[327] J.A. Lauber, S. Gascon-Schotkin, R.G. Kellogg and G.R. Martinez, “Energy dependence of damage to Si PIN diodes exposed to β radiation,” *Nucl. Inst. And Meth. A*, Vol. 396, pp. 165-171 (1997).

[328] O. Biebel, S. Braibant et al., “Radiation Monitoring and Beam Dump System of the OPAL silicon Microvertex Detector,” *Nucl. Instr & Meth. In Phys. Res. A*, Vol. 403, pp. 351-362 (1998).

[329] Falkiner High Energy Physics Department, University of Sydney, “Radiation Monitoring System,” www.physics.usyd.edu.au/hienergy/belle_local.html#radiation.

[330] G.P. Summers, E.A. Burke, P. Shapiro, S.R. Messenger and R.J. Walters, “Damage Correlations in Semiconductors Exposed to Gamma, Electron and Proton Radiations,” *IEEE Trans. Nucl. Sci*., Vol. 40, No. 6, p. 1372-1379 (1993).

[331] G. Linstrom, “Displacement Damage in Silicon,” http://sesam.desy.de/~gunnar/Si-dfuncs.html.

[332] S.J. Watts, *Nucl. Instr. & Meth. A*, Vol. 386, p. 149 (1997).

[333] D.E. Aspnes, “Optical Functions of Intrinsic Si: Table of Refractive Index, Extinction Coefficient and Absorption Coefficient vs Energy (0 to 400 eV),” EMIS Datareview RN=17807, *INSPEC London and New York*, ISBN 0 85296 475 7, p. 72 (1988).

[334] J.M. Allen in "X-Rays in Theory and Experiment," edited by A.R. Compton and S.K. Allison, D. Van Nostrand Company (1935).

[335] F.H. Attix, "Introduction to Radiological Physics and Radiation Dosimetry," Wiley-Interscience Publication, ISBN 0-471-01146-0 (1986).

[336] A.G. Holmes-Siedle & K. Zaininger, *IEEE Trans. Reliability,* Vol. 17, p. 34 (1968).

[337] A. Holmes-Siedle & L. Adams, "RADFET: A Review of the Use of Metal-Oxide-Silicon Devices as Integrating Dosimeters," *Radiat. Phys. Chem.*, Vol. 28, No. 2, pp. 235-244 (1986).

[338] N.G. Blamires, D.H.J. Totterdell, A.G. Holmes-Siedle and & L. Adams, "pMOS Dosimeters: Long-Term Annealing and Neutron Response," *Rad. Prot. Dosimetry,* Vol. 33, No.1/4, pp. 175-178 (1990).

[339] A.K. Tipping and R.C. Newman, "Semiconductor Science & Technology," Vol. 2, pp. 389-398 (1987).

[340] K.S.A. Butcher, D. Alexiev and J.W. Boldeman, *Nucl. Instru. & Meth. in Phys. Res. Section B,* Vol. 95, pp. 355-370 (1995).

[341] A. Abashian et al., "The Belle Detector," *Nucl. Instru. & Meth. in Phys. Res. Section A*, Vol. 479, pp. 117-232 (2002).

LIST OF PUBLICATIONS

Journal Publications

High Purity Silicon as a Basic Material for Manufacturing of Radiation Detectors and Integral Dosimeters
M.I. Reinhard, A. Rosenfeld, D. Alexiev, V.I. Khivrich, M.D. Varentsov, P.G. Litovchenko, A.I. Anokhin and O.S. Zinets
IEEE Transactions on Nuclear Science, Vol. 43, No. 6, pp. 2687-2692 (1996).

A System for Radiation Damage Monitoring
A.B. Rosenfeld, M.I. Reinhard, D. Marinaro, P. Ihnat, N. Freeman, G. Taylor, L. Peak and A. Holmes-Siedle
IEEE Transactions on Nuclear Science, Vol. 47, No. 6, pp. 1766-1773 (1999).

A Transient Conductance Technique for Characterisation of Deep Level Defects in Highly Irradiated Detector Grade Silicon
D. Alexiev, M.I. Reinhard, L. Mo and A. Rosenfeld,
Nuclear Instruments and Methods in Physical Research A, Vol. 434, pp. 103-113 (1999).

Conference Proceedings

Determination of 1 MeV Equivalent Neutron Fluence Using a P-I-N Dosimeter Diode
M.I. Reinhard, A. Rosenfeld and D. Alexiev.
Presented at the "4th Australian Experimental High Energy Physics Meeting and Workshop", ANSTO 11th –12th Dec. (1995).

Radiation Hardness Study of High Purity Detector Grade Silicon
M.I. Reinhard, A. Rosenfeld and D. Alexiev.
Presented at the "1996 Conference on Optoelectronic and Microelectronic Materials and Devices", Australian National University 8th –11th Dec. (1996). IEEE catalog number: 96TH8197, ISBN 0-7803-3374-8.

Radiation Hardness Study of High Purity Silicon and the Effect of Room Temperature Annealing on the Defect Structure

M.I. Reinhard, A. Rosenfeld, D. Alexiev, V.I. Khivrich, M.D. Varentsov, P.G. Litovchenko, A.I. Anokhin, O.S. Zinets.
Presented at the "5th Australian Experimental High Energy Physics Meeting and Workshop", University of Sydney, 16th –18th Dec. (1996).

Radiation Hardness of Silicon Detectors
M.I. Reinhard, A. Rosenfeld, D. Alexiev, V. Perevertailo, O.S. Frolov, F. Lemeilleur.
Presented at the "6th Australian Experimental High Energy Physics Meeting and Workshop" University of Sydney, 15th –16th Dec. (1997).

Physics of Room Temperature Annealing of Radiation Defects in Silicon Detectors Irradiated with Fast Neutrons
M.I. Reinhard, A. Rosenfeld, D. Alexiev, V. Perevertailo, O.S. Frolov, F. Lemeilleur.
Presented at the "Hiroshima at Melbourne 3rd International Symposium on Semi-Conductor Detectors Devices," Melbourne, Australia, Dec. (1997).

Radiation Hardness of High Purity 'Detector Grade' Silicon
M. Reinhard and A. Rosenfeld.
Presented at the "International Biennial Materials Conference of IMEA," The Materials Society of IEAust, Wollongong, Australia, 6-8th July (1998).

A System for Radiation Damage Monitoring
A.B. Rosenfeld, M.I. Reinhard, D. Marinaro, P. Inhat, G. Taylor, L. Peak, N. Freeman, D. Alexiev, A. Holmes-Siedle.
Presented at the 36th Annual International "Nuclear Space Radiation Effects Conference (NSREC)," Virginia, USA, (1999).

Radiation Damage in High Purity Silicon: Comparison between Neutron and Electron Irradiation
M. Reinhard, A. Rosenfeld and D. Alexiev.
Presented at the "8th Australian Experimental High Energy Physics Meeting and Workshop", School of Physics, University of Melbourne, 9th –11th Dec. (1999).

A System for Radiation Damage Monitoring on HEP Accelerators
A.B. Rosenfeld, M.I. Reinhard, N. Freeman, P, Ihnat, M. Lerch, D. Alexiev, G.N. Taylor, L. Peak, A. Backich, S. Mao and A. Holmes-Siedle.

Presented at 18th Nuclear and Particle Physics Conference, University of Adelaide, Adelaide, SA, Australia, 10th-15th December (2000). ISBN 0 9577217 5 7

PIN Dosimeter Diodes for Radiation Damage Monitoring of Silicon based Devices in Mixed Radiation Fields

M.I. Reinhard, A.B. Rosenfeld and D. Alexiev.

Presented at "Radiation 2000", ISBN 0 9577217 3 0, AINSE, Lucas Heights, NSW, Australia, 26th-28th November (2000). ISBN 0 9577217 3 0.